

→ Space Laser Library

57

NASA CONTRACTOR REPORT

LASER
PIP, BCNASA CR-134952
C75-537/501

NASA CR-134952

UNCLASSIFIED

DISTRIBUTION STATEMENT A

Approved for public release
Distribution Unlimited

ANALYSIS AND DESIGN OF A HIGH POWER LASER ADAPTIVE PHASED ARRAY TRANSMITTER

19980309 346

Prepared By:

G. E. Mevers, J. F. Soohoo, J. Winocur, N. A. Massie
W. H. Southwell, R. A. Brandewie, and C. L. Hayes

DTIC QUALITY INSPECTED 4

PLEASE RETURN TO:

BMD TECHNICAL INFORMATION CENTER
BALLISTIC MISSILE DEFENSE ORGANIZATION
7100 DEFENSE PENTAGON
WASHINGTON D.C. 20301-7100

Prepared for:

National Aeronautics and Space Administration
Lewis Research Center
Cleveland, Ohio

UNCLASSIFIED

U4152

Accession Number: 4152

Publication Date: Mar 01, 1977

Title: Analysis and Design of a High Power Laser Adaptive Phased Array Transmitter

Personal Author: Mevers, G.E.; Soohoo, J.F.; Winocur, J.; Massie, N.; et al.

Corporate Author Or Publisher: Rockwell International, 3370 Miraloma Avenue, Anaheim, CA 92803

Report Number: NASA CR-134952

Report Prepared for: NASA Lewis Research Center, 21000 Brookpark Road, Cleveland, OH 44135 Report

Number Assigned by Contract Monitor: SLL 80-711; CR75-537/501

Comments on Document: Archive, RRI, DEW

Descriptors, Keywords: Analysis Design High Power Laser Adaptive Phased Array Transmitter Optics
Effect Beam Physics Atmosphere Satellite Track Coherence Isoplanatic Patch Weight Size

Pages: 00277

Cataloged Date: Dec 11, 1992

Contract Number: NAS3-18937

Document Type: HC

Number of Copies In Library: 000001

Record ID: 25782

Source of Document: DEW

1. Report No. CR134952		2. Government Accession No.		3. Recipient's Catalog No.	
4. Title and Subtitle Analysis and Design of a High Power Laser Adaptive Phased Array Transmitter				5. Report Date March 1977	
				6. Performing Organization Code	
7. Author(s) G. E. Mevers, J. F. SooHoo, J. Winocur, N. A. Massie, W. H. Southwell, R. A. Brandewie, and C. L. Hayes				8. Performing Organization Report No. C75-537/501	
				10. Work Unit No. V6567	
9. Performing Organization Name and Address Rockwell International 3370 Miraloma Avenue Anaheim, California 92803				11. Contract or Grant No. NAS3-18937	
				13. Type of Report and Period Covered FINAL REPORT	
12. Sponsoring Agency Name and Address NASA Lewis Research Center 21000 Brookpark Road Cleveland, Ohio 44135				14. Sponsoring Agency Code	
15. Supplementary Notes None					
16. Abstract The feasibility of delivering substantial quantities of optical power to a satellite in low earth orbit from a ground based High Energy Laser (HEL) coupled to an adaptive antenna was investigated. These investigations included diffraction effects, atmospheric transmission efficiency, adaptive compensation for atmospheric turbulence effects, including the servo bandwidth requirements for this correction, and the adaptive compensation for thermal blooming. To evaluate possible HEL sources, our atmospheric investigations were performed for CO ₂ , ¹² C ¹⁸ O ₂ isotope, CO and DF wavelengths. For all of these considerations, output antenna locations of both sea level and mountain top (3.5 km above sea level) were used. In general, the results of these investigations indicate that both excellent atmospheric and adaption efficiency can be obtained for mountain top operation with a ¹² C ¹⁸ O ₂ isotope laser operating at 9.1 μm, or a CO laser operating single line (P10) at about 5.0 μm, which was a close second in the evaluation. Four adaptive power transmitter system concepts were generated and evaluated, based on overall system efficiency, reliability, size and weight, advanced technology requirements and potential cost. The winner of the evaluation, titled Multiple Source Phased Array, was selected for detailed conceptual design. This system uses a unique adaption technique of phase locking independent laser oscillators which allows it to be both relatively inexpensive and most reliable with a predicted overall power transfer efficiency of 53%					
17. Key Words (Suggested by Author(s)) Adaptive Optics Atmospheric effects on laser beams Atmospheric physics Satellite tracking			18. Distribution Statement Unclassified - Unlimited.		
19. Security Classif. (of this report) Unclassified		20. Security Classif. (of this page) Unclassified		21. No. of Pages	
				22. Price*	

* For sale by the National Technical Information Service, Springfield, Virginia 22161

UNCLASSIFIED

FOREWORD

This final report is submitted in accordance with the Contract NAS3-18937, "Analysis and Design of a High Power Laser Adaptive Phased Array Transmitter." It relates the results of a study to investigate the feasibility of using a ground-based high energy laser coupled to an adaptive antenna to deliver power to a low-earth orbit satellite. It is submitted by the Electronics Operations of Rockwell International, through the Electronics Device Division, Electronics Research Center, Lasers & Advanced Radiation Systems Group, to the National Aeronautics and Space Administration, Lewis Research Center, Cleveland, Ohio. Dr. Richard A. Brandewie was the Program Manager, and Mr. Gus E. Mevers was the Principal Investigator. The NASA Project Monitor for this work was Dr. Robert M. Stubbs. Significant contributions to the technical effort were made by the following Rockwell personnel:

R. Brandewie
W. Davis
C. Hayes
N. Massie
G. Mevers
J. SooHoo
W. Southwell
J. Winocur

TABLE OF CONTENTS

<u>SECTION</u>	<u>PAGE</u>
I. INTRODUCTION	1
II. TRANSMISSION EFFICIENCY.	9
A. Diffraction Efficiency	9
B. Atmospheric Transmission	12
C. Conclusions	42
III. QUALITY OF ADAPTION FOR ATMOSPHERIC TURBULENCE	45
A. Atmospheric Coherence Length	45
B. Isoplanatic Patch Size	53
C. Adaption Performance Calculations.	58
IV. SERVO BANDWIDTH REQUIREMENTS FOR TURBULENCE CORRECTION	95
A. Antenna Gain	95
B. Vertical Distribution Models	100
C. Numerical Results.	103
D. Conclusions	114
V. THERMAL BLOOMING EFFECTS	117
VI. SYSTEM CONCEPT GENERATION	155
A. System Concepts.	155
B. System Evaluations	191
VII. DETAILED CONCEPTUAL DESIGN	203
A. System Details	204
B. Servo Systems	219
C. Intermediate Optics Considerations	228
D. Tracking Mount	231
E. Weight and Size Considerations	250

	<u>PAGE</u>
F. Technology Development Requirements	253
G. MSPA System Details	256
VIII. CONCLUSIONS	259
APPENDIX A - Thermal Blooming Distortion Parameter as a Function of Altitude.	267

ILLUSTRATIONS

<u>NUMBER</u>	<u>TITLE</u>	<u>PAGE</u>
I-1	Ground-to-Space Power Transmission Scenarios	3
II-1	Scenario Description - Transmission to Satellite	11
II-2	Transmission Range vs Time for Various Offset Distances. . .	13
II-3	Efficiency vs Time for Various Transmitter Diameters and an 0 km Offset Distance	14
II-4	Efficiency vs Time for Various Transmitter Diameters and a 185 km Offset Distance	15
II-5	Efficiency for Total Encounter vs Transmitter Aperture Diameter for Various Offset Distances.	16
II-6	10.6 μm Absorption Coefficient vs Altitude - from McCoy. . .	18
II-7	10.6 μm Absorption Coefficient vs Altitude - from McCoy for July	19
II-8	10.6 μm Absorption Coefficient vs Altitude - from McClatchey	22
II-9	Fractional Transmission vs Transmitter Altitude for Various Atmospheric Models of McCoy.	25
II-10	Fractional Transmission vs Transmitter Altitude for Various Models of McClatchey	26
II-11	Atmospheric Transmission Efficiency for 10.6 μm vs Encounter Time for Various Transmitter Altitudes and Offset Distances	28
II-12	Time Averaged Transmission Efficiency (10.6 μm) for Entire Encounter vs Transmitter Altitude for Various Offset Distances	29
II-13	Atmospheric Extinction vs Altitude	32
II-14	Atmospheric Absorption vs Altitude	33
II-15	Isotope Lasing Bands - from Ref. 9	34
II-16	Atmospheric Extinction vs Altitude	37
II-17	Absorption Coefficients vs Altitude for Two CO Laser Lines - Mid-Latitude Summer Atmospheric Model.	38

ILLUSTRATIONS (Cont.)

<u>NUMBER</u>	<u>TITLE</u>	<u>PAGE</u>
II-18	Comparison of Lasers at Sea Level	40
II-19	Comparison of Lasers at 3.5 km Above Sea Level (Mountain Top Operation).	41
III-1	C_N^2 vs Altitude Above Sea Level	48
III-2	r_o vs Zenith Angle for 3.8 μ m, 5.0 μ m, and 10.6 μ m (Transmitter at Altitude 10 M and Target at Altitude 185 km).	50
III-3	Normalized r_o vs Engagement Time.	51
III-4	Isoplanatic Patch Size vs Zenith Angle for 3.8 μ m, 5.0 μ m, 9.1 μ m, and 10.6 μ m (Target Altitude = 185 km, Transmitter Altitude = 10 M).	56
III-5	Percentage of Transmitted Power into 2-Meter Bucket Due to Isoplanatism	59
III-6	Normalized Constant C vs Ensemble Size (Mesh Size = 4 CM, Mesh Number = 1024)	64
III-7	Eight Screen Representation of Vertical Distribution of Turbulence	66
III-8	Average Relative On-Axis Intensity vs Ensemble Size for D = 4.8 M.	68
III-9	PSYCAT - Flow Chart	75
III-10	Relative Intensity Distribution in Target Plane ($\theta = 0$, Range = 185000 M, 10.6 μ m Propagation in Vacuum). . .	76
III-11	Relative Intensity Distribution in Target Plane ($\theta = 0$, Range = 185000 M, Three 1.6 M, and Five 0.96 M Subapertures, Phase Adaption or Phase Conjugation in Vacuum Considering 10.6 μ m Propagation)	77
III-12	Effects of Finite Element Size in Matching Wavefront Shape	79
III-13	Relative Intensity Distribution in Target Plane ($\theta = 0$, Range = 185000 M, Five 0.96 M Subapertures, Pointing Plus Phase Adaption for 10.6 μ m Propagation in Vacuum) . . .	80
III-14	Relative Intensity Distribution in Target Plane ($\theta = 0$, Range = 185000 M, Three 1.6 M Subapertures, Pointing Plus Phase Adaption for 10.6 μ m Propagation in Vacuum) . . .	81

ILLUSTRATIONS (Cont.)

<u>NUMBER</u>	<u>TITLE</u>	<u>PAGE</u>
III-15	Example of Relative Intensity Distribution in Target Plane ($\theta = 0$, Range = 185 KM, 0.96 M Elements, Phase Adaption or Multidither in Turbulence, 10.6 μm Propagation).	82
III-16	Example of Relative Intensity Distribution in Target Plane ($\theta = 0$, Range = 185 KM, 0.96 M Elements, Phase Conjugation with Lens in Turbulence, 10.6 μm Propagation).	83
III-17	Example of Relative Intensity Distribution in Target Plane ($\theta = 0$, Range = 185 KM, 0.96 M Separation Between Actuators, Deformable Mirror Plus Lens, 10.6 μm Propagation).	84
III-18	Example of Relative Intensity Distribution in Target Plane ($\theta = 0$, Range = 185 KM, 0.96 M Elements, Phase Conjugation Plus Elements Pointed at Target in Turbulence, 10.6 μm Propagation)	85
III-19	Example of Relative Intensity Distribution in Target Plane ($\theta = 0$, Range = 185 KM, 0.96 M Elements, Phase Conjugation Plus Elements Pointed Along Angle of Arrival, 10.6 μm Propagation)	86
III-20	Percentage of Transmitted Power into a 2-Meter Receiver at Altitude 185 KM (Average of 10 Different Realizations) . .	90
III-21	Percentage of Transmitted Power into a 2-Meter Receiver at Altitude 185 KM (Average of 5 Different Turbulence Realizations)	92
IV-1	Phase Error Determination	96
IV-2	Analytical Model for Wind vs Altitude	101
IV-3	C_N^2 vs Altitude Above Sea Level	102
IV-4	Analytical Model for the Refractive-Index Structure Constant C_N^2 vs Altitude.	104
IV-5	Adaption Results with Finite Servo Bandwidth.	105
IV-6	Bandwidth Requirements for 19-Element Array (4.8 M Diameter).	107

ILLUSTRATIONS (Cont.)

<u>NUMBER</u>	<u>TITLE</u>	<u>PAGE</u>
IV-7	Bandwidth Required for 90% Correction	108
IV-8	System Performance for a Seven-Element Array at $\lambda = 9.1 \mu\text{m}$. . .	109
IV-9	System Performance for a Seven-Element Array at $\lambda = 5.0 \mu\text{m}$. . .	110
IV-10	System Performance for a Seven-Element Array at $\lambda = 3.8 \mu\text{m}$. . .	111
IV-11	System Performance Comparing Seven-Element Arrays Scaled According to Wavelength. Propagation Angle was 60°	112
IV-12	Required Servo Bandwidth for 90% Full Correction of Atmospheric Turbulence as a Function of Propagation Angle from the Vertical	113
V-1	Satellite Orbital Geometry.	118
V-2	Seven-Element Transmitter Configuration. Dimensions are Scaled with Wavelength	119
V-3	Kinetic Cooling Diagram for CO_2	121
V-4	Absorption Coefficients vs Altitude	123
V-5	Atmospheric Transmission vs Altitude. Zenith Angle $\theta_z = 0^\circ$, and Wavelengths $\lambda = 10.6 \mu\text{m}$	125
V-6	Atmospheric Transmission vs Altitude. Zenith Angle $\theta_z = 60^\circ$, and Wavelengths $\lambda = 10.6 \mu\text{m}$	126
V-7	Atmospheric Wind Velocity Distribution Model.	127
V-8	Atmospheric Temperature Distribution Model.	128
V-9	Comparison of Far-Field Intensity Patterns.	130
V-10	Comparison of Transmission Efficiency of a Seven-Element Array and a Single Aperture, as a Function of Laser Power for a $10.6 \mu\text{m}$ Laser Beam Propagated from a Ground Site at 10 m Elevation to a Satellite Directly Overhead.	131
V-11	Thermally Bloomed $10.6 \mu\text{m}$ CO_2 Laser Beam Profiles	133
V-12	Relative Power Collected in a 2 m Diameter Bucket vs Transmitter Power	135
V-13	Relative Power Collected in a 2 m Diameter Bucket vs Transmitter Power	136

ILLUSTRATIONS (Cont.)

<u>NUMBER</u>	<u>TITLE</u>	<u>PAGE</u>
V-14	Relative Power Collected in a 2 m Diameter Bucket vs Zenith Angle	138
V-15	Relative Power Collected in a 2 m Diameter Bucket vs Zenith Angle	139
V-16	Relative Power Collected in a 2 m Diameter Bucket vs Zenith Angle	141
V-17	Target Plane Plot of Adaptively Compensated 2-MW 10.6 μm Laser Beam	143
V-18	Target Plane Plot of Adaptively Compensated 5-MW 10.6 μm Laser Beam	143
V-19	Distribution of Phase in the Receiver Plane for Wavefront Returned from Target.	144
V-20	Seven-Element Array Adaption Phase Distribution	144
V-21	Comparison of Received Phase () and Best Fit Mirror Surfaces () for a Line of Data Points Passing Through the Center of the Array Perpendicular to Wind Velocity Vector.. . . .	145
V-22	Target Plane Intensity Distribution for Adaption Using Deformable Mirrors of Unlimited Spatial Frequency Response in Each of the Seven Channels of the Transmitter Array	149
V-23	Thermally Bloomed 10.6 μm CO ₂ Laser Beam Profile, Including Kinetic Cooling Effects	151
V-24	Thermal Blooming Correction with Piston and Tilt Phase Compensation Only	151
V-25	Thermal Blooming Correction when all Orders of Compensation are Applied	152
VI-1	Block Diagram of a Coelostat Hartmann Sensor.	157
VI-2	Coelostat Hartmann Sensor	158
VI-3	Coelostat Mirrors and Torque Motor.	159
VI-4	Hartmann Plate and Processor for Wavefront Sensing and Reconstruction.	161

ILLUSTRATIONS (Cont.)

<u>NUMBER</u>	<u>TITLE</u>	<u>PAGE</u>
VI-5	Signal-to-Noise Ratio vs Spot Diameter at Target	162
VI-6	Signal Power to Backscatter Power from Reflective Components	164
VI-7	Block Diagram of Modified Multidither Concept.	166
VI-8	Multidither Optical Schematic.	167
VI-9	Beam Clean Up Sensors and Processors for Multidither Concept.	168
VI-10	Multidither Concept Information Processors	169
VI-11	Multidither Adaption Processor	171
VI-12	Multiaperture MOPA System Block Diagram.	175
VI-13	Multiaperture MOPA System Optical Schematic.	176
VI-14	Expected MOPA System Doppler Frequency	178
VI-15	Multiple Source Phased Array Block Diagram	181
VI-16	Multiple Source Phased Array Optical Schematic	183
VI-17	Pointing Mount Array Configuration	186
VI-18	Pointing System Cost vs Diameter	188
VI-19	Cost Saving Factor for Hexagonal Close-Packed Array.	190
VII-1	Multiple Source Phased Array Detailed Block Diagram for a Single Channel	205
VII-2	Optical Configuration for Providing a Common Local Oscillator to all Channels	208
VII-3	Gimbal Relay Optic Circuit	210
VII-4	Beam Expansion Telescope Model	211
VII-5	Multiple Source Phased Array Operation Chronology.	215
VII-6	Basic Control Loop	220
VII-7	Modified Control Loop.	223

ILLUSTRATIONS (Cont.)

<u>NUMBER</u>	<u>TITLE</u>	<u>PAGE</u>
VII-8	Beam Clean-Up Control Loop (Target Adaption Control Loop)	225
VII-9	Azimuth-Elevation Tracking Mount Configuration.	232
VII-10	Azimuth Angle vs Time for Various Track Offsets	234
VII-11	Azimuth Angular Velocity vs Time for Various Track Offsets. . .	235
VII-12	Azimuth Angular Acceleration vs Time for Various Track Offsets	236
VII-13	Elevation-Declination Tracking Mount Configuration.	237
VII-14	Elevation Angle vs Time	239
VII-15	Elevation Angular Velocity vs Time.	240
VII-16	Elevation Angular Acceleration vs Time.	241
VII-17	Declination Angle vs Time for Various Track Offsets	242
VII-18	Declination Angular Velocity vs Time for Various Track Offsets	244
VII-19	Declination Angular Acceleration vs Time for Various Track Offsets	245
VII-20	Seven-Element Output Antenna Array of Multiple Source Phased Array System Using Elevation Declination Configured Tracking Mounts.	246
VII-21	MSPA System Tracking Mount and Output Telescope -- One Element of Antenna Array.	247

TABLES

<u>NUMBER</u>	<u>TITLE</u>	<u>PAGE</u>
II-1	10.6 μm Absorption Coefficients vs Altitude from McCoy	20
II-2	10.6 μm Absorption Coefficients vs Altitude from McClatchey.	21
II-3	CO ₂ Isotope Selection:	35
III-1	Percentage of Transmitted Power into 2-Meter Bucket Averaged Over Engagement Time (~ 80 sec) Due to Isoplanatism	60
III-2	Adaptive Optic Transmitter/Receiver Combinations Investigated	69
V-1	Transmitter Dimensions	124
V-2	Compensation of Thermal Blooming	147
V-3	Compensation of Thermal Blooming	148
VI-1	Transmission Efficiency of System Concepts	192
VI-2	Reliability of System Concepts	194
VI-3	Weight and Size Estimates for the Different Concepts	196
VI-4	Technology Advancement Requirements for the Four Concepts. . .	197
VI-5	Estimated Cost (\$M) of Major System Components for Four Concepts.	199
VI-6	Overall Concept Evaluation for Mountain Top Operation (3.5 km) Considering 0.5, 1.0, and 5.0 MW Operation.	201
VII-1	Filter Type.	221
VII-2	Volume Formulae for MSPA System Major Moving Parts	251
VII-3	Moving Weight for MSPA System.	252
VII-4	MSPA System Details.	257

I. INTRODUCTION

With the proviso that the required technology advancement in energy conversion systems can be accomplished, High Energy Lasers (HEL) appear to have considerable potential for space applications. First, there is electrical power generation that can be used for such situations as geosynchronous satellites which have very large energy needs. By delivering the energy from a ground or space based laser, the satellite mass that must be transported into orbit can be significantly reduced and the time on station can also be increased. The second, and perhaps the more important application, is inter-orbital transfer maneuvers. Using laser radiation as the energy input to a rocket engine, a series of propulsion maneuvers of a satellite during successive ground station over-flights can add delta-V to the system and, as a result, transfer large payloads economically between low initial orbits and higher energy orbits. One could consider transferring satellites from a geocentric to selenocentric or heliocentric orbit using a space-to-space laser propagation system. This situation would make use of very large transmit antennas (> 30 m) more feasible and would allow for long power transfer periods. Perhaps a more modest situation, however, would be to assist in establishing a synchronous orbit for a satellite initially in near earth orbit using a ground based laser. A method of accomplishing this latter task that appears promising is to transmit the laser power when the satellite is at perigee. Thus, not only can an efficient Hohmann transfer¹ be performed, but the propagation distance is also minimized. For the ground-to-space situation, however, very serious questions arise regarding our ability to transport useful power levels through the earth's atmosphere, with sufficient angular

accuracy to deposit energy efficiently into a reasonable size satellite-borne collecting aperture. The atmosphere absorbs energy, and spreads the beam because of turbulence and thermal blooming. Although little can be done, other than appropriate selection of laser wavelengths, to counteract atmospheric absorption of energy, adaptive optical techniques can be used with excellent advantage to reduce energy loss caused by turbulence and thermal blooming. Adaptive optics can also be used to implement the precise angle tracking which is required. This report is principally concerned with the analysis and conceptual development of adaptive optical systems for efficiently transmitting up to 5 MW of power to satellites in orbit.

The scenario which we have examined in this effort is illustrated in Figure I-1. Here we have a ground based laser transmitter arranged to track the satellite at any angle within a 60° cone about the vertical, and transmit energy into a 2-meter diameter collector aperture on the satellite during transit through this cone angle. Two transmitter elevations, 10 m and 3.5 km above sea level, are considered. The satellite is assumed to be in a low (185 km) circular earth orbit. A small corner reflector (10 cm) is located in the center of the 2-m collecting aperture, to provide high level returns for angle tracking.

In this report we present the results of three tasks directed toward development of an efficient energy transport system. We begin by assessing the pertinent atmospheric effects which influence system performance. Our assessments include absorption, thermal blooming, and turbulence. Although emphasis was given to $10.6\text{ }\mu\text{m}$ CO_2 lasers, because of their relatively advanced state of development, attention was also directed to $9.1\text{ }\mu\text{m}$ (CO_2), $5.0\text{ }\mu\text{m}$ (CO), and $3.8\text{ }\mu\text{m}$ (HF) lasers. Since the scenario investigated in this

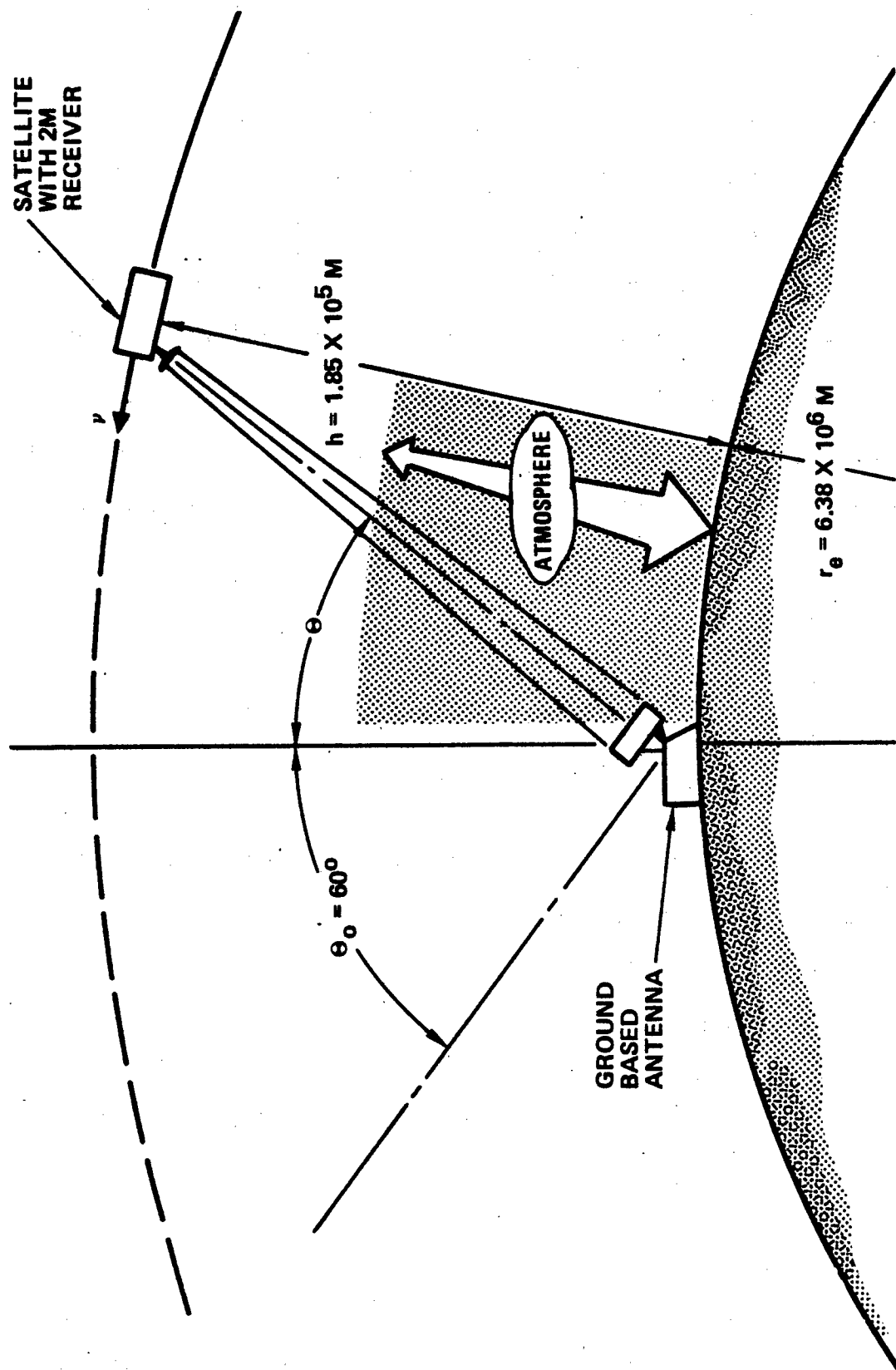


Figure I-1. Ground-to-Space Power Transmission Scenarios

effort was for vertical, or near vertical, propagation, we have collected the best data available at the time and constructed detailed vertical profile models for absorption, atmospheric turbulence (C_N^2), wind speed, temperature, and other parameters necessary to calculate the performance of candidate systems. In the process of evaluating the candidate systems, detailed calculations were performed of the performance limitations of various types of adaptive control systems. Correction for atmospheric turbulence and thermal blooming was examined in detail, and the required spatial and temporal resolution was calculated.

Our next task was the conceptual development and preliminary analysis of candidate energy transfer systems. Four different systems were developed. They are

- Coelostat Hartmann Tracker
- Modified Multidither Receiver
- Multiaperture MOPA System
- Multiple Source Phased Array.

Each of these systems were found to meet the performance requirements. They were evaluated with respect to

- Overall efficiency
- Reliability
- Size and weight
- Technology advanced development requirements
- Potential cost

Evaluation was done using a quantitative index for each of these criteria. Based on this evaluation, the Multiple Source Phased Array was recommended by Rockwell and selected by NASA for more detailed design, analysis, and

development. The Multiple Source Phased Array uses independent phase locked laser oscillators, and independent synchronized tracking mounts and thus circumvents, to a large extent, requirements for high power laser and large tracking mount development.

The Multiple Source Phased Array is then examined in considerable detail. The system was defined in detailed block diagram form and layouts were developed for the various optical elements. The acquisition and tracking sequence for system operation was determined, and all servo control loops were defined and specified. The final preferred configuration is a seven-element hexagonal close packed array of individual tracking telescopes, each fed in a separate channel from seven independent phase locked CO₂ oscillators of 715 KW each, for a total generated laser power of 5 MW. Each telescope in the array initially acquires the target independently, based on accurate a priori information on the satellite ephemeris. Return signal is received in each channel, adaptive control loops are used to correct wavefront errors, and the beams are progressively narrowed and phased to near diffraction limited operation. Finally, an evaluation was made of the relative state of technological development of the various components in this system, with particular attention given to those which are beyond the current state-of-the-art. Thus, this effort will help define future required research and advanced development programs.

Many important conclusions were reached during the course of this study. Some of the more significant are summarized here. The rest are discussed in detail in Chapter VIII. The following conclusions may be noted:

- For operation at 10.6 μm and considering a single element antenna, an overall aperture diameter greater than 3.5 m is needed to minimize diffraction effects. A value of 4.8 m was selected and used for most of our calculations to minimize both diffraction and thermal blooming effects when segmented arrays were considered.
- Operation from a 3.5 km elevation site is by far preferred. The sea level site should not be considered unless some overriding logistical or economic consideration (not considered in this study) makes it necessary. If a sea level site were to be used, then the laser selected should be a DF laser, operating near 3.8 μm .
- An isotopic $^{12}\text{C}^{18}\text{O}_2$ laser operating at 9.1 μm is the best choice for operation from the 3.5 km site with a 95% transmission averaged over the satellite encounter. A CO laser operating single line (P10) at 5.0 μm would be a close second choice. When averaged over the total time of the encounter, DF has about 6% less transmission than the isotope line, but CO_2 (10.6) is far worse with only about 50% transmission.
- With respect to correction for turbulence induced beam broadening, a seven-element array with phase and tilt adaption will increase the power delivered to 87% on a scale in which a perfect single aperture diffraction limited system delivers 92%. This is considered to be satisfactory performance, and is the recommended approach.

- For all cases studied, the energy loss caused by thermal blooming can be completely eliminated by a seven-element array with phase and tilt adaption if a deformable mirror is used in each channel to correct higher order aberrations.
- The adaptive bandwidth required for 90% correction is 60 Hz at 10.6 μm , 80 Hz at 9.1 μm , 305 Hz at 5.0 μm , and 440 Hz at 3.8 μm .
- The energy loss caused by isoplanatism when time averaged over the total encounter is small ($< 5\%$) for both the 10.6 μm and 9.1 μm wavelength sources, even for offset distances of 200 km. The CO source (5.0 μm) has a significant energy loss ($\sim 15\%$) only when offset distances greater than 100 km are considered, but the DF source (3.8 μm) begins to experience a noticeable loss even for small offset distances.
- Of the four different adaptive control and tracking systems considered, the multiple source phased array received by far the highest valuation relative to the specified evaluation criteria. Further development and experimental test of this concept is recommended.
- For the recommended wavelength and site altitude (9.1 μm , 3.5 km), the overall transmission efficiency calculated is excellent. A value of 53% is predicted, comprised of 72% diffraction efficiency, 95% transmission efficiency, 95% turbulence efficiency, $\sim 100\%$ thermal blooming efficiency, and 82% transmission efficiency in the optics.

- The principal areas of advanced technology development required to implement this system are (1) closed-cycle laser using $^{12}\text{C}^{18}\text{O}_2$ isotope lasant with a continuous output of greater than 700 kw, (2) laser phase control system, (3) moderate power frequency tunable laser oscillator, (4) Hartmann plate high energy beam sampler, (5) wide bandwidth detector arrays, (6) data processor for modal decomposition of phase errors, and (7) deformable mirrors for higher order aberration correction.
- The system described herein shows considerable promise. We believe that a low or moderate power system feasibility test would be of benefit and merit. Such a test could be carried out using the NASA pilot laser facility. We recommend that planning for such a test program be initiated.

In summary, we believe that we have shown, not only that a ground to satellite high power radiant energy transport system is possible and reasonable, but also that the Multiple Source Phased Array system provides a system concept for energy transport that can be implemented with minimal requirements for advanced technology development.

Reference

1. R. H. Battin, "Astronautical Guidance," McGraw-Hill, Inc., 1964.

II. TRANSMISSION EFFICIENCY

In the three chapters that come after this one, detailed discussions will be presented on how well adaptive optics concepts can recover transmitted power loss due to atmospheric turbulence and thermal blooming effects. In this chapter, however, we will be concerned with transmission losses that are nonrecoverable; namely, antenna diffraction losses and atmospheric absorption losses. The diffraction losses are not serious if large transmitter antennas are considered, although some evidence will be presented in the chapter on concept generation that this type of consideration will be costly. The atmospheric absorption, on the other hand, not only produces direct losses, but also stimulates the thermal blooming losses.

A. Diffraction Efficiency

Our calculations for the fraction of the transmitted power received (the transmission efficiency) are based on a uniformly illuminated circular transmitter aperture and a circular collector bucket of two meters diameter. The diffraction pattern of the transmitter at the receiver is given by¹

$$P(x) = \left(\frac{2 J_1(x)}{x} \right)^2 \quad (1)$$

where P = normalized intensity

$J_1(x)$ = first order Bessel function

$x = (2\pi/\lambda)(a)(r/R)$

λ = optical wavelength

a = transmitter aperture radius

r = radius at receiver

R = range to receiver

The normalized power in the bucket will be given by

$$L(x_0) = 2 \int_0^{x_0} \frac{J_1^2(x)}{x} dx, \quad (2)$$

where $x_0 = x$ calculated at bucket radius, $R = 1$ m

The total efficiency for the encounter will be given by

$$L' = \frac{1}{T} \int_0^T L(t) dt. \quad (3)$$

The time dependence of the collected power arises from the time dependence of the range between transmitter and receiver. If we use the scenario description given in Figure II-1, the transmission range as a function of time can be expressed as

$$R(t) = [(OD)^2 + H^2 + (-H \tan \theta_0 + Vt)^2]^{1/2}, \quad (4)$$

where OD is the offset distance

H is the orbital altitude (185 km)

θ_0 is the initial zenith angle (-60°)

t is time, and

V is the satellite linear velocity,

which for a satellite in circular orbit is given by

$$V = \left(\frac{G m_e}{r_e + H} \right)^{1/2}, \quad (5)$$

where G is the gravitational constant

m_e is the earth's mass, and

r_e is the radius of the earth.

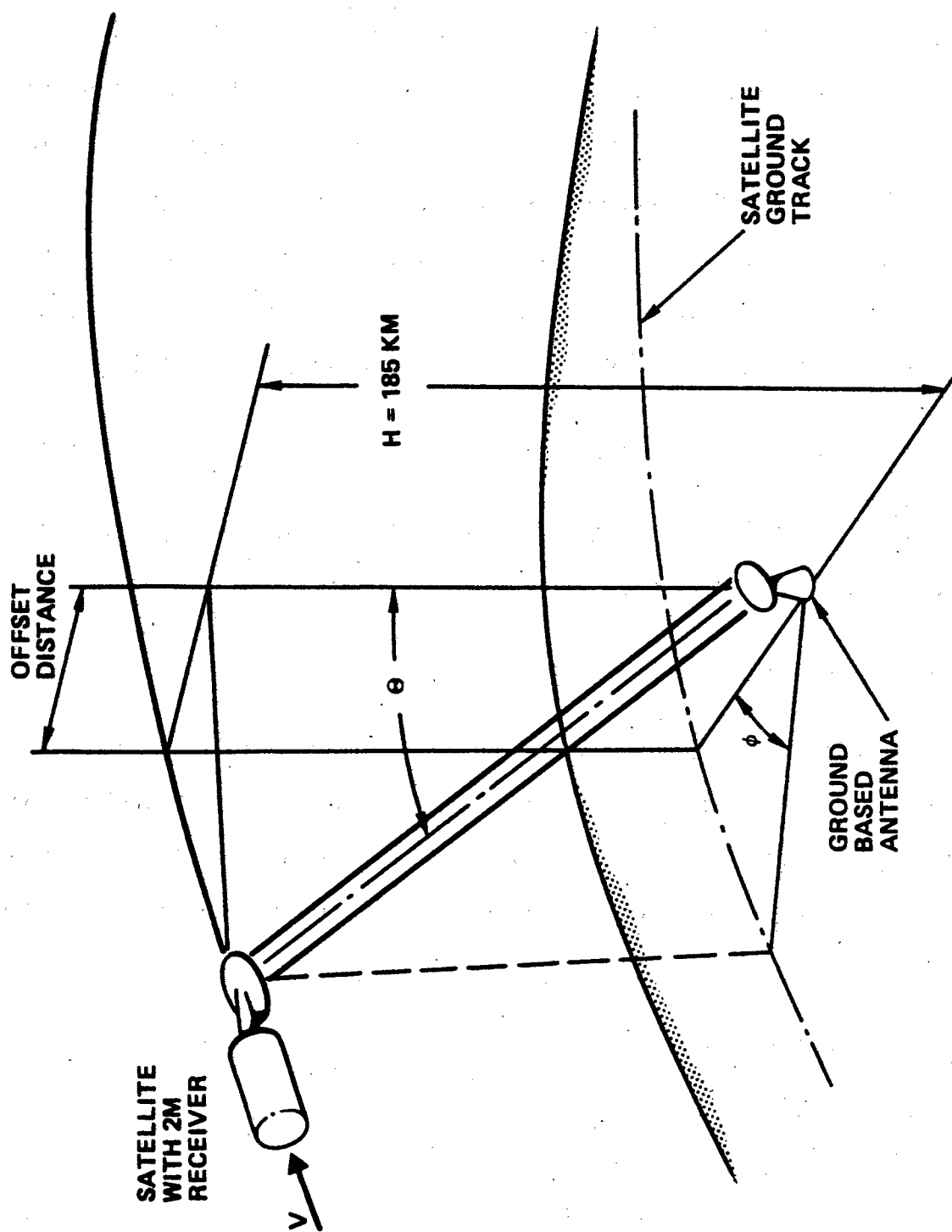


Figure II-1. Scenario Description - Transmission to Satellite

When Eqs. (4) and (5) are combined with the proper constants, the transmission range as a function of encounter time can be calculated to give the results shown in Figure II-2 and from these data the transmission efficiency as a function of time can be calculated. In Figures II-3 and II-4, we show the results of these calculations for 10.6 μm propagation. It appears from these data that an antenna size between 4 and 6 meters is needed for good efficiency. When Eq. (3) is solved using these data, however, we see that on the average good efficiency can be obtained with a smaller antenna diameter (see Figure II-5). These data show that if the transmitter diameter is scaled as

$$D_T = 1.22 \lambda H \sec \theta_0 \quad (6)$$

we can have an overall efficiency of slightly greater than 0.85, but with a decrease in size by a factor of 1.5 to

$$D_T = 0.8 \lambda H \sec \theta_0, \quad (7)$$

the overall efficiency is reduced to only 0.8. Unfortunately, as we will show later, reducing the antenna size, although the increase in diffraction loss is small, increases the output power density and aggravates the thermal blooming. Therefore, we have used the larger antenna scaling for this contract effort.

B. Atmospheric Transmission

1. 10.6 μm Transmission

Absorption by the atmosphere of 10.6 μm laser radiation is almost exclusively due to the H_2O continuum and the CO_2 P(20) line. Aerosols play essentially no part at this wavelength. Various authors have computed the absorption coefficients as a function of altitude, season, and location. We

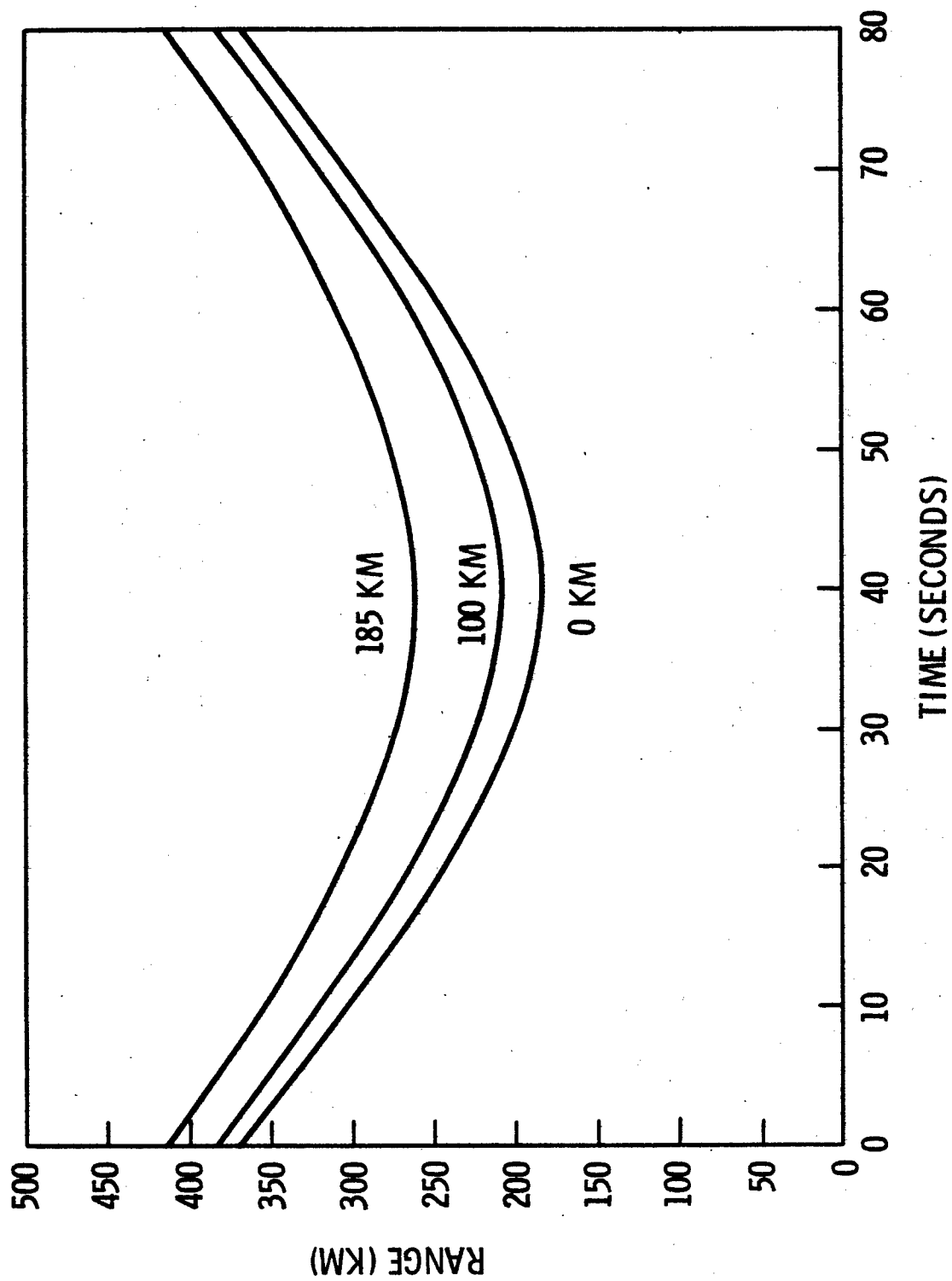


Figure II-2. Transmission Range Versus Time for Various Offset Distances

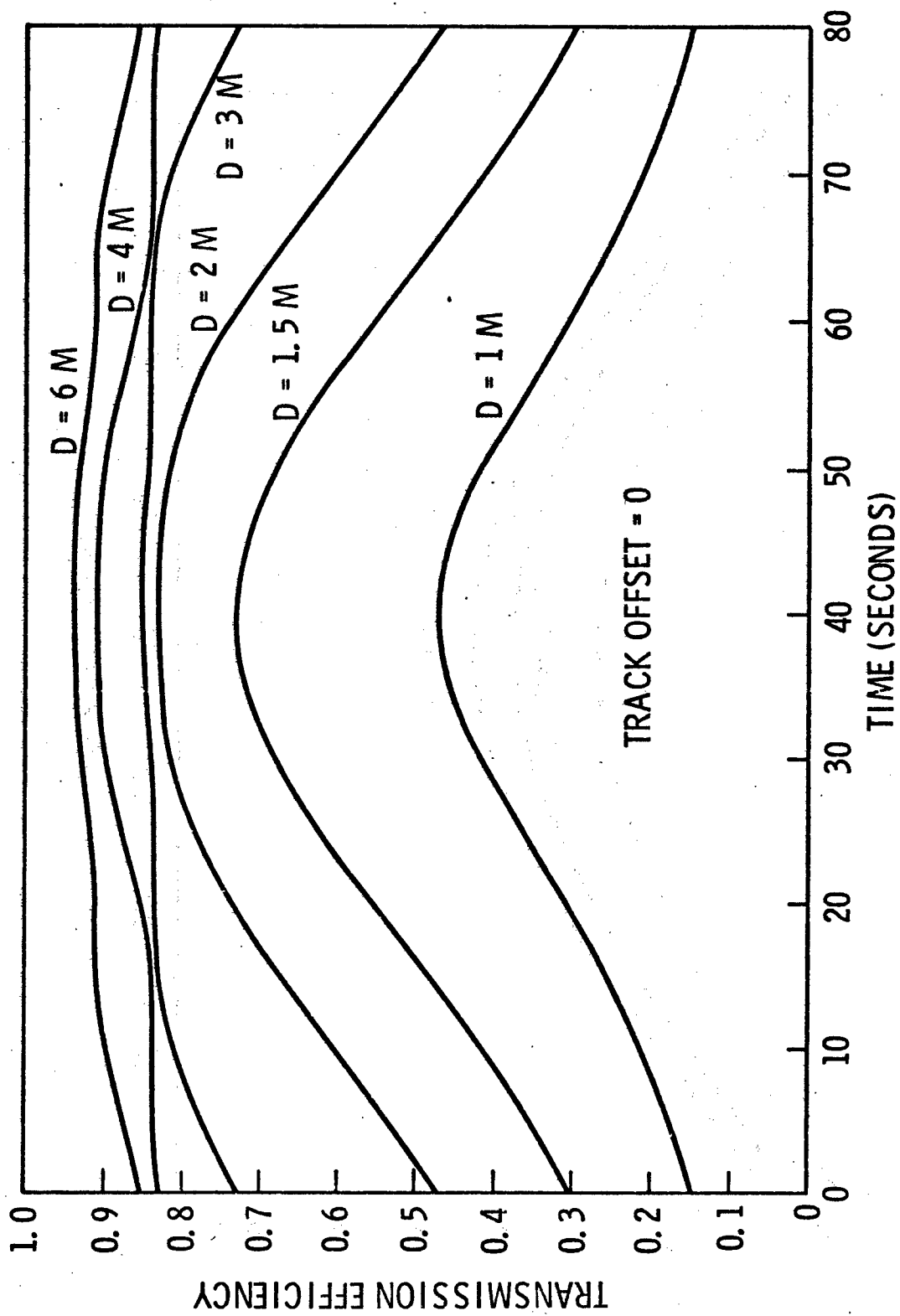


Figure II-3. Efficiency Versus Time for Various Transmitter Diameters and a 0 km Offset Distance

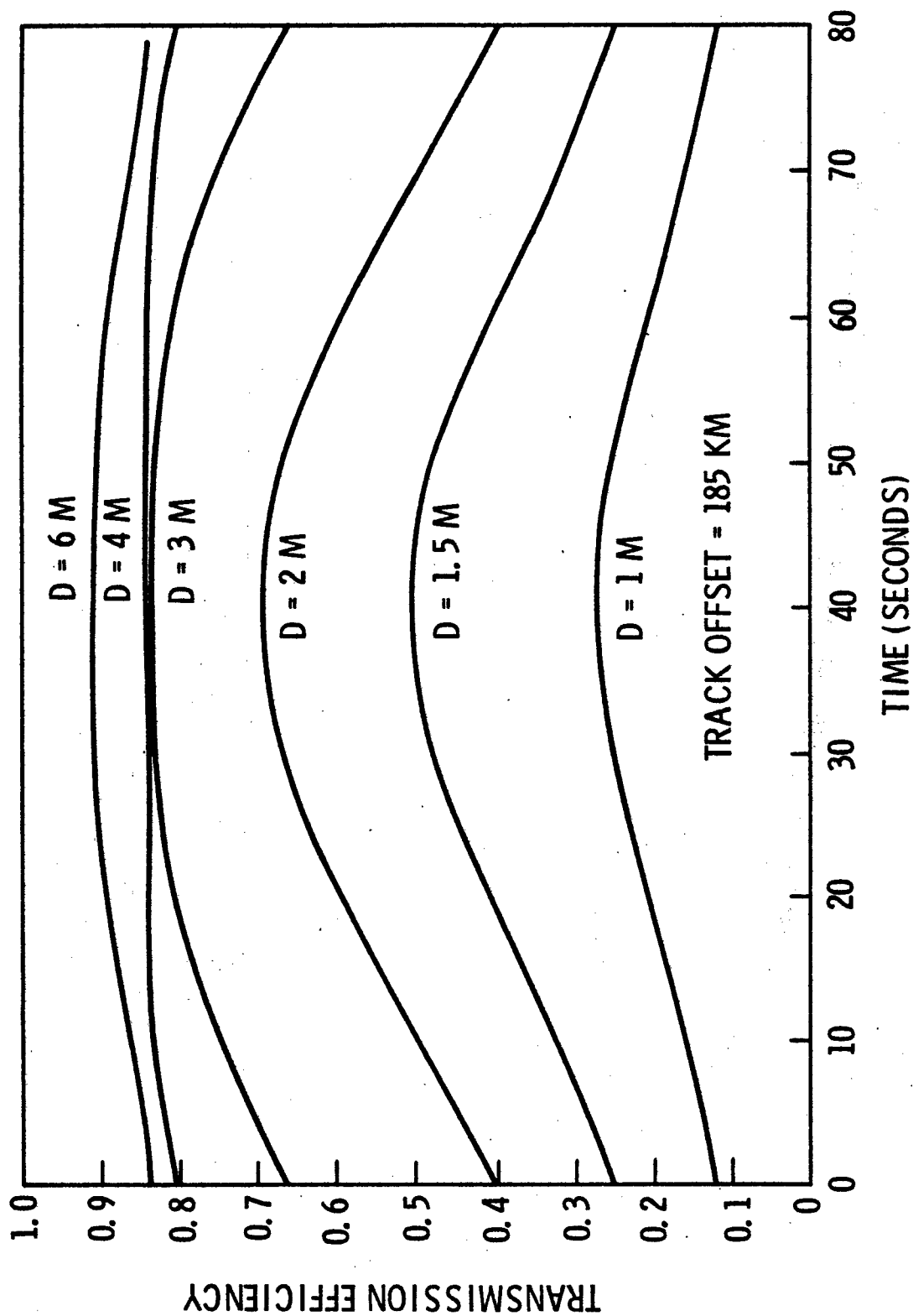


Figure II-4. Efficiency Versus Time for Various Transmitter Diameters and a 185 km Offset Distance

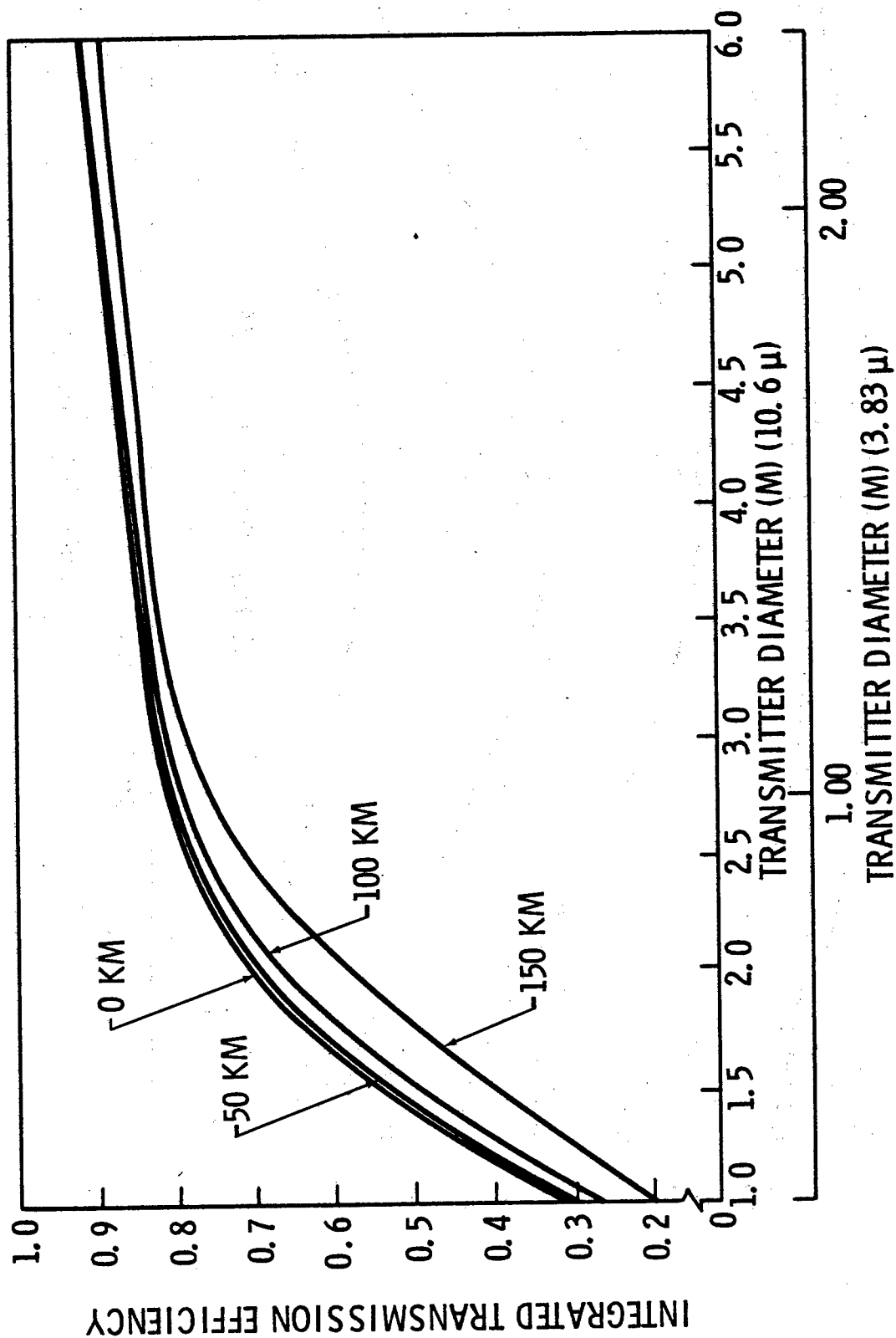


Figure II-5. Efficiency for Total Encounter Versus Transmitter Aperture Diameter for Various Offset Distances

compare their results, and calculate the total absorption for a transversal from a transmitter at an altitude H to the vacuum.

The reported absorption coefficients are contained primarily in reports by McCoy² or McClatchey.³ We discuss the results of McCoy's data first.

The density of water in the atmosphere falls off exponentially up to about 12 km.⁴ The absorption is effected by not only this decreasing density, but by pressure as well. McCoy⁵ gives the altitude dependence for water vapor absorption as

$$\alpha \text{ (1/km)} = (.0334)(\exp - 0.705H) + (0.101)(\exp - 1.15H) \quad (8)$$

for January, and

$$\alpha \text{ (1/km)} = (0.075)(\exp - 0.635H) + (0.433)(\exp - 1.01H) \quad (9)$$

for July. These equations probably should be considered as the "typical" variability, but not the limits of such. They represent at H = 0 a relative humidity of 35% and 75%, respectively. McCoy uses the CO₂ absorption calculated by Yin and Long.⁶ The absorption due to CO₂, H₂O and the combination is plotted in Figures II-6 and II-7, and listed in Tables II-1 and II-2.

The results of the report of McClatchey do not separate the absorption due to CO₂ and H₂O. However, he does calculate coefficients for a wider range of atmospheres than McCoy. The results of his calculations are plotted in Figure II-8, and listed in Table II-2. By comparison, McCoy's values are generally higher than those of McClatchey. Note though that only a slight difference in the definition of the atmosphere will make a large difference in the absorption at the lower altitudes. McCoy gives absorption as a function of relative humidity of water due to water alone, and these results are:

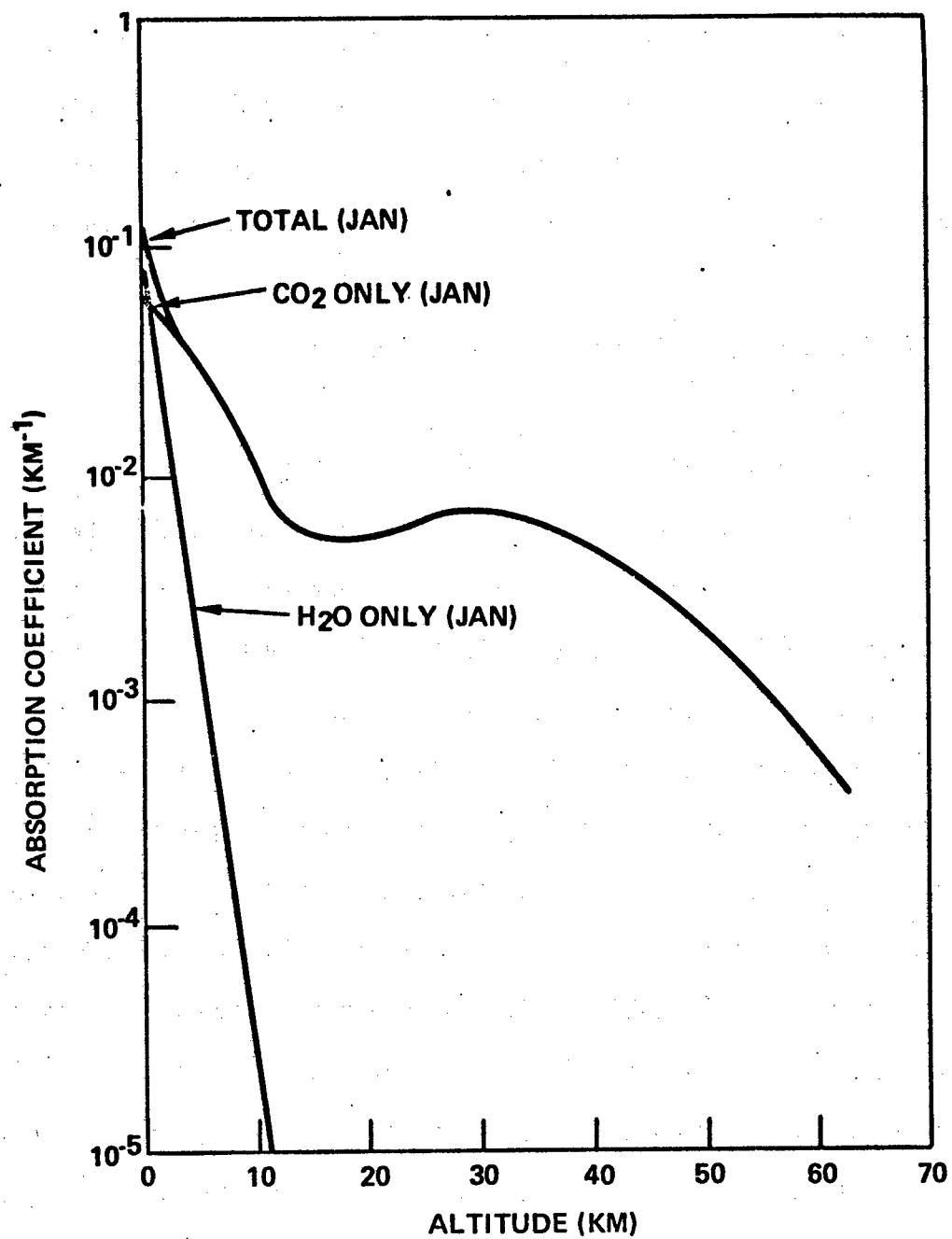


Figure II-6. 10.6 μm Absorption Coefficient Versus Altitude - from McCoy

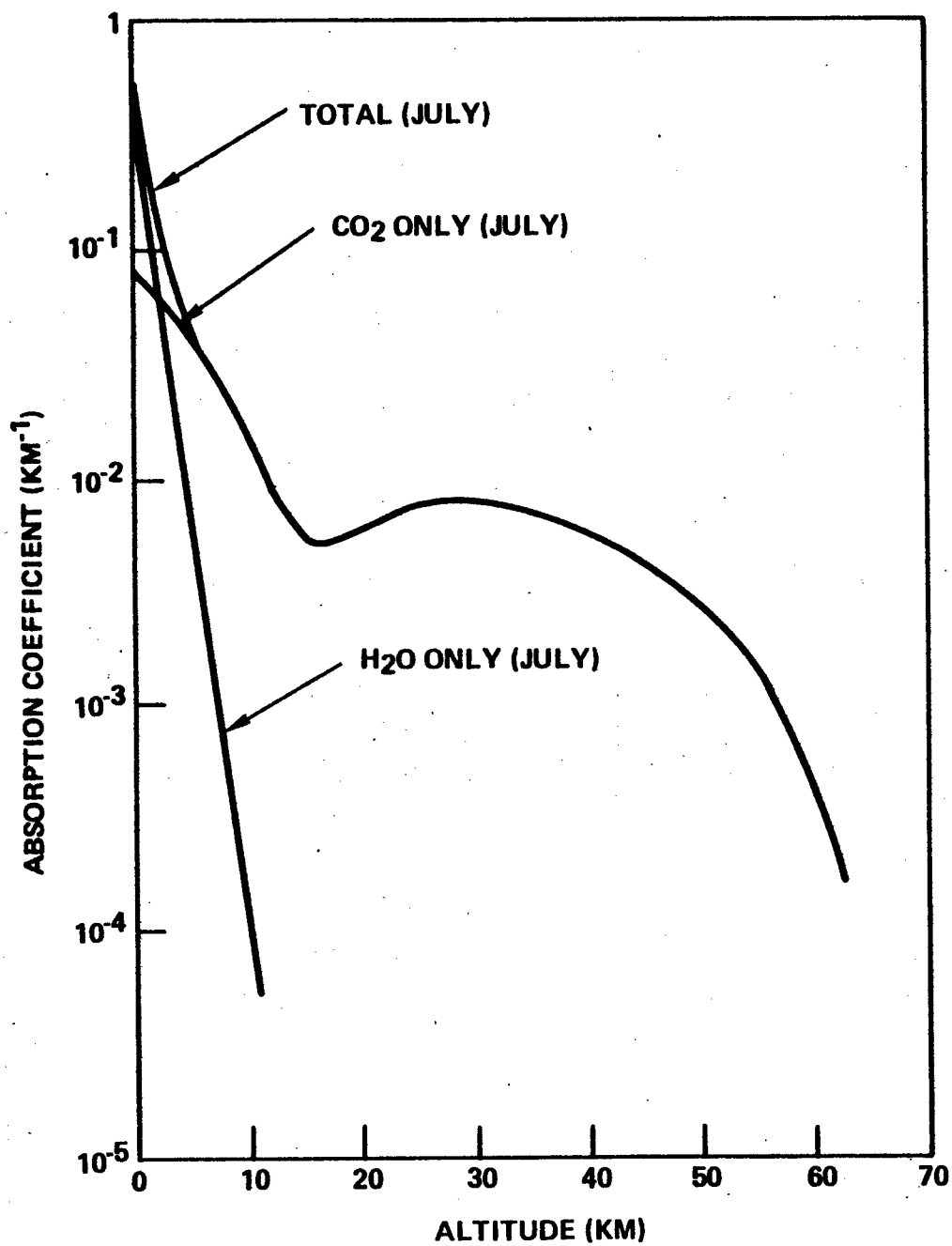


Figure II-7. 10.6 μ m Absorption Coefficient
Versus Altitude - from McCoy for July

Table II-1

10.6 μ m Absorption Coefficients vs Altitude
from McCoy

<u>H(km)</u>	January			July		
	<u>CO₂</u>	<u>H₂O</u>	<u>Total</u>	<u>CO₂</u>	<u>H₂O</u>	<u>Total</u>
0.5	6E-2	8E-2	1.4E-1	7.9E-2	3.16E-1	3.95E-1
1.5	5.5E-2	3E-2	8.5E-2	6.9E-2	1.24E-1	1.93E-1
2.5	5.0E-2	1.1E-2	6.1E-2	6.0E-2	5.0E-2	1.10E-1
3.5	4.2E-2	4.6E-3	4.7E-2	5.3E-2	2.1E-2	7.4E-2
4.5	3.5E-2	2.0E-3	3.5E-2	4.6E-2	8.9E-3	5.5E-2
5.5	3.0E-2	8.7E-4	3.0E-2	4.0E-2	4.0E-3	4.4E-2
6.5	2.5E-2	4.0E-4	2.5E-2	3.4E-2	1.8E-3	3.6E-2
7.5	2.1E-2	1.9E-4	2.1E-2	2.8E-2	8.6E-4	2.9E-2
8.5	1.7E-2		1.7E-2	2.4E-2	4.2E-4	2.4E-2
9.5	1.3E-2		1.3E-2	1.8E-2	2.1E-4	1.8E-2
11	9.5E-3		Same	1.3E-2		Same
16	5.13E-3		As	5.4E-3		As
22	5.8E-3		CO ₂	6.5E-3		CO ₂
27	6.7E-3			8.0E-3		
31	7.0E-3			8.0E-3		
36	5.8E-3			6.8E-3		
45	3.4E-3			4.3E-3		
55	1.1E-3			6.4E-3		
62.5	4E-4			2.0E-3		

absorption in units of (1/km)

Table II-2

10.6 μ m Absorption Coefficients vs Altitude
from McClatchey

H(km)	Tropical	Midlatitude Summer	Midlatitude Winter	Subartic Summer	Subartic Winter
0	6.094E-01	3.852E-01	9.575E-02	2.238E-01	5.214E-02
0-1	4.586E-01	2.977E-01	8.576E-02	1.802E-01	5.315E-02
1-2	2.766E-01	1.841E-01	7.137E-02	1.247E-01	5.083E-02
2-3	1.640E-01	1.218E-01	6.096E-02	9.268E-02	4.492E-02
3-4	1.045E-01	8.901E-02	5.093E-02	7.322E-02	3.917E-02
4-5	7.809E-02	6.849E-02	4.179E-02	5.808E-02	3.178E-02
5-6	6.346E-02	5.745E-02	3.416E-02	4.774E-02	2.527E-02
6-7	5.143E-02	4.879E-02	2.810E-02	3.711E-02	1.984E-02
7-8	4.174E-02	3.948E-02	2.273E-02	2.976E-02	1.540E-02
8-9	3.454E-02	3.123E-02	1.853E-02	2.348E-02	1.266E-02
9-10	2.729E-02	2.568E-02	1.428E-02	1.812E-02	1.179E-02
10-11	2.177E-02	2.073E-02	1.295E-02	1.577E-02	1.178E-02
11-12	1.698E-02	1.637E-02	1.252E-02	1.623E-02	1.176E-02
12-13	1.366E-02	1.259E-02	1.235E-02	1.559E-02	1.153E-02
13-14	9.747E-03	1.101E-02	1.233E-02	1.623E-02	1.203E-02
14-15	7.725E-03	1.149E-02	1.189E-02	1.613E-02	1.174E-02
15-16	5.717E-03	1.121E-02	1.155E-02	1.540E-02	1.158E-02
16-17	4.379E-03	1.104E-02	1.132E-02	1.606E-02	1.130E-02
17-18	4.695E-03	1.118E-02	1.129E-02	1.589E-02	1.099E-02
18-19	5.743E-03	1.130E-02	1.089E-02	1.583E-02	1.083E-02
19-20	6.857E-03	1.178E-02	1.057E-02	1.605E-02	1.040E-02
20-21	8.279E-03	1.212E-02	1.080E-02	1.565E-02	1.027E-02
21-22	9.857E-03	1.282E-02	1.081E-02	1.594E-02	9.925E-03
22-23	1.102E-02	1.333E-02	1.077E-02	1.593E-02	9.511E-03
23-24	1.193E-02	1.469E-02	1.069E-02	1.581E-02	9.668E-03
24-25	1.307E-02	1.466E-02	1.105E-02	1.682E-02	9.019E-03
25-30	1.587E-02	1.750E-02	1.067E-02	1.916E-02	9.551E-03
30-35	1.366E-02	1.523E-02	7.821E-02	2.648E-02	6.468E-03
35-40	1.192E-02	1.381E-02	7.221E-03	1.518E-02	5.460E-03
40-45	9.253E-03	1.113E-02	6.251E-03	1.245E-02	4.243E-03
45-50	6.178E-03	7.711E-03	4.490E-03	8.396E-03	3.135E-03
50-70	9.095E-04	1.088E-03	2.765E-04	1.109E-03	7.810E-04
70-100	1.535E-05	1.743E-05	1.580E-04	1.762E-05	1.785E-05

absorption in units of (1/km)

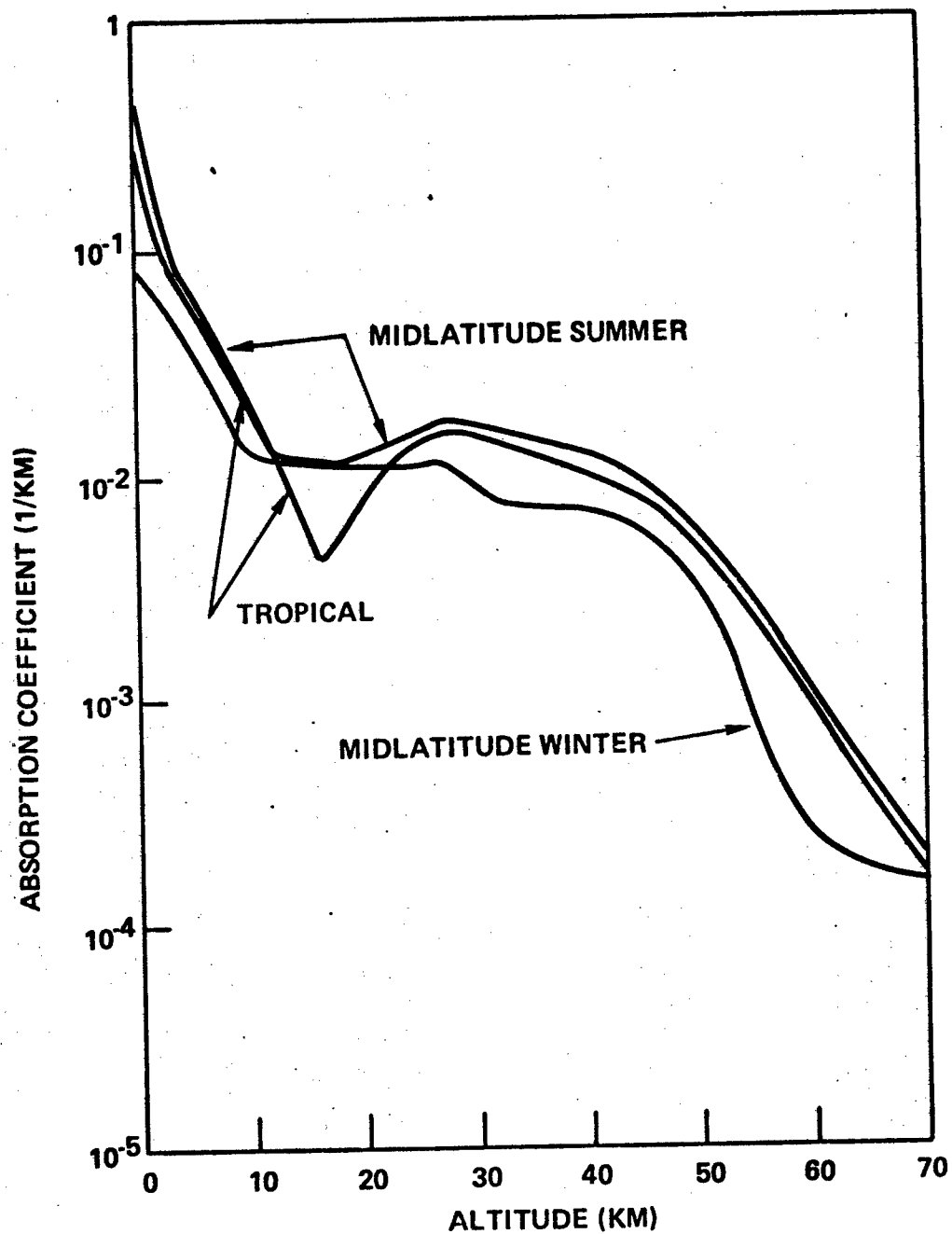


Figure II-8. $10.6 \mu\text{m}$ Absorption Coefficient Versus Altitude - from McClatchey

<u>R.H. (%)</u>	<u>α (1/km)</u>
10	0.0125
20	0.0338
30	0.0653
40	0.107
50	0.157
60	0.215
70	0.284
80	0.363

Since H₂O absorption is not only quite variable, but a significant value, we emphasize the importance of selecting a dry site. By scaling the H₂O absorption with the relative humidity for H = 0, we can estimate the impact of a site dryer than the atmosphere of McCoy. The results are:

	<u>H = 0</u>	<u>H₂O</u>	<u>CO₂</u>	<u>Total</u>
<u>January</u>	<u>R. H.</u>	<u>Fractional Trans.</u>	<u>Fractional Trans.</u>	<u>Fractional Trans.</u>
	35%	.88	.55	.49
Change to	10%	.98	.55	.55
<u>July</u>				
	75%	.59	.50	.29
Change to	20%	.95	.50	.47

So, the selection of a dryer site will provide transmission increases of 12% and 62%.

The total transmission given by

$$T = \exp\left(-\int_z^{\infty} \alpha(z') dz'\right), \quad (10)$$

where z is the transmitter altitude above sea level and $\alpha(z')$ is the absorption coefficient as a function of altitude was computed for the various models and plotted as a function of transmitter altitude in Figures II-9 and II-10. McCoy calculates the absorption from altitude zero, and we are in agreement with his results.

To compare the various results, we list below the absorption coefficients at ground zero and the fractional transmission for the various models.

<u>Model</u>	<u>$\alpha(1/\text{km})$ at $H = 0$</u>	<u>Fractional Transmission</u>
<u>McCoy</u>		
July	0.395	29%
January	0.14	49%
<u>McClatchey</u>		
Tropical	0.609	17%
Midlatitude Summer	0.385	22%
Midlatitude Winter	0.0958	32%
Subartic Summer	0.224	26%
Subartic Winter	0.052	53%

While the results vary, we suggest that so does the atmosphere. To attempt a more specific characterization would be meaningless. What can be said, though, is that the atmosphere varies a good deal, and we have probably specified this variance.

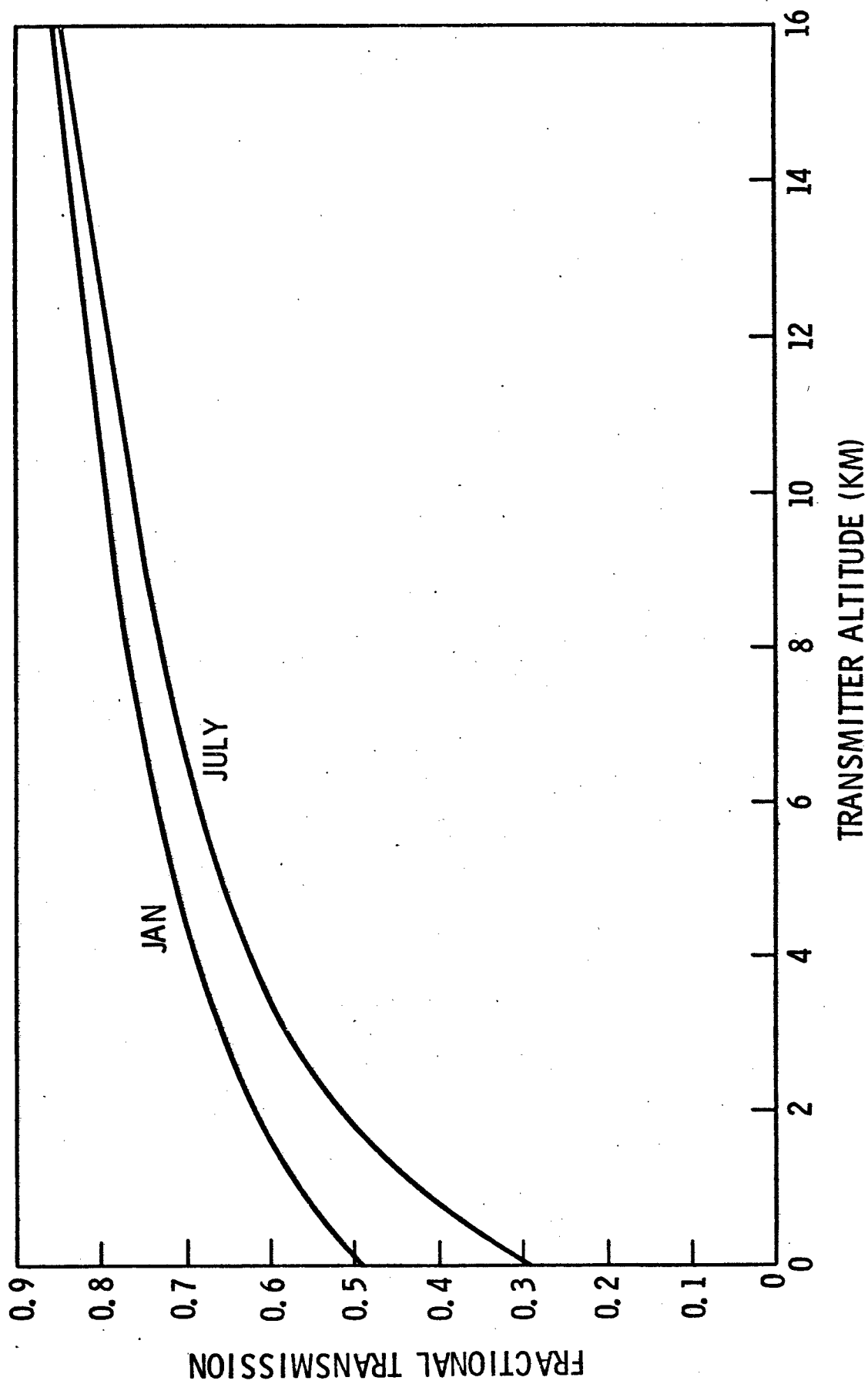


Figure II-9. Fractional Transmission Versus Transmitter Altitude for Various Atmospheric Models of McCoy

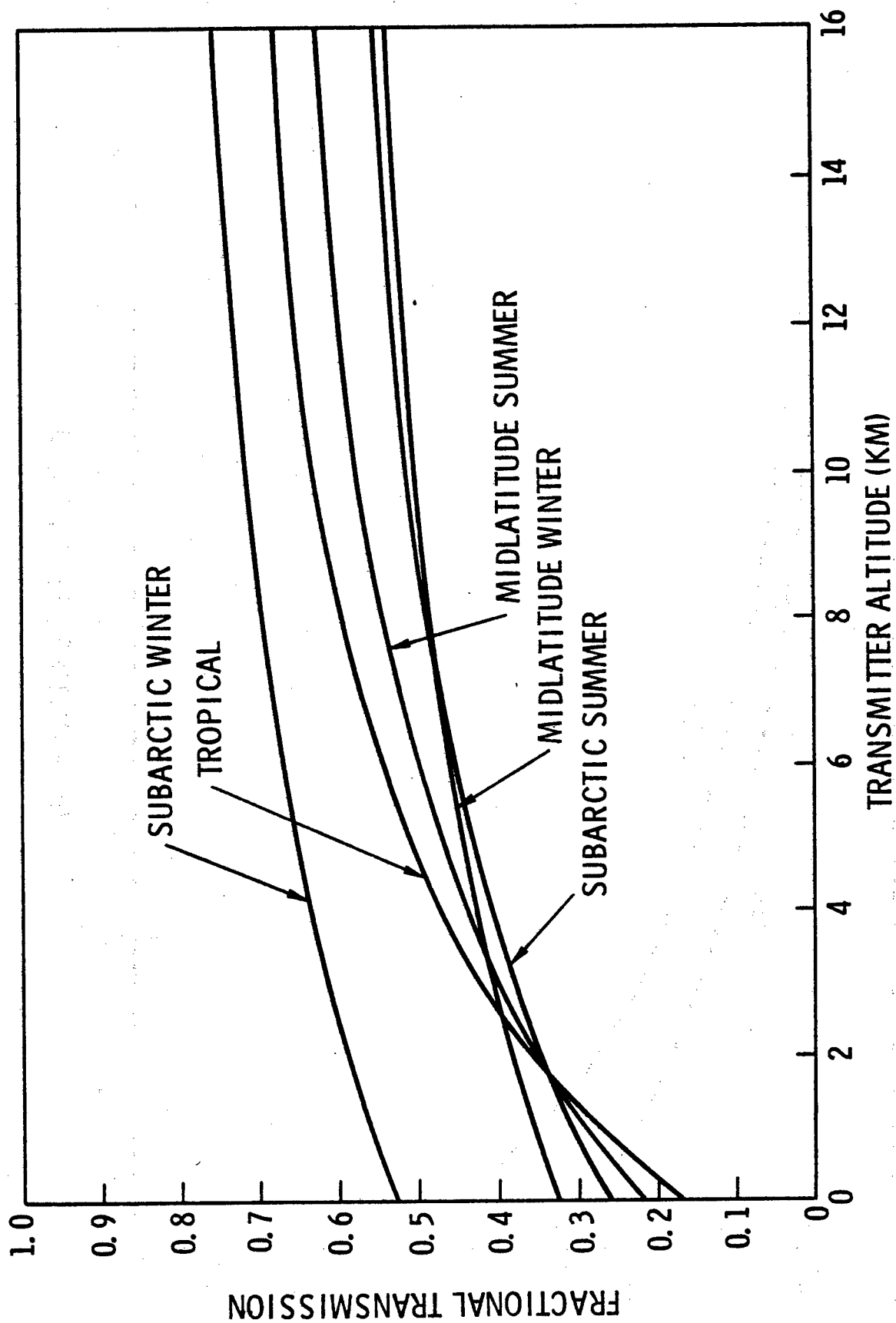


Figure II-10. Fractional Transmission Versus Transmitter Altitude for Various Models of McClatchey

Because the McCoy models separate out the CO_2 and H_2O absorption coefficients, which is required for the thermal blooming calculations that will be discussed in a later chapter, we have selected them to use in the effort. To determine the expected atmospheric transmission at $10.6 \mu\text{m}$, we have used the summer model of McCoy, because it has a total absorption which is about an average of the other modes. The transmission efficiency for the satellite encountered is calculated by combining Eqs. (4), (5), and (10). The results of these calculations are shown in Figure II-11. These data were then integrated over the encounter time to provide average transmission efficiency values which are shown in Figure II-12. Here, we see that for a sea level site that the expected average transmission for a satellite encounter is only between 15 and 18%, which would tend to exclude it from consideration. For the mountain top operation (3.5 km above sea level), the expected average transmission increases to around 50%.

2. DF Laser Atmospheric Absorption

The Deuterium Fluoride (DF) laser will run on a set of lines, and this set can be varied. We obtained an estimate of three such sets from the Rocketdyne Division of Rockwell International.⁷ They are:

<u>Case</u>	<u>Relative % Power</u>	<u>Wave Number (cm^{-1})</u>	<u>Relative Total Power</u>
A	10%	2665.2	100%
	40%	2580.16	
	40%	2546.37	
	10%	2463.25	
B	10%	2611.1	82%
	40%	2580.16	
	40%	2496.61	
	10%	2414.89	
C	10%	2611.1	47%
	40%	2527.47	
	40%	2445.29	
	10%	2414.89	

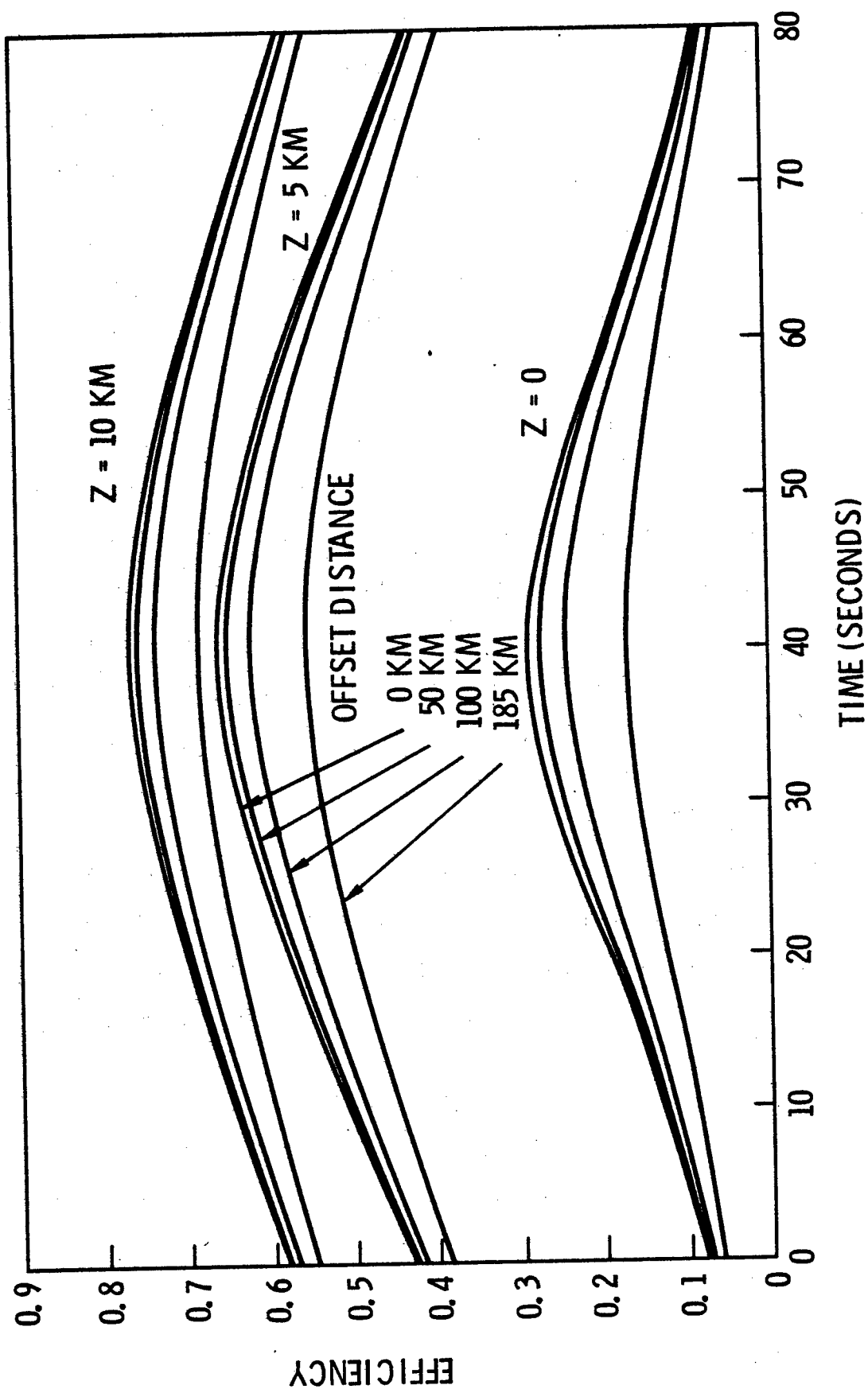


Figure II-11. Atmospheric Transmission Efficiency for $10.6 \mu\text{m}$ Versus Encounter Time for Various Transmitter Altitudes and Offset Distances

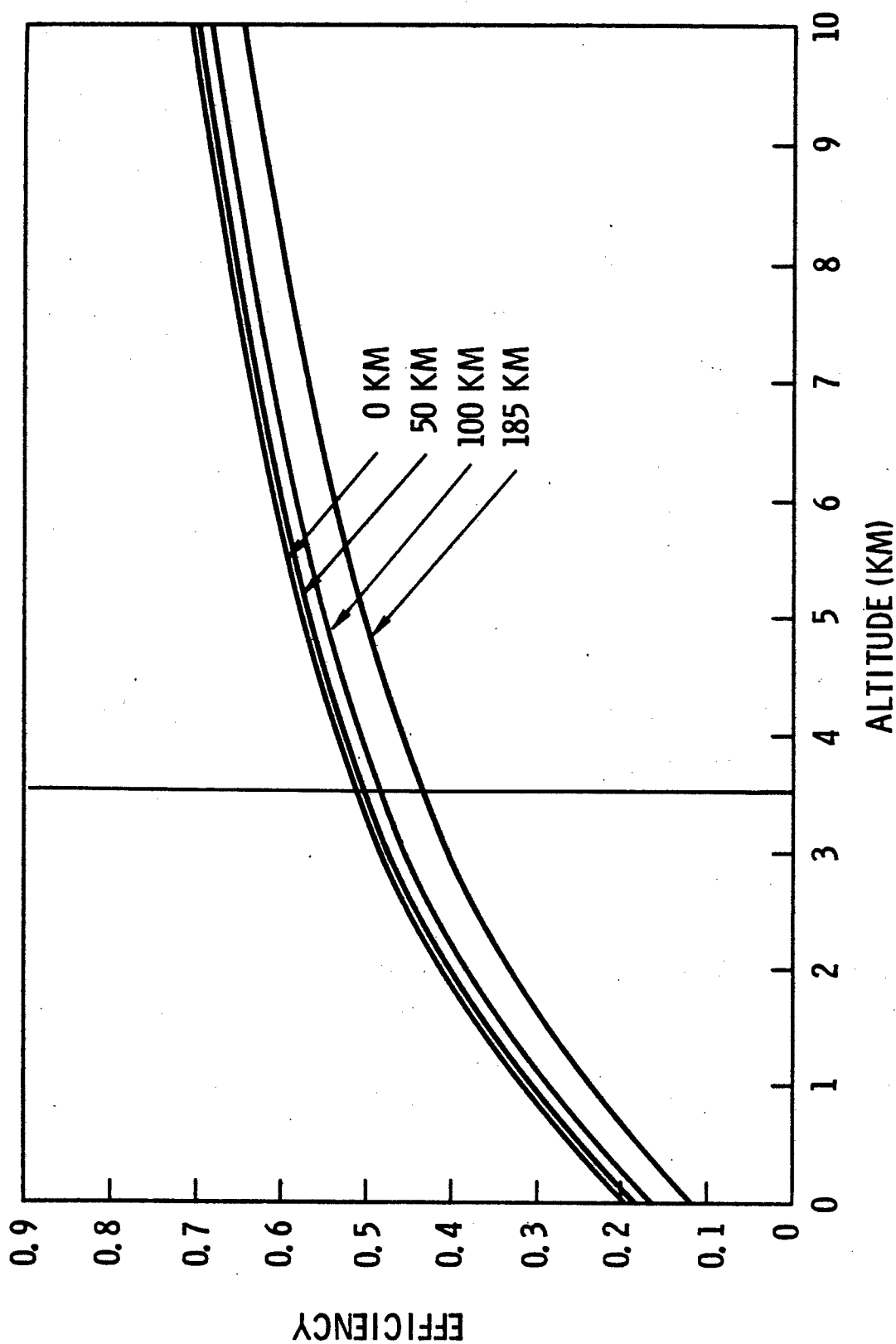


Figure II-12. Time Averaged Transmission Efficiency ($10.6 \mu\text{m}$) for Entire Encounter Versus Transmitter Altitude for Various Offset Distances

The total power out of the laser varies as can be seen, but we are concerned with total power in the bucket. Due to varying atmospheric absorption, this could be higher for the lower power case. From McClatchey's data⁸ for the individual lines, we computed a weighted average of the absorption coefficients as a function of altitude for each of the line sets. These data were then used for our transmission considerations.

We have accumulated data for both hazy and clear weather, but even the most rudimentary site selection would make the clear data appropriate. Also, we separate absorption from extinction, the former needed for thermal blooming and the latter for transmission. To evaluate these data of the different cases considering both the winter and summer atmospheric models of McClatchey, we computed the total absorption for vertical propagation as follows

$$\beta = \int_z^{\infty} \alpha(z') dz',$$

where $\alpha(z')$ is the absorption coefficient as a function of altitude. These results are presented below.

<u>Case A</u>	<u>β</u>
Mid Lat Sum	0.1825
Mid Lat Win	0.178
<u>Case B</u>	
Mid Lat Sum	0.174
Mid Lat Win	0.167
<u>Case C</u>	
Mid Lat Sum	0.204
Mid Lat Win	0.194

The average is $\beta = 0.183$ and the average deviation is 0.010, or 5.6%. With the spread being so small, we let β for the chemical laser be set at 0.183 and selected the mid-latitude summer model of Case A for the thermal blooming calculations. These data are given in Figures II-13 and II-14.

3. CO₂ Isotope Transmission

Since approximately one half of the atmospheric absorption of CO₂ laser radiation is due to CO₂ molecular absorption, the use of isotopes of CO₂ for the lasant is highly recommended. We examine the choice of isotope and the question of the atmospheric absorption of isotopic radiation.

In Figure II-15, we show the isotopic bands compared to the non-isotopic bands.⁹ In the areas of overlap, some lines are coincidental, but generally not to within several GHz. The homogeneous broadening of CO₂ is nominally 6.5 MHz/torr, giving a value of linewidth of 4.9 GHz at sea level, which, of course, falls off with altitude.¹⁰ So, first, we will pick a CO₂ line in the band that gives the shorter wavelengths -- this minimizes diffractive losses. Secondly, we verify that the selected line is not coincident with a non-isotopic line to several GHz. Thirdly, we verify that no other molecular species has a resonant absorption at this wavelength.

Table II-3 has a display of four choices for consideration. We list here the CO₂ non-isotopic coincidence factor. From available high resolution absorption data,³ we can readily assess the isotopic radiation absorption. The general level of absorption at the sea level altitude is due to the water vapor continuum. Table II-3 lists an assessment of the results.

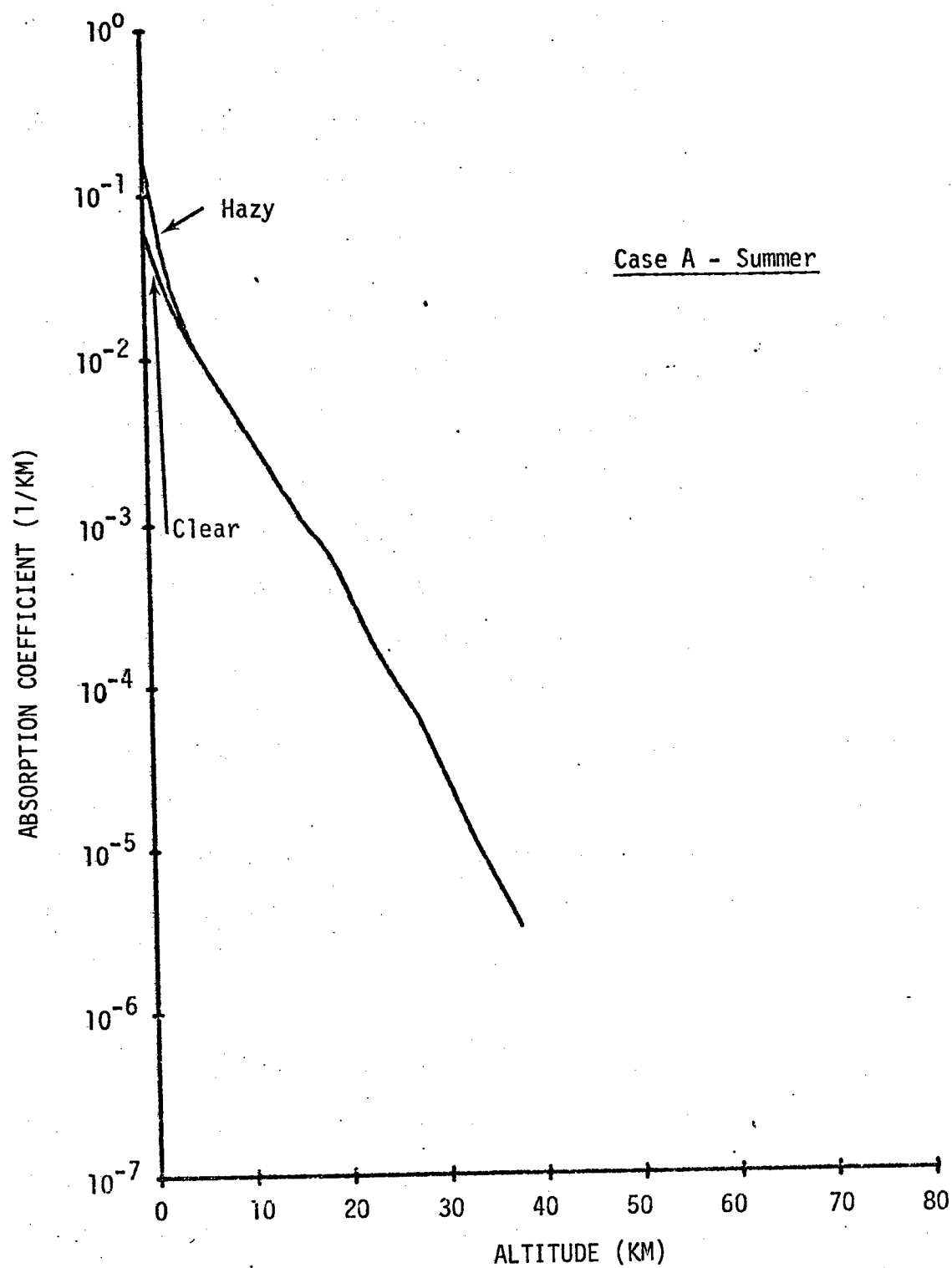


Figure II-13. Atmospheric Extinction vs Altitude

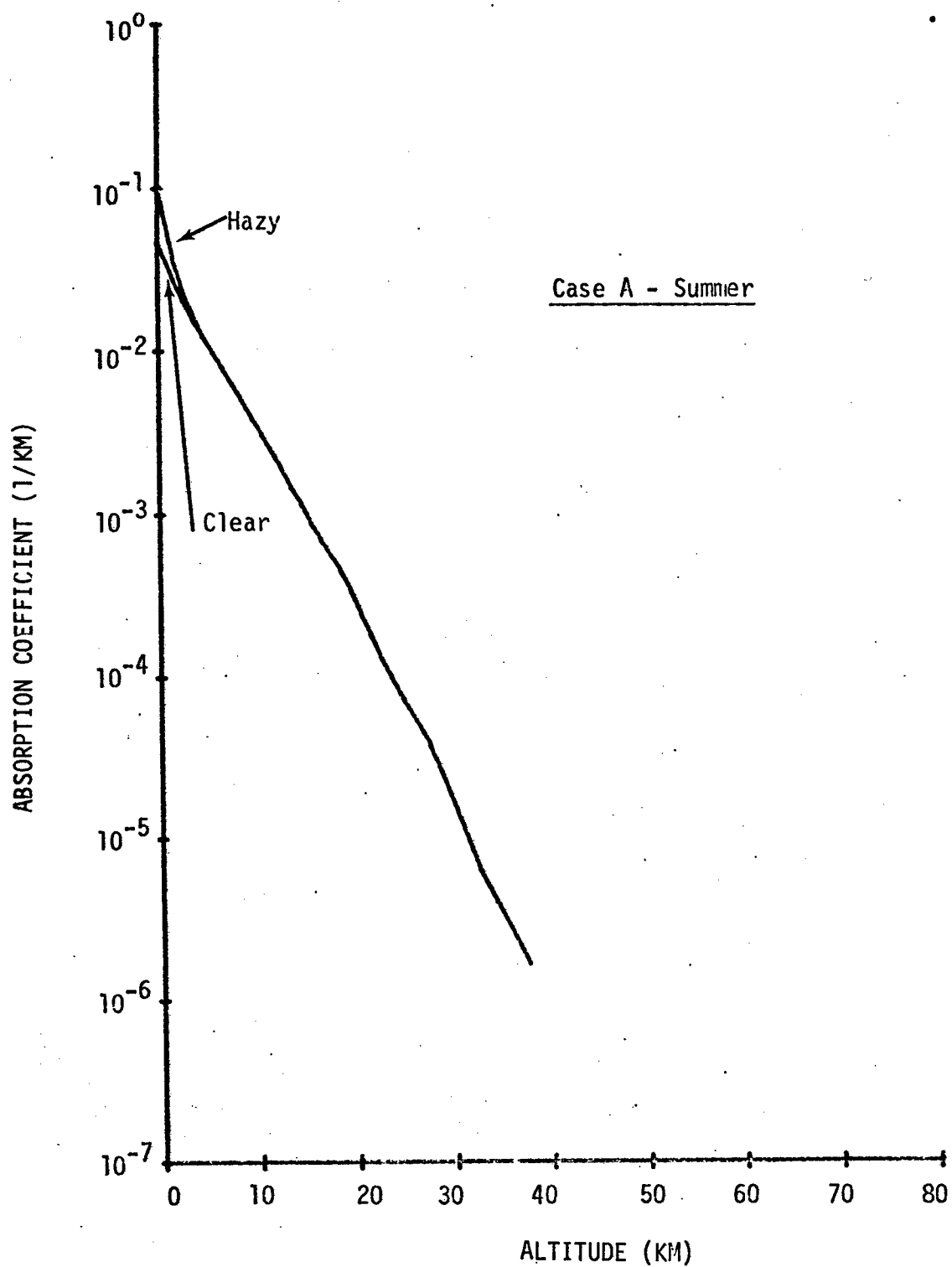


Figure II-14. Atmospheric Absorption vs Altitude

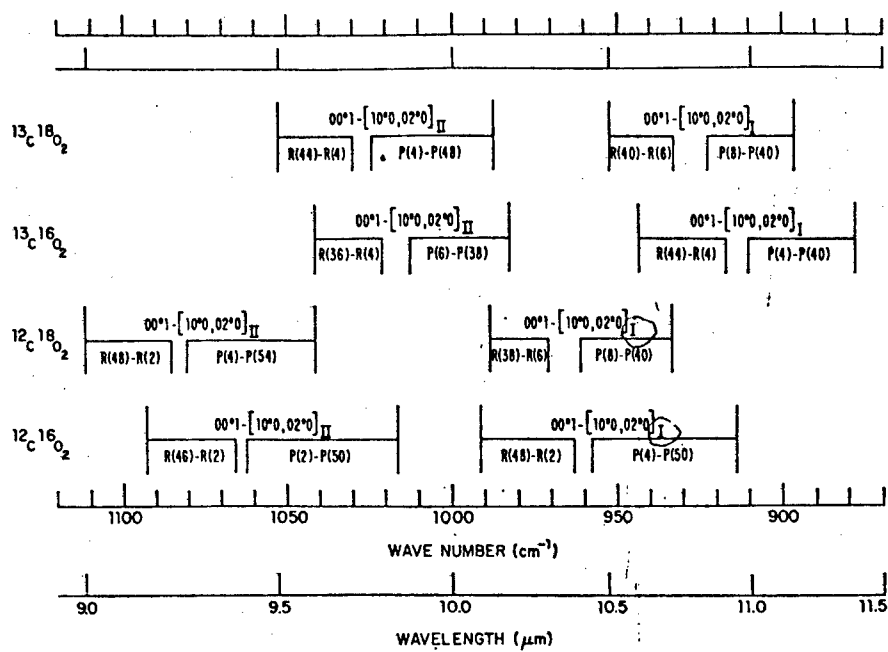


Figure II-15. Isotope Lasing Bands - from Ref. 9

Table II-3
CO₂ Isotope Selection

Isotope*	Transition	Wavelength (Microns)	¹² C ¹⁶ O ₂ Coincidence	Comments
¹² C ¹⁸ O ₂	P(20)	9.355	-2.15 GHz from R(6)	OK
¹³ C ¹⁶ O ₂	P(20)	9.935	None	Good line, but could be better at 12 km
¹³ C ¹⁸ O ₂	P(20)	9.881	None	Poor at Altitude
¹² C ¹⁸ O ₂	R(20)	9.114	None	Very good at all Altitudes

*Band II considered only

So, for the indicated choice of CO_2 isotopic line in the short wavelength band, we can virtually eliminate CO_2 absorption as a loss factor. By the choice of a dry site, we can also greatly eliminate water vapor as a loss factor. Figure II-16 shows a comparison of water vapor only at $10.6 \mu\text{m}$ and $3.8 \mu\text{m}$. As can be seen, a dry site (this graph is for 35% RH) or a high site can produce a situation where CO_2 isotope absorption is less than $3.8 \mu\text{m}$ absorption. The β values for H_2O absorption only from (1) are then 0.130 for January and 0.527 for July.

4. CO Laser Absorption

When operated warm the carbon monoxide laser has a multiline output that is, in general, highly absorbed by the atmosphere near sea level, mostly by water vapor. It has been indicated,¹¹ however, that recent research has shown the output of a high power CO electrical discharge laser (EDL) can be shifted to lower vibrational numbers which have much lower atmospheric absorption. On the basis of this result, we have used the absorption coefficient data given¹¹ for the most efficient lines (see Figure II-17). The β for the P11 line considering sea level operation is slightly greater than 3, which makes it unreasonable for use, so the P10 line, which has a β of 0.415 (0.046 for mountain top operation), was selected for the thermal blooming calculations.

5. Average Transmission

For a slant range to the satellite, the atmospheric transmission is given by

$$T = \exp (- \beta / \cos \theta), \quad (12)$$

where θ is the zenith angle. Since θ is a function of time, if we wish to compute the transmission weighted over the entire mission, we should calculate

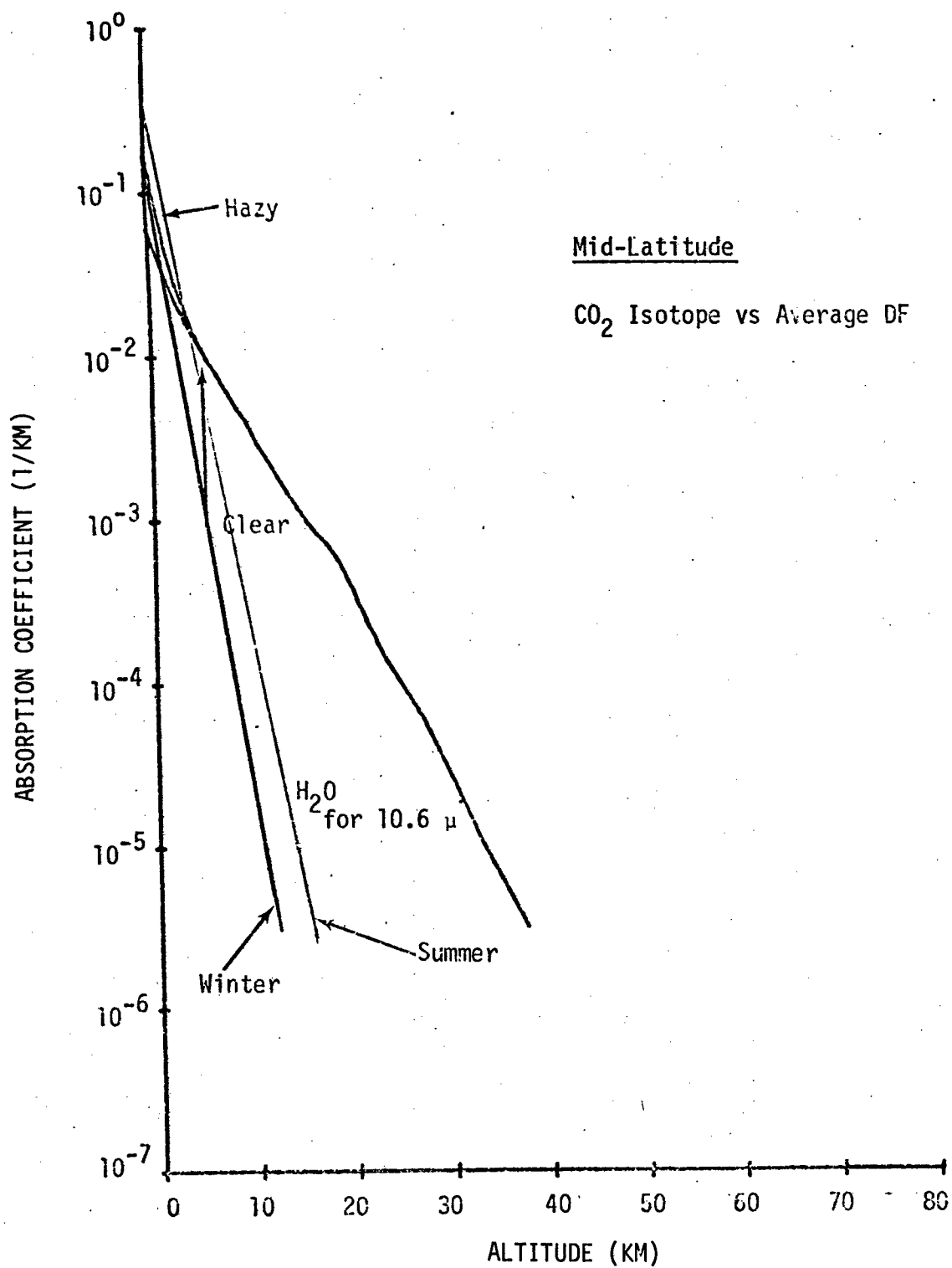


Figure II-16. Atmospheric Extinction vs Altitude

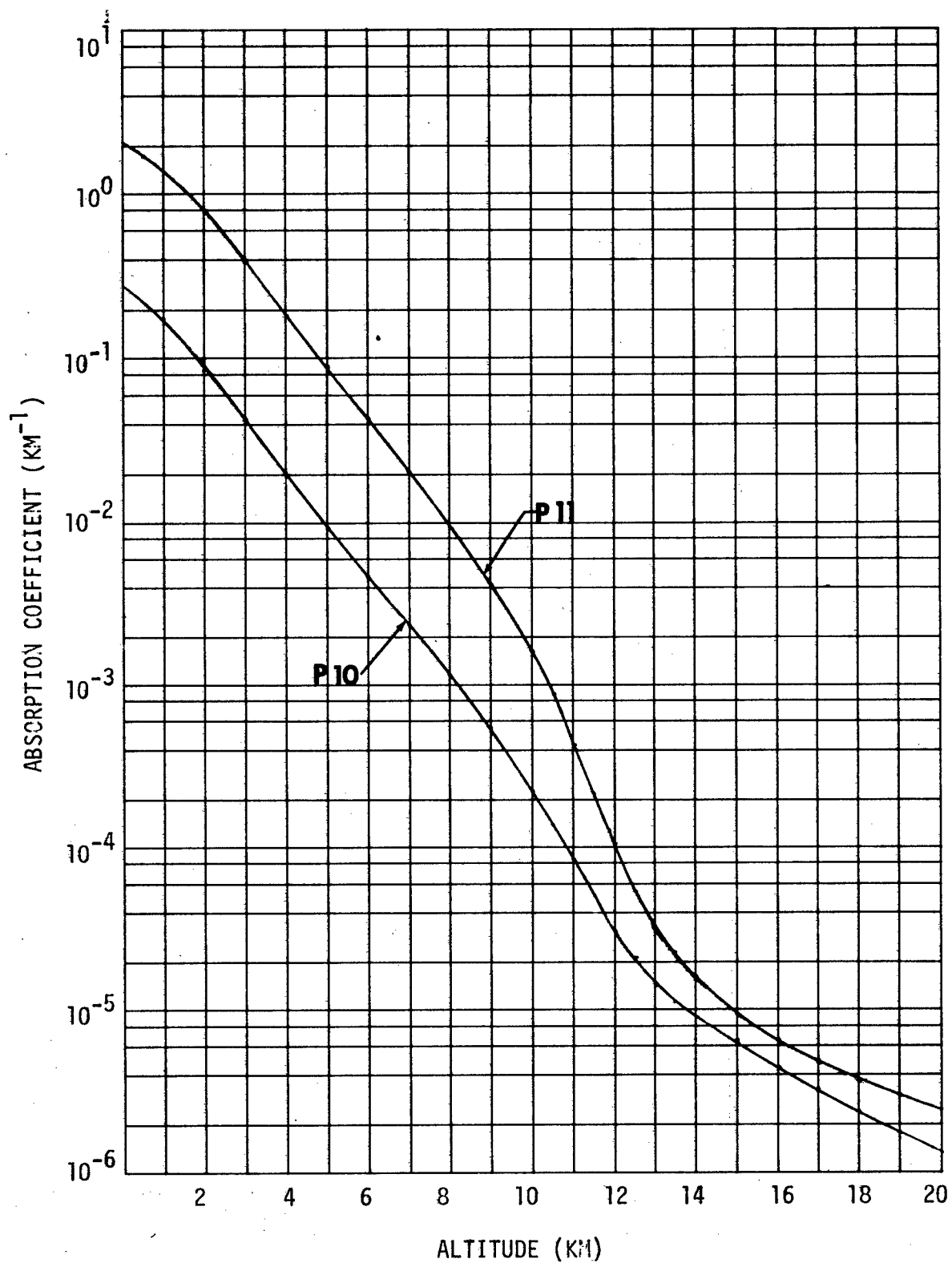


Figure II-17. Absorption Coefficients Versus Altitude for Two CO Laser Lines - Mid-Latitude Summer Atmospheric Model

$$\bar{T} = \frac{1}{2T_0} \int_{-T_0}^{T_0} \{\exp - \beta / \cos \theta(t)\} dt.$$

Figure II-18 shows the plot for sea level operation, considering a zero offset distance, of β versus \bar{T} described earlier. We have marked the points corresponding to the lasers discussed. In tabular form, these results are:

<u>Lasant</u>		<u>Line</u>	<u>β</u>	<u>\bar{T}</u>
$^{12}C^{16}O_2$	(Summer)	10.59 μm	0.978	0.27
	(Winter)		0.527	0.48
$^{12}C^{18}O_2$	(Summer)	9.11 μm	0.527	0.48
	(Winter)		0.130	0.83
DF	(Average)	$\sim 3.83 \mu m$	0.183	0.77
CO	(Summer)	$\sim 5.0 \mu m$	0.415	0.57

When we consider mountain top operation (3.5 km above sea level), however, the improvement in atmospheric transmission is substantial, even when the worst case models are considered. These data are presented below in tabular form and Figure II-19 is a plot of β versus \bar{T} for this condition. We have included the CO_2 data with this group for purposes of a full comparison.

<u>Lasant</u>		<u>Line</u>	<u>β</u>	<u>\bar{T}</u>
$^{12}C^{18}O_2$	(Summer)	9.11 μm	0.036	0.947
	(Winter)			
DF	(Average)	$\sim 3.83 \mu m$	0.086	0.897
CO	(Summer)	$\sim 5.0 \mu m$	0.046	0.936
CO_2	(Summer)	10.6 μm	0.510	0.495

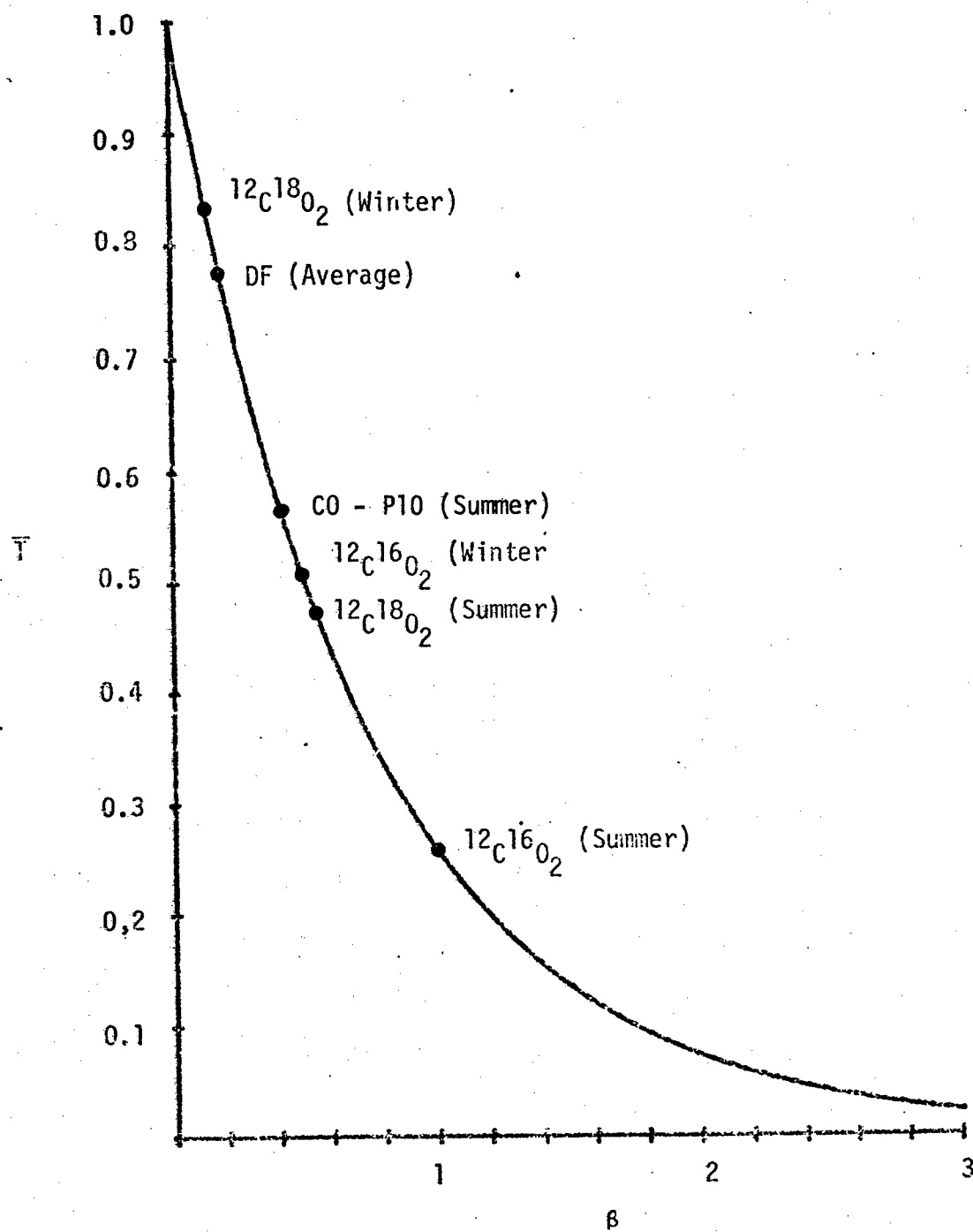


Figure II-18. Comparison of Lasers at Sea Level

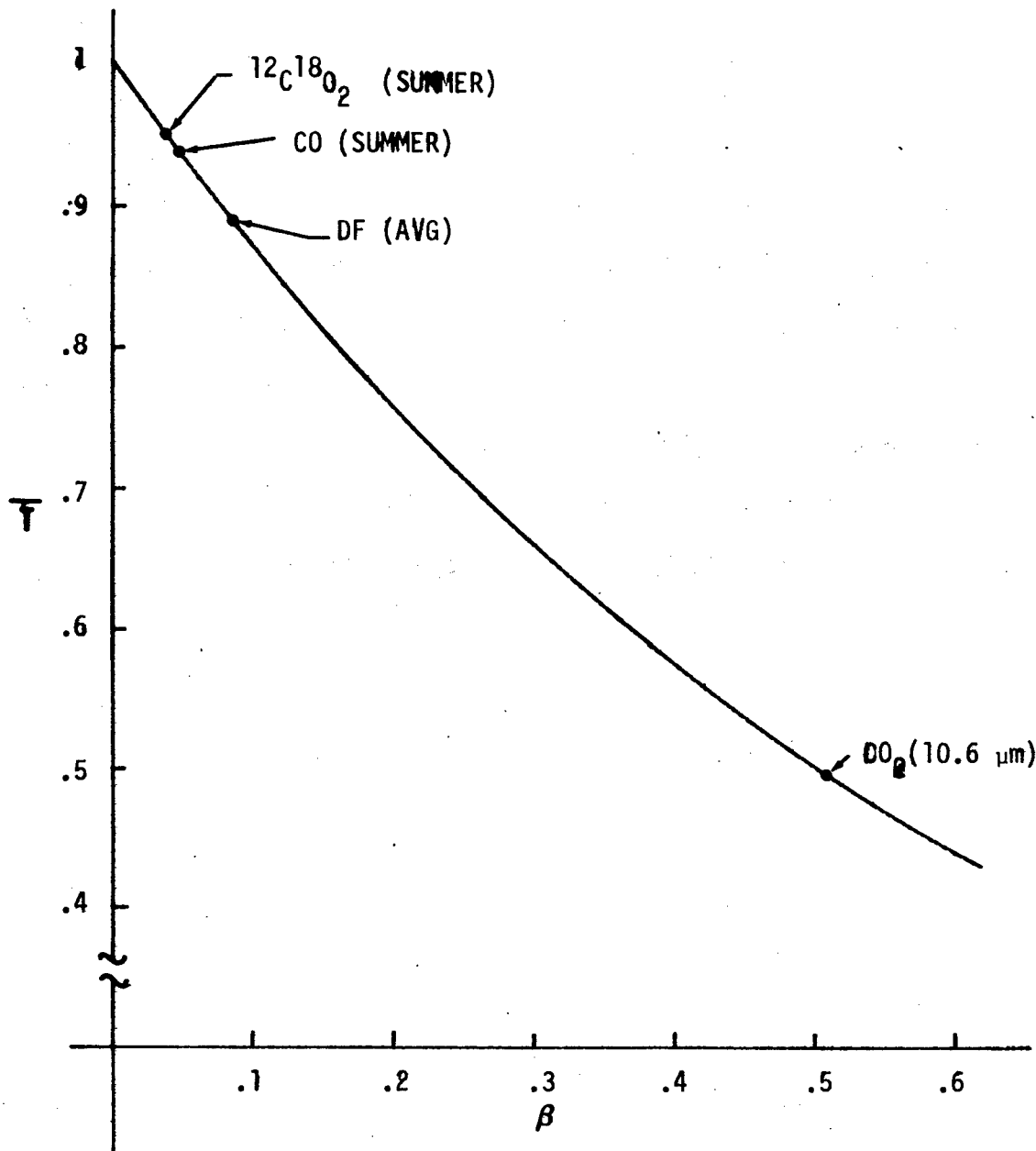


Figure II-19. Comparison of Lasers at 3.5 km Above Sea Level (Mountain Top Operation)

C. Conclusions

Our prime consideration for this program was directed toward the use of a CO₂ laser and, as will be evident throughout this report, we have followed this directive. It would appear, however, from these data on atmospheric absorption that CO₂ operation at sea level is not a viable consideration. If one were to operate at sea level, the DF source would provide the best atmospheric transmission efficiency, but the striking improvement for mountain top operation would strongly favor selection of this location. For mountain top operation, the ¹²C¹⁸O₂ isotope and the carbon monoxide P10 line appear to provide about the same performance with almost 95% transmission averaged over the encounter. For our final system, we have selected the ¹²C¹⁸O₂ source because it is characterized by a more developed laser technology.

References

1. M. Born and E. Wolf, "Principles of Optics," Third Edition, Pergamon Press, Oxford, 1965.
2. "Atmospheric Absorption of Carbon Dioxide Laser Radiation Near Ten Microns," J. H. McCoy, The Ohio State University, Electro-Science Laboratory, Department of Electrical Engineering, Columbus, Ohio 43212, Technical Report 2472-2, 10 September 1968.
3. "Atmospheric Transmittance, 7-30 μ m: Attenuation of CO₂ Laser Radiation," R. A. McClatchey and J. E. A. Selby, Air Force Cambridge Research Laboratories, L. G. Hanscom Field, Bedford, Mass., AFCRL-72-0611, 12 October 1972.
4. Handbook of Geophysics, Revised Edition, USAF Air Research Development Command, The MacMillan Co., New York 1960.
5. J. H. McCoy, D. B. Rensch and R. K. Long, Appl. Opt. 8, No. 7, 1471-1478, July 1969. See also Errata, Appl. Opt. 8, No. 12, 2610, December 1969.
6. P. K. L. Yin and R. K. Long, Appl. Opt. 7, No. 8, 1551-1553, August 1968.
7. J. Viecelli, private communication.
8. R. A. McClatchey and J. E. A. Selby, "Atmospheric Attenuation of HF and DF Laser Radiation," AFCRL-72-0312, 23 May 1972.
9. C. Freed and A. H. M. Ross, Journal of Molecular Spectroscopy, 49, 439 (1974).
10. A. E. Siegman, "An Introduction to Lasers and Masers," McGraw-Hill Book Co., 1971.
11. K. W. Billman and P. D. Rowley, "A Comparison of Near Vertical Atmospheric Transmission of Selected CO and CO₂ Laser Wavelengths," NASA/Ames Research Center, June 1976.

III. QUALITY OF ADAPTION FOR ATMOSPHERIC TURBULENCE

In this section and the one to follow, we shall assess the effects of atmospheric turbulence on an adaptive antenna system transmitting from ground to space. These assessments will cover the calculations of (1) the characteristic coherence length in order to evaluate the dimensions of the control segments for an adaptive array, (2) the expected loss in adaption performance when the tracking lead angle (transit time effect) becomes large as compared to the isoplanatic path size, and (3) the quality of adaptive compensation for atmospheric turbulence effects for several different adaption systems. Our major emphasis in these calculations was directed toward 10.6 μm propagation; however, to a lesser extent, they were extended to 9.1, 5.0 and 3.8 μm for comparison purposes.

A. Atmospheric Coherence Length

Temperature fluctuations originating from large scale phenomena, such as solar heating of the earth's surface, result in turbulent fluctuations of the atmospheric refractive index. These spatio-temporal variations in the index of refraction, in turn, produce random variations in the phase of a propagating optical beam causing the beam to wander or spread. The spatial statistics of the wavefront deformation are generally described by the phase structure $D_\phi(\bar{\rho})$, which is defined as the ensemble average mean square variation of the phase ϕ between two observation points separated by a distance $\bar{\rho}$; i.e.,

$$D_\phi(\rho) = \langle [\phi(\bar{r} + \bar{\rho}) - \phi(\bar{r})]^2 \rangle \quad (1)$$

It has been shown that the statistics and shape of the deformed wavefront can be represented by an infinite series of orthonormal polynomials.¹ By taking

appropriate combinations of the first six terms in the series, he was able to describe the total wavefront phase variance over a receiver aperture of diameter D , as well as show how this phase variance was reduced as the average tilt, average spherical deformation, and average quadratic deformation was removed. The total atmospheric-produced mean square phase deformation was shown to be

$$\langle \phi^2 \rangle_{\text{TOTAL}} = 1.013 (D/r_0)^{5/3} \quad (2)$$

and if the average linear tilt is removed from the received wavefront, the variance of the phase error becomes

$$\langle \phi^2 \rangle_R = 0.13 (D/r_0)^{5/3}, \quad (3)$$

where r_0 is a characteristic coherence length defined by

$$r_0 = (6.88/A)^{3/5} \quad (4)$$

and where

$$A = 2.91 (2\pi/\lambda)^2 \int_{\text{PATH}} ds C_N^2(s) W(s). \quad (5)$$

Here λ is the optical wavelength, $C_N^2(s)$ is the refractive index structure constant along the path of propagation, and $W(s)$ is a weighting factor depending on the nature of the source. For an infinite plane wave source, $W(s)$ is unity, while for a point source (spherical wave), it is $(S/Z)^{5/3}$, where Z is the total path length and S is the distance along the path of propagation with $S = 0$ at the source. Other work^{2,3} has also shown that reciprocity exists between the performance of an aperture, as measured by its effective coherence size, functioning as a transmitter or as part of an optical receiver. Thus, r_0 also represents the limiting aperture size beyond

which the transmitter gain is severely limited by effects of turbulence. Consequently, the calculation of this coherence length was necessary to set bounds on the size of the adaptive array transceiver elements considering different wavelengths and different adaption modes, such as piston only phase correction or both piston and tilt correction. These calculations were performed using the computer program VITURB and a model for the vertical distribution of C_N^2 and numerically solving Eqs. (4) and (5) considering spherical wave propagation.

The model for the vertical distribution of atmospheric turbulence we used in these calculations, shown in Figure III-1, is made up from several sources of data. The very near ground values (< 100 m) are derived from optical measurements previously made by this group.^{4,5} The intermediate data ($> 10^2 < 10^4$ m) are from thermal probe measurements made during aircraft flights^{6,7} and the high altitude data ($> 10^3 < 10^5$ m) are based on balloon borne thermal probe measurements. The upper altitude data we have used were obtained from Fried⁸ who, in turn, used Bufton's⁹ raw data from several balloon flights and then smoothed and averaged the measurements.

We have checked our C_N^2 model by calculating the coherence length r_0 , and the log-amplitude variance, σ_L^2 , for $\lambda = 0.55 \mu\text{m}$ considering vertical propagation and then comparing the results with available astronomical data. To make these calculations, we used a 3000 point numerical integration computer program and solved the infinite plane wave theory equations:

$$r_0 = \left\{ 0.423 \left(\frac{2\pi}{\lambda} \right)^2 \int_0^L C_N^2(s) ds \right\}^{-3/5} \quad (6)$$

and

$$\sigma_L^2 = 0.56 (2\pi/\lambda)^{7/6} \int_0^L C_N^2(s) (s)^{5/6} ds, \quad (7)$$

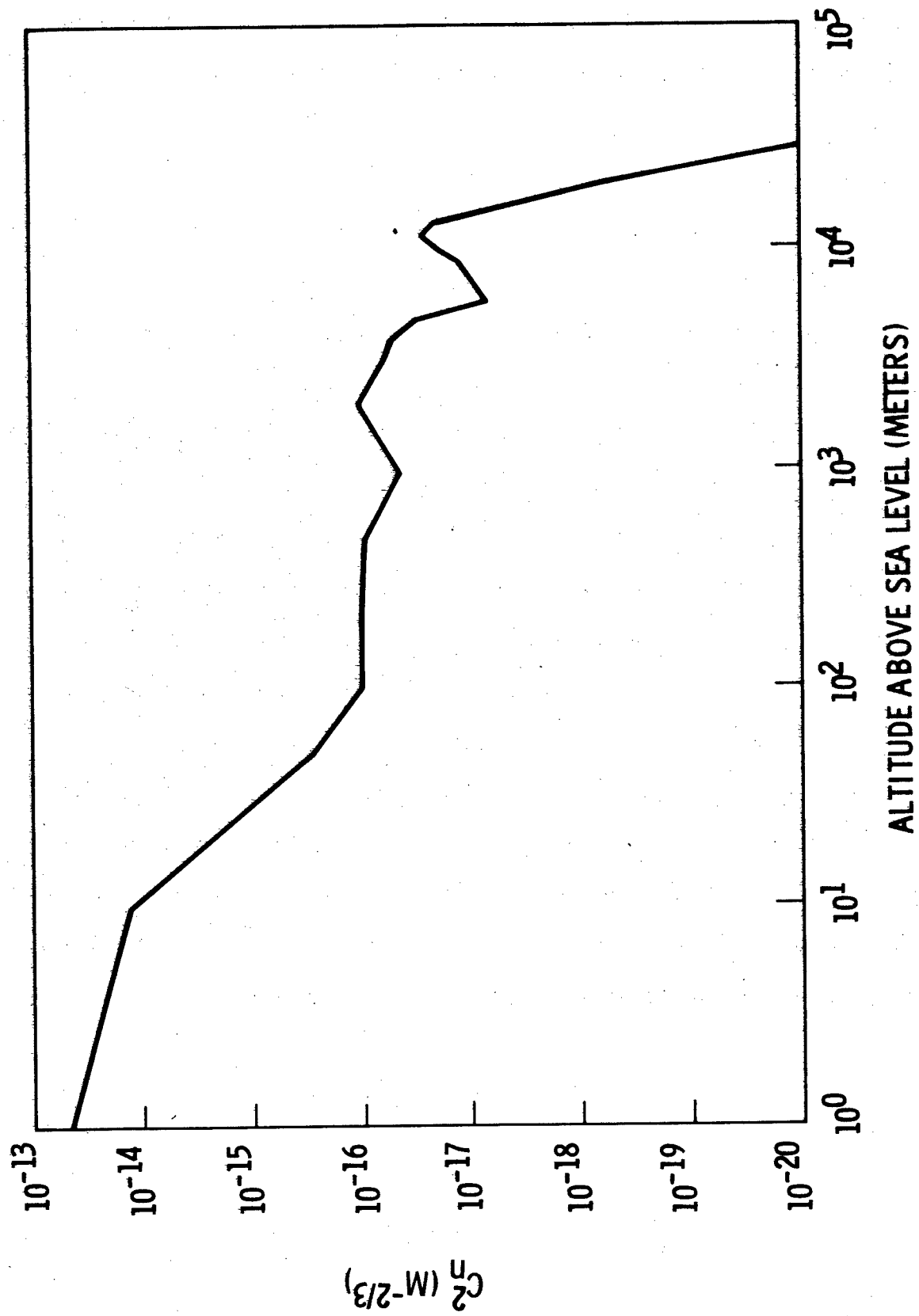


Figure III-1. C_N^2 Versus Altitude Above Sea Level

where λ is the optical wavelength, L is the total path length, and the integration is from the source at $s = 0$. Our results indicate that r_0 should equal 0.117 meters which is in good agreement with the median of measured values, 0.114,¹⁰ and for the computed scintillation, we obtained a value for the log-amplitude variance, $\sigma_\ell^2 = 0.07$, which again is close to the measured value of 0.05.¹¹

In all measurements of the strength of optical turbulence, the data have shown a large variance^{5,6,7,9} and more recently measurements at high altitudes¹² have given rise to questions about variations in the assumed spatial frequency spectra of the refractive index. Our model does not consider these problems, although both of these conditions can seriously affect the outcome of any optical propagation event. As we have stated, our model is based on the average of many measurements of C_N^2 and can be used to obtain results which agree with data based on the average of many turbulence effect measurements. Therefore, the results computed, especially when the propagation path includes the total atmospheric layer, we feel are a valid prognosis of the median effect.

The results of the r_0 calculations for propagation with several wavelengths are given in Figure III-2. These data can be closely approximated by the expression

$$r_0 \approx 4.1 (\lambda/1.06 \times 10^{-5})^{6/5} (\cos \theta)^{3/5}, \quad (8)$$

where θ is the zenith angle. In Figure III-3, we show the time dependence of r_0 considering the satellite target in a circular orbit of 185 km. When r_0 is averaged over the time of the engagement (~ 80 seconds for -60° to $+60^\circ$ zenith angles, considering a zero offset distance) we find

$$\bar{r}_0 = 0.844 r_0 (\theta = 0^\circ). \quad (9)$$

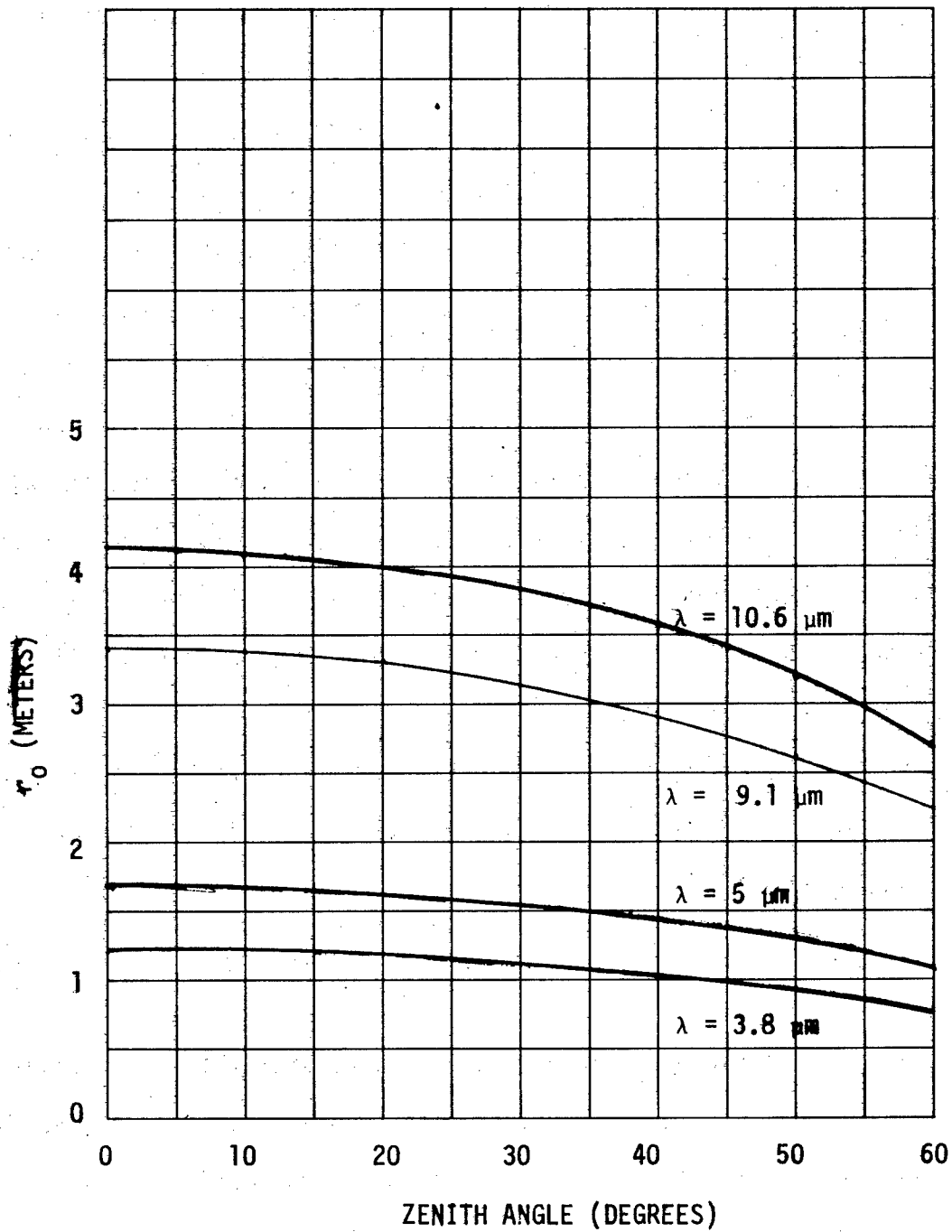


Figure III-2. r_0 vs Zenith Angle for $3.8 \mu\text{m}$, $5 \mu\text{m}$, and $10.6 \mu\text{m}$
(transmitter at altitude 10 M and target at altitude 185 km)

TIME AVERAGED

$$\bar{r}_0 = 0.844 r_0 (\theta = 0^\circ)$$

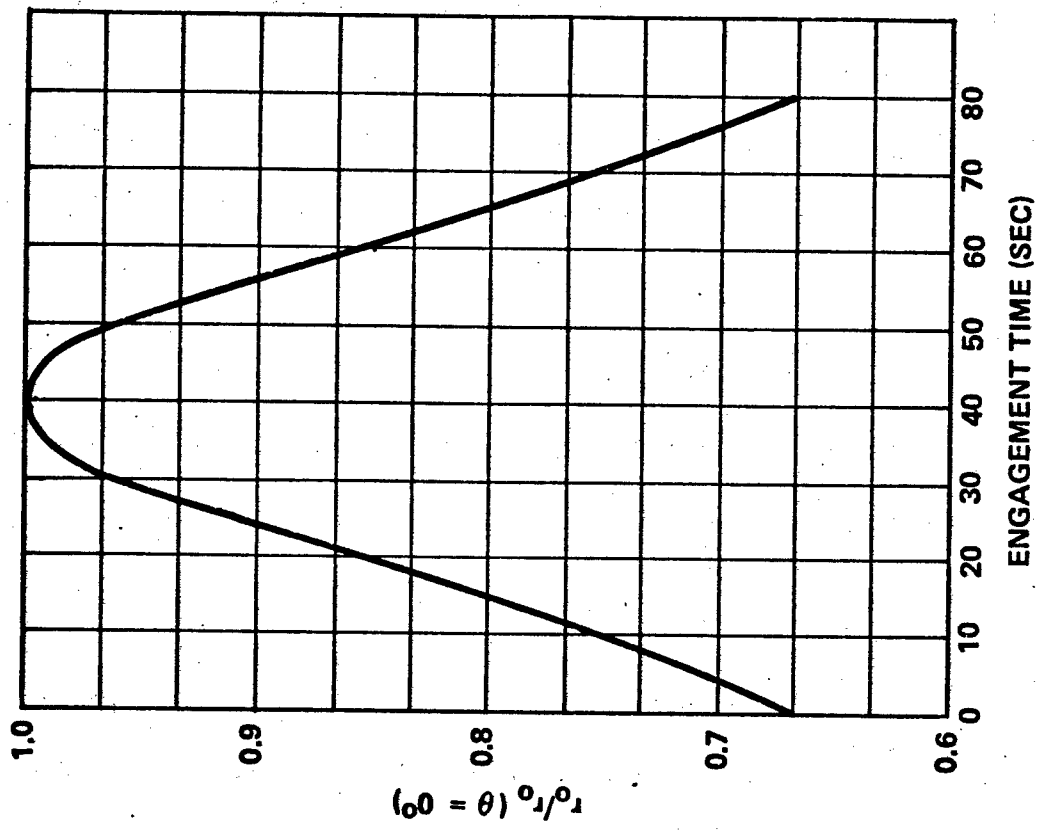


Figure III-3. Normalized r_0 Versus Engagement Time

With these data, we can now estimate the proper ratio of the overall antenna size to the adaptive element size. Since the collector at the satellite is given as two meters, we have, in an effort to maximize the transmission efficiency, selected the overall diameter of the adaptive array as

$$D_T = \frac{2.44 \lambda h}{2 \cos \theta}, \quad (10)$$

where h is the orbital altitude. Since the maximum zenith angle is 60° , the diameter is

$$D_T \approx 4.5 \times 10^5 \lambda. \quad (11)$$

If we assume a Strehl definition for the adaptive segments of at least .95 (i.e., $e^{-\langle \phi^2 \rangle} = .95$) and further assume that both piston and tilt correction will be used in the adaption process, then from Eq. (3)

$$.05 = \langle \phi^2 \rangle_R = 0.13 (A_S/r_0)^{5/3}$$

or

$$A_S/r_0 = 0.57, \quad (12)$$

where A_S is the diameter of a single adaptive element. Now, if we combine Eqs. (8), (9), (11) and (12), we can express the ratio of overall antenna size to adaptive element size as

$$D_T/A_S = 0.246/\lambda^{1/5}. \quad (13)$$

Therefore, for the wavelengths of interest, we have

$$D_T/A_S = 2.4 \text{ for } 10.6 \mu\text{m to}$$

$$D_T/A_S = 3.0 \text{ for } 3.8 \mu\text{m.}$$

Based on these results, we selected a minimum value of three for the ratio of D_T/A_S in our atmospheric turbulence correction calculations.

B. Isoplanatic Patch Size

The results for adaption performance to be presented have been computed based on the assumption that the turbulence-produced index of refractive fluctuations experienced by the wave propagating from the target to the receiver are identical to those encountered by the wavefront propagating from the transmitter to the target. The validity of this assumption is based on two conditions. The first is that the temporal variations of the atmospheric index are negligible in one optical transit time, τ , given by

$$\tau = \frac{2 R \sec \theta}{c}, \quad (14)$$

where R is the satellite orbital altitude,¹³ θ is the satellite zenith angle, and c is the speed of light. Therefore, the characteristic time of the turbulence variation should be greater than τ . The results of our adaption bandwidth calculations, which will be presented in the next chapter, have shown this to be indeed true. The second condition is that the lead angle must be small, as compared to the isoplanatic patch size. Because of the relatively long optical transit time, we must lead the traveling satellite by a small angle so that the transmitted beam will intercept the target correctly. Consequently, the wavefront arriving at the receiver from the target travels through a slightly different part of the atmosphere than that being transmitted to the target.¹⁴ If we are to adapt for the atmospheric-produced phase perturbations, the spatial variations in the refractive index along these different paths must be well correlated. The included angle over which the index of refractive fluctuations are correlated is referred to as the isoplanatic patch.

In order to see how well we meet this second condition, first, let us evaluate the lead angle which can be expressed as

$$\theta_L = \frac{2 V_N}{c}, \quad (15)$$

where θ_L is the lead angle, and V_N is the satellite velocity component normal to the optical propagation direction. For zenith angle $\leq 60^\circ$, V_N is approximately given by

$$V_N = v \cos \psi, \quad (16)$$

where ψ is the satellite elevation angle, v is the satellite velocity tangent to the earth's surface and for a circular orbit is given as

$$v = \left[\frac{G m_e}{r_e + R} \right]^{1/2}, \quad (17)$$

where G is the gravitational constant ($6.67 \times 10^{-11} \text{ (M/kg)}^2$), m_e is the earth's mass ($5.98 \times 10^{24} \text{ kg}$), r_e is the earth's radius ($6.3714 \times 10^6 \text{ M}$), and R is the satellite orbital altitude ($1.85 \times 10^5 \text{ m}$). When the arithmetical manipulations of Eq. (17) are completed and the results combined with Eqs. (15) and (16), we can express the lead angle as

$$\theta_L = 5.2 \times 10^{-5} \cos \psi. \quad (18)$$

Fried¹⁵ has shown that the isoplanatic patch size is proportional to the ratio of the characteristic length r_0 to the turbulence-weighted path between the target and the receiver and is given by

$$\theta_{IP} = \left\{ 0.423 k^2 \int_0^L ds c_N^2(s) \left[\frac{s}{L} (L - s) \right]^{5/3} \right\}^{-3/5} \quad (19)$$

where the integration is from the target location at $S = 0$ to the receiver at $S = L$. For the present configuration, where the target is at altitude 185 km

and the transmitter at altitude 10 M, θ_{IP} , as a function of zenith angle, is that shown in Figure III-4.

The data presented in Figure III-4 can be modeled in a near exact fashion by the expression

$$\theta_{IP} = 7.4 \times 10^{-4} \left(\frac{\lambda}{1.06 \times 10^{-5}} \right)^{6/5} (\cos \theta)^{8/5}. \quad (20)$$

Therefore, if we consider the case of zero offset distance, so $\psi = \theta$, the ratio of the lead angle to the isoplanatic patch size can be expressed as

$$\theta_L / \theta_{IP} = 7.5 \times 10^{-8} (\lambda^2 \cos \theta)^{-3/5}. \quad (21)$$

The effect of this ratio on optical system performance has been expressed, at least for the on-axis intensity, or Strehl approximation, as

$$I/I_0 = \exp \left[-6.88 (\theta_L / \theta_{IP})^{5/3} \right]. \quad (22)$$

If we combine Eqs. (21) and (22), the system performance can be expressed as

$$I/I_0 = \exp - (9.2 \times 10^{-12} \frac{\sec \theta}{\lambda^2}). \quad (23)$$

Therefore, for 10.6 μm

$$\theta = 0^\circ, I/I_0 = 0.92$$

and

$$\theta = 60^\circ, I/I_0 = 0.85.$$

This may appear as a serious reduction in performance, especially at $\theta = 60^\circ$, but it must be remembered that our concern is for the energy in the 2-m central diameter of the focal spot (satellite collector diameter is 2 meters), not just that on-axis. Consequently, for $\theta = 0^\circ$, where the central lobe of the far-field pattern is only about one meter at the target, the isoplanatic patch

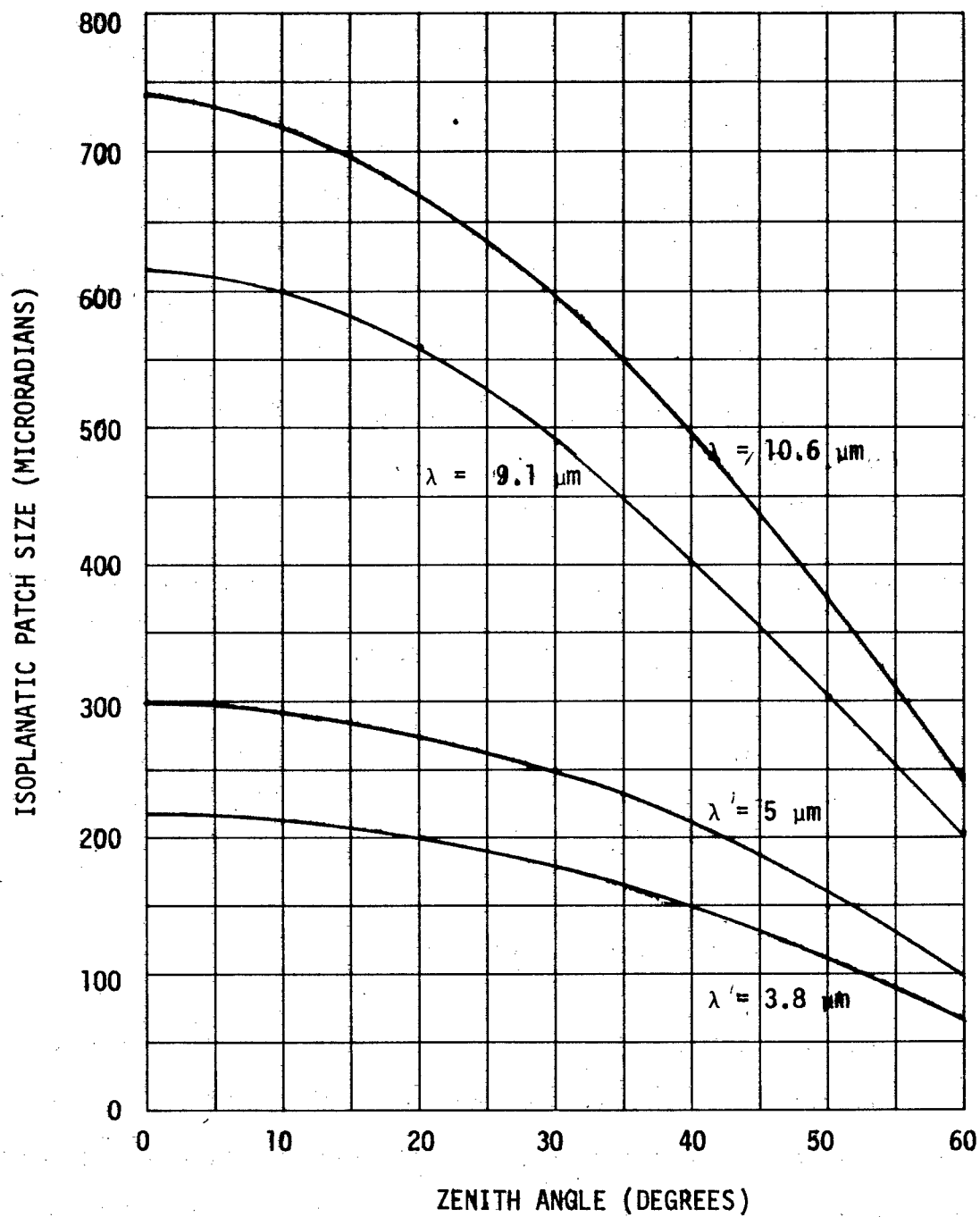


Figure III-4. Isoplanatic Patch Size vs Zenith Angle for 3.8 μm , 5.0 μm , 9.1 μm , and 10.6 μm (target altitude = 185 km, transmitter altitude = 10 M)

size effect on system performance is negligible. For the extreme case at $\theta = 60^\circ$, however, the diffraction limited central lobe of the transmitted beam is about the same diameter as the collector used at the satellite. Here, the uncorrectable atmospheric beam spreading is noticeable, but still not severe. We can show this in the following way. If we substitute a Gaussian beam approximation for the classical Airy pattern, such that the transmitted intensity distribution at the satellite in the absence of atmospheric turbulence can be expressed as

$$I(r) = I_0 \exp(-2(r/r_1)^2), \quad (24)$$

where I_0 is the on-axis intensity and $r_1 \approx .9 \lambda R/D_T$, D_T being the overall transmitter aperture. To account for the isoplanatic effects on beam spreading, we can express the resultant intensity distribution, I_T , as

$$I_T = \alpha I_0 e^{-2(r/r_T)^2}, \quad (25)$$

where α is just the loss factor given by the right-hand side of Eq. (23), and r_T is the effective half beamwidth resulting from beam spreading. Since the medium is assumed to be lossless, we can relate r_T to r_1 using Eqs.(24) and (25) as follows (conservation of energy):

$$\alpha I_0 \int_0^\infty e^{-2(r/r_T)^2} r dr = I_0 \int_0^\infty e^{-2(r/r_1)^2} r dr.$$

Thus,

$$r_T = r_1 / \sqrt{\alpha}. \quad (26)$$

The maximum received power due to isoplanatic effects is then given by

$$B = \frac{\alpha \int_0^{D/2} e^{-2\alpha(\frac{r}{r_1})^2} r dr}{\int_0^{D/2} e^{-2(\frac{r}{r_1})^2} r dr}, \quad (27)$$

which simplifies to

$$B = \frac{1 - e^{-\alpha D^2 / 2 r_1^2}}{1 - e^{-D^2 / 2 r_1^2}}, \quad (28)$$

where $D = 2 \text{ M}$, the receiver aperture. In Figure III-5 we show the results from Eq. (28) for different wavelengths and zenith angles. The results indicate that the system performance degradation due to the effects of isoplanatism at the shorter wavelengths and larger zenith angles is serious. Since the time rate of change of zenith angle is nonlinear, it is therefore more meaningful to consider the time averaged performance over the engagement period. Table III-1 lists the calculated values for the time-averaged percentage of power into the 2-meter receiver for different wavelengths and different satellite ground track offsets. We see that, on the average, the isoplanatic effect is negligible ($< 5\%$ loss) for both CO_2 and isotopic CO_2 sources, even considering maximum satellite offset distances. For the CO source, however, the loss becomes noticeable for offset distances greater than 100 km and for the $3.8 \text{ } \mu\text{m}$ source the loss is apparent, even for directly overhead satellite passes.

C. Adaption Performance Calculations

In what follows, we calculate and evaluate the atmospheric turbulence effects on the performance of several basic adaption systems for transmitting power to a 2-meter collector in a 185 km circular orbit. For reasons of economy and simplicity in our calculations, the spatial variation transverse to the propagation direction is limited to one dimension. Since we are primarily interested in the relative performance of the systems, and because

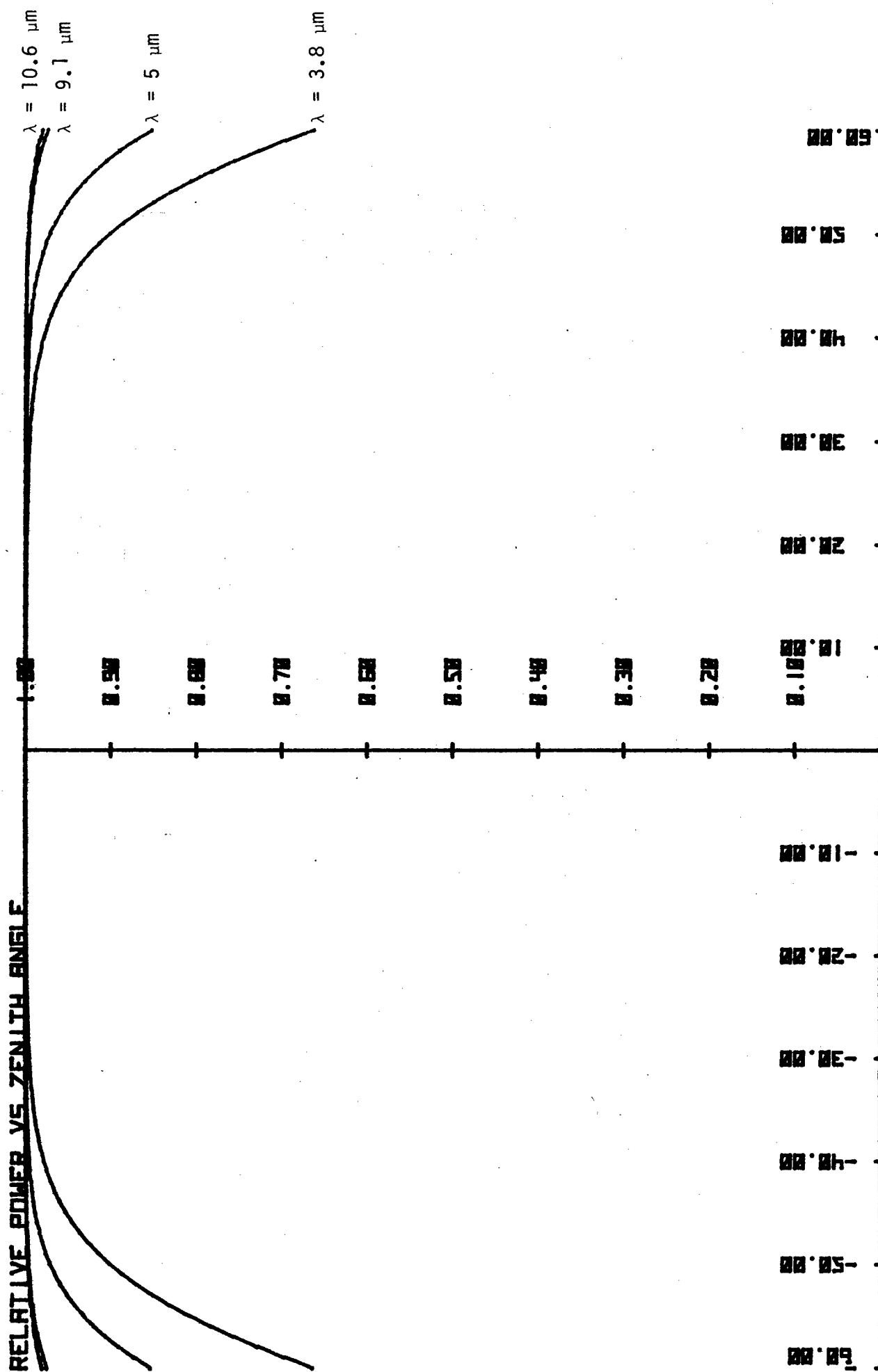


Figure III-5. Percentage of Transmitted Power into 2-Meter Bucket Due to Isoplanatism

Table III-1.

Percentage of Transmitted Power into 2-Meter
Bucket Averaged Over Engagement Time (~ 80 sec)
Due to Isoplanatism

Offset \ λ	3.8 μm	5.0 μm	9.1 μm	10.6 μm
0 (overhead)	91.8%	96.9%	99.5%	99.7%
100 km	87.1%	95.2%	99.3%	99.5%
200 km	59.2%	33.2%	97.5%	98.3%

the atmospheric-produced turbulence can be considered isotropic, this limitation should not be an important factor in the performance evaluation. The basic calculation of these effects is carried out by dividing the propagation path between the transmitter and receiver into short segments. Then, the accumulative turbulence-produced phase distortion within each segment is lumped at a single plane within that segment. Starting from the transmitter plane, the beam is first free-space propagated via the Fast Fourier Transform (FFT) algorithm from one plane to the next and then multiplied by an appropriate phase function to account for the turbulence effects within the segment. In the subsections to follow, we will discuss the significant details of the propagation model, as well as the calculational procedure. Then, a brief description of the adaptive systems under consideration will be given and finally the numerical results.

1. Approach

Propagation of a beam wave along the z direction in a weakly inhomogeneous medium, such as the turbulent atmosphere, is characterized by the parabolic wave equation

$$(\nabla_T^2 + i2k \frac{\partial}{\partial z} + 2k^2 N_1) U = 0, \quad (29)$$

where U is the complex field amplitude, N_1 is the random part of the refractive index, ∇_T^2 is the transverse Laplace operator, and k is equal to 2π divided by the free space wavelength λ . The magnitude of N_1 for the atmosphere is only on the order of 10^{-6} , and therefore approximate solutions of Eq. (29) via perturbational analysis are valid for most cases of interest. In the phase-screen approach employed here, the propagation path between the transmitter and the receiver is divided into sufficiently short segments so that perturbational analysis of Eq. (29) yields

$$U_N \approx U_{N-1,N} e^{i\gamma_N}, \quad (30)$$

where U_N is the complex field amplitude at $z = z_N$, $U_{N-1,N}$ is the field free-space propagated from z_{N-1} to z_N , and γ_N is the random optical path-length induced by the turbulence within segment N and is given by

$$\gamma_N = k \int_{z_{N-1}}^{z_N} N_1 dz. \quad (31)$$

By choosing the segments properly so that the magnitude of N_1 does not vary appreciably within each segment, γ_N may be approximated by its average, $\bar{\gamma}_N$, that is,

$$\gamma_N \approx \bar{\gamma}_N = k \bar{N}_1 \Delta z_N, \quad (32)$$

where \bar{N}_1 is the average of N_1 in $\Delta z_N = z_N - z_{N-1}$.

For the present model, we assume a one-dimensional variation in the transverse direction and so \bar{N}_1 is a random function of x and z only. We also make the usual assumption that \bar{N}_1 has zero ensemble average and obeys Gaussian statistics in the generalized sense. With the above assumption, we can proceed to construct an ensemble of \bar{N}_1 distributions by assigning Gaussian random numbers to the x - z space. It has been suggested from theoretical consideration that the appropriate turbulence spectrum function, φ_N , for calculations corresponding to two-dimensional space is of the form¹⁶

$$\varphi_N = \frac{0.056 C_n^2(z) \left(\frac{2\pi}{L_0}\right)^{-8/3}}{\{1 + (K_x^2 + K_z^2)/(2\pi/L_0)^2\}^{4/3}}, \quad (33)$$

where $C_n^2(z)$ is the structure constant characterizing the turbulence strength at z , L_0 is the outer scale of turbulence defining the region over which the turbulence is approximately uniform and, K_x and K_z are, respectively, the spatial frequency variables in the x and z directions. φ_N of Eq. (33) is derived from the Von Karman spectrum function, by neglecting the inner-turbulence-scale dependence and followed by integrating over K_y -space. Since the inner turbulence scale is only on the order of millimeters, the neglect of its effect is indeed justifiable for computer calculations using a mesh size, Δx , greater than a few millimeters. (A mesh size of 4 cm is used in the present calculations. The phase function φ_Y for propagation over an incremental distance Δz_N in a uniform turbulence is related to φ_N by¹⁷

$$\varphi_Y = 2\pi k^2 \Delta z_N \varphi_N, \quad (34)$$

and, by definition, the phase structure function $D(x_1, x_2)$ corresponding to φ_Y is¹⁶

$$D(x_1, x_2) = \langle [\gamma_N(x_1) - \gamma_N(x_2)]^2 \rangle \quad (35)$$

where $\langle \rangle$ denotes an ensemble average. Moreover, D is a function of $\rho \equiv |x_1 - x_2|$ and, in the limit of infinitely large L_0 , is of the form¹⁷

$$D(\rho) = 2.91 C_n^2(z) k^2 \Delta z_N \rho^{5/3}. \quad (36)$$

As we shall see, Eqs. (32) through (36) are used in the construction of the \bar{N}_1 distributions.

A refractive index distribution of proper spatial frequency distribution and statistics can be constructed as follows. At $z=z_N$, we assign a set of normalized Gaussian random numbers $f_i(x)$ to the mesh points of the computational field size along the x axis, where the subscript i is used to indicate that $f_i(x)$ is only a particular member of a large ensemble. Applying Eq. (33) and the argument that the Fourier transform of $f_i(x)$ is random and uncorrelated, we have

$$C \bar{N}_1(x, z_N) = \int_{-\infty}^{\infty} dK_x \sqrt{\phi_N} F_i(K_x) e^{iK_x x}, \quad (37)$$

where $F_i(K_x)$ is the Fourier transform of $f_i(x)$ and C is a normalization constant depending upon the mesh number and size used in the computation. The advantage with this approach is that the computation of the Fourier transformations can be performed economically and rapidly using the FFT algorithm. Having constructed an ensemble of \bar{N}_1 in the manner described by Eq. (37) and the function $D(x_1, x_2)$ of Eq. (35), we can determine C by letting L_0 approach infinity and equating $D(x_1, x_2)$ to the right-hand side of Eq. (36). For mesh number 1024 and mesh size 4 cm, we found that the average value of C as a function of ensemble size is that shown in Figure III-6. As might be expected, C is independent of both Δz_N and C_n^2 . Note in Figure III-6 that C tends to be a limiting value as the ensemble size increases.

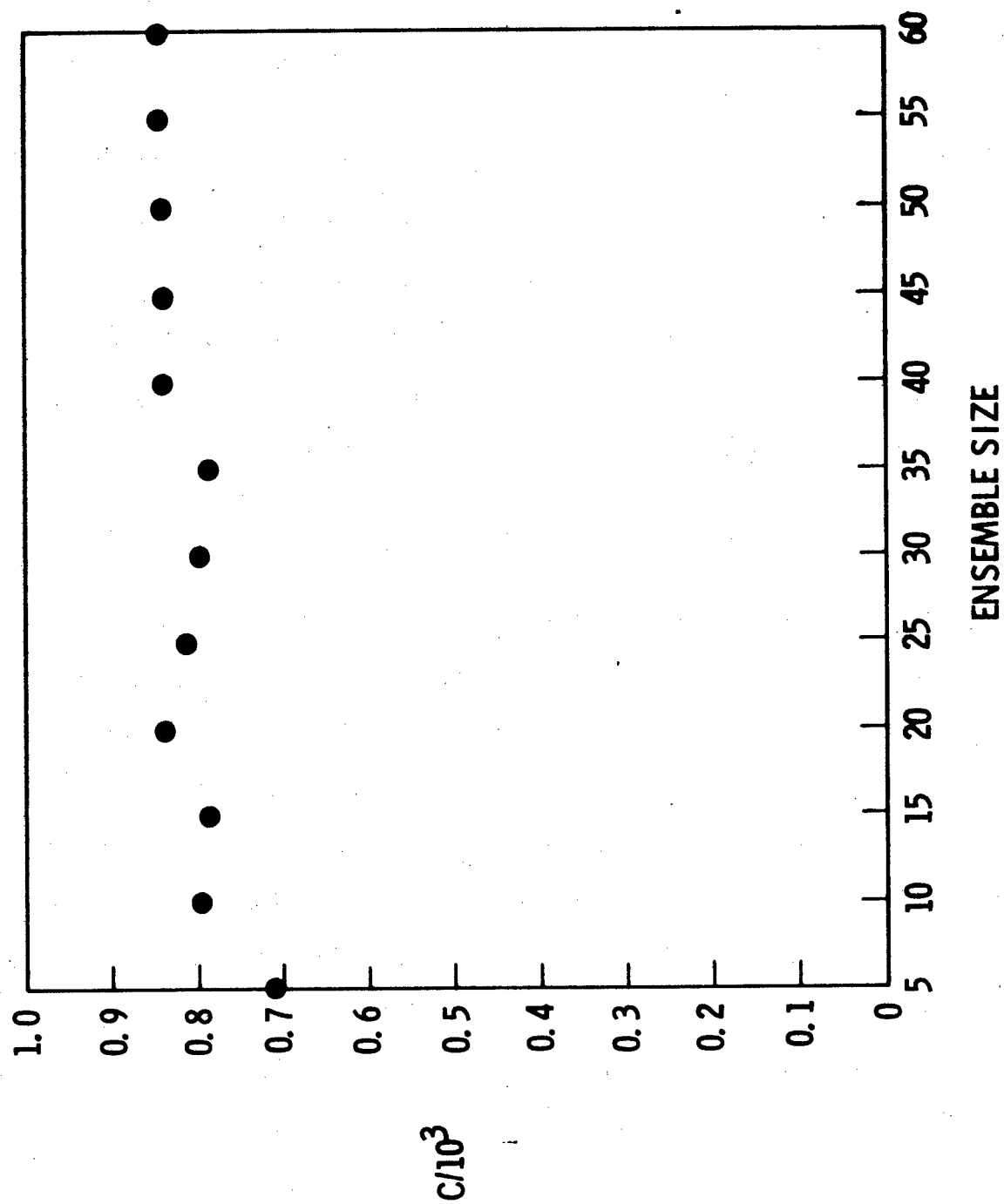


Figure III-6. Normalization Constant C vs Ensemble Size
(Mesh Size = 4 CM, Mesh Number = 1024)

With the constraints $\bar{\gamma}_N \ll k\Delta x$ and $\bar{\gamma}_N \ll k\Delta z_N$, as required for the validity of the phase-screen approach, the turbulence effects on vertical propagation between altitudes 10 M and 200 KM can be adequately represented by using the vertical distribution model for the refractive index structure constant, C_n^2 , shown in Figure III-1 and then representing the model with eight phase screens as depicted in Figure III-7. The strength of the Nth random screen is characterized by $\overline{C_n^2}$, where

$$\overline{C_n^2} = \frac{1}{\Delta z_N} \int_{z_{N-1}}^{z_N} C_n^2(z) dz. \quad (38)$$

Some remarks about the phase-screen distribution are in order. Referring to Figure III-3, the separation Δz_N between any two adjacent screens is much greater than the average outer turbulence scale at the altitudes where the screens are located. Thus, the effects of the random screens are uncorrelated in the z direction, as should be. The condition $\Delta z_N \gg L_0(z)$ allows the weak dependence of ψ_N on K_z to be neglected in the calculations. Furthermore, the area, $C_n^2 \Delta z_N$, is approximately equal to that under the curve $C_n^2(z)$ from z_{N-1} to z_N , so that the important effect of the turbulence location is accounted for.

We now describe a computer experiment that has been used to test the validity of the phase-screen model developed. For a focused beam, initially uniform across the transmitter aperture, the ensemble average on-axis intensity $\langle I \rangle$ in the focal plane is given by¹

$$\frac{\langle I \rangle}{I_0} = \exp\left(-1.013(D/r_0)^{5/3}\right) \quad (39)$$

where D is the aperture diameter, r_0 is the characteristic length depending upon the turbulence strength and location in the path of propagation, and I_0

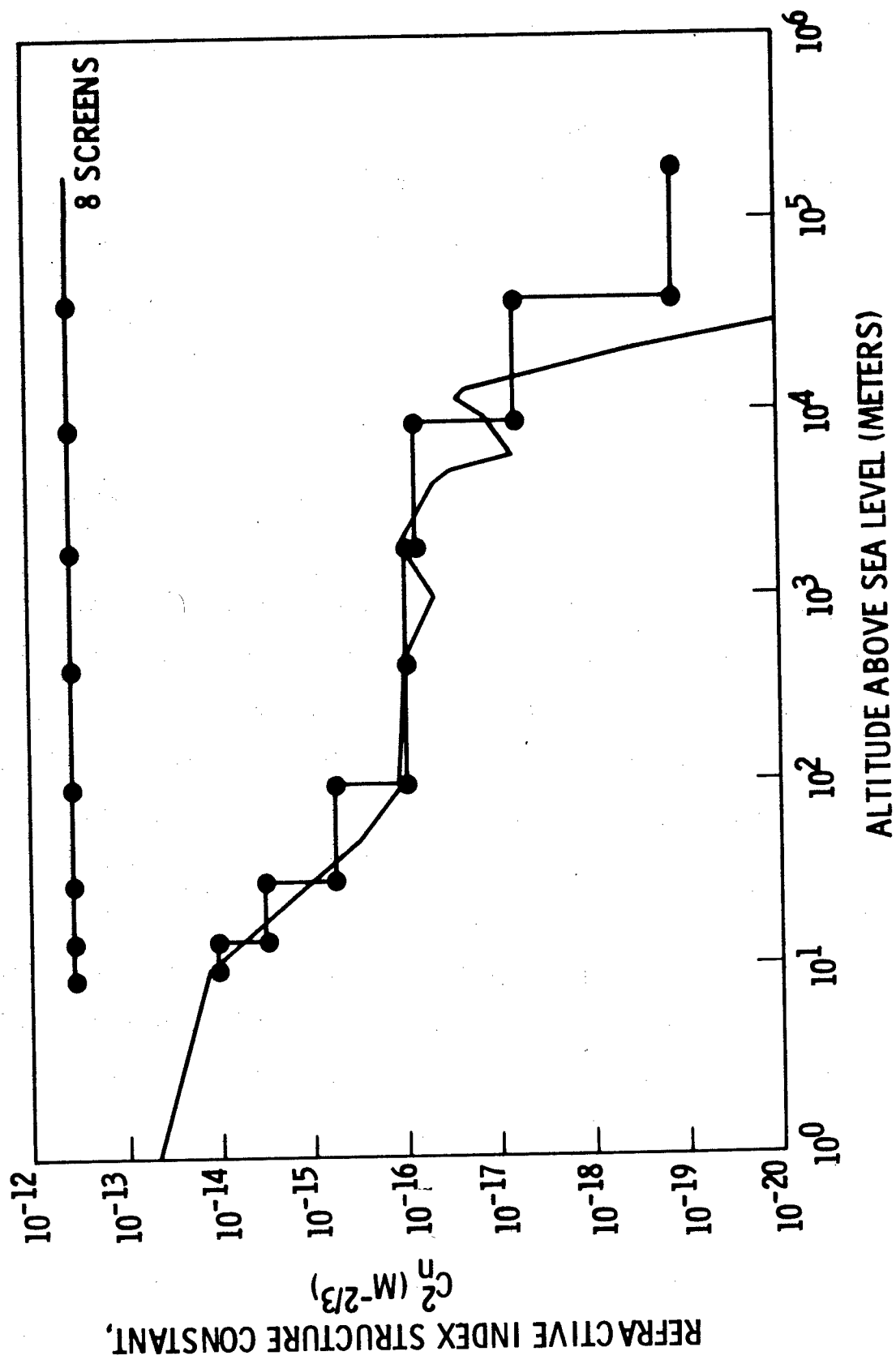


Figure III-7. Eight Screen Representation of Vertical Distribution of Turbulence

is the on-axis intensity in the absence of any perturbations. For propagation from altitudes 10 M to 185 KM, in the vertical direction, we found from previous calculations (see Figure III-2) that $r_0 = 4.1$ M. Substituting this value of r_0 into Eq. (39), we have

$$\frac{\langle I \rangle}{I_0} = 0.26$$

for $D = 4.8$ M. Using the phase screen model and from Eq. (10) $D = 4.8$ M, the calculated $\langle I \rangle / I_0$ as a function of ensemble size is that shown in Figure III-8. Thus, the present model yields results in good agreement with the theoretical prediction of Eq. (39).

2. Adaption System Implementation

The application of adaptive systems to localize the transmitted energy at a distant target through phase compensation is reasonably well understood, and several methods of system implementation have been suggested. In Table III-2 we have listed various transmitter and receiver configurations that have been considered for adaptive optics systems and have indicated with a dot those combinations which were investigated in this study. All of the receivers listed are characterized by a set of closely spaced subapertures except the single aperture detector which is normally used in the classical multidither system. The transmitter, or beam corrector, approaches are likewise made up of segmented arrays which exhibit phase and amplitude discontinuities in the transmitted beam. The one exception is the continuous surface deformable mirror. Although this approach does not have discontinuities, it does, as with the other techniques, have a limited number of actuators and consequently has spatial frequency limitations. The adaptive transmitter/receiver combinations we have chosen may be divided into three categories: Phase adaption, phase and phase gradient adaption, and multidither. A brief description of these methods is given below.

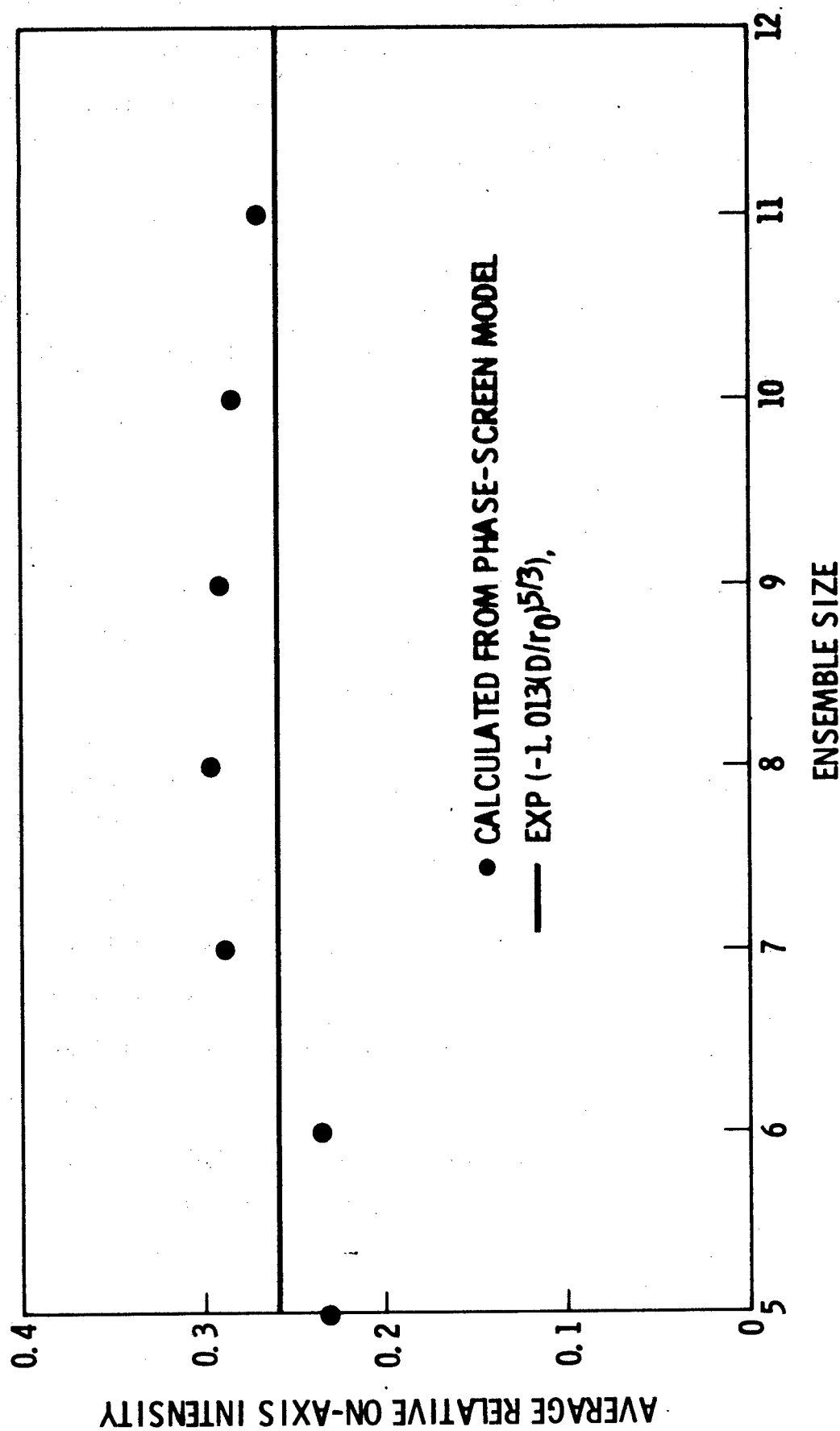


Figure III-8. Average Relative On-Axis Intensity vs Ensemble Size for $D = 4.8 \text{ M}$

Table III-2
ADAPTIVE OPTIC TRANSMITTER/RECEIVER COMBINATIONS INVESTIGATED

RECEIVER TRANSMITTER	SEGMENTED ARRAY				SINGLE APERTURE PHOTON BUCKET
	DIRECT PHASE MEASUREMENT	ANGLE OF ARRIVAL MEASUREMENT	COMBINATION OF ANGLE OF ARRIVAL AND PHASE MEASUREMENT	DIFFRACTION ANGLE RECEIVER WITH SUBAPERTURE PHASE DITHER	
PHASE CORRECTION ONLY	•	•		•	
PHASE CORRECTION ONLY WITH SUBAPERTURE PHASE DITHER					•
PHASE AND PHASE GRADIENT CORRECTION		•	•		
CONTINUOUS SURFACE DEFORMABLE MIRROR	•				

a. Phase Adaption (PA)

In the implementation of phase adaption systems, the average phase of the return wave across each subaperture is first determined, and then, in the transmitting mode, the phase across the same subaperture is set equal to the negative of the average. In practice, phase detection of the return wave is usually accomplished through optical heterodyning, which is rather cumbersome if a large number of subapertures is used. A conceptually simpler method of phase detection is the Hartmann plate method. The Hartmann plate measures the angle of arrival which, in turn, the relative phase can be calculated. Having determined the return phase, the target-medium image can be constructed by adjusting the phase across the subapertures, either through the use of electro-mechanical components or the use of a deformable mirror. In the latter case, the image is constructed by reflecting a uniform wavefront off the deformable mirror whose shape is predetermined by actuator displacements. The phase adaption method described above is a zero th-order wavefront matching scheme in that only the average image across the transmitter aperture is constructed. In terms of localizing the transmitted energy at the target, the performance of phase adaption is dependent upon the target complexity and, of course, the size and number and the arrangement of the subapertures. If the target is a single-glnt structure, optimum performance can be achieved with a single adaption to the target. In the case when the location of the target is known and is within the near field of the array, the performance can be significantly improved by telescoping the beam or by pointing the individual subapertures at the target in conjunction with phase adaption. This may not be surprising, because the dominating effect of atmospheric turbulence is beam tilting.

b. Phase and Phase Gradient Adaption (PPGA)

The significant difference between phase adaption and phase gradient adaption is that, in constructing the image of the target-medium combination, the latter takes into account the average linear tilt of the return wavefront across the subapertures. PPGA should therefore be more efficient, but its implementation requires the measurement of both tilt and phase across the subapertures. One method for measuring the tilt may be as follows. Since the centroid displacement of a focused beam is proportional to the angle of arrival or tilt in the plane of the lens, the tilt at a given subaperture can be determined by focusing that portion of the beam passed through the subaperture and followed by measuring the centroid displacement. An alternate, and perhaps much simpler, method of determining both tilt and phase across the subapertures is the use of the Hartmann plates previously mentioned. Performance calculations involving both methods of tilt and phase measurement have been made and are given in the next section. Again, the implementation of phase and phase gradient adaption is similar to that of phase adaption alone, with the important exception that for the former the transmitting subapertures are tilted to compensate for the angle of arrival.

c. Multidither (MD)

There are two forms of multidither that can be used for adaption systems. The first, which we refer to as classical multidither, uses a segmented array transmitter and phase dither at each of the transmitter segments. The hypothesis behind the multidither method is that if the phase of the output beam is controlled so that the return power detected near the transmitter aperture is at a maximum value, then the incident power at the target also must be maximum. This is clear for a single-glint target and has been verified in the past. As

the complexity of the target increases, however, the performance of multi-dither can become very sensitive to both the number and locations of the receivers. With a multi-glint target, for example, the maximization of the received power can be solely due to constructive interference of weak signals returning from all the glints. Fortunately, for adaption to the satellite we can work with a single glint target, so this problem will not affect the system performance. The second form of multi-dither uses a segmented phase dither array in front of a single aperture collector. Here, a spatial frequency filter equal in size to the collector diffraction angle is placed in the focal plane of the collector. By synchronous demodulation of the dither the phase bias required at each segment to maximize the power going through the filter can be determined. These measured phase adjustments are then, in turn, transferred to the transmitter beam so that the power on target will be maximized.

Two modes of phase-dithering have been suggested for the implementation of multi-dither: temporal dithering and spatial dithering. In the temporal case, the phase across all the transmitting subapertures is dithered simultaneously in time, but at a slightly different RF frequency. For the spatial mode to be considered here, the phase at each subaperture is first advanced and then retarded by a small phase excursion $\delta\phi$, while keeping that at the other subapertures fixed. The corresponding change in the received power at the end of each incremental phase change is recorded. When all the subapertures have been phase-dithered once in each direction sequentially, the phase at the i th subaperture is changed to $G\alpha_i\delta\phi$, where G is the fixed gain constant common to all the subapertures and α_i is the weighting factor for subaperture i . In order for the received power to converge to its maximum value, the value of $G\alpha_i$ must approach zero when the received power tends to its maximum value.

This condition is satisfied by letting α_i equal to $(P_i^+ - P_i^-)/P$, where P_i^+ and P_i^- are the received power resulting from, respectively, $+\delta\phi$ and $-\delta\phi$ changes in the phase at subaperture i . The quantity P is the received power at the end of the previous adaption loop, which increases monotonically with the number of adaption loops. Effectively, $G\alpha_i$ is the variable gain constant (or AGC) of the system that minimizes the effects of receiver size on the signal received.

3. Computer Results

In this section the calculations obtained from applying the phase-screen model discussed previously are presented. We use these calculations to evaluate in detail the various adaptive system implementation methods at $10.6 \mu\text{m}$ wavelength. Subsequently, results will also be presented for shorter wavelengths. Each of the implementation methods is evaluated in terms of maximizing the transmitted power at a single-glint target 185 km above sea level. In particular, we are primarily interested in localizing the power within ± 1 meter centered about the glint, as well as maximizing the on-axis intensity. The overall transmitter aperture for $10.6 \mu\text{m}$ is 4.8 M in width, formed by placing either three or five equal subapertures closely spaced together and located at 10 M above sea level. Other pertinent parameter values are given in previous discussions and also in the figures to be followed. A simple calculation using the given parameter values would show that the target is in the near field of the transmitter aperture and that the diffraction-limited lobe for vertical propagation is about 80 cm.

All of our results, which will be presented in the following paragraphs, were obtained using a computer program entitled Plane Wave Synthesis for Coherent Atmospheric Transmission, or PSYCAT. This code is a two-dimensional

full wave optical program that simulates the open or closed loop operation of an adaptive optical array, using the Fast Fourier Transform (FFT) algorithm. The program, as shown in Figure III-9, simulates transmitter/receiver operation, including effects of spatial frequency response and signal-to-noise ratio, atmospheric transmission (turbulence effects), target characteristics, and phase control algorithms.

a. Adaption in Vacuum

For reference and guideline purposes, this paragraph summarizes the calculations pertinent to the vertical propagation case in the absence of any perturbations. Figure III-10a is the normalized intensity distribution in the target plane produced by a diffraction-limited system, that is, produced by focusing a uniform aperture distribution at the glint. For this ideal case, $P = 92\%$, where P is the percentage of the transmitted power delivered into the "2-meter bucket." When the uniform aperture distribution is not focused, the intensity distribution takes the near-field form shown in Figure III-10b. Here, $P = 40\%$ and $I = 0.12$, where I is the on-axis intensity relative to that for the diffraction-limited case. The results of phase adaption in vacuum using three and five subapertures are shown in Figures III-11a and III-11b. Although the subaperture sizes for the two cases are quite different, the differences in I and P are insignificantly small. These results indicate that, for the aperture sizes used, phase adaption in the usual sense is not very effective in localizing the transmitted power at the target. The reason is wavefront mismatch; that is, with the planar arrangement of such large subapertures, the average phase detected at a given subaperture is not a good approximation of the true phase distribution across the entire subaperture, and therefore a true image cannot be constructed from the average phase values.

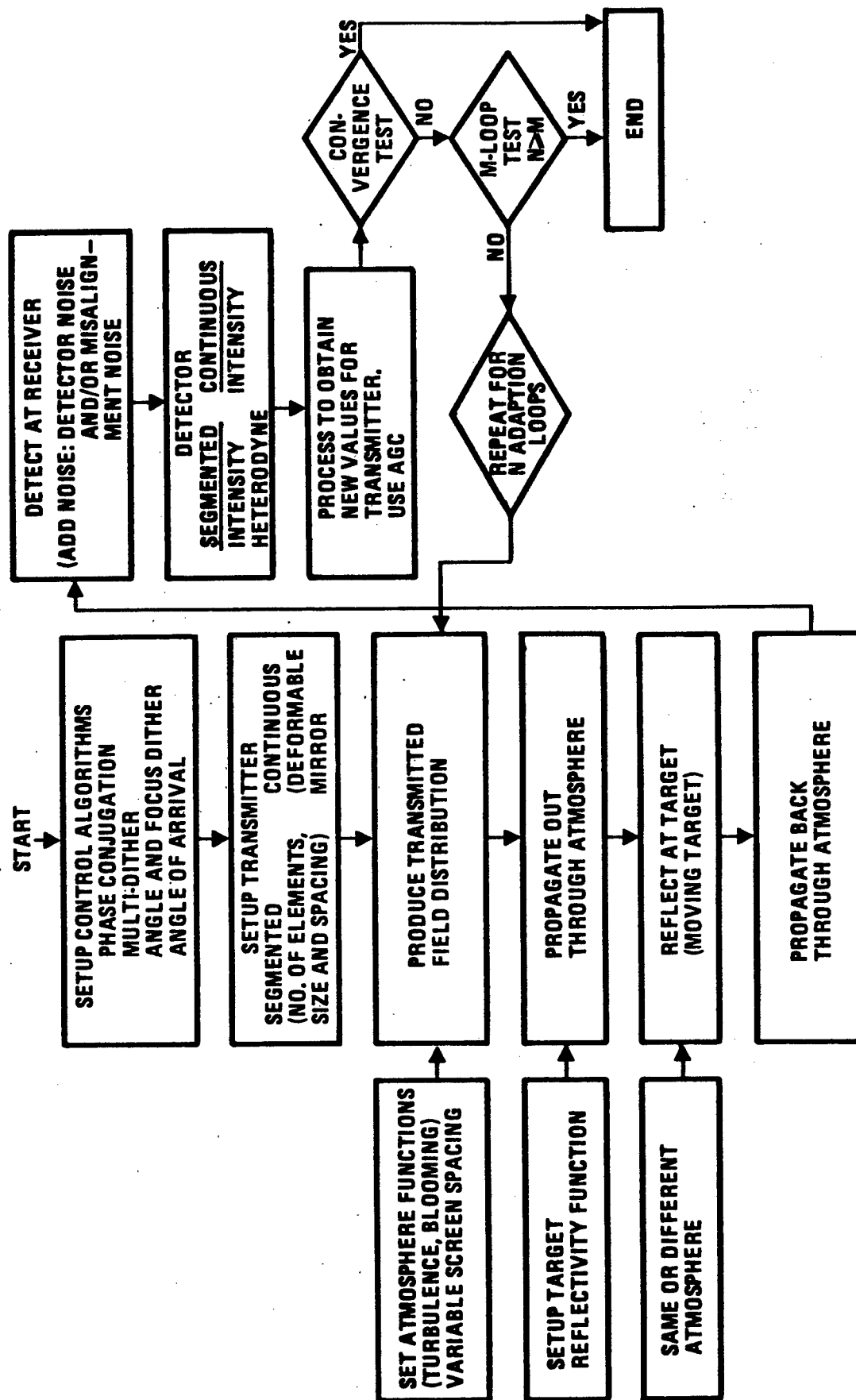
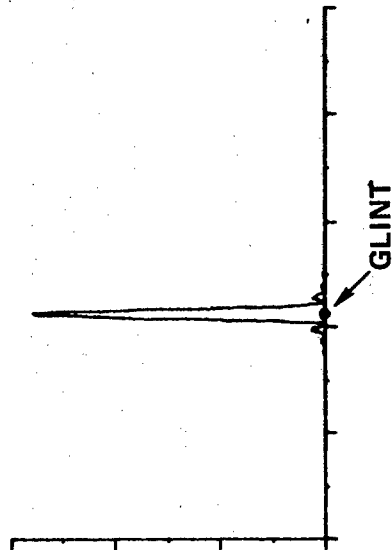


Figure III-9. PSYCAT - Flow Chart

(a) FOCUSED
 $P = 92\%$
 $I = 1$



(b) UNFOCUSED
 $P = 40\%$
 $I = 0.12$

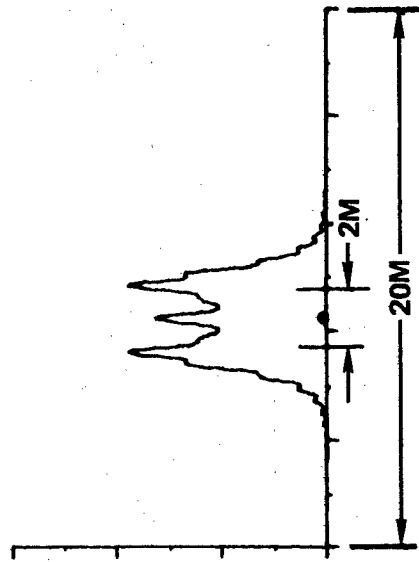
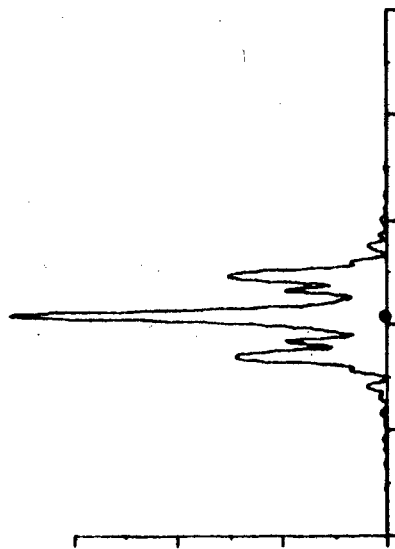


Figure III-10. Relative Intensity Distribution in Target Plane
 $(\theta = 0, \text{Range} = 185000 \text{ M}, 10.6 \mu\text{m} \text{ Propagation in Vacuum})$

(a) THREE 1.6M SUBAPERTURES

P = 45%
I = 0.258



(b) FIVE 0.96M SUBAPERTURES

P = 46%
I = 0.264

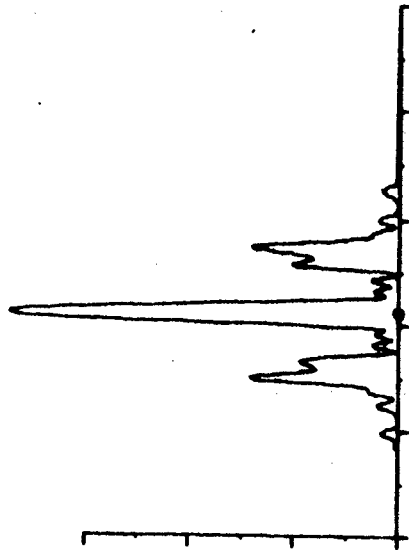


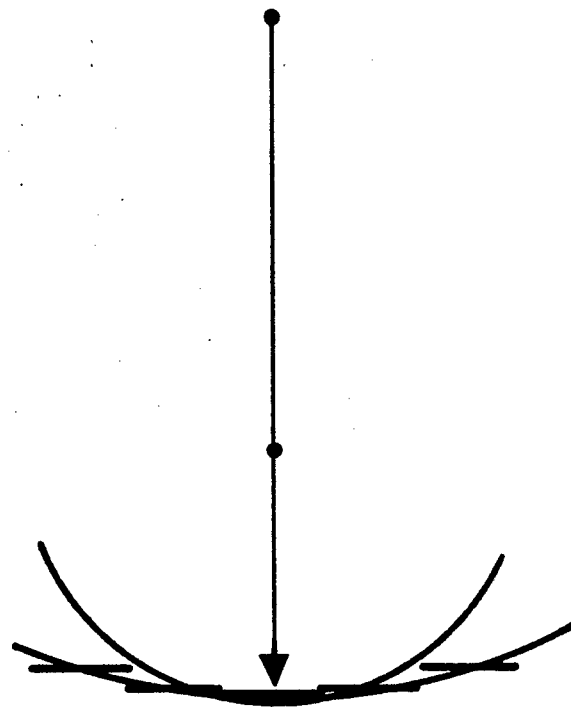
Figure III-11. Relative Intensity Distribution in Target Plane
($\theta = 0$, Range = 185000 M, Three 1.6 M and Five
0.96 M Subapertures, Phase Adaption or Phase
Conjugation in Vacuum Considering 10.6 μ m Propagation)

More important, sizable phase discontinuities are usually associated with large wavefront-mismatch, which, in turn, generate high spatial frequency components. The high frequency components will, in turn, contribute to the "wing-structure" in the intensity distribution. The obvious solution to reducing wavefront-mismatch is, of course, the use of much smaller subapertures, but that is a problem in itself for reasons of economy and system complexity. As might be expected, wavefront-mismatch also can be significantly reduced simply by pointing the individual subapertures to the target glint (see Figure III-12). That it is indeed true can be concluded from the results shown in Figures III-13 and III-14. For free space operation, phase adaption in conjunction with pointing the subapertures to the target is, of course, equivalent to phase and phase gradient adaption. To summarize, if there were no perturbations of any kind, a diffraction-limited system delivers 92% of the transmitted power into the 2-meter bucket, phase adaption using 3(5) subapertures delivers 45% (46%), phase and phase gradient adaption using 3(5) subapertures delivers 85% (91%). The corresponding on-axis intensity values are 1, 0.25 (.26) and 0.94 (1).

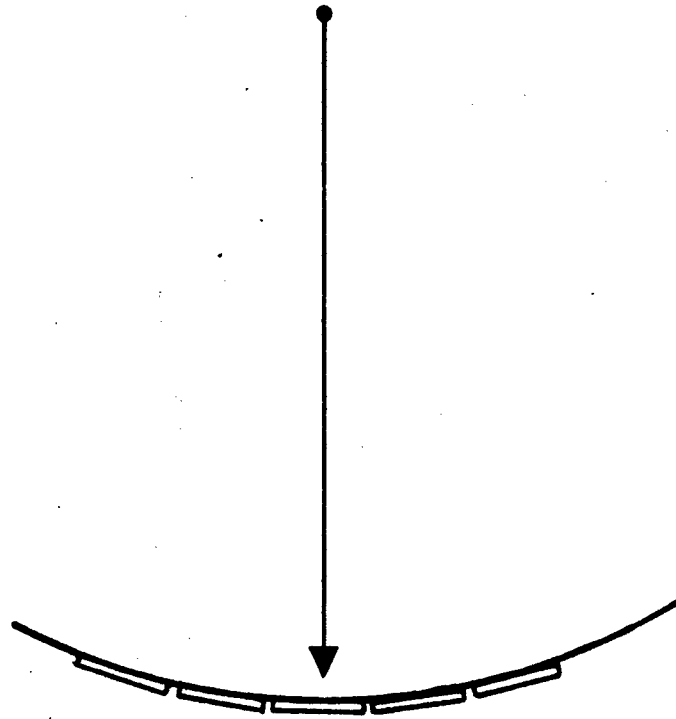
b. Adaption in Turbulence

The set of intensity plots given in Figures III-15 through III-19 is an example which shows the effects of atmospheric turbulence. These plots are calculated from using the phase-screen model developed previously. The effectiveness of each adaptive system implementation method for compensating the turbulence effects may be evaluated by comparing the adapted intensity distribution with that produced by the diffraction-limited system.

With the phase adaption method only, for example, the on-axis intensity value increased from 0.09 to a substantial value of 0.32, but the



(a) PHASE ADAPTION ONLY

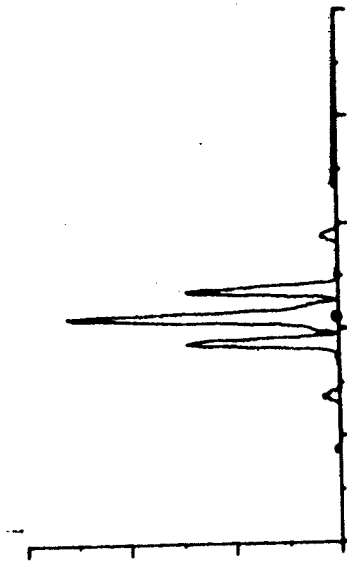


(b) PHASE AND TILT ADAPTION

Figure III-12. Effects of Finite Element Size in Matching Wavefront Shape

POINTING BUT UNADAPTED

P = 68%
I = 0.46



POINTING PLUS PHASE ADAPTION

P = 91%
I = 1

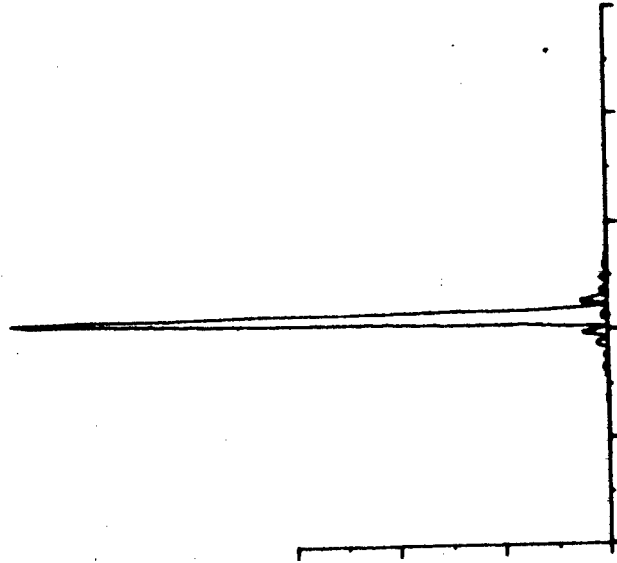
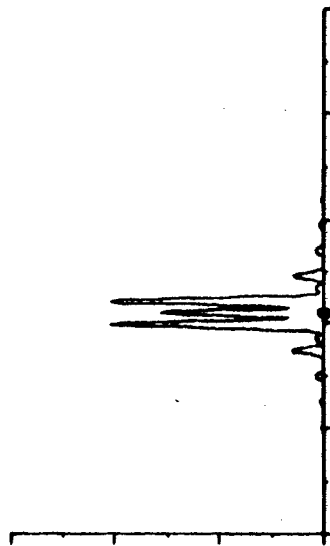


Figure III-13. Relative Intensity Distribution in Target Plane
($\theta = 0$, Range = 185000 M, Five 0.96 M Subapertures,
Pointing Plus Phase Adaption for 10.6 μ m Propagation in Vacuum)

POINTING BUT UNADAPTED

P = 80%
I = 0.28



POINTING PLUS PHASE ADAPTION

P = 85%
I = 0.94

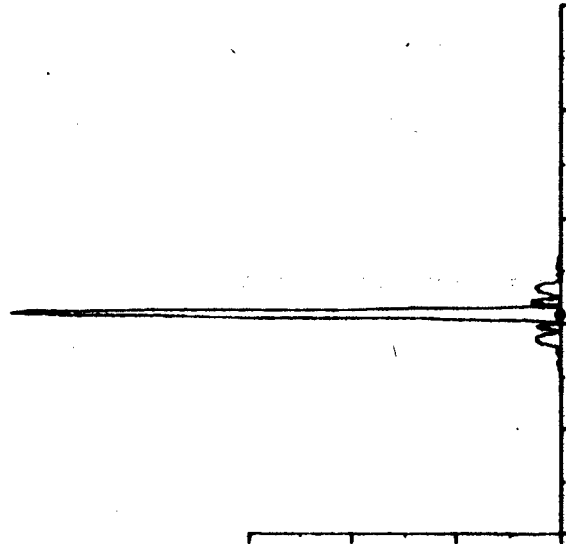


Figure III-14. Relative Intensity Distribution in Target Plane
($\theta = 0$, Range = 185000 M, Three 1.6 M Subapertures,
Pointing Plus Phase Adaption for 10.6 μ m Propagation
in Vacuum)

UNADAPTED

P = 39%
I = 0.09

ADAPTED

P = 42%
I = 0.32

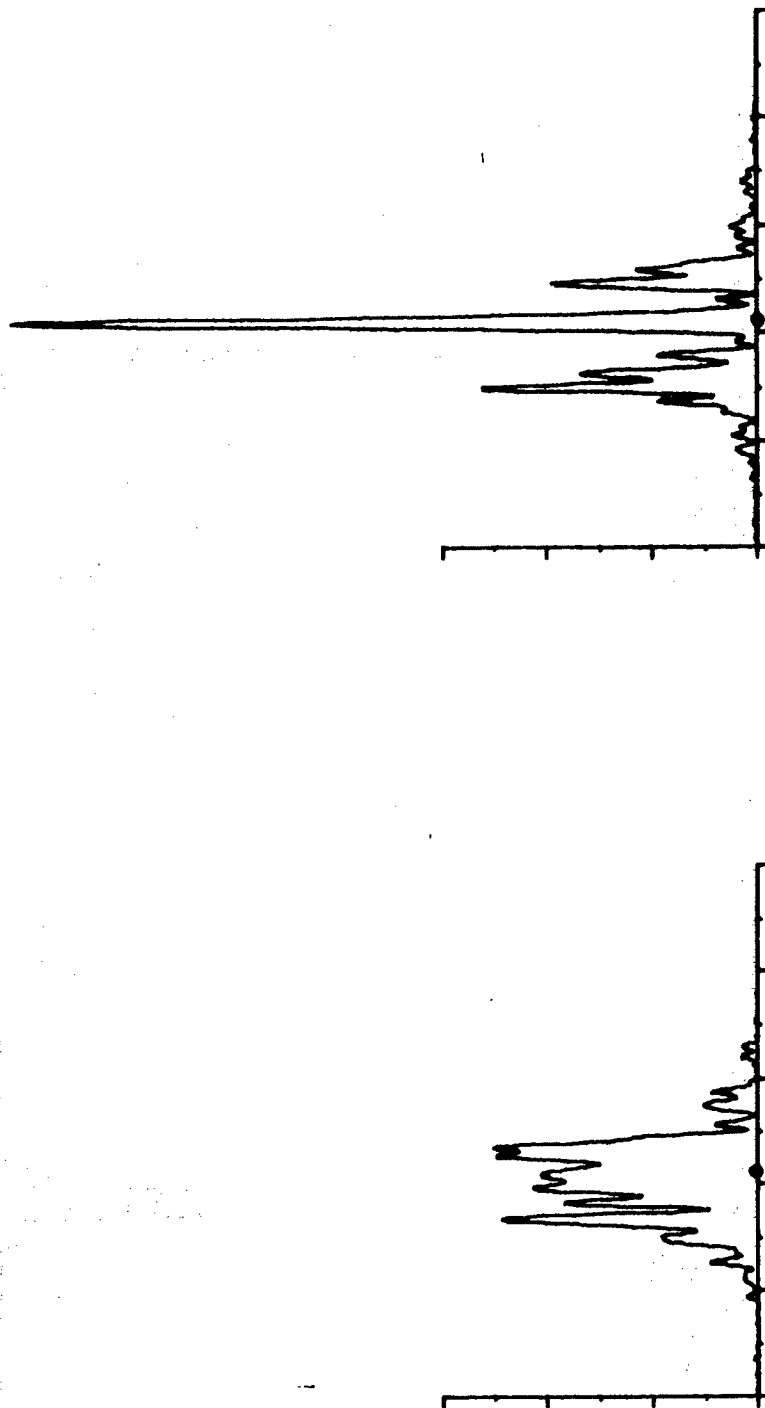
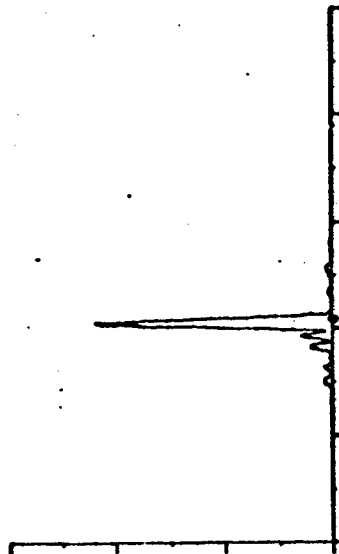


Figure III-15. Example of Relative Intensity Distribution in Target Plane ($\theta = 0$, Range = 185 KM, 0.96 M Elements, Phase Adaption or Multidither in Turbulence, 10.6 μ m Propagation

UNADAPTED

P = 78%
I = 0.21



ADAPTED

P = 75%
I = 0.78

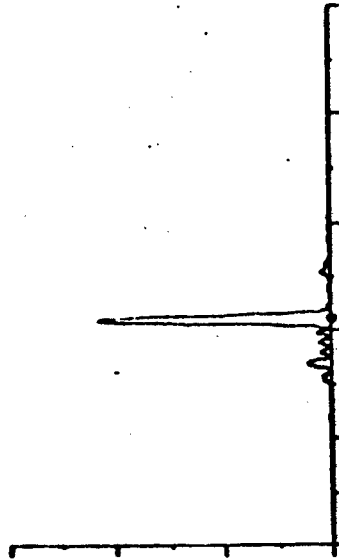
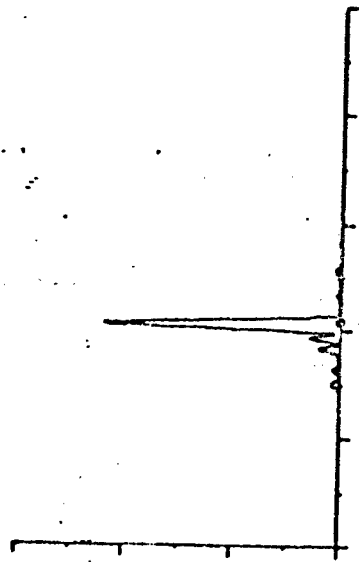


Figure III-16. Example of Relative Intensity Distribution in Target Plane
($\theta = 0$, Range = 185 KM, 0.96 M Elements, Phase Conjugation
with Lens in Turbulence, 10.6 μ m Propagation)

UNADAPTED

P = 78%
I = 0.29



ADAPTED

P = 79%
I = 0.37

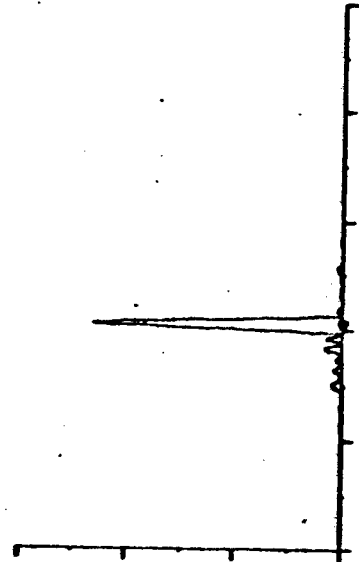
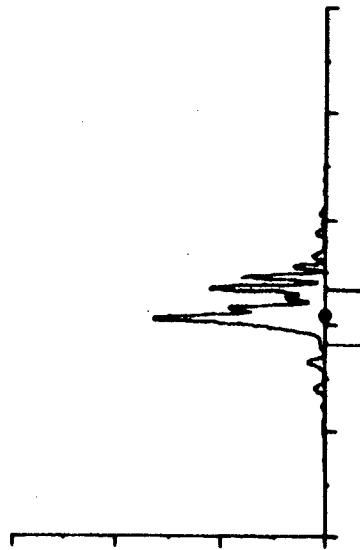


Figure III-17. Example of Relative Intensity Distribution in Target Plane
($\theta = 0$, Range = 185 KM, 0.96 M Separation Between Actuators,
Deformable Mirror Plus Lens, 10.6 μ m Propagation)

UNADAPTED

P = 55%
I = 0.25



ADAPTED

P = 66%
I = 0.65

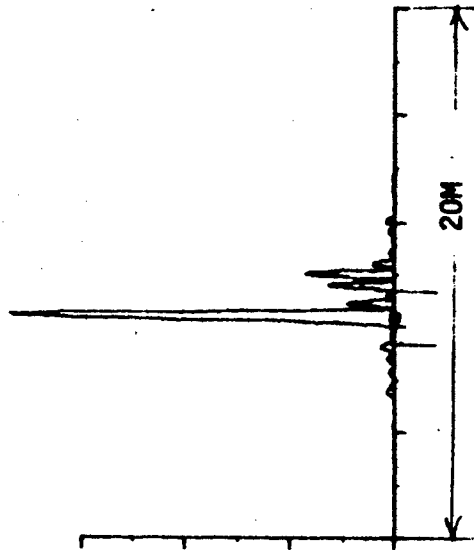


Figure III-18. Example of Relative Intensity Distribution in Target Plane
($\theta = 0$, Range = 185 Km, 0.96 M Elements, Phase Conjugation
Plus Elements Pointed at Target in Turbulence, 10.6 μ m Propagation)

Figure III-19. Example of Relative Intensity Distribution in Target Plane
 ($\theta = 0$, Range = 185 KM, 0.96 M Elements, Phase Conjugation
 Plus Elements Pointed Along Angle of Arrival, 10.6 μm
 Propagation)

ADAPTED

P = 84%
 I = 0.90

UNADAPTED

P = 39%
 I = 0.09



power-in-bucket value increased only by about 3% when adapted (see Figure III-15). The small increase of power in the 2-meter region when adapted is not too surprising, simply because the corresponding vacuum case yields only 46% (see Figure III-11). Again, the negligible increase of power in the 2-meter region, coupled with the increase in the wing structure, is attributed to the sizable phase discontinuities in the constructed image as in the vacuum case. The present results suggest that the performance is not only limited by the turbulence, but also by the planar arrangement of the subapertures.

Multidither operation in the usual sense is the maximization of the received power in the vicinity of the transmitter aperture. For a single-glint target, the received power can be maximal only when the incident power at the glint is also maximal; consequently, the performance of multidither is identical to that of phase conjugation for a single glint target (see Figure III-15). Another approach to implementing the multidither operation is to dither the initially returned wavefront across the receiving subapertures until the intensity is maximal at the focus of a lens placed directly behind the receiving subapertures. Here, the phase excursions required to maximize the intensity at the focus are necessarily equal, but opposite to the turbulence-induced phase excursions. Thus, these phase excursions can be directly transferred to the transmitter for turbulence compensation. As might be expected, the computed results for this case are identical to those shown in Figure III-15.

In addition to confining the initially transmitted power closer to the target, placing a lens in front of the transmitter aperture also minimizes the phase discontinuities between array elements, and hence reduces the high spatial frequency content of the transmitted wavefront. Phase adaption in conjunction with a focused lens should therefore be more

efficient than just phase conjugation alone (see Figure III-16). Here, the slightly higher initial value of power-in-bucket is due to the randomly focusing effect of the particular turbulence distribution. That the adapted values of both I and P are still appreciably less than those for the diffraction-limited case is an indication that the higher order aberrations (at least the tilt) cannot be adequately compensated with the planar arrangement of the subapertures.

As might be expected, the use of a deformable mirror in conjunction with a focused lens to implement phase adaption is an improvement over the previous methods. The purpose of the lens is two-fold; to reduce the phase excursions and, hopefully, to eliminate the " 2π ambiguities." The adapted intensity distribution shown in Figure III-17 is for a five-actuator deformable mirror placed behind a focused lens. Although the on-axis intensity is only 0.37, the power-in-bucket value of 79% is sizable. For this particular case, the method is simulated as follows. First, the average phase of the signal wave measured at a given subaperture is relayed to a corresponding actuator whose displacement is proportional to the negative of that phase value. The wavefront to be transmitted back to the target is then constructed by reflecting a plane wave off the deformable mirror.

For the planar arrangement of rather large subapertures, the results presented thus far indicated that the performance of the above methods is far from diffraction-limited. This is not unexpected, since we have found for the vacuum case that near optimum performance also requires pointing and tilt correction. In the presence of atmospheric turbulence, pointing the subapertures to the glint without phase adaption gives $P = 55\%$ and $I = 0.25$, as compared to $P = 68\%$ and $I = 0.46$ for the corresponding vacuum case (see

Figures III-14 and III-18). With phase adaption, the corresponding values of P and I are, respectively, 66% and 0.65, which are still considerably less than 91% and 1.0 for the corresponding vacuum case. This is a clear indication that the turbulence-induced tilt is pronounced and must be compensated. In order to implement tilt correction, additional measurements must be made to determine the angle of arrival at the individual subapertures. As previously mentioned, the angle of arrival at each subaperture can be determined from measuring the centroid of the return intensity at that subaperture, or from measuring the wavefront tilt using the Hartmann plates method. The results of phase and phase gradient adaption in the presence of atmospheric turbulence, with either method of angle measurements, are shown in Figure III-19. Since the adapted values of P and I are, respectively, 89% and 0.90, the turbulence effect, for the most part, is adequately compensated with phase and phase gradient adaption.

4. Summary

Using a particular turbulence distribution, we have simulated the effects of atmospheric turbulence on the performance of several adaptive systems. In terms of localizing the transmitted power at the target and maximizing the on-axis intensity, we have found that phase and phase gradient adaption is far superior to the others. While the particular turbulence distribution used in the calculations is of proper spatial frequency variation and of proper statistics, it is nevertheless only a particular distribution out of infinitely many. In order to increase our confidence in the present approach, several different turbulence distributions have been used. The average performance of each system for ten different turbulence distributions considering $10.6 \mu\text{m}$ propagation is shown in Figure III-20, which also indicates

LENS IN VACUUM
(DIFFRACTION LIMITED)

PHASE AND TILT
ADAPTION USING SEG-
MENTED DEFORMABLE
MIRROR

PHASE ADAPTION USING
CONTINUOUS DEFORMA-
BLE MIRROR AND LENS

PHASE ADAPTION USING
SEGMENTED DEFORMA-
BLE MIRROR AND LENS

PHASE ADAPTION USING
SEGMENTED DEFORMA-
BLE MIRROR AND
POINTED

PHASE ONLY ADAPTION
USING SEGMENTED
DEFORMABLE MIRROR
(OR MULTI-DITHER)

UNADAPTED UNIFORM
APERTURE DISTRIBUTION

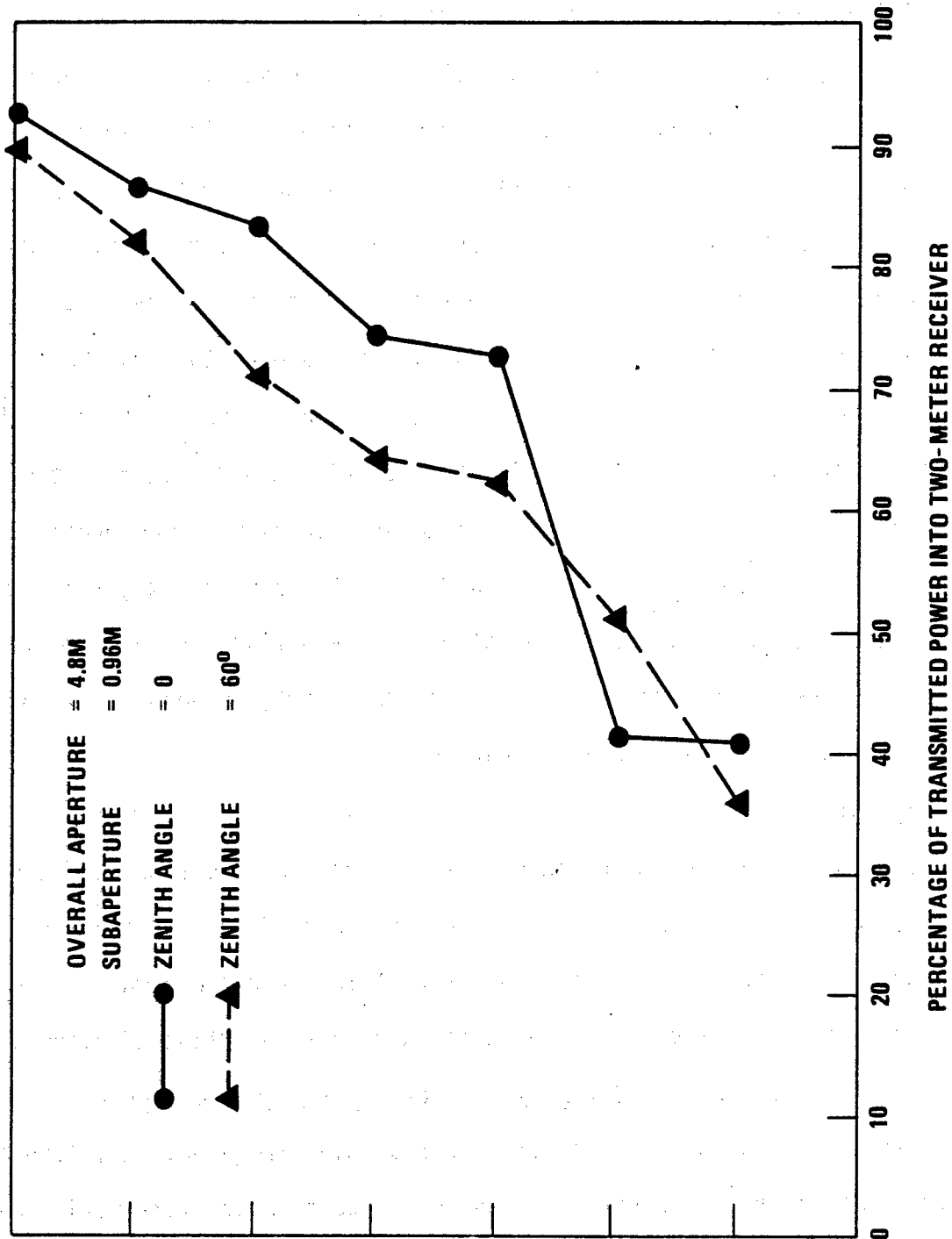


Figure III-20. Percentage of Transmitted Power into a 2-Meter Receiver at Altitude 185 KM (Average of 10 Different Realizations)

that the phase and phase gradient adaption method is superior. The performance calculations for the three subaperture case, in general, agree with those for the five subaperture case. However, in terms of localizing the power and maximizing the on-axis intensity, the three subaperture configuration is less efficient. This should be expected because of larger subaperture size. The detailed results that were presented for 10.6 μm propagation included only vertical direction transmission; however, with minor modification of the screen locations and strength, the 8-screen model was readily applicable to other zenith angles. In particular, extensive calculations corresponding to the 60° zenith angle case have also been made, and the results are included in Figure III-20. Note that the phase adaption method is more efficient for the 60° case. The glint target at 60° is farther away; consequently, the return wavefront is flatter and there is less wavefront mismatch. Thus, more energy is confined near the target.

For purposes of comparison, similar calculations as those done for 10.6 μm were also performed for 5.0 and 3.8 μm (the differences between 10.6 and 9.1 μm were insignificant). As with the 10.6 μm case, the system performance is evaluated in terms of the system's ability to localize the transmitted power within two meters about the target glint. In order to compare the relative performance of the systems at the different wavelengths, the overall aperture size is chosen to be wavelength dependent, given by Eq. (11). As with the 10.6 μm case, the overall aperture is formed by placing five equal subapertures closely spaced together. Figure III-21 shows the average performance of the adaptive systems, based upon five different turbulence realizations. As might be expected, the performance is somewhat poorer at the shorter wavelengths. Note that the phase and phase gradient adaption method is superior compared with the others, which is in agreement with the results obtained for the 10.6 μm case.

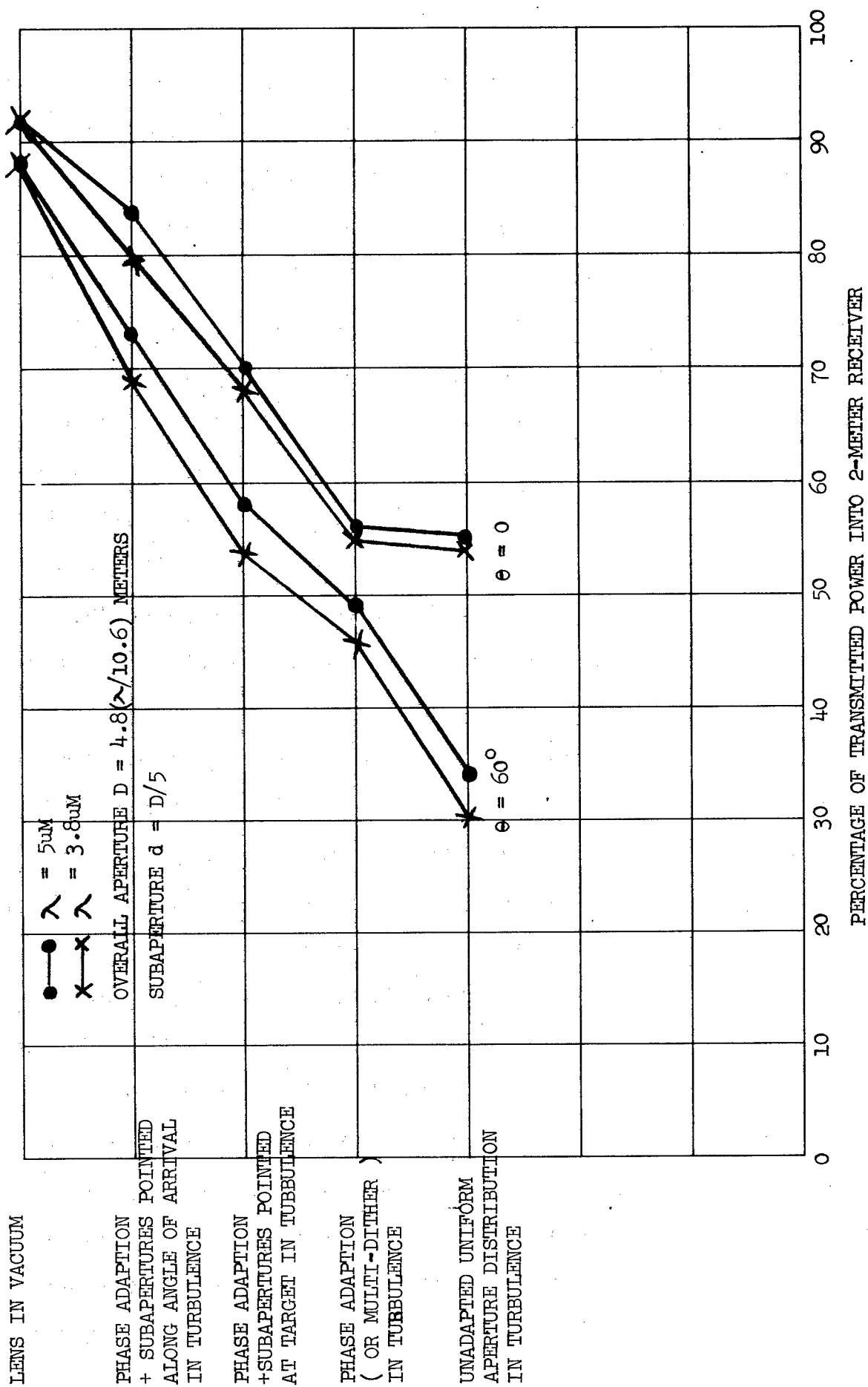


Figure III-21. PERCENTAGE OF TRANSMITTED POWER INTO A 2-METER RECEIVER AT ALTITUDE 185KM
(AVERAGE OF 5 DIFFERENT TURBULENCE REALIZATIONS)

References

1. D. L. Fried, J. Opt. Soc. Am. 11, 1427 (1965).
2. R. F. Lutomirski and H. T. Yura, Appl. Opt. 10, 1652 (1971).
3. D. L. Fried and H. T. Yura, J. Opt. Soc. Am. 62, 600 (1972).
4. D. L. Fried, G. E. Mevers, and M. P. Keister, Jr., Opt. Soc. Am. 57, 787 (1967).
5. "Optical Propagation Measurements at Emerson Lake - 1968," G. E. Mevers, M. P. Keister, Jr., and D. L. Fried, NASA Contract Report CR-1733.
6. V. M. Koprov and L. R. Tsvang, "Characteristics of Very Small Scale Turbulence in a Stratified Boundary Layer," Atmos. and Oceanic Phys. 22, 1142 (1966) (English Translation Journal, p. 705).
7. R. S. Lawrence, G. H. Ochs, and S. F. Clifford, J. Opt. Soc. Am. 60, 826 (1970).
8. D. L. Fried, "A New Model for the Vertical Distribution of the Optical Strength of Turbulence in the Atmosphere," Optical Science Consultants Report No. TR-132.
9. J. L. Bufton, Appl. Opt. 12, 1785 (1973).
10. D. L. Fried and G. E. Mevers, Appl. Opt. 13, 2620 (1974).
11. J. J. Burke, J. Opt. Soc. Am. 60, 1262 (1970).
12. L. E. Pape, D. D. Duncan, and S. A. Collins, "Refractive Index Measurements at High Altitudes," 1975 Annual Meeting OSA, Paper FE15.
13. This is the correct definition for the general case, but it can be argued that for "return wave" or phase conjugation adaption algorithms this dimension is the height of the meaningful atmosphere.
14. In this encounter scenario, where we have a cooperative target, it is possible to avoid transmitting and receiving through different volumes of atmosphere and consequently any problem with isoplanatic patch size. This could be accomplished by simply extending the satellite retroreflector on a boom in the direction of the satellite velocity by an appropriate amount (for the conditions considered, about 10 m). In this manner the lead angle problem could be avoided, but the corner reflector return signal would be greatly reduced, especially at the shorter wavelengths where isoplanatic effects are more important.
15. D. L. Fried, "Isoplanatic Dependence of Self-Referenced Prediction Compensation Imaging," Optical Science Consultants Report No. TR-144, July 1974.
16. W. P. Brown, Jr., "High Energy Laser Propagation," Hughes Research Laboratories Technical Report for Contract N00014-74-C-0460 (August 1973).
17. V. I. Tatarski, Wave Propagation in a Turbulent Medium, McGraw-Hill Book Co., Inc. (1961).

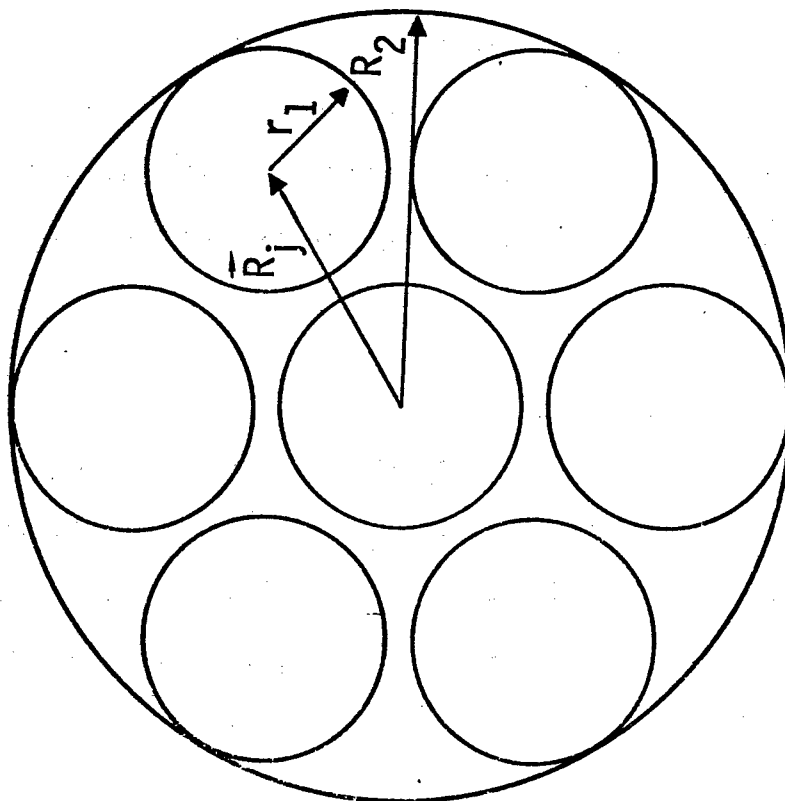
IV. SERVO BANDWIDTH REQUIREMENTS FOR TURBULENCE CORRECTION

In the previous chapter we discussed the quality of correction for atmospheric turbulence effects that could be obtained with adaptive optical systems. In those calculations, it was implicit that the systems considered had unlimited temporal bandwidth. Now we will evaluate the servo bandwidth requirements for turbulence correction. In performing these calculations, our prime consideration was for 10.6 μm propagation; however, as with the other atmospheric effects assessed, our efforts were extended to include 9.1, 5.0, and 3.8 μm . The results, in general, indicate that for good atmospheric correction over the full range of zenith angles ($\pm 60^\circ$), the 10.6 μm system will require about 60 Hz adaption bandwidth and as the source wavelength becomes shorter, the bandwidth requirement increases until at 3.8 μm about 450 Hz is needed.

The formulation of the theory we used for the bandwidth requirements of an adaptive antenna was developed previously, and a computer code (BRCAT) written to provide numerical results.¹ We cite here only a brief review of the approach to the bandwidth evaluation, the models of wind speed and turbulence that had to be developed for vertical propagation, and the numerical results obtained.

A. Antenna Gain

The adaptive antenna used in these calculations is in general considered to be an array of circular segments, or subapertures, that can be displaced in both piston and two-axis tilt motion. The quantity to be corrected by servoing these motions is the atmospheric-produced phase error which is defined in Figure IV-1. It is the difference between the average phase over one subaperture and the average phase over the entire array.



$\bar{\phi}(t) = \text{AVE PHASE OVER } R_2$

$\bar{\phi}(\bar{R}_j, t) = \text{AVE PHASE OVER } \bar{R}_j$

$\Delta\phi(\bar{R}_j, t) = \bar{\phi}(\bar{R}_j, t) - \bar{\phi}(t) \quad \text{PHASE ERROR}$

Figure IV-1. Phase Error Determination

For this evaluation we wish to determine the antenna gain or Strehl definition S . In our case, this is a degradation factor of the far field irradiance due to the presence of a servo system of finite bandwidth trying to follow the fluctuations produced by atmospheric turbulence. This factor is given by

$$S = \exp (- \overline{\epsilon^2}),$$

where $\overline{\epsilon^2}$ is the average over all subapertures of the mean square phase error. This mean square phase error can be written as a frequency integral over that portion of the temporal phase error power spectrum that is not "tracked" by the servo system. For the j^{th} element we have

$$\epsilon^2(\vec{R}_j) = \int_0^\infty df \Phi_{\Delta\phi}(\vec{R}_j, f) E(f, f_0),$$

where $E(f, f_0)$ is the servo transfer function, which for a type 1 servo system is given by

$$E(f, f_0) = \frac{(f/f_0)^2}{1 + (f/f_0)^2}.$$

Now the temporal phase error power spectrum is the Fourier Transform of the phase error temporal covariance function $C_{\Delta\phi}(\vec{R}_j, \tau)$.

$$\Phi_{\Delta\phi}(\vec{R}_j, f) = \int_{-\infty}^{\infty} d\tau C_{\Delta\phi}(\vec{R}_j, \tau) \exp (- 2\pi i f \tau).$$

The phase error temporal covariance function is a measure of how the average phase error at the j^{th} element at time t is related to the error at that point at a time $t + \tau$. This temporal covariance function is defined as an ensemble average over the product of phase errors

$$C_{\Delta\varphi}(\vec{R}_j, \tau) = \langle \Delta\varphi(\vec{R}_j, t) \Delta\varphi(\vec{R}_j, t + \tau) \rangle.$$

It can be shown that this expression can be written as an aperture average over the more general spatial-temporal phase structure function $D_\phi(\vec{r} - \vec{r}', \tau)$.

$$C_{\Delta\varphi}(\vec{R}_j, \tau) = -\frac{1}{2} \int d\vec{r} D_\phi(\vec{r}, \tau) K(\vec{r}, \vec{R}_j),$$

where the integral is over aperture coordinates and K is a geometrical factor which includes the limits on the integrations. The spatial-temporal phase structure function measures how the phase at aperture position \vec{r} and time t is related to the phase at position \vec{r}' and time $t + \tau$. It is defined as

$$D_\phi(\vec{r} - \vec{r}', \tau) = \langle [\varphi(\vec{r}, t) - \varphi(\vec{r}', t + \tau)]^2 \rangle.$$

To obtain an analytical form for the expression we need, we use a result due to Lutomirski and Buser,² which also identifies source points as well as receiver points.

$$\begin{aligned} D(\vec{x} - \vec{x}', \vec{y} - \vec{y}', t - t) &= \langle [\varphi(\vec{x}, \vec{y}, t) - \varphi(\vec{x}', \vec{y}', t)]^2 \rangle \\ &= 8\pi^2 \left(\frac{2\pi}{\lambda}\right)^2 \int_{\text{Path}} dS \int_0^\infty du u \phi_n(u) \left\{ 1 - J_0[u | (\vec{y} - \vec{y}') \frac{(\vec{L} - \vec{S})}{L} + (\vec{x} - \vec{x}') \frac{\vec{S}}{L} |] \right\} \end{aligned}$$

The x vectors denote receiver aperture positions, while the y vectors denote source point positions. The function ϕ_n is the spatial turbulence power spectrum. We assume the atmosphere follows a Kolmogorov spectrum given in terms of path position and frequency by

$$\phi_n(s, u) = 0.033 C_n^2(s) u^{-11/3},$$

where $C_n^2(s)$ is the refractive index structure constant.

Although this structure function has no explicit time dependence, it does contain time implicitly when we introduce a relationship between the source points and the aperture points. We use the Taylor hypothesis of frozen turbulence, which states that the turbulence structure does not change with time, but is simply transported by an effective wind. This concept is compatible with the time dependence associated with a moving target or transmitter. We may relate the propagation effects between source point \vec{y} and aperture point \vec{x} at time t to the effects at time $t + \tau$ by merely considering the new source point \vec{y}' and aperture point \vec{x}' . These new points are given by

$$\vec{y}' = \vec{y} + (\vec{V} - \vec{W}) \tau,$$

$$\vec{x}' = \vec{x} + (\vec{U} - \vec{W}) \tau,$$

where \vec{V} is the target velocity, \vec{U} is the receiver velocity ($= 0$ if using a ground based transmitter), and \vec{W} is the wind velocity. All three velocities are the components normal to the line of sight.

Putting these expressions in and simplifying the results, we obtain for the mean square residual phase error,

$$\overline{\epsilon^2} = \int_0^\infty \int_0^\infty df d\tau \mathcal{E}(f/f_0) \cos(2\pi f\tau) \int dx \int dy [D_\varphi(x, y, \tau) + D_\varphi(-x, y, \tau)] \bar{K}(x, y),$$

where

$$D_\varphi(x, y, \tau) = 2.92 \left(\frac{2\pi}{\lambda}\right)^2 L \int_0^1 ds C_N^2(s) \left[([W-V + (V-U)S] \tau + xs)^2 + y^2 S^2 \right]^{5/6},$$

where L is the propagation path length.

B. Vertical Distribution Models

All of the parameters given in the previous equations are constants except W , the wind speed, and C_N^2 , the refractive index structure constant. Both of these parameters vary with altitude. Therefore, to perform the necessary integrations over the path of propagation with relative ease, we developed analytical models for these parameters. The horizontal wind speed as a function of altitude was modeled from data taken from the Handbook of Geophysics.³ The wind speed is represented by the expression

$$W(h) = \frac{12 W_{\max}}{12 + (h - 11.7)^2 + 0.1(h - 11.7)^3 + 0.01(h - 11.7)^4},$$

where h is the altitude in kilometers and W_{\max} is the maximum speed, which we have set to occur at 11.7 km. The reference data indicates that W_{\max} may vary from about 30 to 75 m/s. For our calculations, we used $W_{\max} = 50$ m/s. A plot of this distribution is shown in Figure IV-2. An analytical expression for C_N^2 as a function of altitude was also derived by a least squares adjustment of the measured data model,⁴ shown in Figure IV-3, subject to the constraint that the value of r_0 calculated from the analytical model agreed with experimental results for vertical propagation through the atmosphere.⁵

The model is

$$\begin{aligned} C_N^2(h) \times 10^{17} = & \frac{35 a_1}{35 + a_2 (h-1)^2 + a_3 (h-1)^3} + \frac{a_4 a_5}{a_5 + (h-200)^2} \\ & + \frac{a_6 a_7}{a_7 + (h-2000)^2} + \frac{a_8 a_9}{a_9 + (h-12000)^2} \end{aligned}$$

where C_N^2 is in MKS units and h is the altitude in meters. The least squares values of the adjustable parameters are:

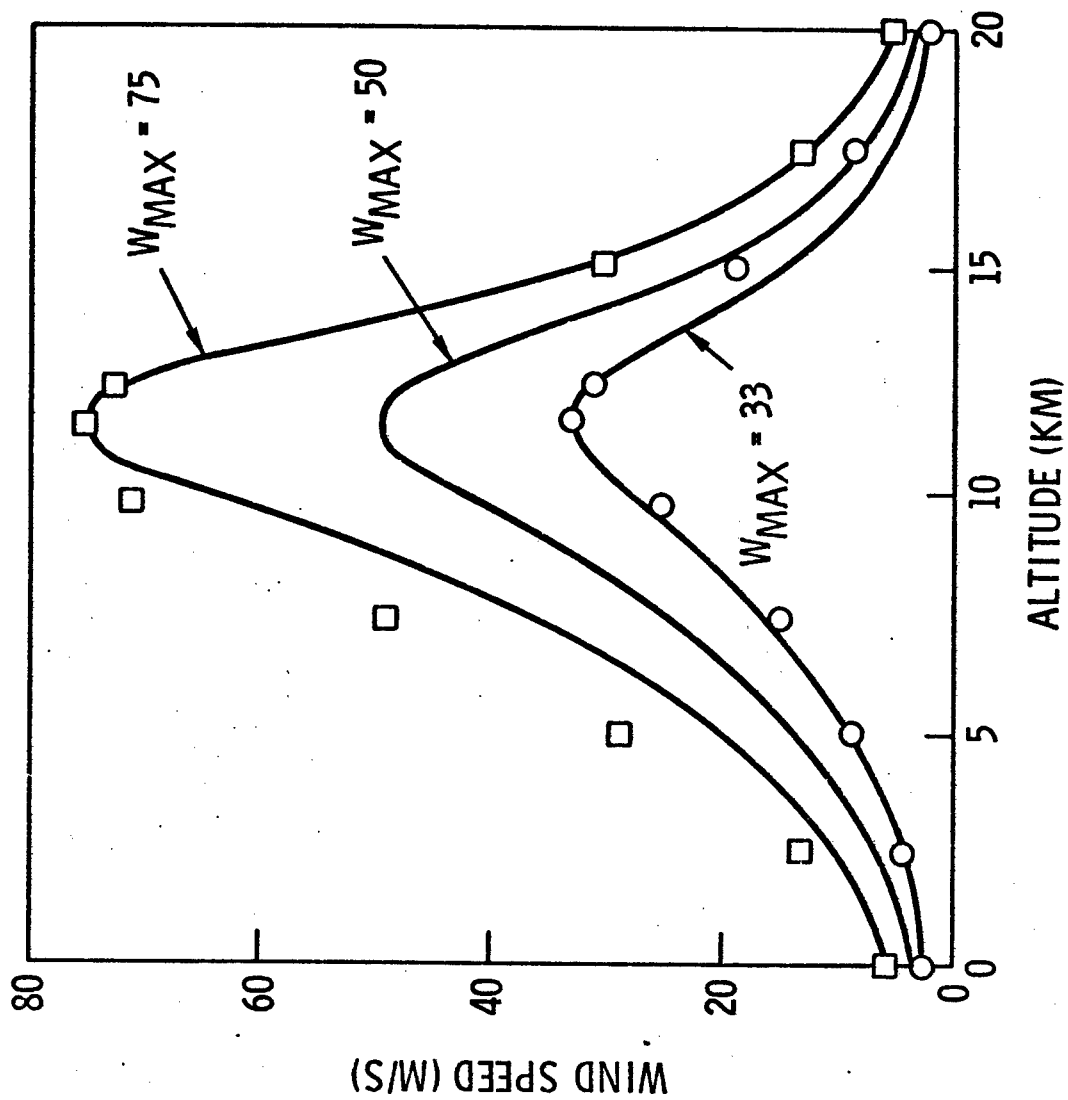


Figure IV-2. Analytical Model for Wind Versus Altitude

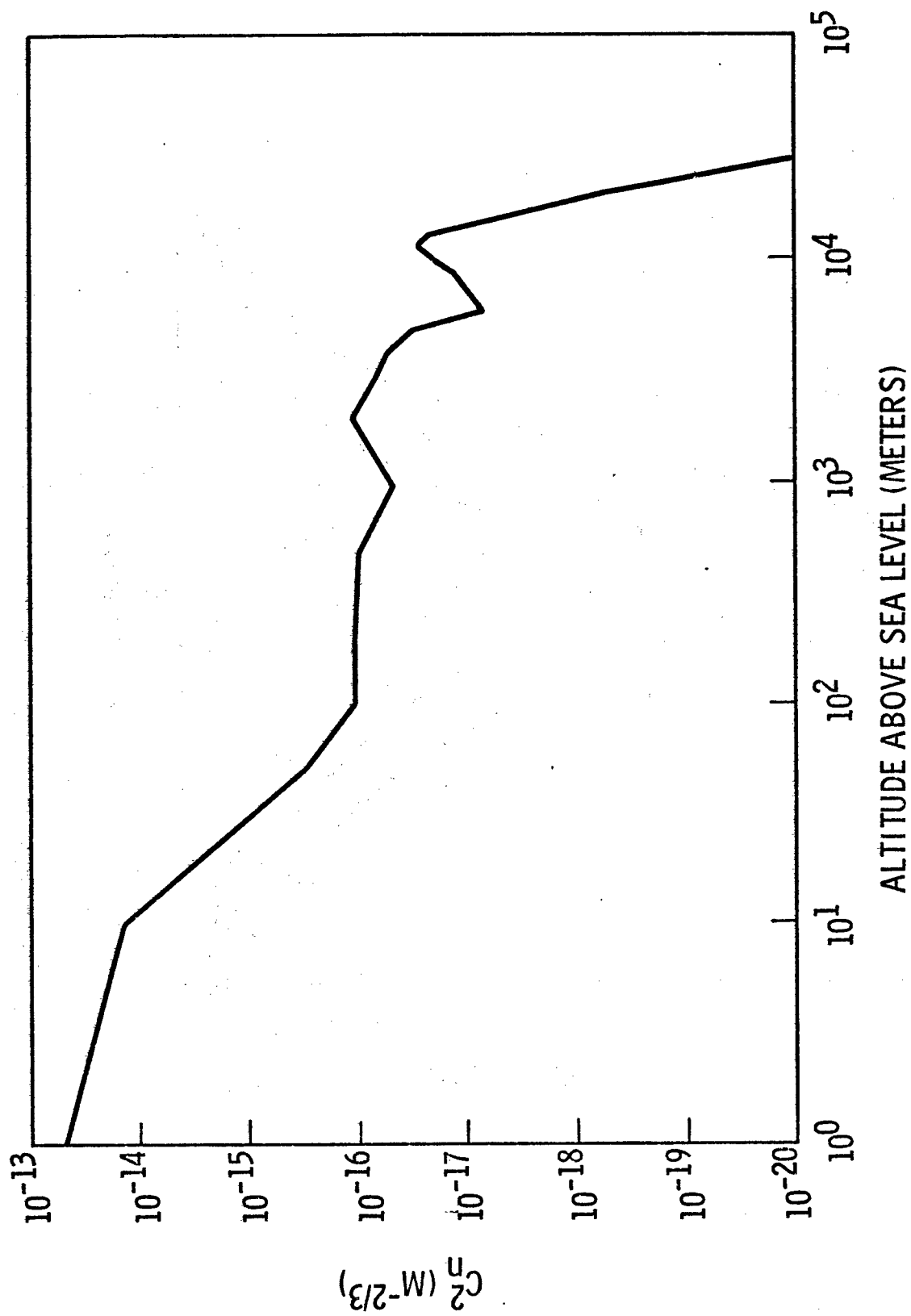


Figure IV-3. C_N^2 Versus Altitude Above Sea Level

$$a_1 = 4991.17$$

$$a_2 = 0.5003$$

$$a_3 = 0.05712$$

$$a_4 = 8.7236$$

$$a_5 = 95432.4$$

$$a_6 = 13.1993$$

$$a_7 = 937362$$

$$a_8 = 2.65818$$

$$a_9 = 6365880$$

A plot of C_N^2 as a function of altitude using this model is shown in Figure IV-4.

This model agrees well with the data, except for altitudes above about 18000 m, where the model doesn't fall off as rapidly as the data indicates. However, for this work, the results were the same as those obtained using a piece-wise fit to the data.

C. Numerical Results

For the particular problem of interest to us here, that is of transmitting power to a satellite, we ran the bandwidth code with the transmitter and target parameters shown in Figure IV-5. The wavelength was 10.6 μm . Shown in Figure IV-5 is the peak irradiance at the target as a function of the servo bandwidth. We see that for the 4.8 meter seven-element array, that phase and tilt adaption provides good correction. The curve marked "Perfect Deformable Mirror Adaption" assumes that all the higher order spatial modes are also employed in the adaption.

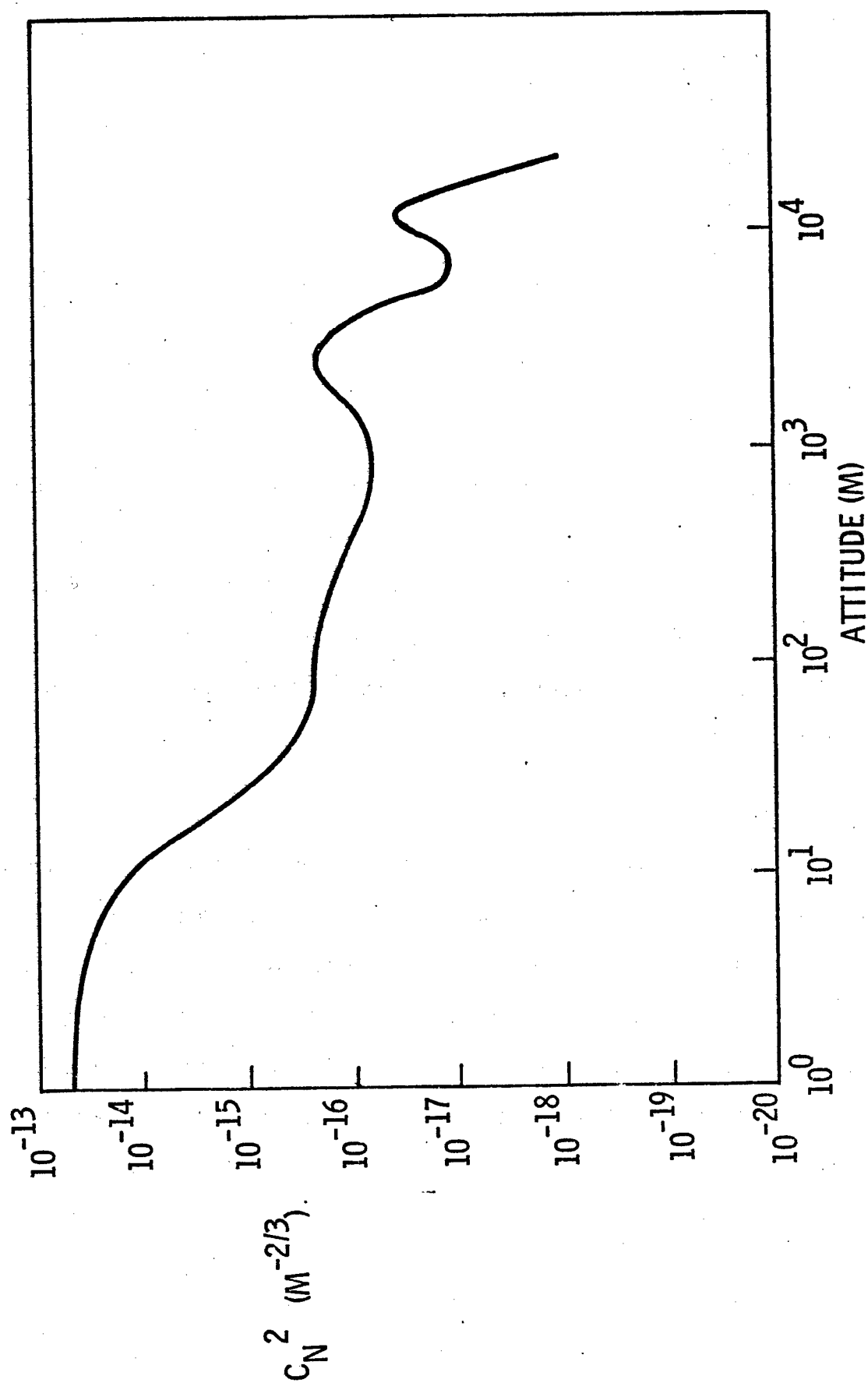


Figure IV-4. Analytical Model for the Refractive-Index Structure Constant C_N^2 vs Altitude

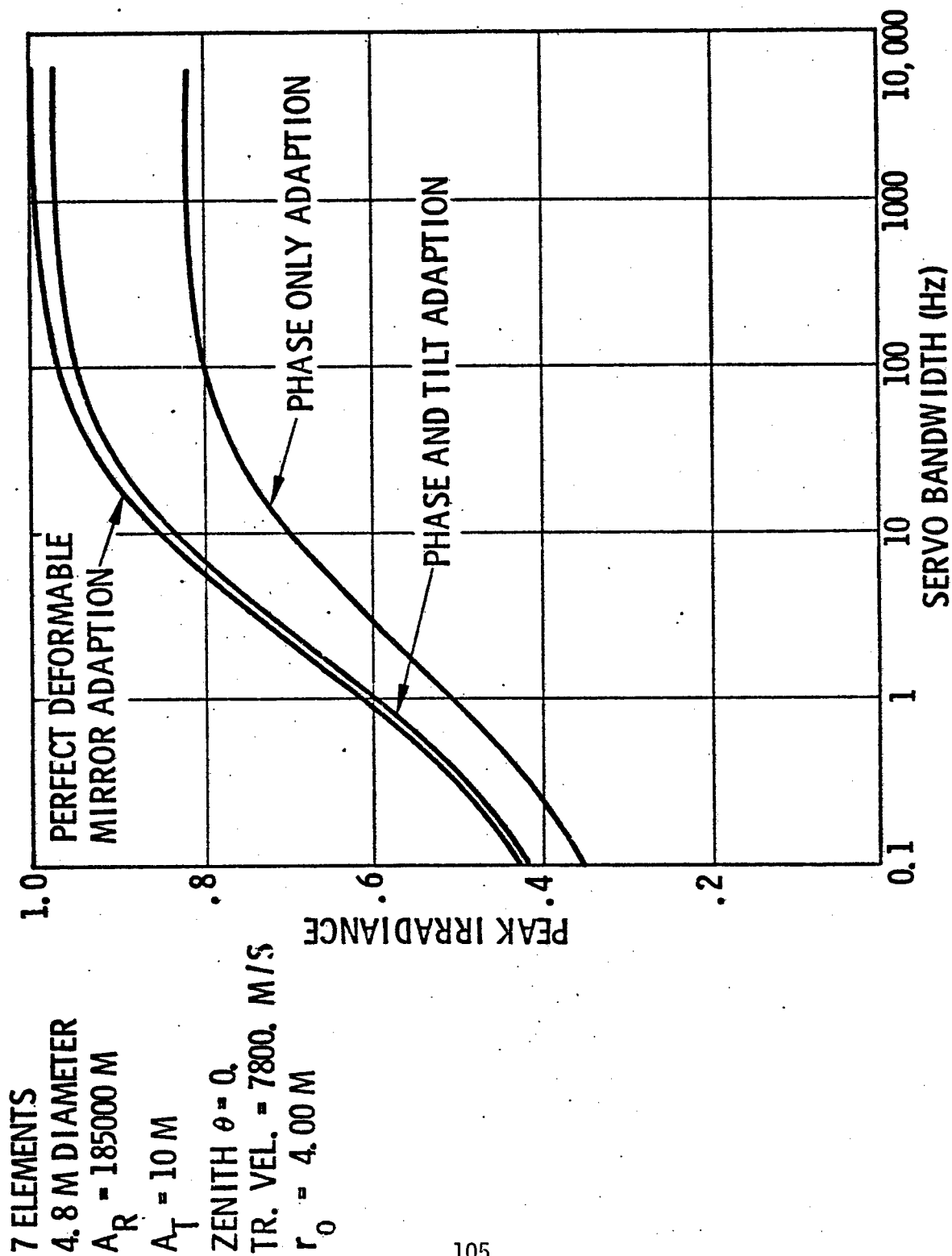


Figure IV-5. Adaption Results with Finite Servo Bandwidths

A comparison was made for 0° zenith angle and 60° zenith angle propagation. Figure IV-6 shows the results for phase and tilt adaption for a 19-element 4.8 meter array. We see that only a small difference in the bandwidths are observed. One would expect that due to the longer turbulence path at 60° zenith, that higher bandwidths would be required. The fact that not much difference was observed may be explained by noting that at the higher zenith angles, the slew rates are less, which tends to offset the effects of increased turbulence path.

Figure IV-7 is a summary graph giving the bandwidths required for 90% peak irradiance correction for a variety of aperture configurations. We notice generally that less than 60 Hz bandwidths are required for ground based transmission of $10.6 \mu\text{m}$ power.

Figures IV-8 through IV-10 are plots of the system performance versus servo bandwidth for the three alternate wavelengths: 9.1, 5.0, and $3.8 \mu\text{m}$. Performance curves are shown for both vertical propagation and 60° from the vertical.

Figure IV-11 shows the results for 60° propagation (the worse case) for each of the three wavelengths.

Figure IV-12 is a plot of the bandwidth required for 90% full correction as a function of zenith angle for the three bandwidths. It is seen that the bandwidth requirements rise rather sharply for angles higher than about 40° from the zenith. It is also seen that up to 450 Hz bandwidths are required for the $3.8 \mu\text{m}$ case.

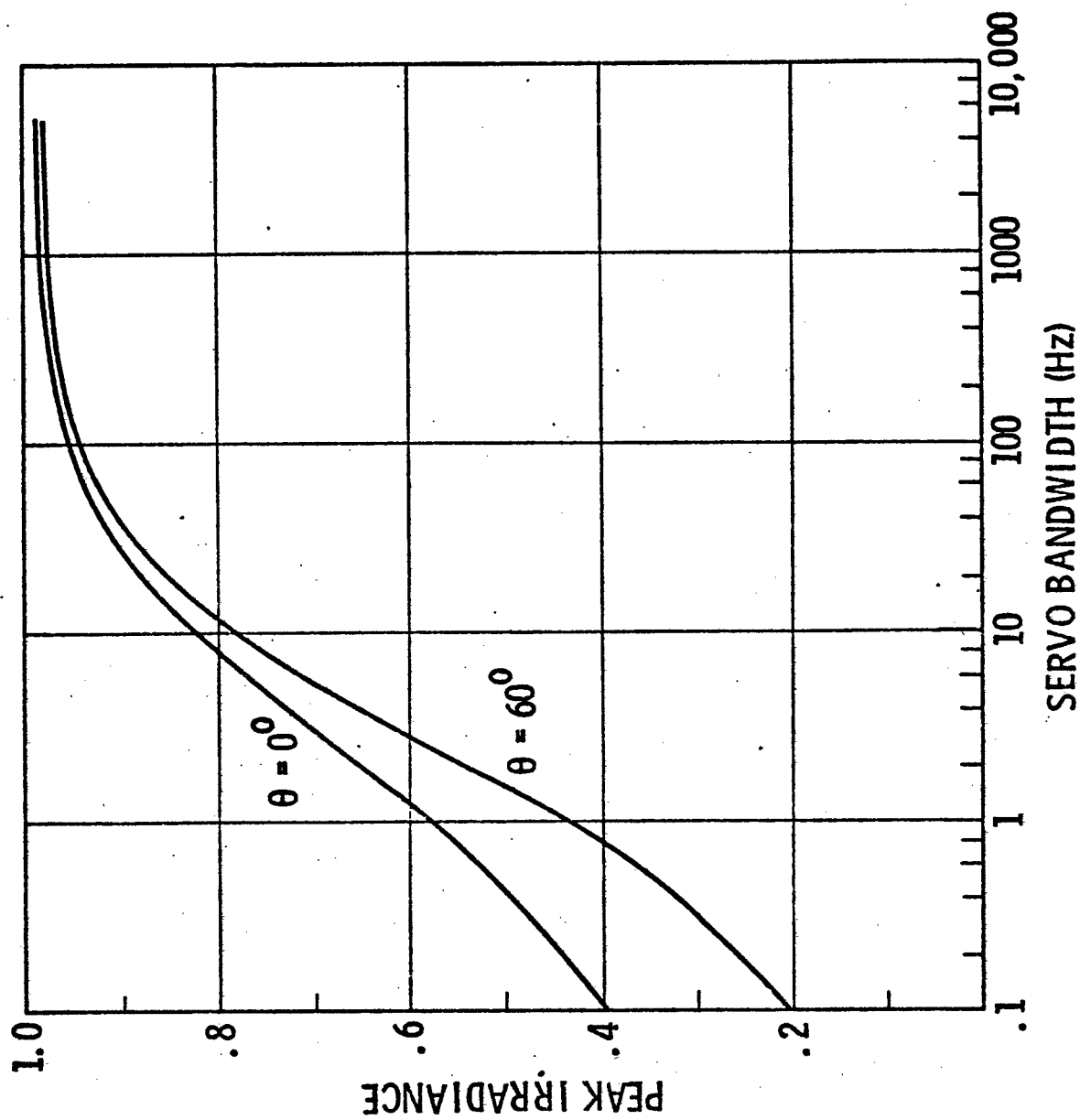


Figure IV-6. Bandwidth Requirements for 19-Element Array (4.8 M Diameter)

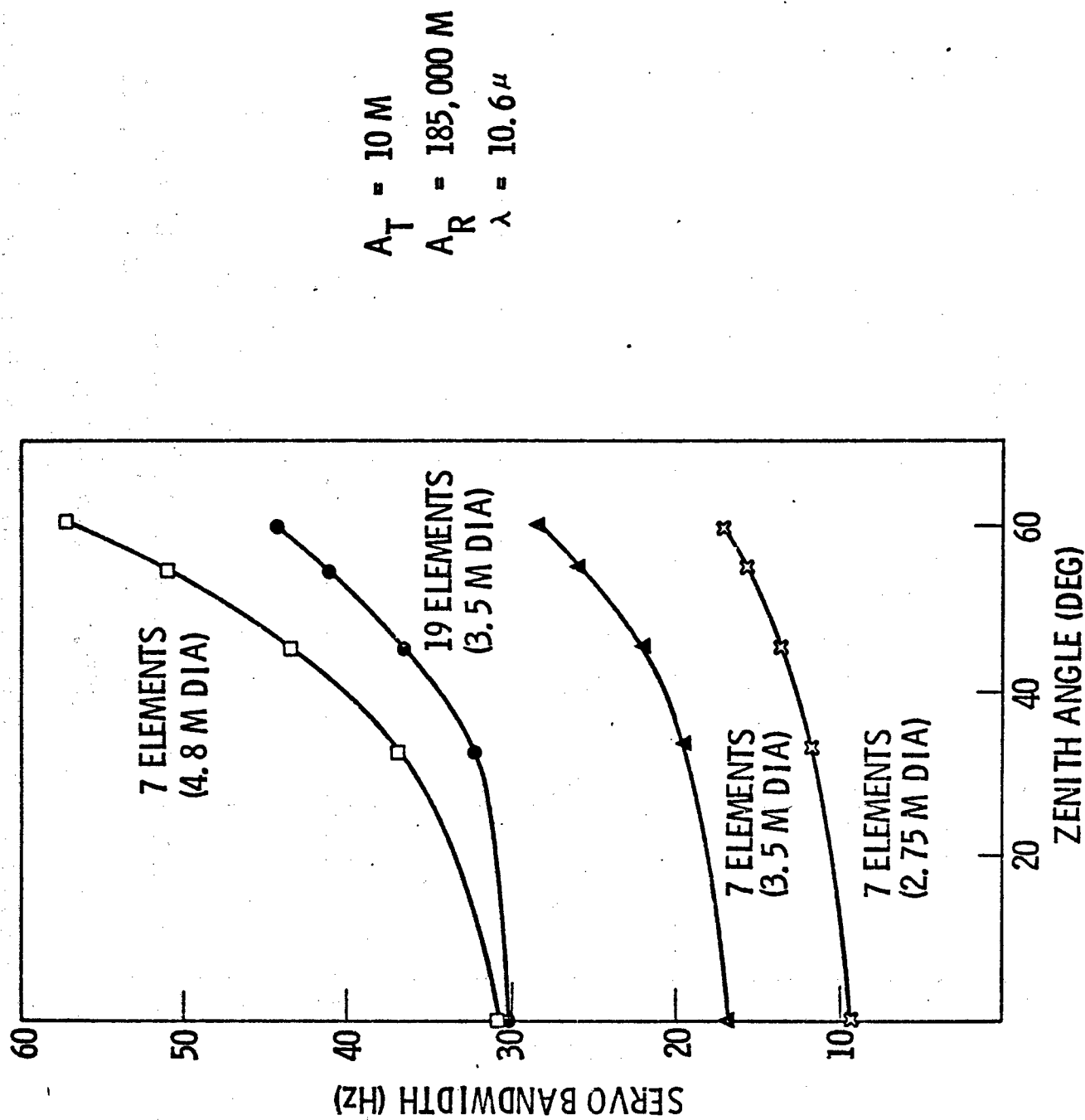


Figure IV-7. Bandwidth Required for 90% Correction

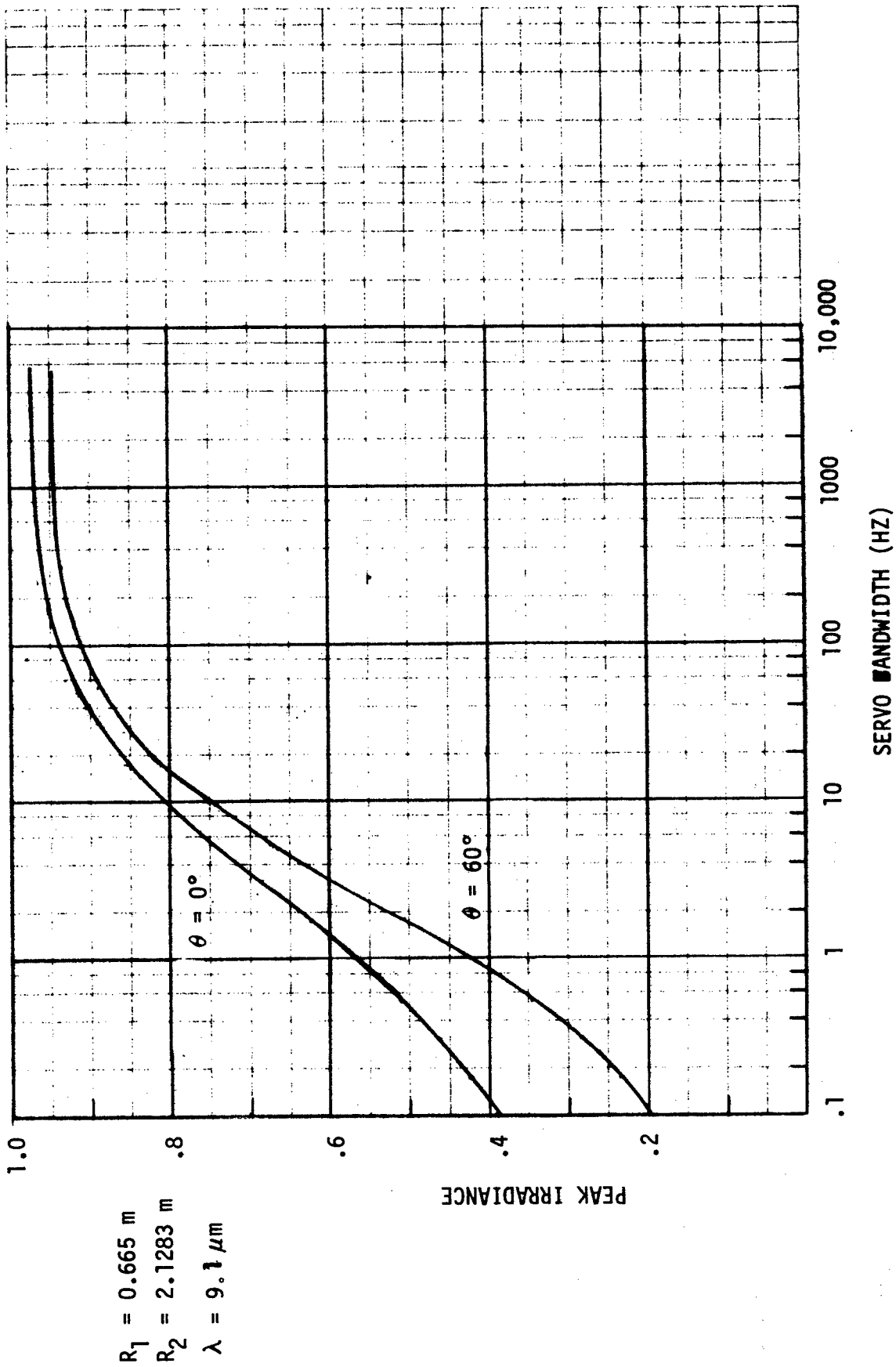


Figure IV-8. System Performance for a Seven-Element Array at $\lambda = 9.1 \text{ } \mu\text{m}$.

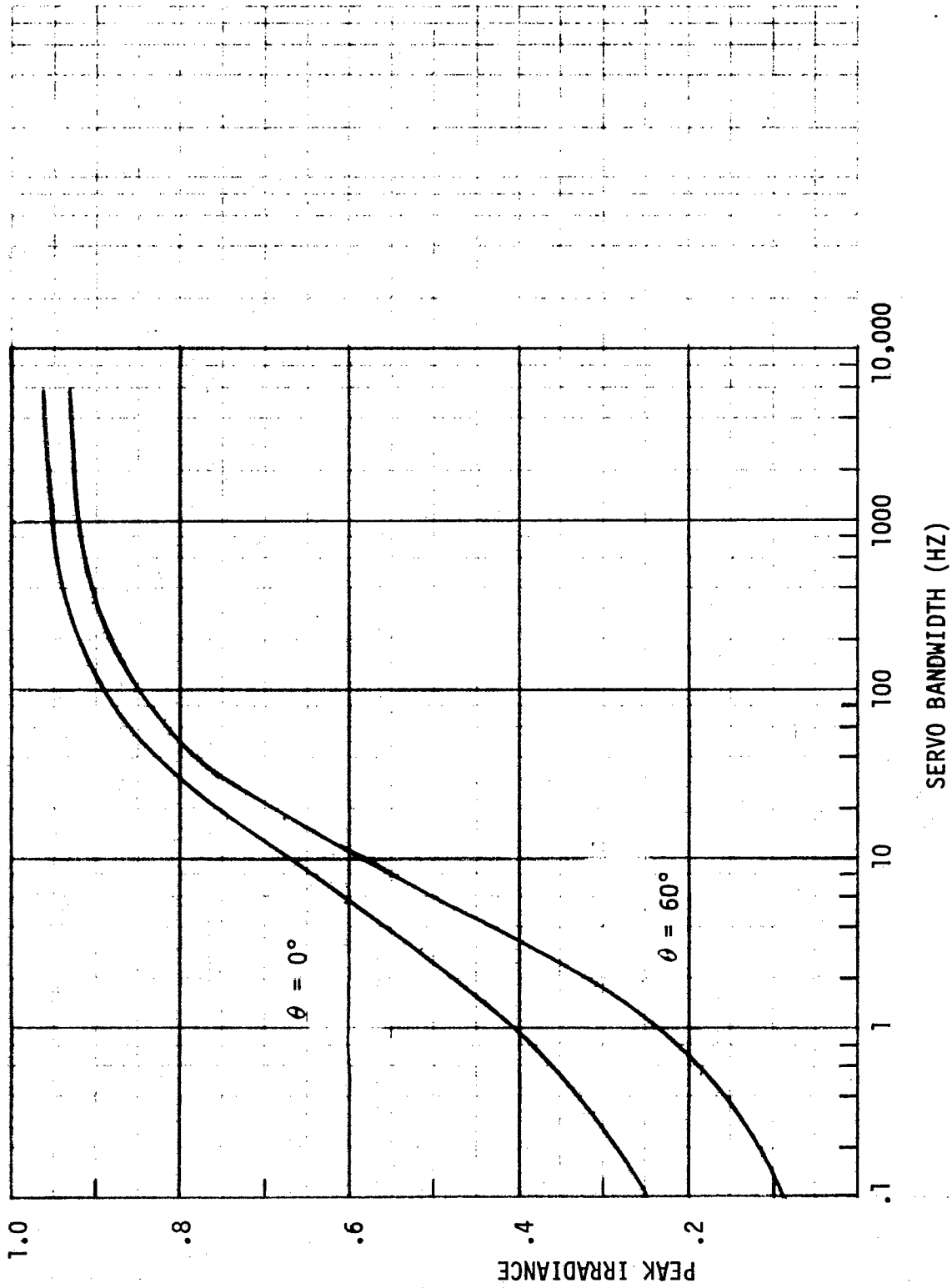


Figure IV-9. System Performance for a Seven-Element Array at $\lambda = 5 \text{ } \mu\text{m}$

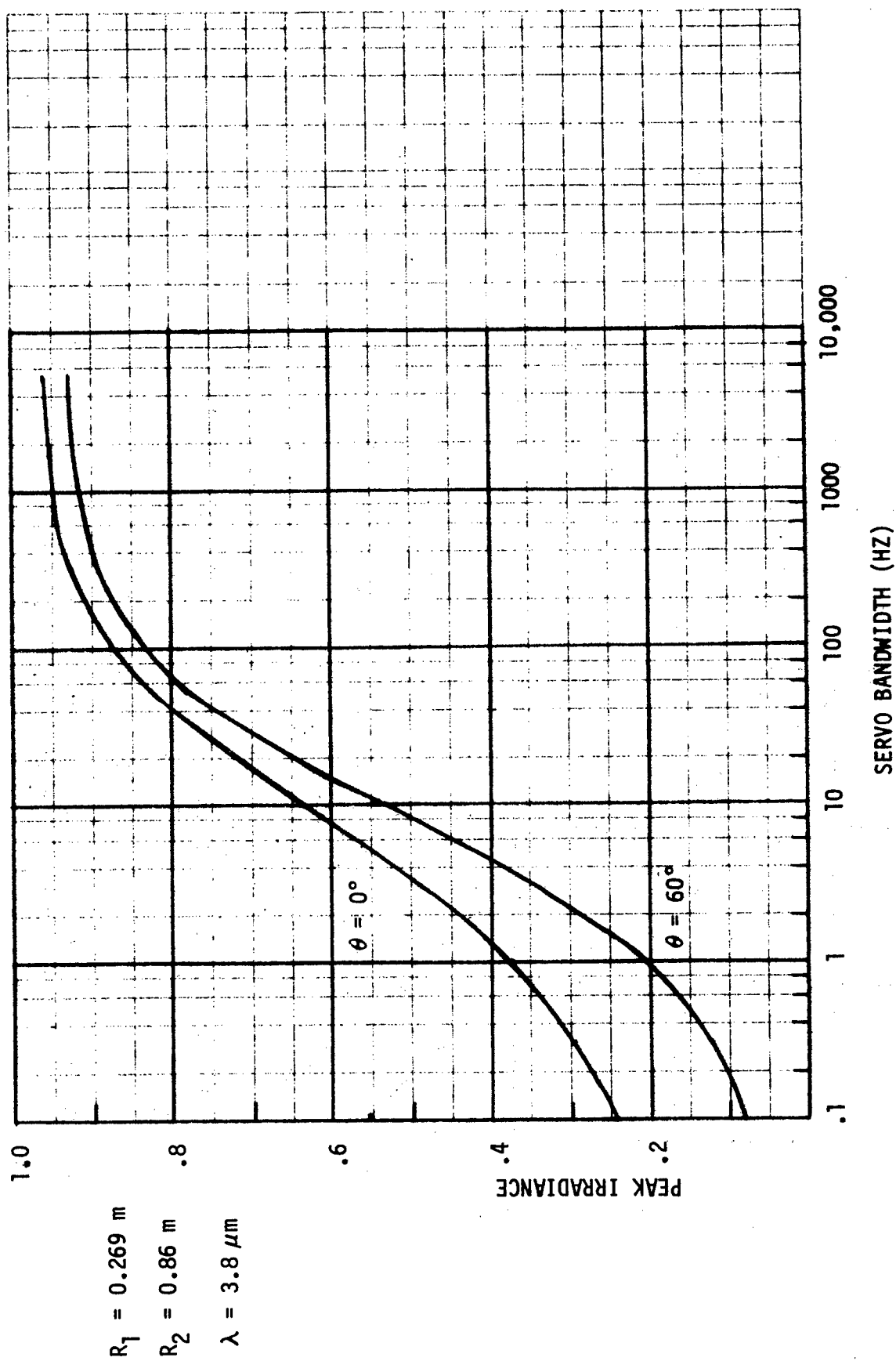


Figure IV-10. System Performance for a Seven-Element Array at $\lambda = 3.8 \mu\text{m}$

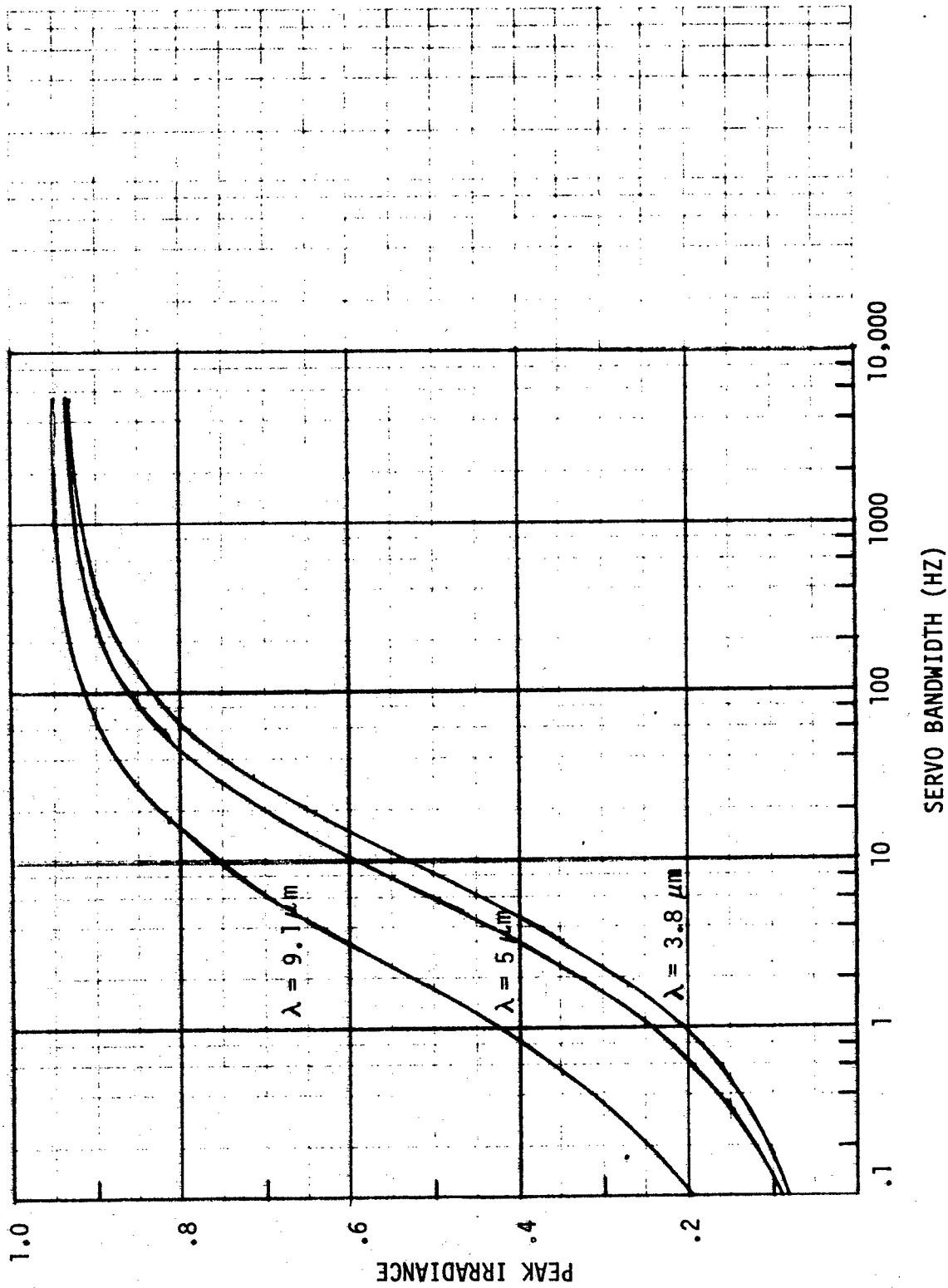


Figure IV-11. System Performance Comparing Seven-Element Arrays Scaled According to Wavelength. Propagation Angle was 60°.

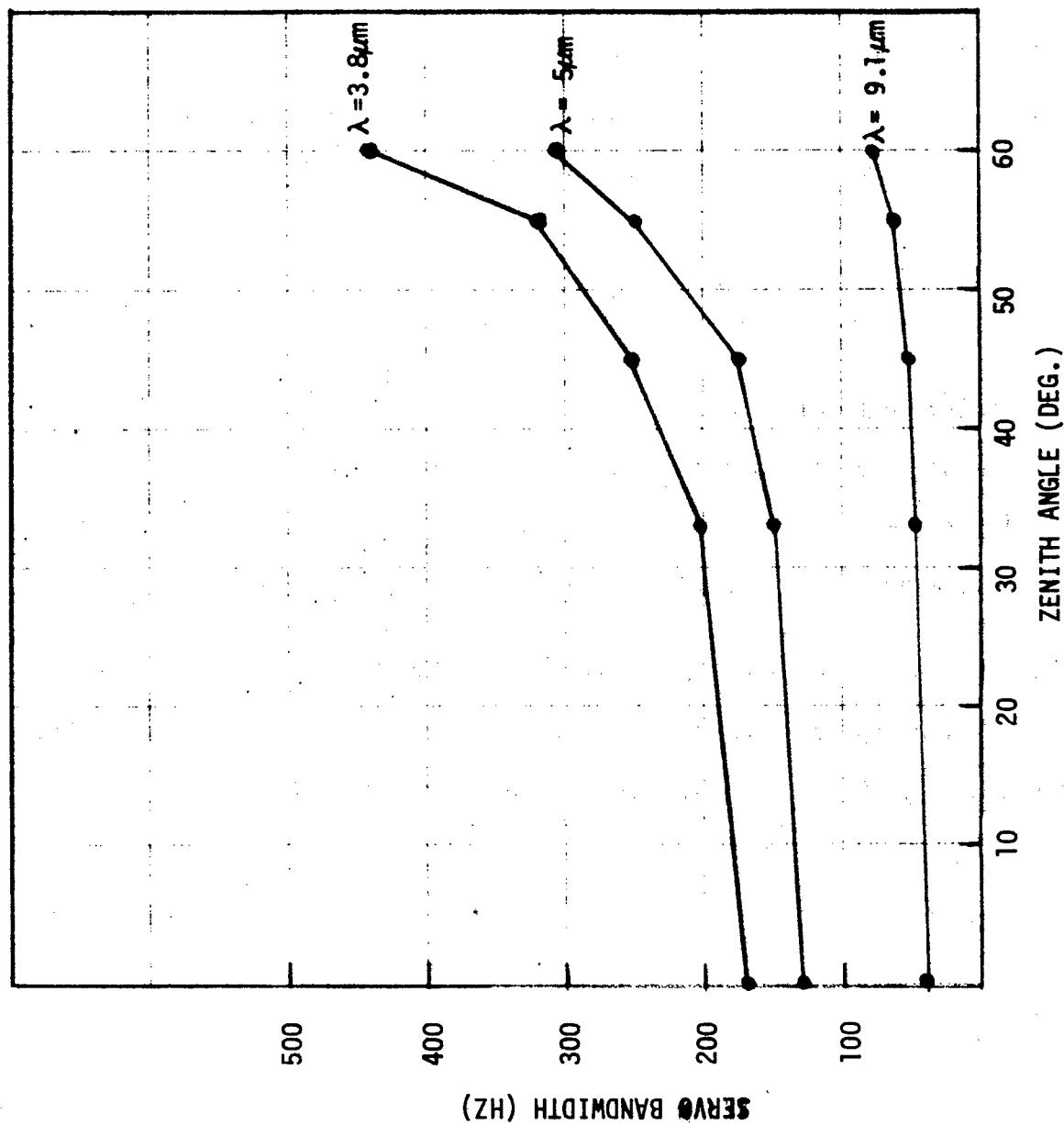


Figure IV-12. Required Servo Bandwidth for 90% Full Correction of Atmospheric Turbulence as a Function of Propagation Angle from the Vertical

D. Conclusions

These data indicate that the servo bandwidth requirements for atmospheric turbulence correction are such that present continuous surface deformable mirror technology is sufficient for the 10.6 μm and 9.1 μm . For the 5.0 or 3.8 μm wavelength, however, it would probably require technology advancement for operation at zenith angles greater than about 45°. The bandwidth requirements calculated for the 5.0 and 3.8 μm wavelengths give rise to another problem. This is concerned with outgoing wave, or dither, systems and the optical transit times. The operation of such systems must satisfy the condition

$$\frac{2 C}{h \sec \theta} > \Delta f,$$

where C is the speed of light

h is the satellite orbit altitude (185 km)

θ is the zenith angle, and

Δf is the adaption bandwidth requirement.

For 10.6 μm and 9.1 μm wavelengths, this condition is met over the full range of zenith angles. The 3.8 μm wavelength fails to meet this condition at approximately 40° and the 5.0 μm wavelength at about 50°.

References

1. J. Winocur, "Adaptive Optics Technology Study," Final Report, Contract N60921-74-C-0221.
2. R. F. Lutomirski and R. G. Buser, Appl. Opt. 12, 2153 (1973).
3. U.S. Air Force, Handbook of Geophysics, revised edition, MacMillan, New York (1960).
4. The measurements background for this model is given in the previous chapter of this document.
5. D. L. Fried and G. E. Mevers, Appl. Opt. 13, 2620 (1974).

V. THERMAL BLOOMING EFFECTS

The effects of thermal blooming on the transmission of power from a ground based laser to a satellite in circular orbit at 185 km altitude have been studied for four different wavelengths of interest. The satellite orbital geometry is illustrated in Figure V-1, which shows that zenith angles up to 60° are of interest. Because of the severe absorption problem for a laser transmitter at sea level, ground site elevations of 10 m and 3500 m were considered. The four wavelengths studied are 10.6, 9.1, 5.0, and 3.8 microns, with the emphasis being placed on the longer two wavelengths.

The satellite is assumed to have a 2 m diameter receiver with a small corner cube reflector at its center. This reflector provides a strong return signal which is sampled for atmospheric induced wavefront aberrations back at the transmitter. The phase distribution of the transmitter can be adjusted to help correct for these wavefront errors. The transmitter is assumed to be a phase locked array of seven circular apertures arranged in a close packed hexagonal pattern, with one aperture in the center, as illustrated in Figure V-2. Each element is adjustable in displacement and tilt angle, and a deformable mirror can be included in the optical circuit of each element in order to provide higher order phase error correction. All elements of the transmitter array are assumed to have the same constant intensity level. The phase is assumed to be initially uniform, but can be adjusted across each element to maximize the energy collected by the 2 m diameter "bucket."

The thermal blooming study was performed with the aid of the Rockwell International High Energy Laser Coherent Atmospheric Transmission (HELCAAT) computer code. HELCAAT is a three-dimensional, full wave optical program

SATELLITE ORBITAL GEOMETRY

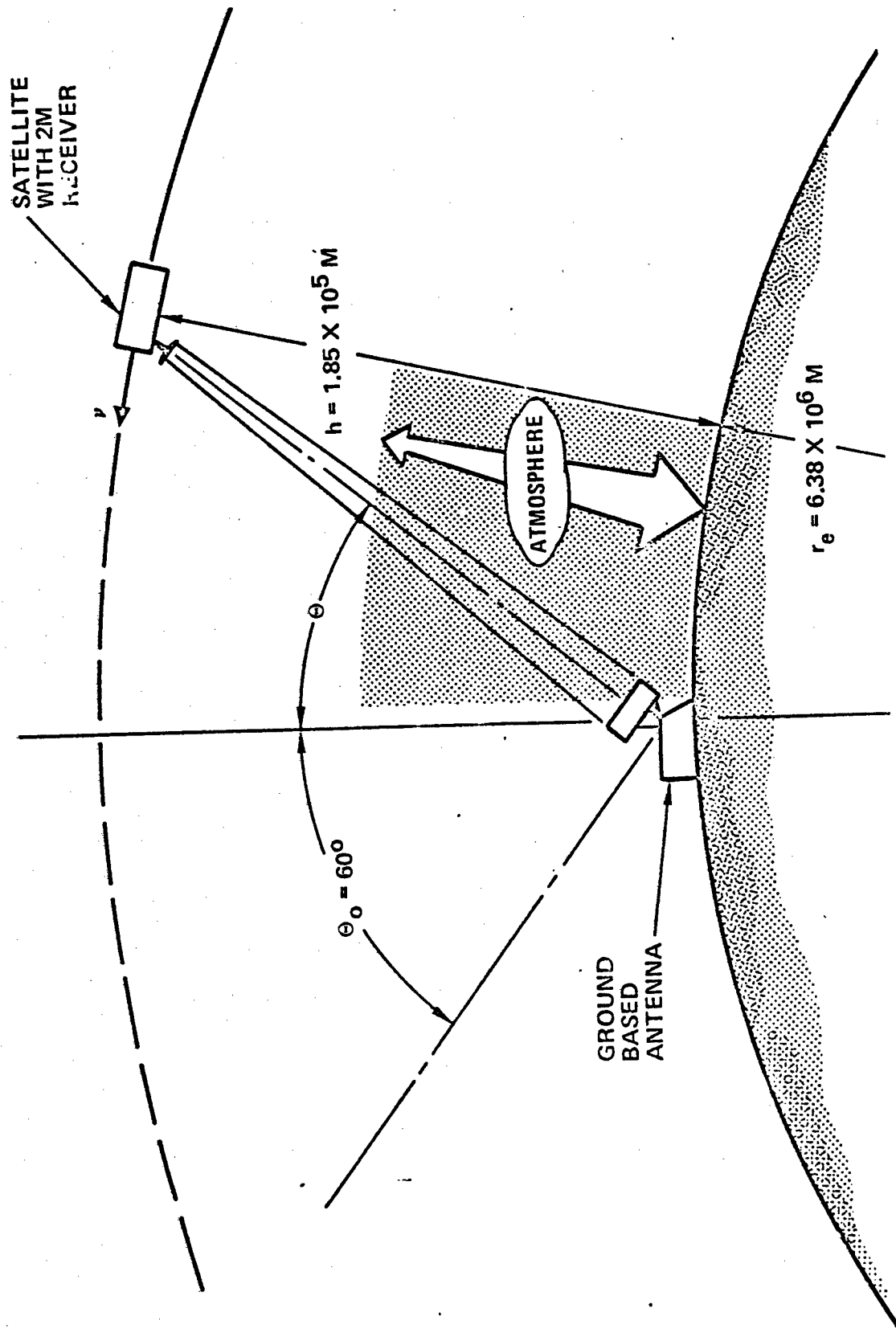


Figure V-1. Satellite Orbital Geometry

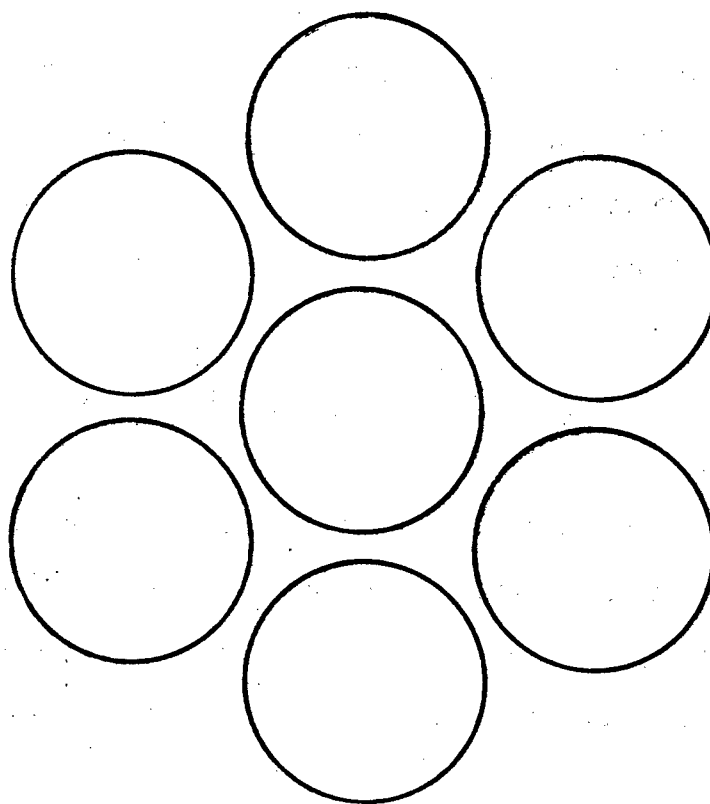


Figure V-2. Seven-Element Transmitter Configuration.
Dimensions are scaled with Wavelength.

for the simulation of open or closed loop operation of high energy laser systems in a thermal blooming environment. Propagation in a thermal blooming atmosphere is represented by transmission through a number of absorbing phase distorting screens. The phase error at each screen is calculated from the laser intensity and atmospheric parameter values at the position of each screen. The refractive index change, $\Delta n(x,y,z)$, due to heating of the atmosphere by a laser beam with slew rate ω , and convective cooling by a wind of effective velocity $V + \omega z$, where V is the wind velocity and z is the propagation distance, is given by

$$\Delta n(x,y,z) = \frac{-\alpha (\partial n_0 / \partial T)}{n_0 \rho c_p V (1 + \omega z/V)} \int_{-\infty}^x I(x',y,z) dx', \quad (1)$$

where n_0 , $\partial n_0 / \partial T$, α , ρ , and c_p are the refractive index, variation of refractive index with temperature, absorption coefficient, density, and specific heat, respectively, of the medium, and $I(x,y,z)$ is the beam intensity. The magnitude of the phase error according to the previous equation is proportional to

$$M_D(z) = \frac{\alpha(z)}{n_0 c_p \rho (z)} \left(\frac{\partial n_0}{\partial T} \right) \quad (2)$$

An analysis presented in Appendix A shows that this can be written in the following simple form

$$M_D(z) = \frac{(n_0 - 1)}{\rho_0 c_p} \frac{\alpha(z)}{T(z)}, \quad (3)$$

where ρ_0 is the air density at ground level and $T(z)$ is the air temperature. By substituting this last equation into Eq. (1), it is easy to show that the laser wavefront phase error $\Delta \phi(x,y)$ may be written in mks units as

$$\Delta\phi(x,y) = \frac{1.47 \times 10^{-6}}{\lambda} \int_{-\infty}^x \int_{z_0}^z \frac{\alpha(z) I(x',y,z)}{(V(z) + \omega z) T(z)} dx' dz. \quad (4)$$

Propagation from one phase distorting screen to the next is simulated by using the two-dimensional transfer function

$$H(f_x, f_y) = \exp [jkz (1 - \lambda^2 f_x^2 - \lambda^2 f_y^2)^{1/2}] \quad (5)$$

in the Fourier transform domain. This is an efficient computational algorithm because a fast two-dimensional Fourier transform can be used.

Because the absorption coefficient, beam profile, wind velocity, and temperature vary with altitude, the phase error is strongly altitude dependent. For this reason, it is undesirable to make the screens equally spaced. Instead, the spacings are chosen in such a way that the average phase errors between screens are approximately equal.

For CO₂ laser radiation, kinetic cooling of the atmosphere, which may predominate at altitudes of about 2 km and higher, has a significant effect on propagation characteristics. Kinetic cooling is caused by the absorption of 10.6 μm radiation from the (100) to the (001) vibrational states of CO₂. The (100) state is replenished by energy transfer from translation, cooling the atmosphere. The (001) state transfers energy through N₂ in the atmosphere back to translation, as shown in Figure V-3.

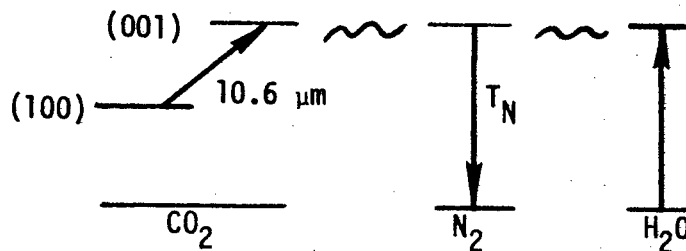


Figure V-3. Kinetic Cooling Diagram for CO₂

The critical parameter is T_N , the vibrational relaxation time of N_2 . A simple mathematical model that assumes instantaneous cooling and delayed heating gives the result²

$$\Delta n(x,y,z) = \frac{N_T(\alpha_{CO_2} + \alpha_{H_2O})}{n_o \rho c_p V(1 + \omega z/V)} \int_{-\infty}^x [1 - \alpha \exp(-\frac{x-x'}{VT_N})] I(x',y,z) dx', \quad (6)$$

where α_{CO_2} and α_{H_2O} are the coefficients of absorption of CO_2 radiation by CO_2 and H_2O , respectively, and

$$\sigma = 2.441 \alpha_{CO_2} / (\alpha_{CO_2} + \alpha_{H_2O}). \quad (7)$$

The relaxation time T_N is calculated from the following equation, which was derived by curve-fitting theoretical and experimental data³

$$T_N = (1/(\gamma_1 + \gamma_2 + \gamma_3))(1 - 5H_R/6) \quad (8)$$

$$\gamma_1 = 287 H_R \exp(-5.75 \times 10^{-4} H) \quad (9)$$

$$\gamma_2 = 24.5 \exp(-1.64 \times 10^{-4} H) \quad (10)$$

$$\gamma_3 = \frac{4.86 H_R}{(1 + 0.001 H)} + 38.6 \exp(-1.7 \times 10^{-4} H) \quad (11)$$

where H is the altitude in meters and H_R is the relative humidity.

The atmospheric absorption models for the four wavelengths of interest are shown in Figure V-4, which is a plot of attenuation coefficient, $\alpha(z)$, versus altitude for the wavelengths 10.6, 9.1, 5.0, and 3.8 microns. Both the July and January models for 10.6 micron radiation are shown. At elevations above about 6 km, where the absorption is predominantly due to CO_2 , these two models are nearly identical. For 9.1 micron radiation, the absorption is assumed to be due to H_2O vapor only, and the July model is shown in the

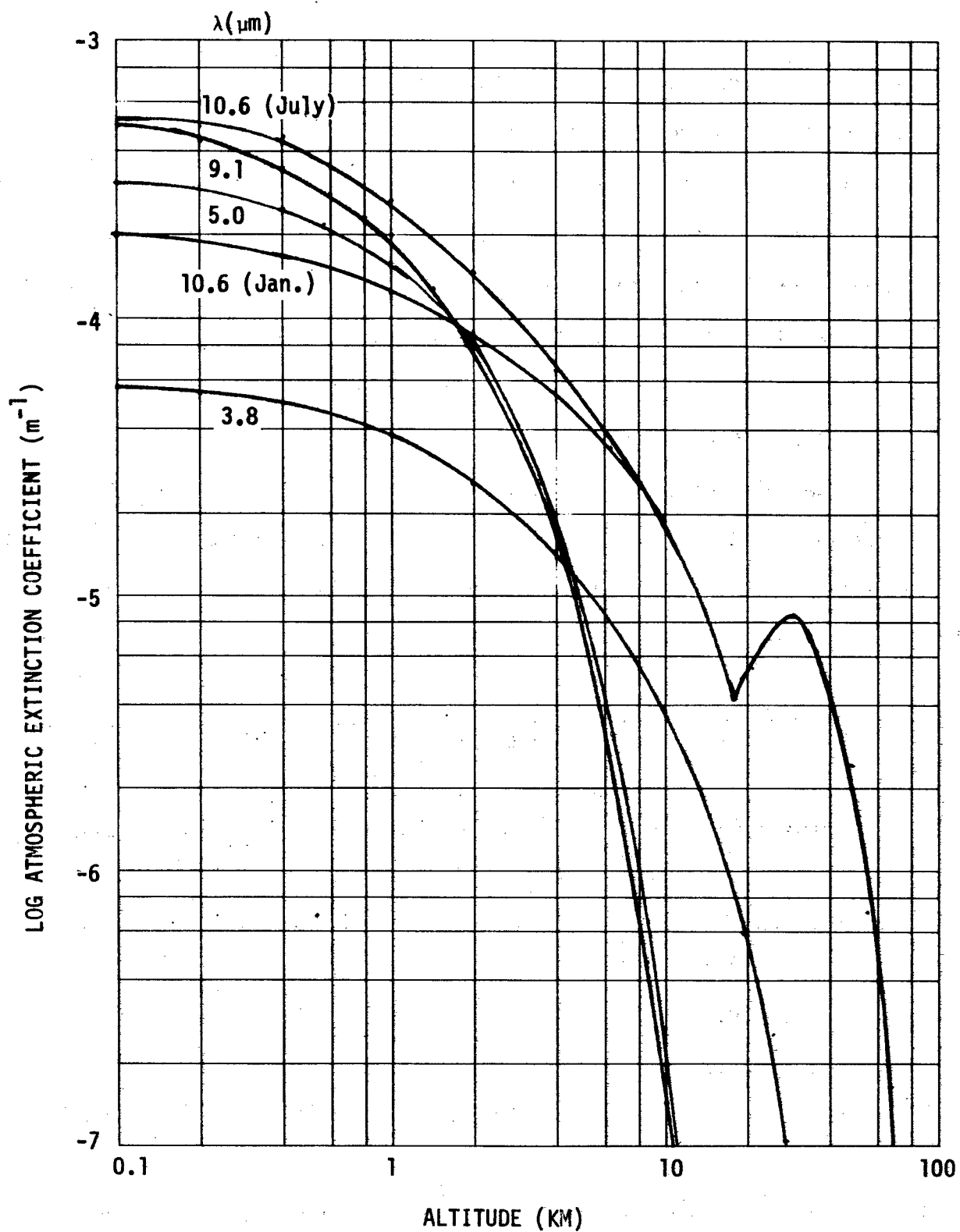


Figure V-4. Absorption Coefficients vs Altitude

figure. In Figure V-5 are plotted atmospheric transmission factors as a function of transmitter elevation for the four wavelengths of interest, and for zenith angle $\theta_z = 0^\circ$. Figure V-6 is a similar family of curves for zenith angle $\theta_z = 60^\circ$. These curves demonstrate the advantages of using shorter wavelengths and higher ground site elevations to reduce atmospheric absorption losses. Wind speed was modeled according to the curve of Figure V-7, which is the same as that presented in the previous chapter for $W_{\max} = 50 \text{ m/x}$. Temperature distribution was modeled as shown in Figure V-8.⁴

The geometry of the seven-element phase locked laser array used in the calculations is illustrated in Figure V-2. The same general shape was used for each wavelength, but the dimensions were scaled as indicated in Table V-1.

Table V-1 Transmitter Dimensions			
Wavelength (μm)	Element Radius (m)	Element Separation (m)	Maximum Diameter (m)
10.6	.740	1.662	4.81
9.1	.636	1.426	4.13
5.0	.349	.784	2.27
3.8	.265	.596	1.72

The transmitter diameter was chosen as 4.8 m for the longest wavelength (10.6 μm) and scaled from there according to wavelength. The choice of 4.8 m is somewhat arbitrary, but this is the diameter that produces a central diffraction lobe equal to the bucket diameter (2 m) at the longest range of interest, which is

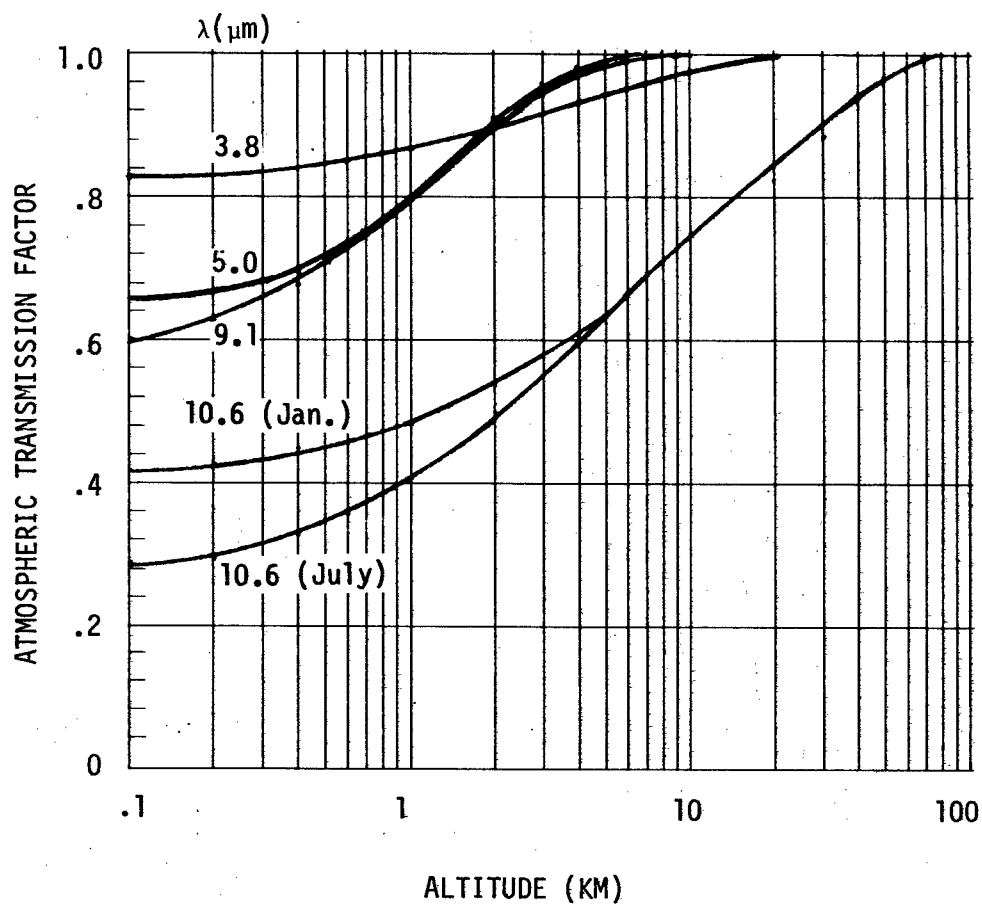


Figure V-5. Atmospheric Transmission vs Altitude. Zenith Angle $\theta_z = 0^\circ$, and Wavelengths $\lambda = 10.6$ (July and January Atmospheric models), 9.1, 5.0, and 3.8 μm .

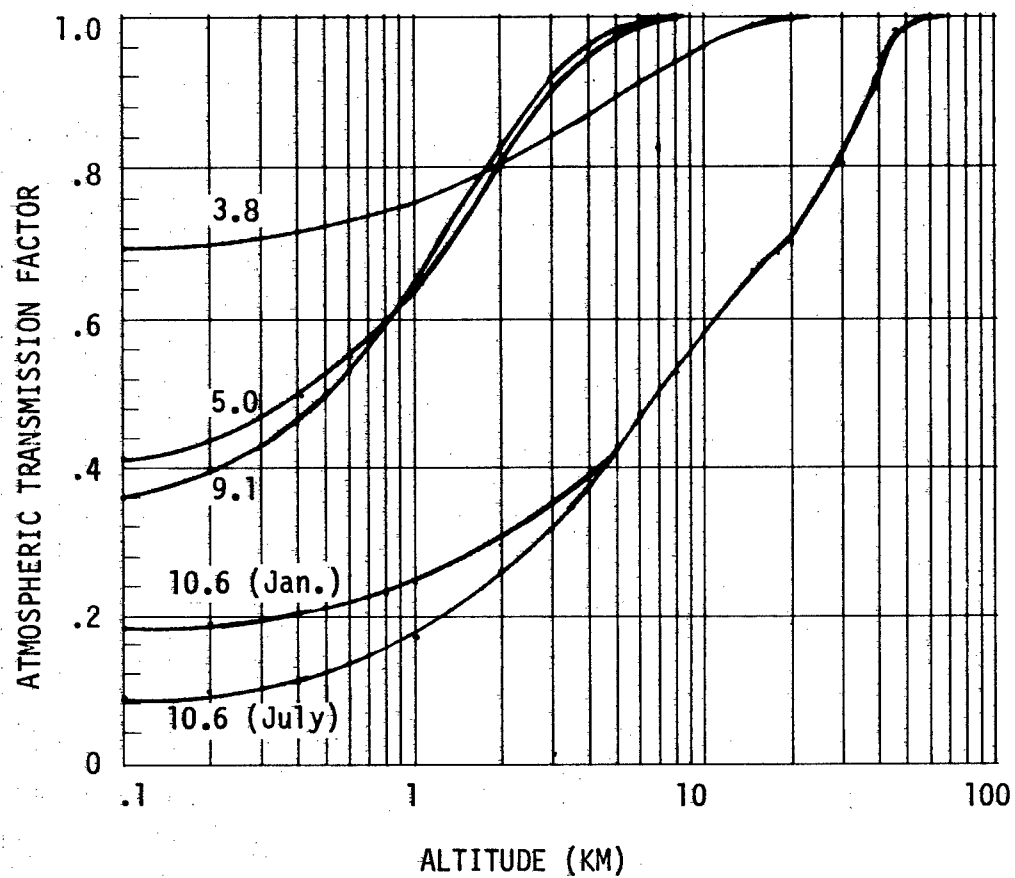


Figure V-6. Atmospheric Transmission vs Altitude. Zenith Angle $\theta_z = 60^\circ$, and Wavelengths $\lambda = 10.6$ (July² and January Atmospheric Models), 9.1, 5.0, and 3.8 μm .

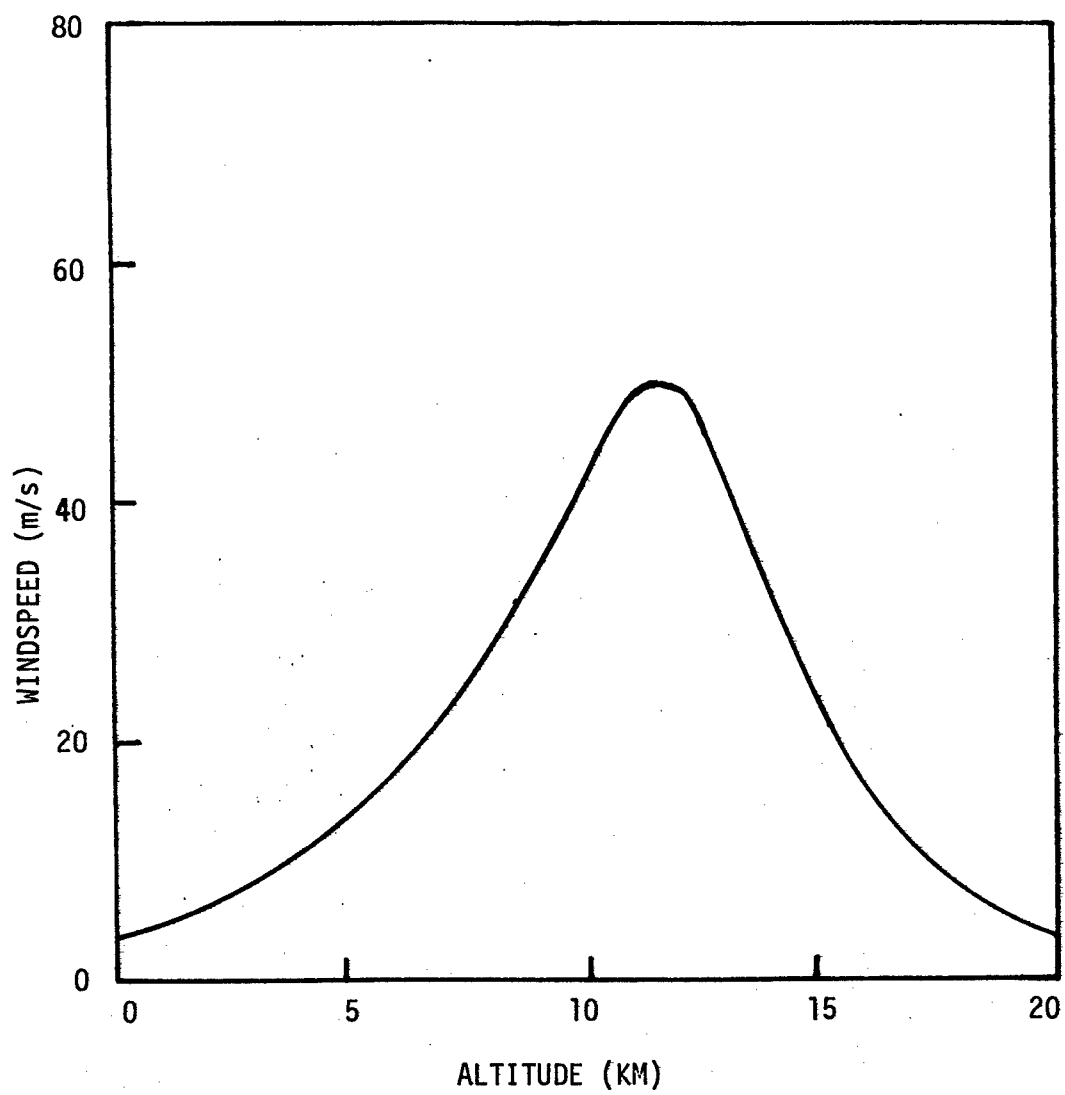


Figure V-7. Atmospheric Wind Velocity Distribution Model

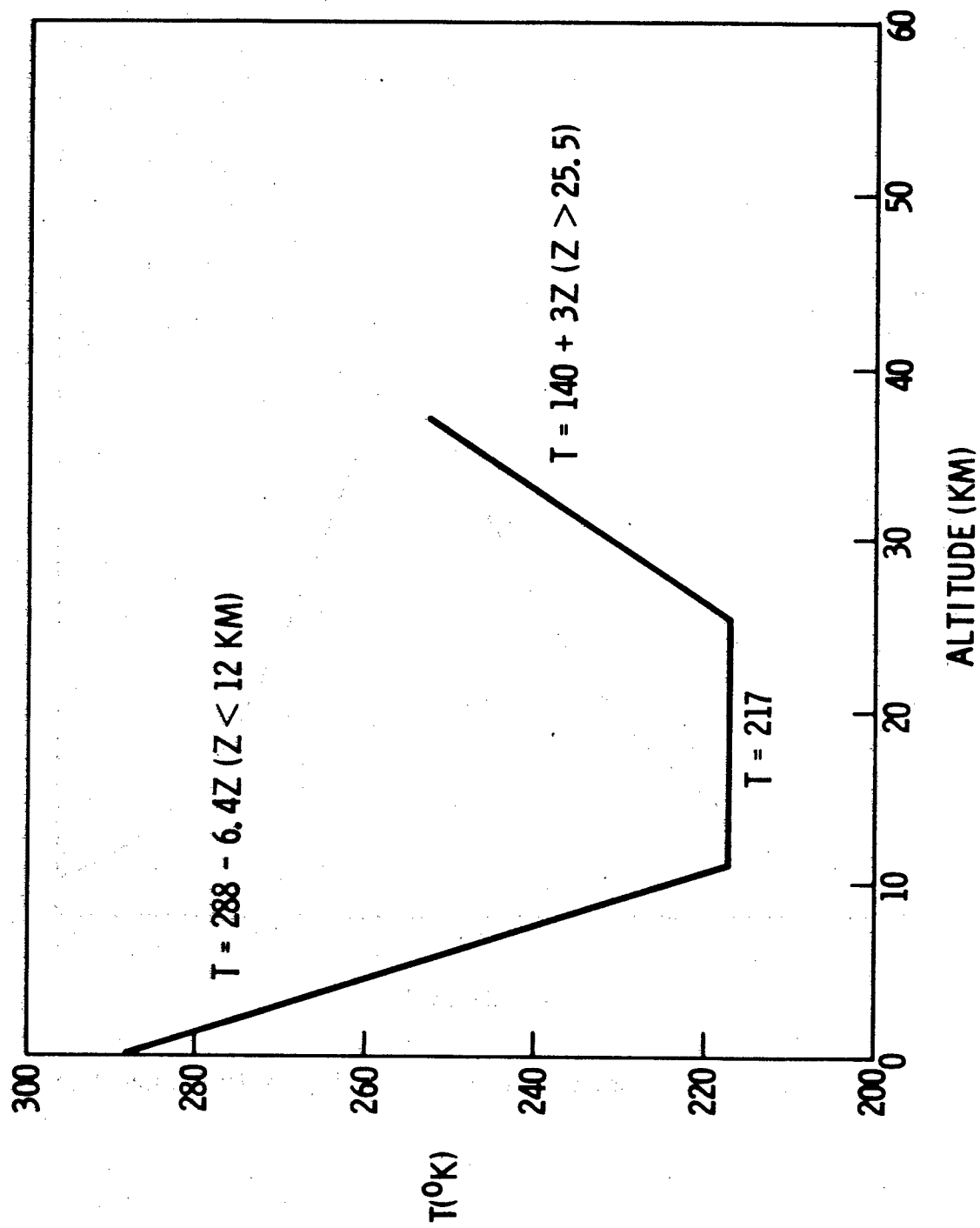


Figure V-8. Atmospheric Temperature Distribution Model

370 km at $\theta_z = 60^\circ$. By scaling transmitter dimensions with wavelength, the same criterion applies at each wavelength. Some calculations were also performed at the shorter wavelengths using the larger transmitter dimensions in order to indicate the advantages of using the larger apertures at the shorter wavelengths.

The far field patterns of a seven element array and a single element of the same major diameter and total power are compared in Figure V-9. The fraction of the total transmitted power contained within a 2 m diameter bucket at the satellite is 0.69 for the seven element array and 0.91 for the single element transmitter, a difference of 24%. The ratio of peak intensities is 0.65. The reason for this discrepancy is that the gaps in the seven element array cause a larger portion of the main beam to be diffracted into the side lobes, as can be seen in Figure V-9. The effects of thermal blooming on a seven element array and a single aperture are compared in Figure V-10, in which relative power collected in a 2 m diameter bucket is plotted as a function of transmitter power, for a $10.6 \mu\text{m}$ laser beam propagated from a ground site at 10 m elevation to a satellite directly overhead. The maximum aperture dimension in both cases is 4.8 m. The effects of thermal blooming are much more severe for the seven element array. The main reason for this is that, because of the gaps, the power density of each element of the seven element array must be 1.5 times that of the single aperture in order to transmit the same total power. By reducing the gap size, the power density and hence the strength of blooming can be reduced. For example, if the elements of the array could be made contiguous, then the ratio of power densities would be reduced from 1.5 to 1.3.

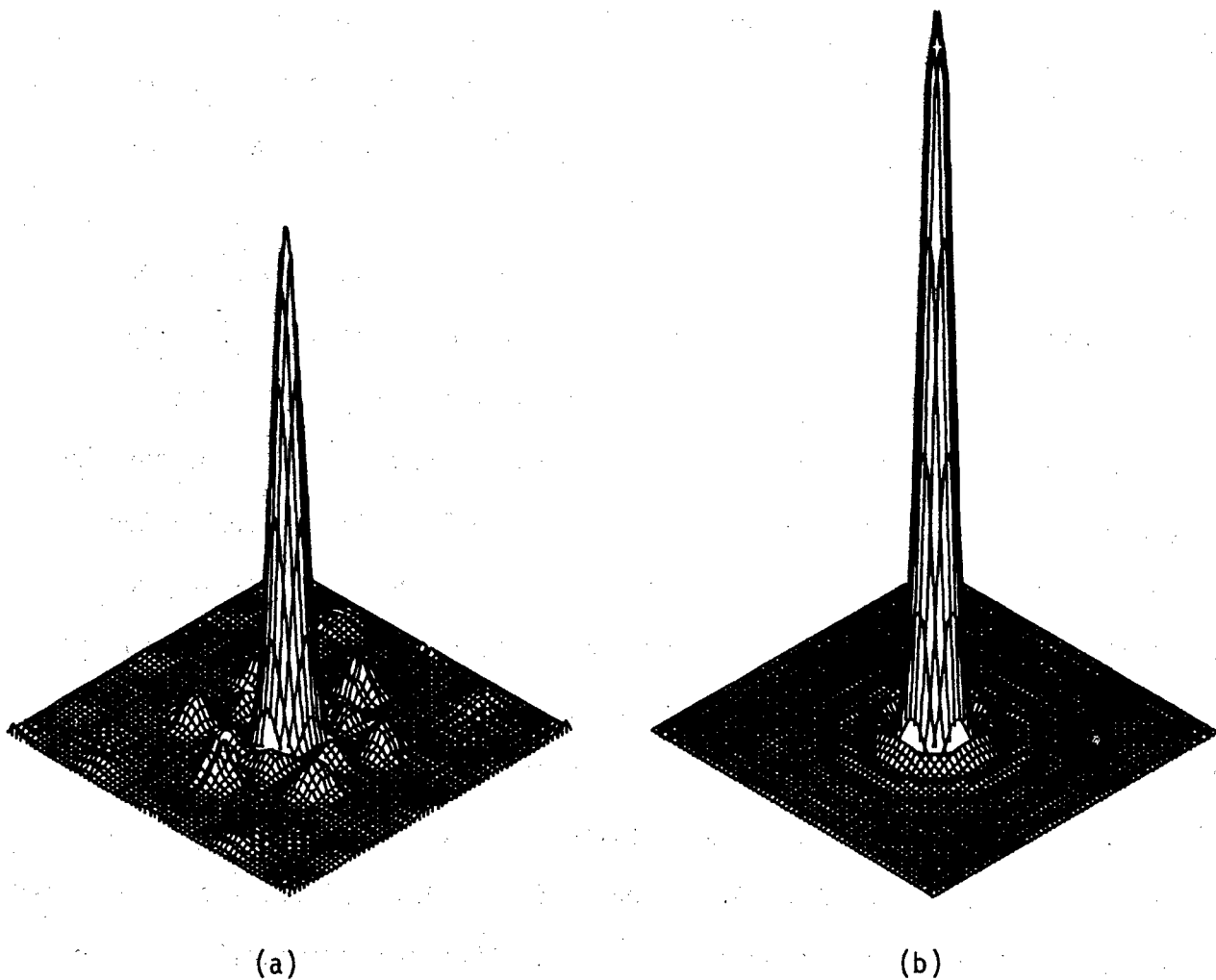


Figure V-9. Comparison of Far-Field Intensity Patterns. On the left (a) is the pattern for a seven-element close-packed hexagonal array and on the right (b) is the pattern for a single aperture of the same major diameter as the array. The total power transmitted is the same for both antennae.

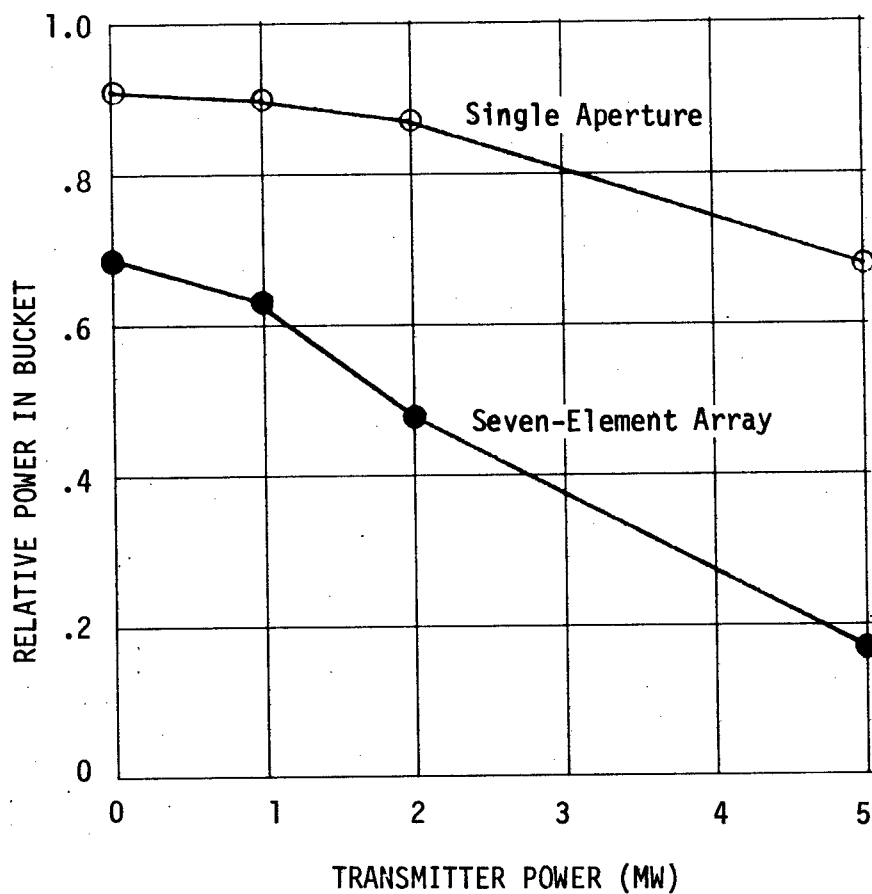


Figure V-10. Comparison of Transmission Efficiency of a Seven-Element Array and a Single Aperture, as a Function of Laser Power for a $10.6\text{ }\mu\text{m}$ laser beam propagated from a ground site at 10 m elevation to a satellite directly overhead. The major aperture dimension is 4.8 m in both cases.

The far field intensity of the thermally bloomed beam from a seven element array is shown in Figure V-11 for (a) 2 MW, and (b) 5 MW of transmitter power. Note that the beam has shifted into the wind and spread, mostly in the direction normal to the wind vector. Also note that the bloomed images do not exhibit the crescent shape characteristics of horizontally propagated laser beams. The crescent normally occurs because the phase gradient is greater at the center of the beam than it is at the edges, causing more bending at the center than at the edges. This effect is most significant with Gaussian shaped beams, but it also occurs with beams of uniform initial intensity distribution, because the propagation process changes the shape of the beam to approximately Gaussian near the focal plane where the phase distortion is greatest. With vertical propagation, most of the phase error occurs near the transmitter where the intensity is still quite uniform, so the beam does not develop a crescent shape.

The effects of thermal blooming in these calculations were simulated with only four phase distorting screens. Their locations are chosen such that approximately 94% of the total phase error is represented nearly equally by the first three screens and 6% of the total phase error is represented by the fourth screen. The last screen is made weaker than the others because the propagation distance from that screen to the target is very large compared to the propagation distances between the first three screens. The phase error is calculated under the assumption that the intensity term in Eq. (4) can be taken outside the integral. This is a valid assumption for the first three screens, and is not a necessary condition for the fourth screen if the thermal blooming effects over the last propagation step are weak. The accuracy of this approach was tested by increasing the number of screens used

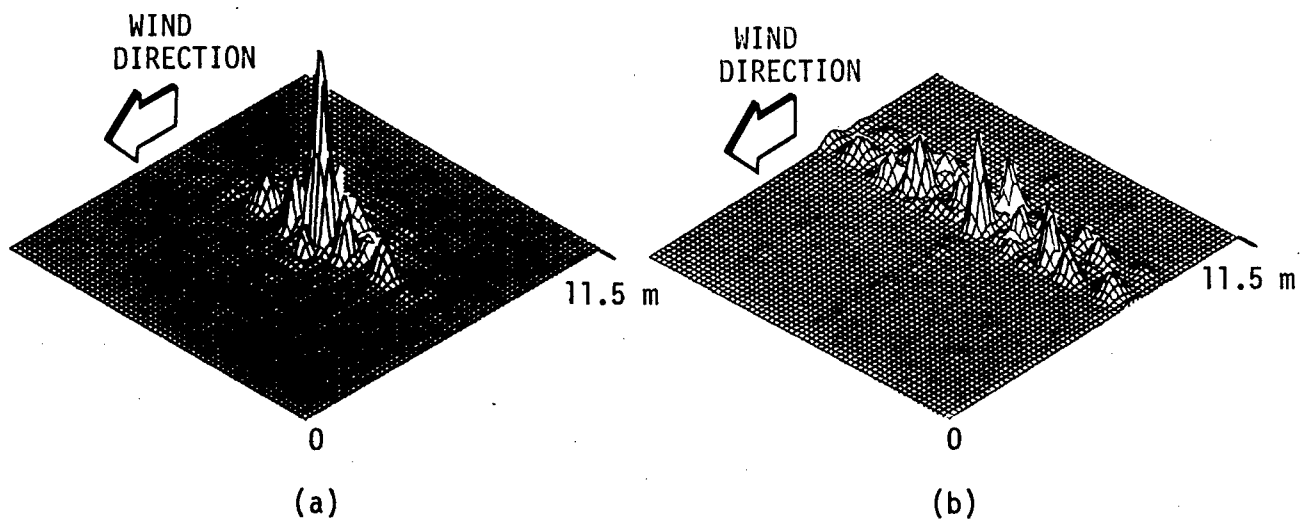


Figure V-11. Thermally Bloomed 10.6 μm CO_2 Laser Beam Profiles. These data are for two different transmitted power levels. On the left (a) is the target plane intensity distribution for 2 MW transmitted power and on the right (b) for 5 MW. In both cases the transmitter antenna is a seven-element hexagonal array at 10 m elevation. The major antenna diameter is 4.8 m, and the propagation is directly vertical (zenith angle = 0°).

in the calculations. No significant change in computed results were found when as many as eight screens were used. The screen locations that fulfill the above criteria for the 10.6 μm radiation calculations previously described are $H = 10, 112, 403, \text{ and } 2680 \text{ m}$. The target range is 185 km. Because the last propagation step is so much larger than the first three (a factor of ~ 70 in the last example), the wavefront is essentially propagated from the near field to the far field in one step. For this reason, it is possible to scale the size of the far field pattern simply by increasing or decreasing the length of the last propagation step and adjusting the focal length of the telescope and the target velocity appropriately. This is a particular advantage when the field size used in the computation is too small with respect to the beam size to accurately represent the beam spread due to thermal blooming.

A similar set of calculations were performed for the wavelengths 10.6 (January model), 9.1 (July and January models), 5.0 (P10 line), and 3.8 μm . The results are summarized by the plots in Figure V-12. These curves display only the losses due to thermal blooming. Absorption effects on beam intensity are included in the computations, but are omitted from the final data. These results indicate that severe thermal blooming losses occur at high power levels, with the possible exception of 9.1 μm , for a January model.

Considering the relative magnitudes of the absorption coefficients as shown in Figure V-4, one might have expected to see weaker blooming effects for the shorter wavelengths. The reason this is not so is because the transmitter diameter was scaled with the wavelength in all of these calculations. If larger diameter transmitters were used for the shorter wavelengths, then much weaker thermal blooming effects would result, as shown in Figure V-13. There the thermal blooming transmission factor is plotted versus power for

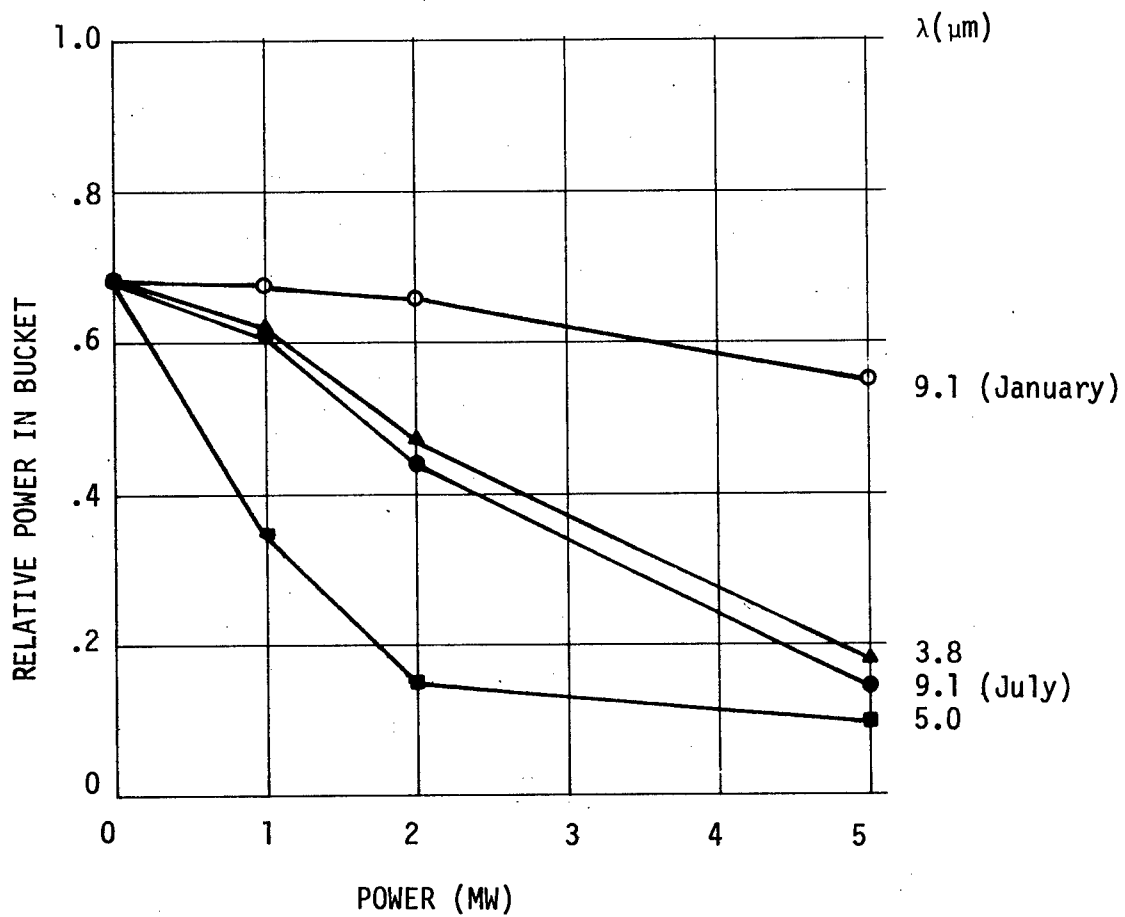


Figure V-12. Relative Power Collected in a 2 m Diameter Bucket vs Transmitter Power. Wavelengths $\lambda = 9.1$ (July and January Atmospheric Models), 5.0, and 3.8 μm . The transmitter antenna is a seven-element array at 10 m elevation with a major diameter of 4.8 m and the propagation direction is directly vertical (zenith angle = 0°).

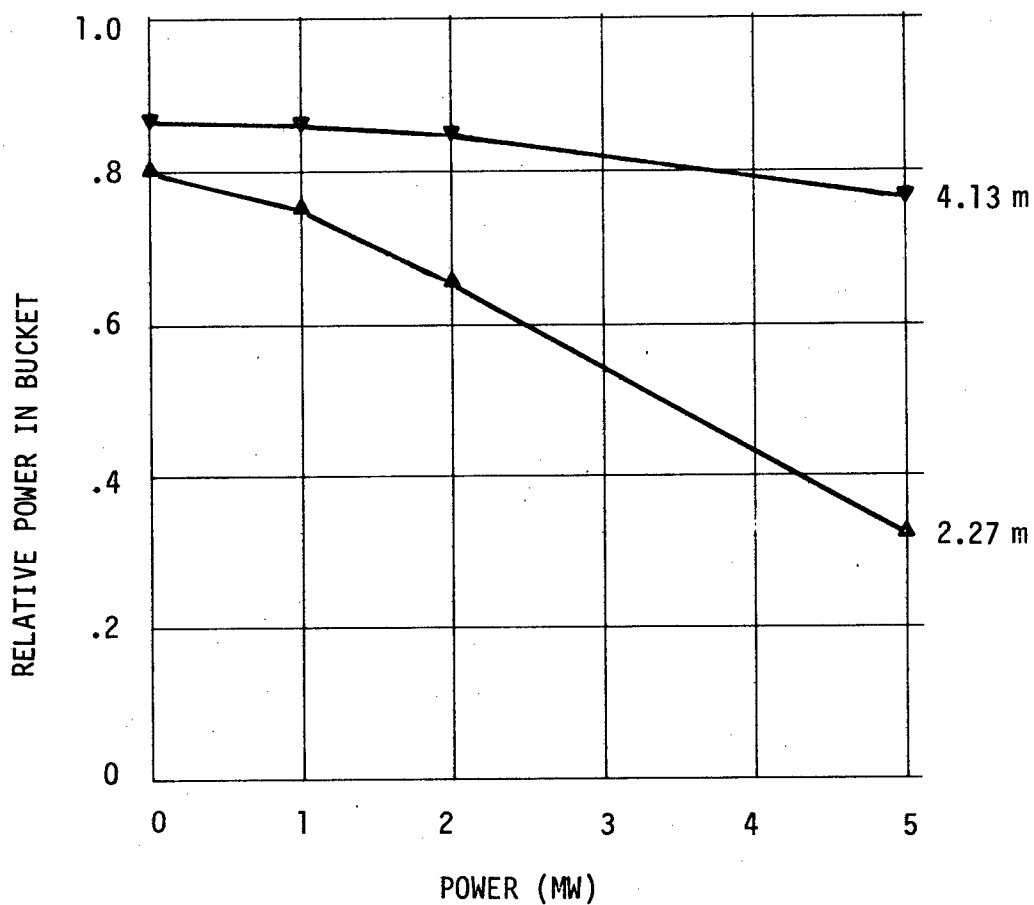


Figure V-13. Relative Power Collected in a 2 m Diameter Bucket vs Transmitter Power. These data are for seven-element hexagonal transmitter arrays with major diameters of 4.13 m and 2.27 m. The wavelength considered is $\lambda = 3.8 \mu\text{m}$, the transmitter antennae are at an elevation of 10 m and the propagation is vertical ($\theta_z = 0^\circ$).

3.8 μm radiation, using the aperture diameters previously associated with 5.0 μm wavelength (2.27 m) and 9.1 μm wavelength (4.13 m). Because of lower power densities, the thermal blooming effects are considerably smaller. Also, because the far field pattern scales with wavelength, the power collected in a bucket is significantly higher at the shorter wavelengths. In fact, a 5 MW, 4.13 m diameter transmitter degraded by thermal blooming delivers more relative power at wavelength 3.8 μm than a 4.13 m diameter transmitter delivers at 9.1 μm in vacuum.

When the satellite is not directly overhead, the effects of thermal blooming increase because of greater path length in the atmosphere and because of the larger diffraction effects at the longer range. In Figure V-14, relative power on target is plotted versus zenith angle for a transmitter at 10 m elevation for wavelength $\lambda = 9.1 \mu\text{m}$, $P = 2 \text{ MW}$, and for $\lambda = 3.8 \mu\text{m}$, $P = 2 \text{ MW}$ and $P = 5 \text{ MW}$. The same aperture diameter, 4.13 m, was used for both wavelengths. The diffraction limited relative power, which varies with zenith angle, is indicated in the same figure by the dotted lines. Thermal blooming losses for wavelengths $\lambda = 10.6 \mu\text{m}$ and $5.0 \mu\text{m}$ are even larger.

Increasing the elevation of the transmitter site from 10 m to 3500 m causes a drastic reduction in thermal blooming effects. Figure V-15 shows the variation of relative power versus zenith angle for a 5 MW transmitter at elevation 3500 m for the four different wavelengths of interest, and the aperture diameters listed in Table I. The power loss at zenith angle 0° is very low, even at the shorter wavelengths and smaller aperture diameters. The July models are used for CO_2 radiation, but the results are not very different at this elevation for the January model. For the wavelength $\lambda = 10.6 \mu\text{m}$, kinetic cooling effects are included in the calculations. (The relative humidity is assumed to be equal to 0.5.) These results show that

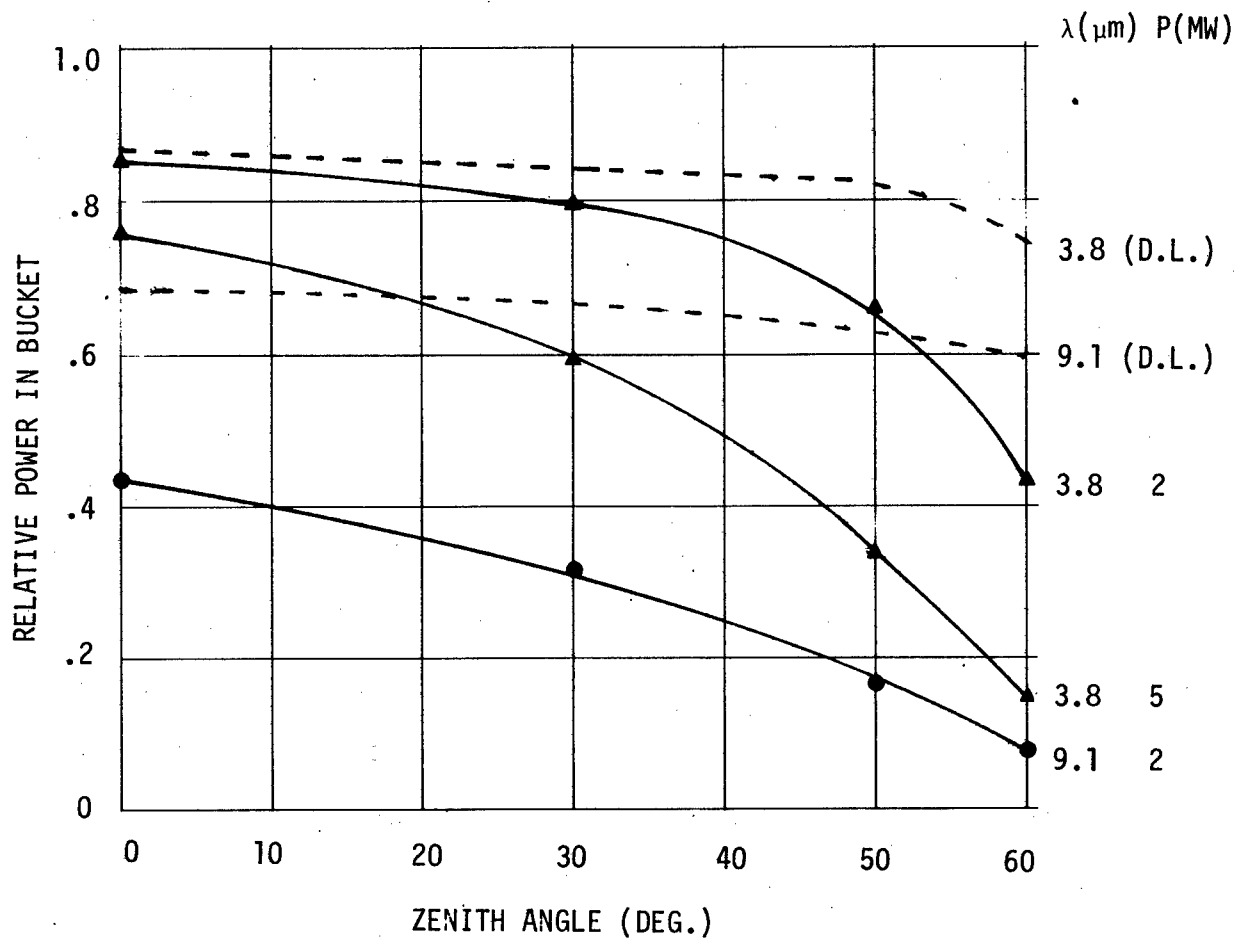


Figure V-14. Relative Power Collected in a 2 m Diameter Bucket vs Zenith Angle. Wavelengths $\lambda = 9.1 \mu\text{m}$ ($P = 2 \text{ MW}$), and $3.8 \mu\text{m}$ ($P = 2$ and 5 MW). For these data the transmitter antenna elevation was 10 m and the major diameter of the array was held constant at 4.13 m. Consequently, the shorter wavelength source inputs a greater percentage of power to the 2-m bucket. Antenna diffraction limited (D.L.) conditions are indicated by the dashed curves.

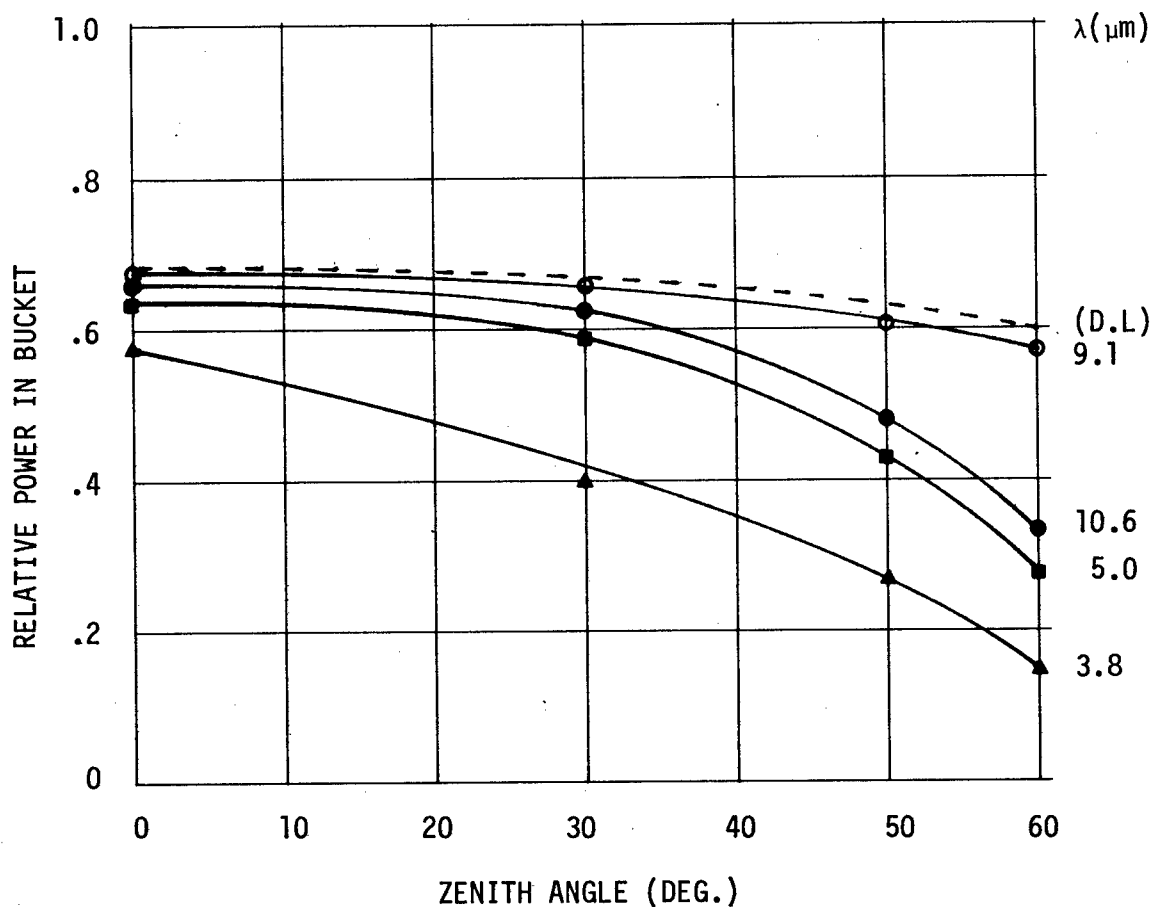


Figure V-15. Relative Power Collected in a 2 m Diameter Bucket vs Zenith Angle. Wavelengths $\lambda = 10.6, 9.1, 5.0,$ and $3.8 \mu\text{m}$. For all cases presented the transmitted power was 5 MW and the transmitter elevation was 3.5 km. Here the major array diameter was scaled with wavelength so the ratio, λ/D , remained constant. The dashed curve indicates diffraction-limited conditions.

thermal blooming is still significant at the larger zenith angles for all wavelengths except $\lambda = 9.1 \mu\text{m}$. However, if a large diameter aperture is used to transmit one of the shorter wavelengths, then thermal blooming losses become quite small, as shown in Figure V-16, where relative power is plotted as a function of laser power for the wavelengths $\lambda = 3.8 \mu\text{m}$ and $5.0 \mu\text{m}$, and aperture diameter 4.13 m. Both wavelengths perform well out to at least 50° zenith angles with this size aperture.

Recent experimental and theoretical analyses indicate that some compensation for thermal blooming can be achieved with the use of adaptive optics. The most commonly used adaptive technique is to measure the phase of the wavefront returned from the target and to retransmit the phase conjugate. There are several different techniques available for measuring the phase of the returned wavefront. These generally include the use of a Hartmann wavefront sensor, a Shearing interferometer wavefront sensor, or a heterodyne detector array. Another technique, called "multi-dither," tags the outgoing wave with a multitude of dither frequencies and uses a "hill-climbing" servo to maximize the power reflected from the target. The outgoing wave algorithm is very costly to simulate with a high speed digital computer, and was not studied for that reason. However, for vertical transmission, we believe that the performance of outgoing and return wave systems will be very similar.

The degree of compensation of thermal blooming phase error possible with the use of adaptive optics was calculated by computer simulation of a return wave adaptive optical system. The phase of the wave returned from an on-axis point reflector is measured across each element of the array. Then the displacement and tilt of each element of the array is adjusted to

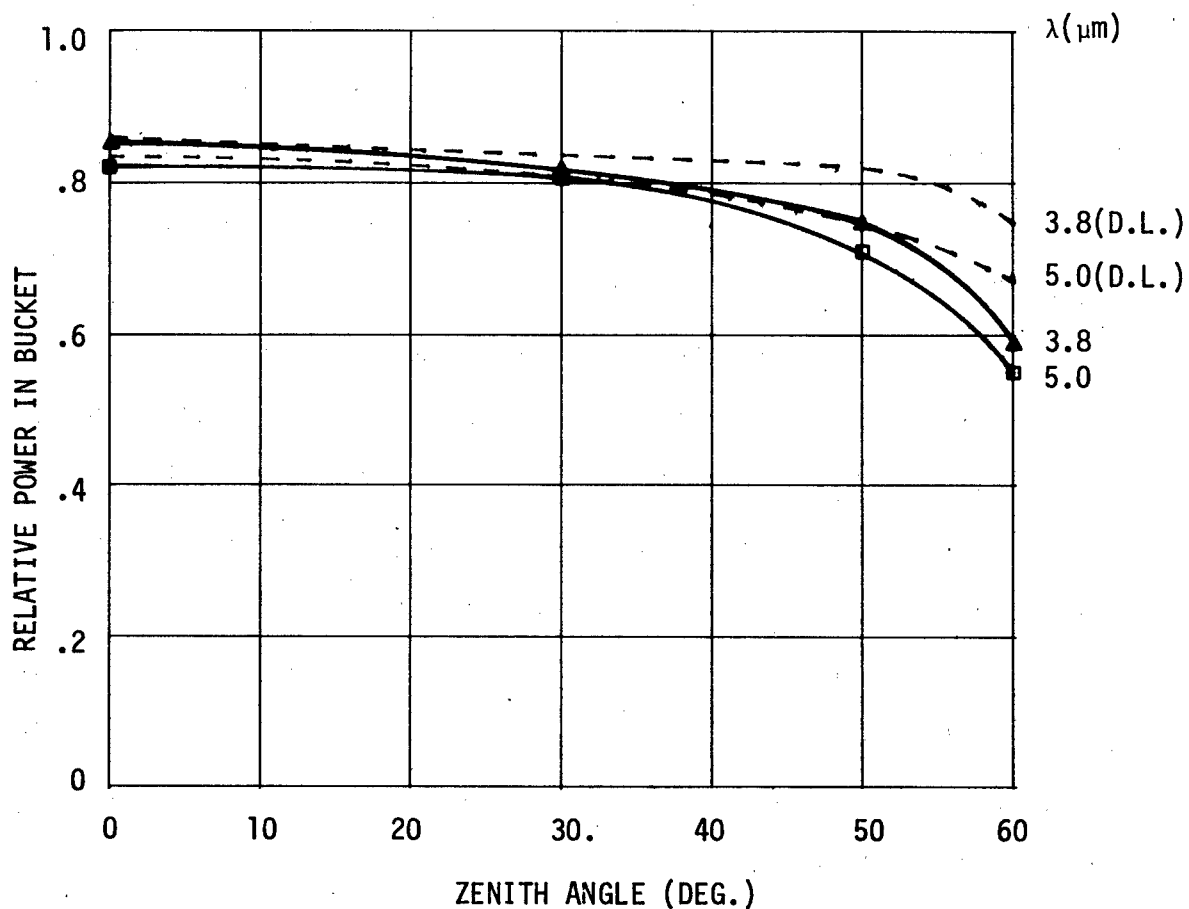


Figure V-16. Relative Power Collected in a 2 m Diameter Bucket vs Zenith Angle. Wavelengths $\lambda = 5.0$ and $3.8 \mu\text{m}$. For these data the transmitted power was 5 MW, the transmitter antenna elevation was 3.5 km, and the major array diameter was held constant at 4.13 m, providing better performance for the shorter wavelength propagation. The dashed curves indicate diffraction limited performance.

best fit the negative of the phase weighted by the intensity. Weighting the phase value by the intensity is equivalent to the operation of a Hartmann sensor or a Shearing interferometer sensor. The new phase front is then propagated through a new series of phase distorting screens calculated from the laser intensity at the screen positions and the previously calculated atmospheric parameters. Figure V-17 shows a plot of the compensated far field intensity of a 2 MW 10.6 μm laser beam propagated from a ground site at 10 m elevation to a satellite directly overhead at an altitude of 185 km. Figure V-18 shows a similar plot for a 5 MW laser beam. These plots should be compared with the uncompensated beam intensities previously shown in Figure V-11. For the 2 MW case, the power in a 2 m diameter bucket, centered on the peak intensity, has increased from 0.96 MW to 1.08 MW. This compares with 1.36 MW for a diffraction limited beam. At 5 MW, the power in a bucket increases from 0.89 MW uncompensated to 1.08 MW compensated, compared to 3.4 MW for a diffraction limited beam. Note that at both the 2 and 5 MW power levels, the correction for overall phase tilt error is excellent, but the correction for higher order aberration is poor. The reason is that displacement and tilt adjustment only of each element is inadequate to properly match the required phase front. Figure V-19, which is a plot of the phase distribution of the received wave for the 5 MW case, shows that there is a good deal of high spatial frequency phase error. Figure V-20 shows the phase distribution of the seven element array that best matches the received phase front. Clearly, the higher order phase errors are poorly matched. To better appreciate the magnitude of this mismatch error, a plot is shown in Figure V-21 of the required phase and the array phase in a direction normal to the wind vector and passing through the optical axis. The phase

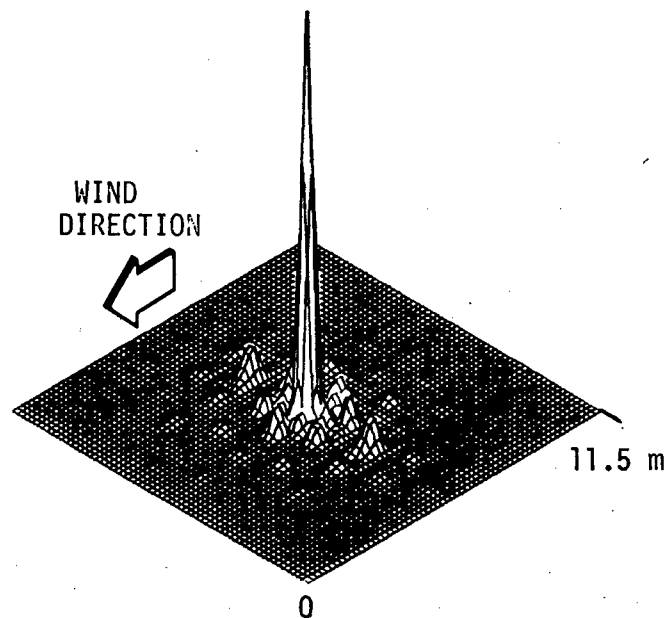


Figure V-17. Target Plane Plot of Adaptively Compensated 2-MW $10.6 \mu\text{m}$ Laser Beam. For this event the seven-element hexagonal transmitter array was at an elevation of 10 m, the major diameter of the array was 4.8 m, and the propagation direction was directly vertical ($\theta_z = 0^\circ$). The adaption process used both piston and tilt motion of each element in the array.

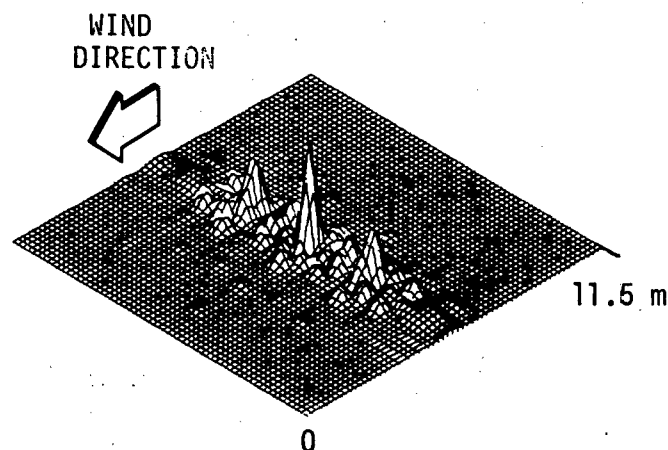


Figure V-18. Target Plane Plot of Adaptively Compensated 5-MW $10.6 \mu\text{m}$ Laser Beam. (Comments for this figure are the same as for Figure V-17.)

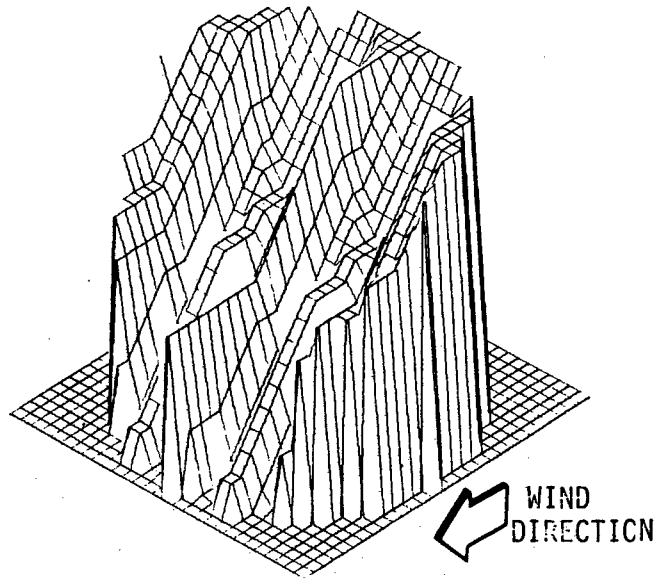


Figure V-19. Distribution of Phase in the Receiver Plane for Wavefront Returned from Target. Here the transmitted power was 5 MW, the transmitter elevation was 10 m, the overall array diameter was 4.8 m, and the direction of propagation was along the zenith.

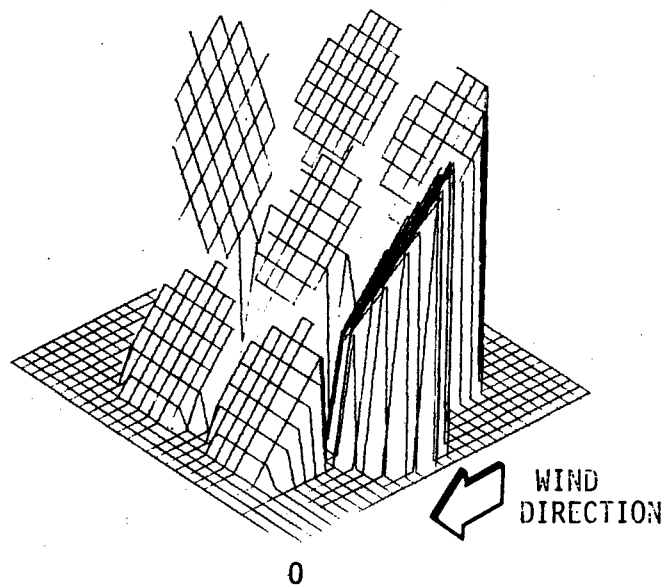


Figure V-20. Seven-Element Array Adaption Phase Distribution. Phase distribution of seven-element array that best fits the received wavefront phase distribution, shown in Figure V-19, with piston and tilt phase correction for each element.

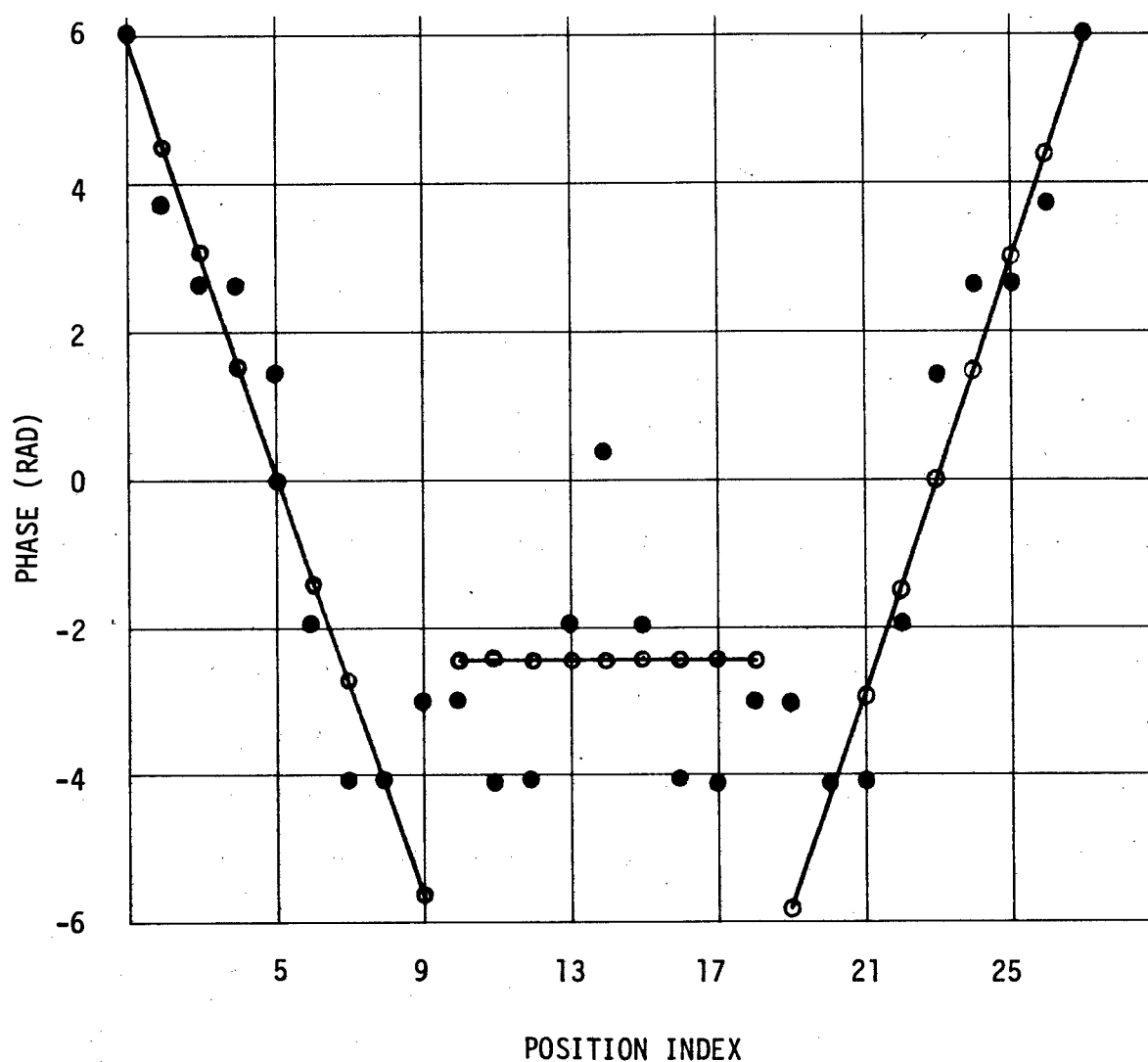


Figure V-21. Comparison of Received Phase (●) and Best Fit Mirror Surfaces (—) for a Line of Data Points Passing Through the Center of the Array Perpendicular to Wind Velocity Vector. Large discrepancy between received wavefront shape and best array element fit limits compensation for thermal blooming.

variance calculated from the mismatch error over the entire seven element array is 1.26 rad. Using the Strehl approximation

$$I/I_0 = \exp (- \phi_{\text{rms}}^2)$$

to estimate the expected loss of on-axis intensity due to residual phase error gives 0.206 for the expected ratio of compensated to diffraction limited peak intensity. This compares quite favorably with the actual value of 0.203. Higher order phase errors can be corrected by a deformable mirror. Using a perfect deformable mirror, i.e., one with unlimited spatial frequency response in each control circuit, yields the adapted beam profile shown in Figure V-22. The peak intensity of the compensated beam is 1.48 kw/cm², which is only about 2% less than the diffraction limit. Table V-2 summarizes the results of the adaptive optics computations at wavelength 10.6 μm , ground base elevation 10 m, zenith angle 0°, and aperture 4.8 m. It shows that near diffraction limited performance is obtainable at any power level up to at least 5 MW if sufficient spatial frequency response of deformable mirrors is available. Similar results were obtained at wavelength 9.1 μm , and they are summarized in Table V-3.

These results contrast sharply with the results obtained by other researchers⁴ for horizontal propagation. Even with perfect phase matching of the transmitted to received wavefronts, the degree of beam quality improvement is quite limited for horizontal propagation. The reason for this difference is that with vertical propagation, most of the phase error occurs near the transmitter, where it is easier to correct.

At the elevated (3500 m) site, the use of adaptive optics may reduce the requirement for large optics, particularly at the shorter wavelengths. To

Table V-2

Compensation of Thermal Blooming

($\lambda = 10.6 \mu\text{m}$, July model, $H = 10 \text{ m}$, $\theta_z = 0^\circ$, $D = 4.8 \text{ m}$)

Transmitter Power (MW)	1	2	5
Peak Intensity (W/cm ²)			
Diffraction Limit	301	603	1507
Uncompensated	208	220	274
Displ. and Tilt Compensation Only	282	462	306
Perfect Deformable Mirror	-	-	1485
Peak Power in Bucket (MW)			
Diffraction Limit	.69	1.38	3.44
Uncompensated	.64	.96	.88
Displ. and Tilt Compensation Only	.65	1.08	1.08
Perfect Deformable Mirror	-	-	3.39
On-Axis Power in Bucket (MW)			
Diffraction Limit	.69	1.38	3.44
Uncompensated	.63	.76	.05
Displ. and Tilt Compensation Only	.65	1.08	1.08
Perfect Deformable Mirror	-	-	3.39
Residual Phase Error Variance (rad ²)	.082	.263	1.58
Strehl Ratio	.935	.769	.206
Ratio of Compensated to Diffraction Limited Beam Peak Intensities	.937	.766	.203

Table V-3

Compensation of Thermal Blooming

($\lambda = 9.1 \mu\text{m}$, July Model, $H = 10 \text{ m}$, $\theta_z = 0^\circ$, $D = 4.1 \text{ m}$)

Transmitter Power (MW)	1	2	5
Peak Intensity (W/cm^2)			
Diffraction Limit	302	603	1510
Uncompensated	216	220	190
Displ. and Tilt Compensation Only	278	462	221
Perfect Deformable Mirror	-	-	1469
Peak Power in Bucket (MW)			
Diffraction Limit	.68	1.38	3.42
Uncompensated	.61	.96	.72
Displ. and Tilt Compensation Only	.63	1.08	.89
Perfect Deformable Mirror	-	-	3.34
On-Axis Power in Bucket (MW)			
Diffraction Limit	.68	1.38	3.42
Uncompensated	.59	.76	.04
Displ. and Tilt Compensation Only	.63	1.08	.89
Perfect Deformable Mirror	-	-	3.34
Residual Phase Error Variance (rad^2)	.082	.263	1.90
Strehl Ratio	.921	.769	.149
Ratio of Compensated to Diffraction Limited Beam Peak Intensities	.921	.766	.146

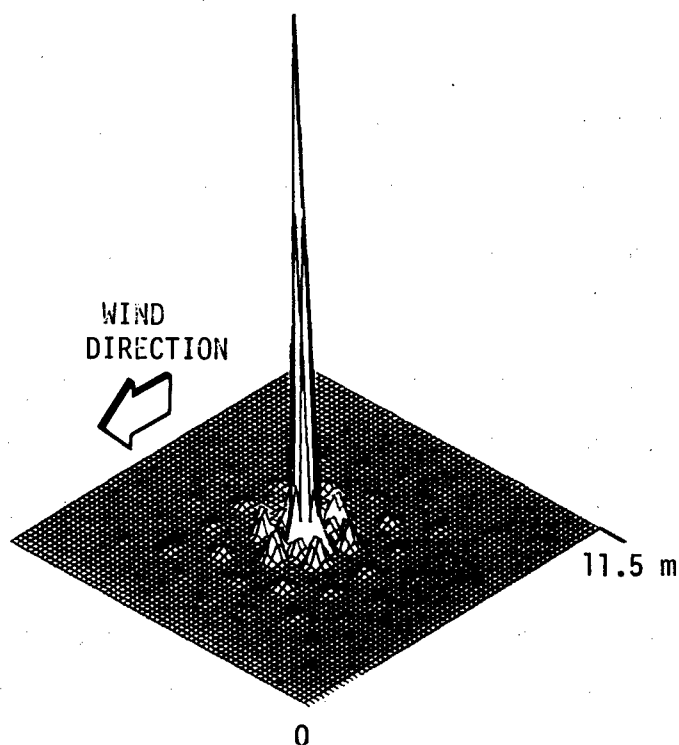


Figure V-22. Target Plane Intensity Distribution for Adaption Using Deformable Mirrors of Unlimited Spatial Frequency Response in Each of the Seven Channels of the Transmitter Array. These data are calculated for $\lambda = 10.6 \mu\text{m}$ with the transmitter antenna at an elevation of 10 m, an overall array diameter of 4.8 m and the direction of propagation along the zenith.

illustrate the improvement possible with the use of adaptive optics at this elevation, particularly at large zenith angles, we chose to study the $10.6\text{ }\mu\text{m}$ system, for two reasons: (1) kinetic cooling effects are of interest, and (2) the far field spot sizes of the shorter wavelengths are inconvenient to work with in the computer. The effects of kinetic cooling on a 4.8 m diameter seven-element array of phase locked lasers of total power 5 MW, transmitted from a ground station at 3.5 km elevation to a satellite at 60° zenith angle, is shown in Figure V-23. The power intercepted by a 2 m diameter bucket is 1.7 MW compared to the diffraction limit of 3.0 MW. By adjusting the displacement and tilt of each element of the array for best fit to the conjugate of the received phase, the power on target of the adapted beam shown in Figure V-24 is 2.3 MW, a significant improvement over the 1.7 MW figure for the uncompensated beam. As in the thermal blooming (heating) situation, the reason for the lack of better compensation is the residual mismatch phase error of the seven-element array. The computed residual error variance is 0.272 rad^2 , and the Strehl ratio is 0.762. This is in good agreement with the ratio of peak intensities of the compensated and diffraction limited beams, which is 0.754. If deformable mirrors of unlimited spatial frequency response are used in each channel, then the compensation is nearly perfect. Figure V-25 shows the adapted beam shape for that case. The power in a bucket is computed to be 2% larger than the 3.0 MW diffraction limit. Apparently, the effects of transmission in the kinetic cooling case act to give slightly better than diffraction limited performance.

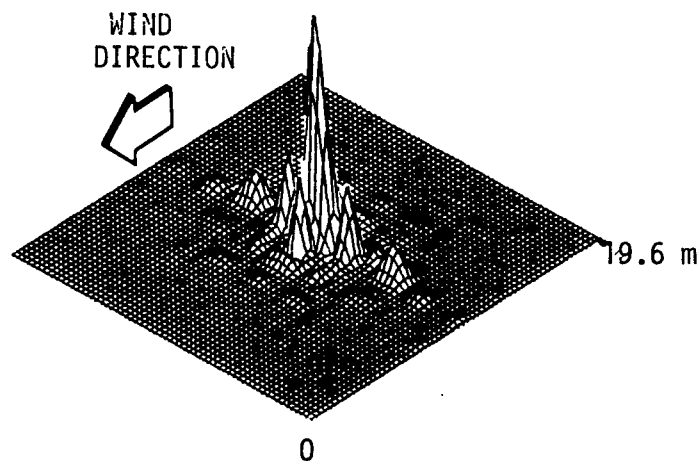


Figure V-23. Thermally Bloomed $10.6 \mu\text{m}$ CO_2 Laser Beam Profile, Including Kinetic Cooling Effects. These data were calculated considering the seven-element transmitter array at an elevation of 3.5 km (mountain top), a transmitted power of 5 MW, a major array diameter of 4.8 m, and a direction of propagation that was 60° from the zenith.

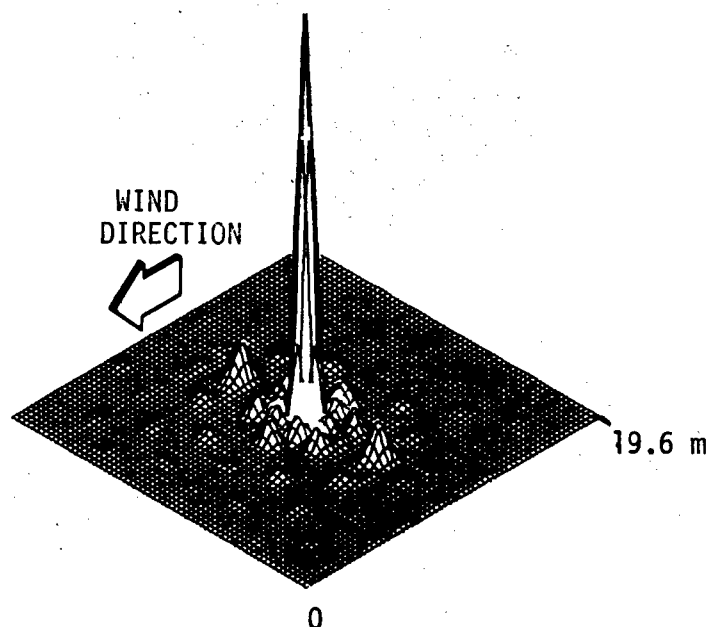


Figure V-24. Thermal Blooming Correction With Piston and Tilt Phase Compensation Only. Here phase and phase gradient (piston and tilt) compensation has been applied to correct for the thermal blooming shown in Figure V-23. (Additional comments are the same as for Figure V-23.)

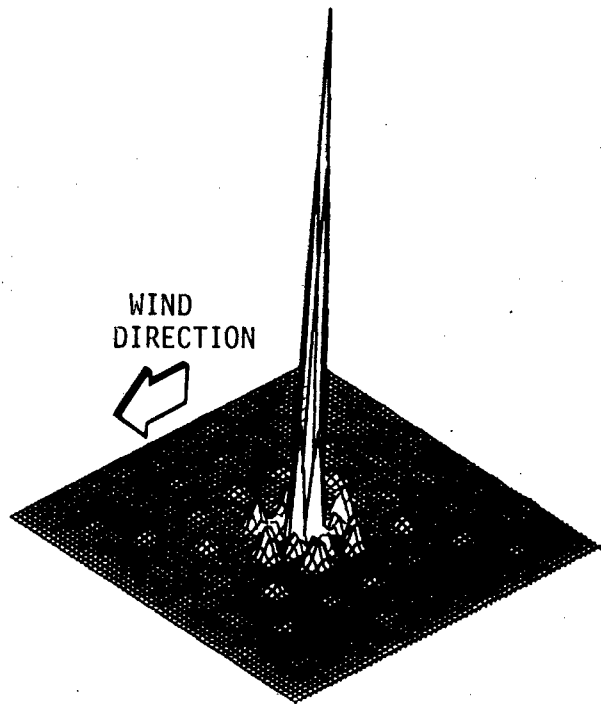


Figure V-25. Thermal Blooming Correction when all Orders of Compensation are Applied. For these calculations deformable mirrors with very high spatial frequency response were added to each channel of the seven-element array to correct for the thermal blooming shown in Figure V-23. (Additional comments are the same as for Figure V-23.)

Conclusions

Thermal blooming effects on transmission of power from a ground site at elevation 10 m to an orbital satellite are severe at all wavelengths and power levels of interest. Good compensation can be provided with adaptive optics, but the loss of power due to absorption is still a problem, particularly for the 10.6 μm wavelength. Power loss due to thermal blooming is considerably less for a transmitter at 3.5 km elevation, and can be almost completely eliminated with the use of adaptive optics. Adaptive optics are particularly attractive at the higher elevation, because it permits the use of smaller apertures in conjunction with shorter wavelength transmitters.

References

1. F. G. Gebhardt and D. C. Smith, "Self-Induced Thermal Distortion in the Near-Field for a Laser Beam in a Moving Medium," IEEE J. Quantum Electronics, Vol. QE-7, No. 2, February 1971.
2. C. B. Hogge, "A Comparison of Several High Energy Laser Systems with Emphasis on the Propagation Aspects," Laser Digest, AFWL-TR-75-140, Air Force Weapons Laboratory, Kirtland AFB, NM, May 1975.
3. R. W. Davis and L. N. Peckham, "A Simplified Propagation Model for Laser System Studies," AFWL-TR-72-95 (Rev.) Suppl., Air Force Weapons Laboratory, Kirtland AFB, NM, November 1974.
4. Handbook of Geophysics, revised edition, U.S. Air Force, MacMillan, New York (1960).

VI. SYSTEM CONCEPT GENERATION

In an effort to select the most applicable high energy laser adaptive system for ground-to-space power transmission, an assessment of existing adaptive phasing techniques was made, including the hardware concepts and control algorithms. These techniques were then incorporated into four separate system concepts, each having some different advantages and disadvantages. When the four concepts were completed, the systems were evaluated based on (1) overall efficiency, (2) reliability, (3) size and weight, (4) technology advancement requirement, and (5) potential cost. These data were then used as the basis for the selection of a single concept to perform a more detailed conceptual design.

For this task, the four system concepts generated were titled:

1. Coelostat Hartmann System
2. Modified Multidither Receiver
3. Multiaperture MOPA System, and
4. Multiple Source Phased Array.

In the sections to follow, we will give a brief description of each concept and then present the results of the system evaluations.

A. System Concepts

1. Coelostat Hartmann System

In this concept, and with the others to follow, we have assumed that the range, velocity, and location of the satellite as functions of time are known well enough to accommodate the initial target acquisition. Since these parameters can be calculated from ephemeris data, with this concept the satellite can be tracked with the relatively slow-moving coelostat mirrors

of the system itself. If we consider that with advanced tracking systems such as the Global Positioning System (GPS), which is to be operational in the near future, that the location of the satellite can be determined to within an uncertainty of much less than 25 meters in radius. Thus, acquisition of the target can be accomplished by spreading the laser beam and observing the return signal from a small corner cube reflector mounted on the satellite.

A block diagram of the Coelostat Hartmann system is shown in Figure VI-1. Prior to transmission, the HEL output is made to pass through the clean-up components. The beam is monitored with a Hartmann sensor which also controls the clean-up components. Similarly, the return wavefront from a 10-cm corner reflector mounted on the satellite collector is sensed by the other Hartmann sensor which, in turn, feeds signals to the adaptive control components to initiate target adaption. An optical schematic of the system is depicted in Figure VI-2. The clean-up components are a beam expander for focus control #1, two-axis tilt mirror #1, and a deformable mirror #1. The adaptive components for atmospheric correction are focus control #2 (output beam expander), two-axis tilt mirror #2, and deformable mirror #2. For either clean-up or target adaption, the tilt mirror and focus control are used for lower order phase correction and the deformable mirror for higher order phase corrections. In order to limit the main lobe of the laser radiation to 2 meters in diameter at the satellite over the entire encounter and to reduce the effects of thermal blooming, an overall transmitter diameter of 4.8 m was used on this concept, as well as the remaining three. This requires that the Coelostat mirrors be at least about 7 meters in diameter. It is expected that the Coelostat mirrors will be driven with torque motors. Figure VI-3 shows the relative dimensions of the output beam, the Coelostat mirrors and the torque motor assembly that

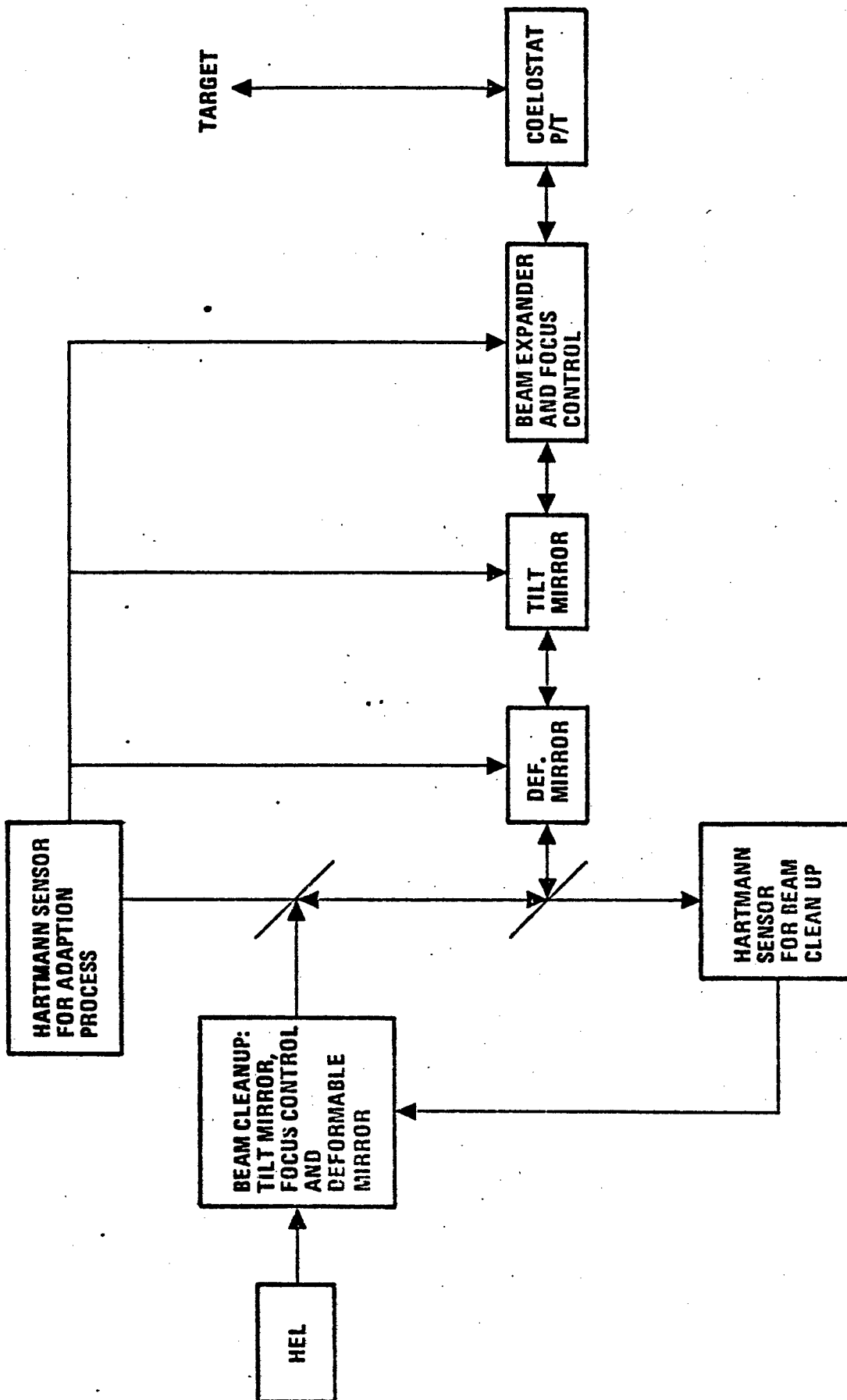


Figure VI-1. Block Diagram of a Coelostat Hartmann Sensor

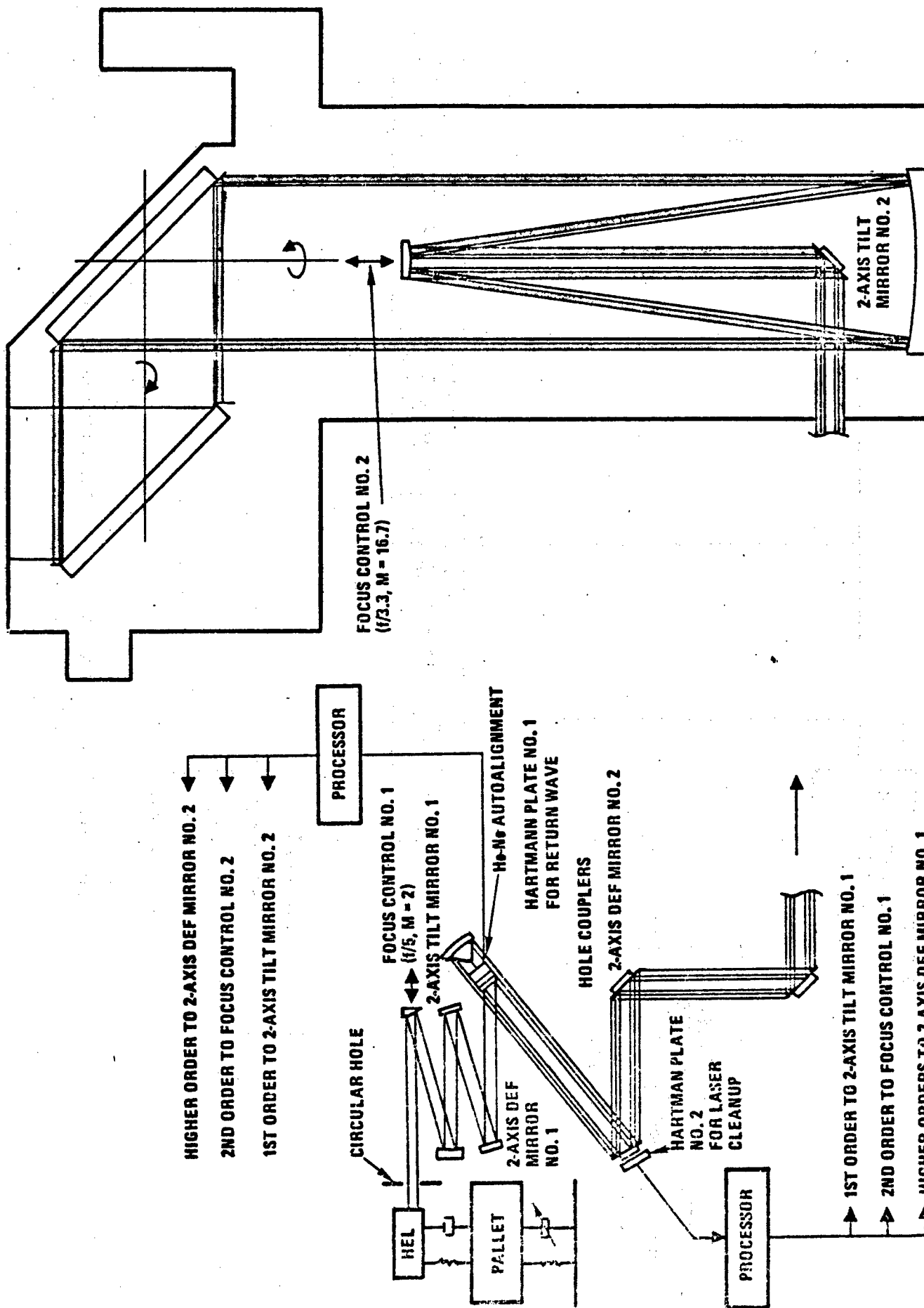
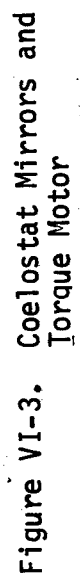


Figure VI-2. Coelostat Hartmann Sensor



may be required. For auto-alignment, a HeNe ring with retro-reflectors mounted on the exit Coelostat mirror is used. For this auto-alignment scheme to function properly, there should be no relative displacement between the hole couplers and, consequently, they must be rigidly connected.

The novelty of the present system is the use of Hartmann sensors for wavefront detection. Referring to Figure VI-4, the Hartmann sensor is basically a hole coupler which allows the average wavefront tilt across each hole to be determined. For sufficiently small hole spacing, the incident wavefront can be reconstructed from the tilt information by curve fitting. The tilt at each hole can be found from measuring the centroid displacement of that portion of the beam passing through the hole. The centroid displacement can be readily measured with state-of-the-art quadrant detectors.

The reliability of the present system depends very much upon the ability to correctly sense the signal from the corner reflector in the presence of noise. A simple analysis for the worst case would show that the signal-to-noise (S/N) associated with the present configuration is given approximately by

$$S/N \approx \left(\frac{D^*}{\sqrt{AB}} \right) \left(\frac{\epsilon_T P_L}{\pi d_s^2/4} \right) \left(\frac{\pi d_c^2}{4} \right) \left(\frac{\delta}{D_B} \right)^2 \quad (1)$$

where ϵ_T is the 2-way transmission efficiency, P_L is the laser power, d_s is the spot diameter at the corner cube with diameter d_c , δ is the hole diameter, D_B is the beam diameter at the hole coupler, and the quantity \sqrt{AB}/D^* is the noise equivalent power which is a function of the detector parameters. Using typical parameter values, S/N as a function of d_s for laser power 0.5 MW and 5 MW is shown in Figure VI-5. We see that the resulting S/N should be more than adequate for the system to function properly. Additionally, we must consider the

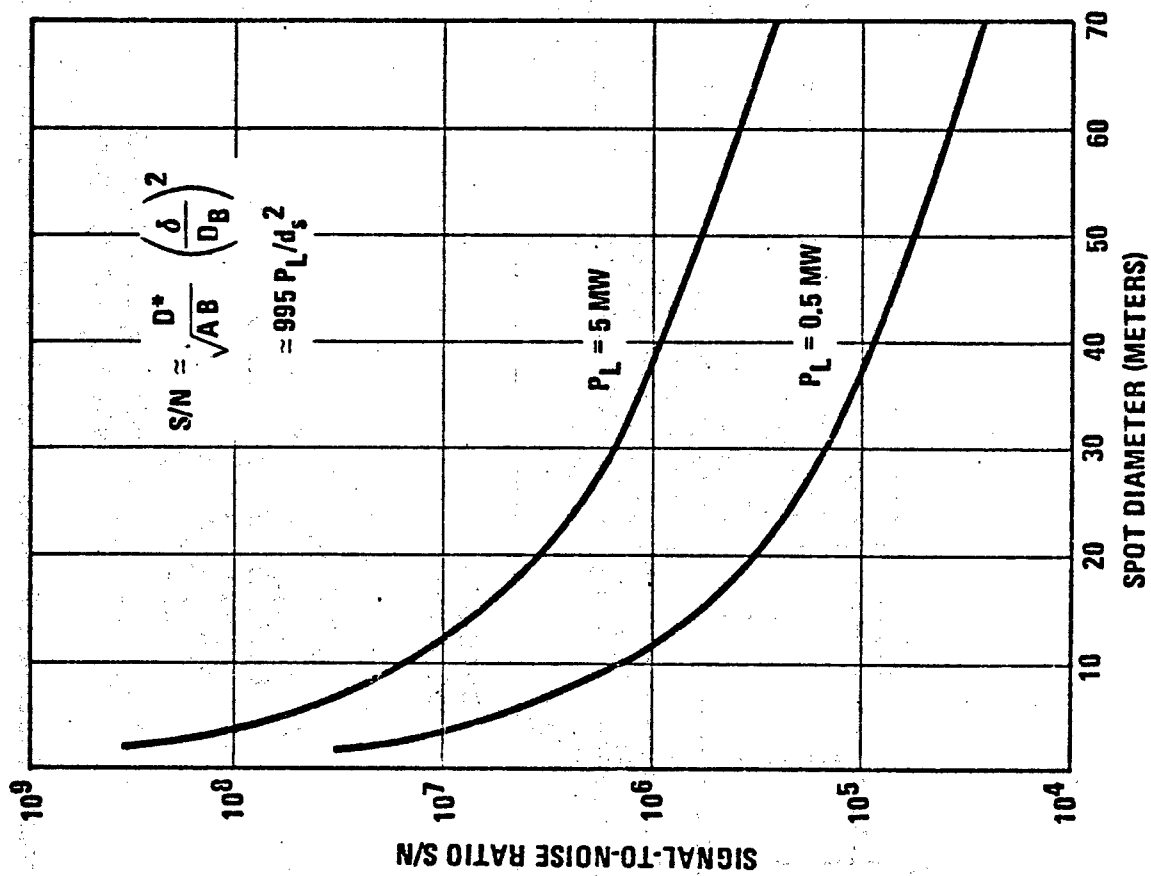


Figure VI-5. Signal-to-Noise Ratio vs Spot Diameter at Target

backscatter noise from components in the optical train. The backscatter power is Lambertian in nature and, to a good estimation, the signal to backscatter power ratio S/S_B is

$$S/S_B \approx \frac{P_S \left(\frac{S}{D_B}\right)^2}{\gamma P_L \sum_i^N \left(\frac{\delta}{2L_i}\right)^2}, \quad (2)$$

where P_S is the signal power, P_L is the laser power, δ is the hole diameter, D_B is the beam diameter at the hole coupler, γ is the surface reflection coefficient, and L_i is the separation between the i^{th} optical component and the hole coupler. For $\delta \sim 1$ MM, $D_B \sim 50$ CM, and $\gamma \sim 10^{-4}$, we find that S/S_B as a function of d_s is that given in Figure VI-6. We see that the signal power is significantly greater than the backscatter power, and therefore backscatter radiation should not be a serious problem.

The present concept is relatively simple, and its implementation is straightforward, but most likely costly because of the Coelostat. It requires neither an external tracking unit nor a movable telescope primary. However, it does require rather large Coelostat mirrors. Although the use of hole couplers is sound in principle, the details of its construction need to be investigated.

2. Modified Multidither Receiver

This system is similar to the first concept in that it makes use of data from the satellite trajectory history for the initial acquisition, but differs in two significant ways. First, an outgoing wave adaption concept is used, rather than a return wave approach. Consequently, it is not necessary to use a shared aperture configuration and the backscatter problem can be avoided. Second, with this concept the beam expansion telescope is mounted in the tracking mount, so that the expense of the two very large coelostat mirrors could be avoided.

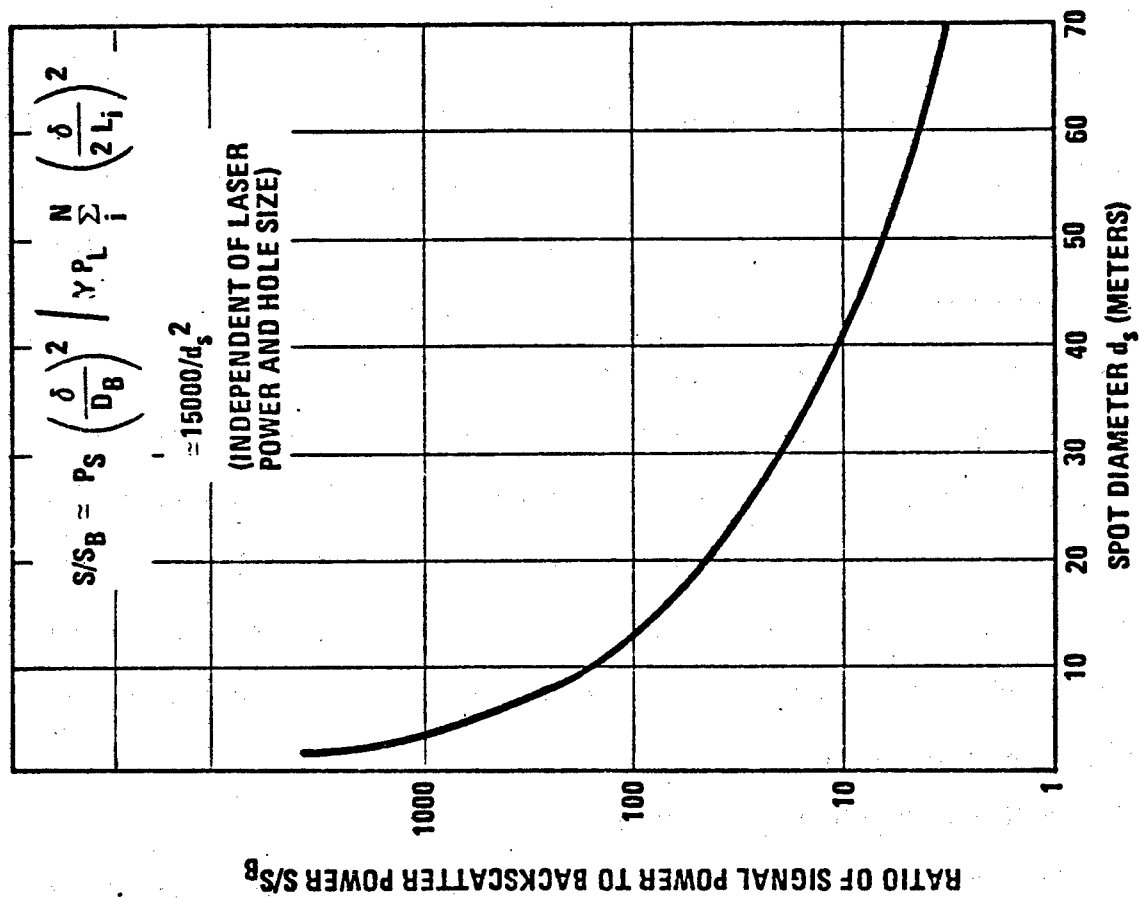


Figure VI-6. Signal Power to Backscatter Power from Reflective Components

The block diagram for this second system concept is shown in Figure VI-7. Here, as with the number one concept, the output of the HEL is directed through a set of beam "clean-up" optics to a beam sampler grating where a portion of the beam is extracted for wavefront analysis using a Hartmann sensor. The details of this optical circuit, which are similar to those used in the first concept, are shown in Figure VI-8b. Here, mirrors M_1 and M_2 are used for controlling beam tilt and translation, mirrors S_1 and P_1 make up a beam expansion telescope that also controls focus error, and DFM_1 is a deformable mirror which removes the higher order phase aberrations. To provide the control signals for these mirrors, the outgoing HEL beam is sampled, as shown in Figure VI-9, with a low efficiency grating and then analyzed using the Hartmann sensor and signal processor as shown. Following the outgoing beam from the beam sampler in Figure VI-7, it is next operated on by the phase dither and phase corrector mirrors. In Figure VI-8, these operations occur at mirrors DFM_2 and DFM_3 . The deformable mirror DFM_2 is used to introduce the dither frequencies on the HEL beam and the second deformable DFM_3 is used for higher order phase corrections. After this pair of deformable mirrors, the beam is directed up through the tracking mount gimbals to a set of tilt correction mirrors, M_6 and M_7 , and then through a beam expansion telescope (mirrors S_2 and P_2) used for focus correction and then out of the final beam expansion telescope toward the satellite. The signal reflected from the corner reflector located at the satellite collector is detected by a receiver mounted on the output telescope (see Figure VI-8). The signal from this receiver, along with the satellite range data, is directed to the multidither processor, as shown in Figure VI-10, where the adaptive changes are calculated and the tilt errors, focus error, and higher order phase correction signals are directed to the appro-

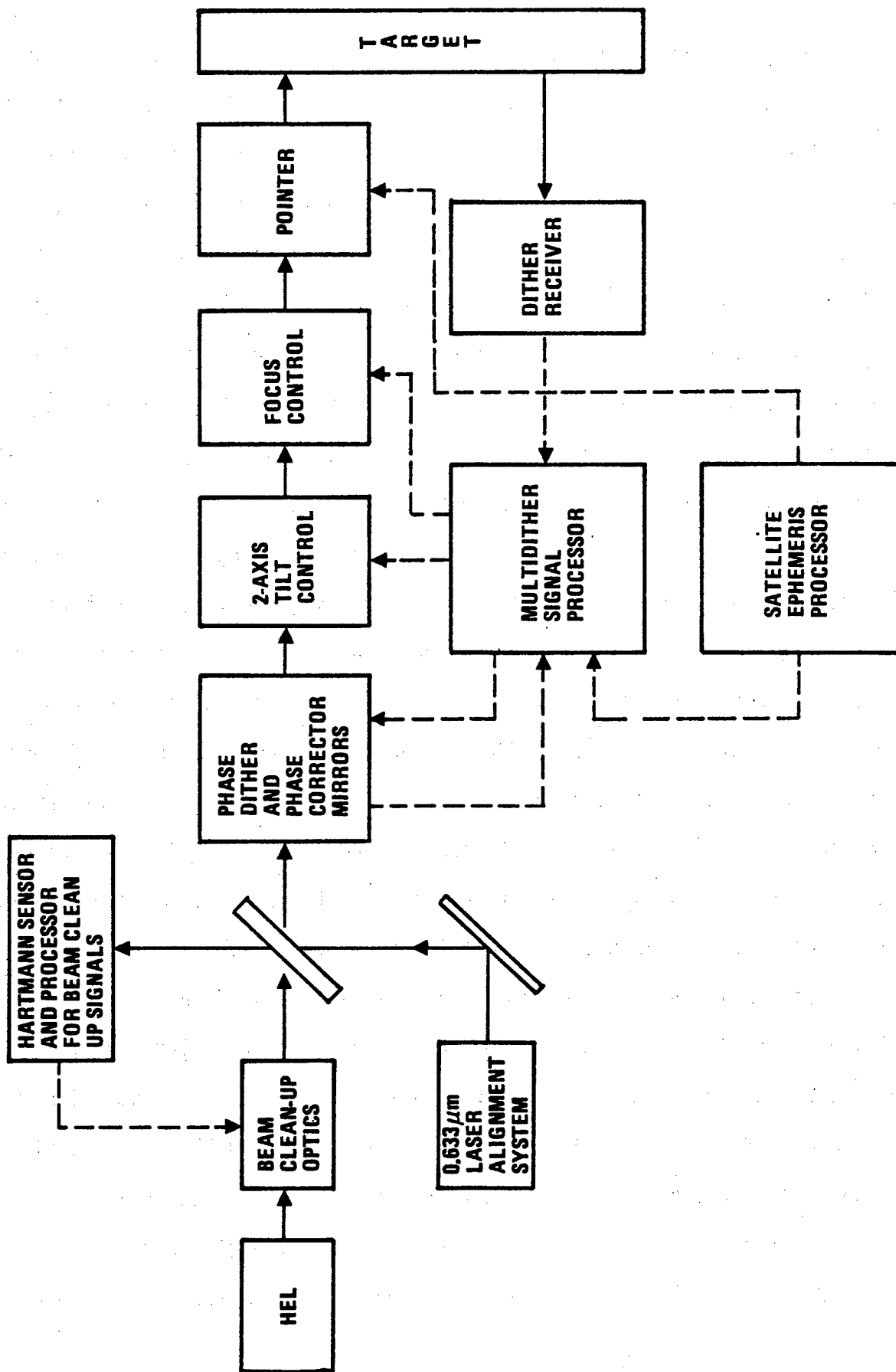
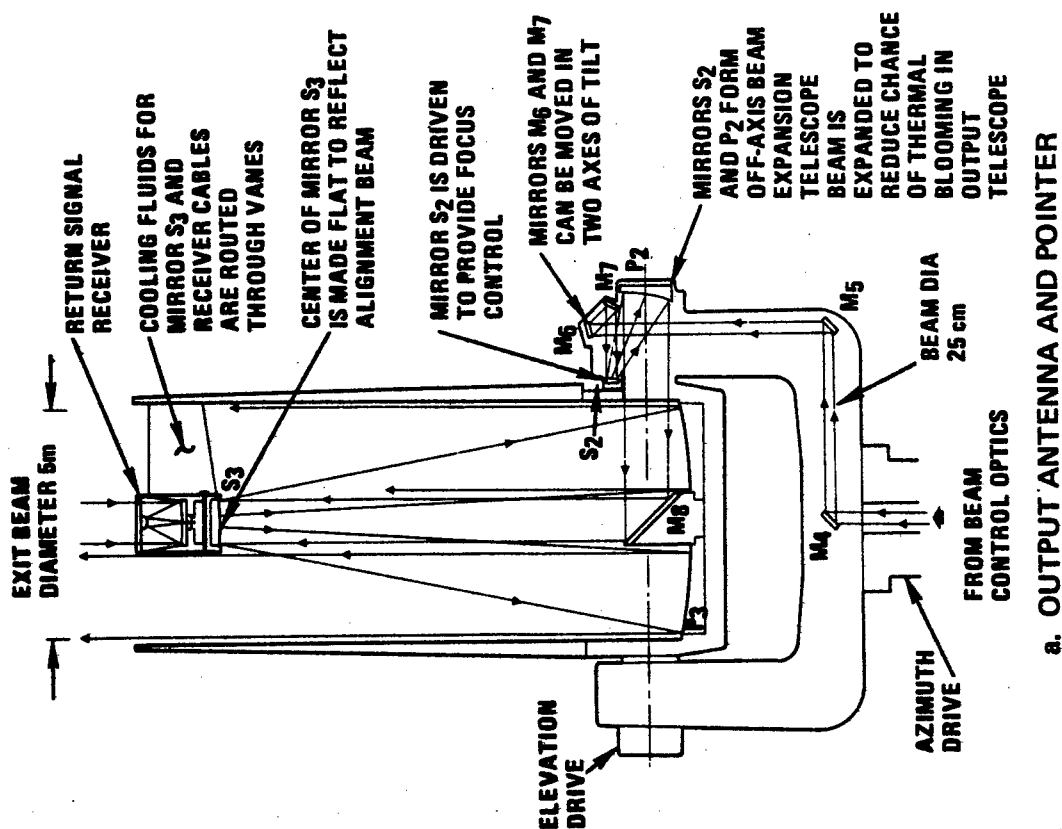
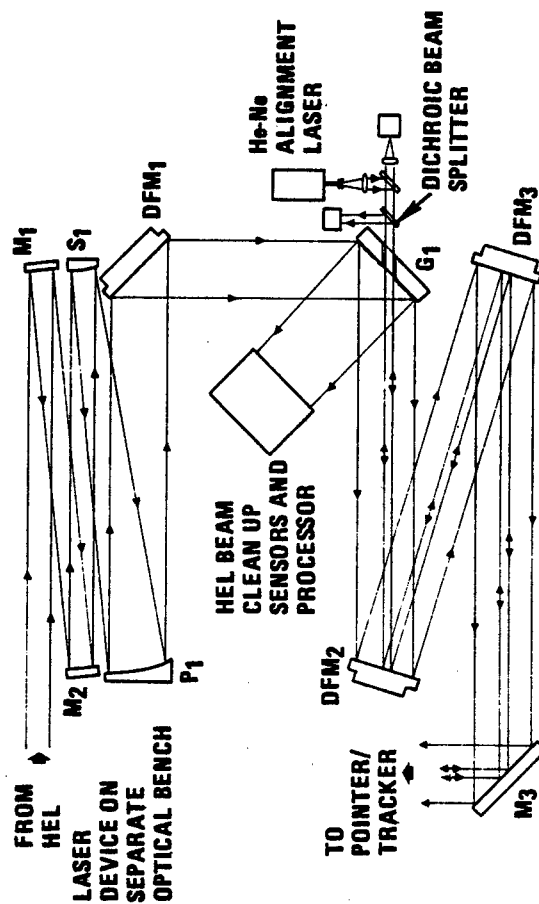


Figure VI-7. Block Diagram of Modified Multidither Concept



a. OUTPUT ANTENNA AND POINTER



b. BEAM CONTROL OPTICS

MOUNTED ON OPTICAL BENCH WITH DRY GAS FLOWING PERPENDICULAR TO PLANE OF OPTICAL CIRCUIT TO REDUCE THERMAL BLOOMING

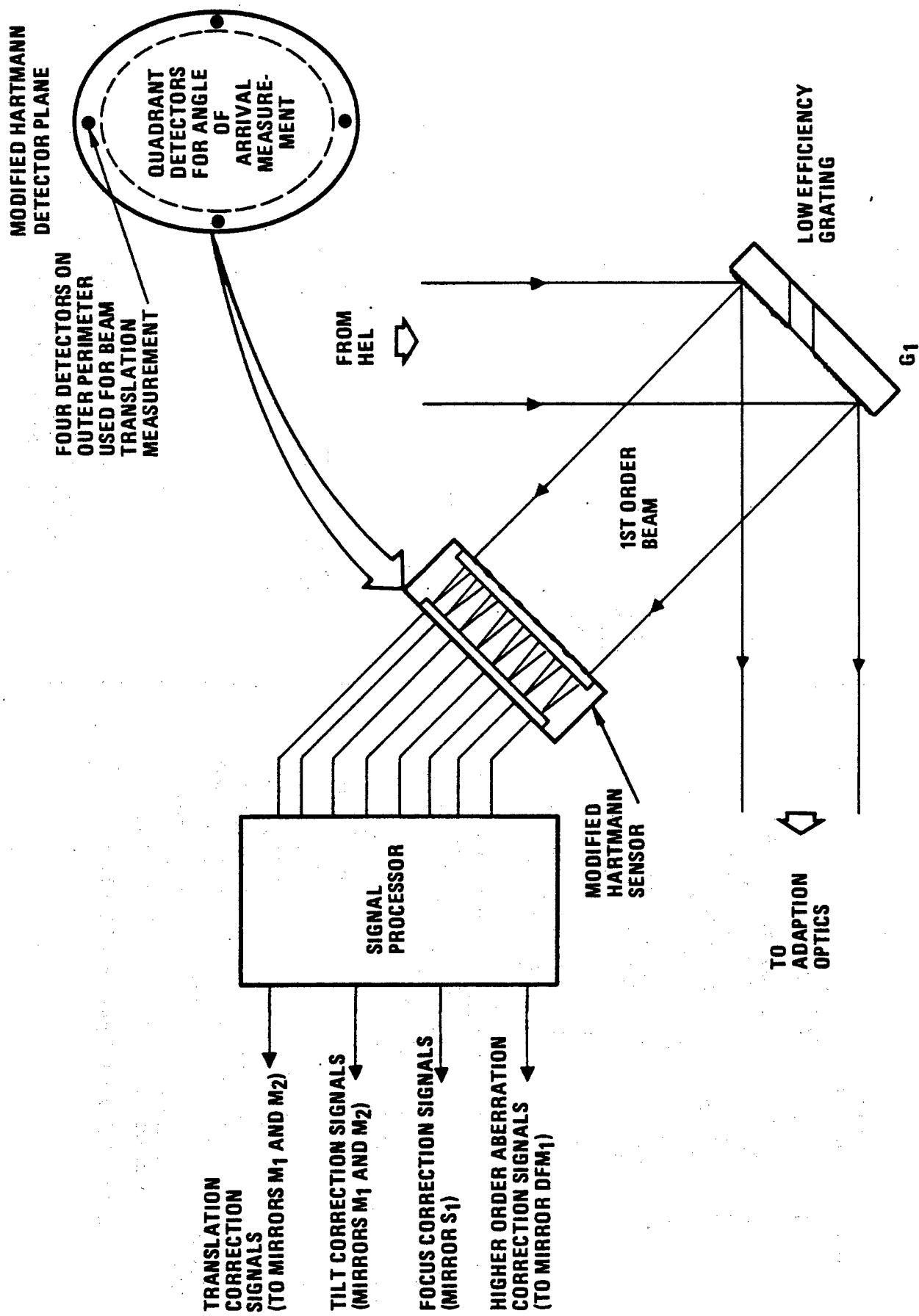


Figure VI-9. Beam Clean Up Sensors and Processors for Multither Concept

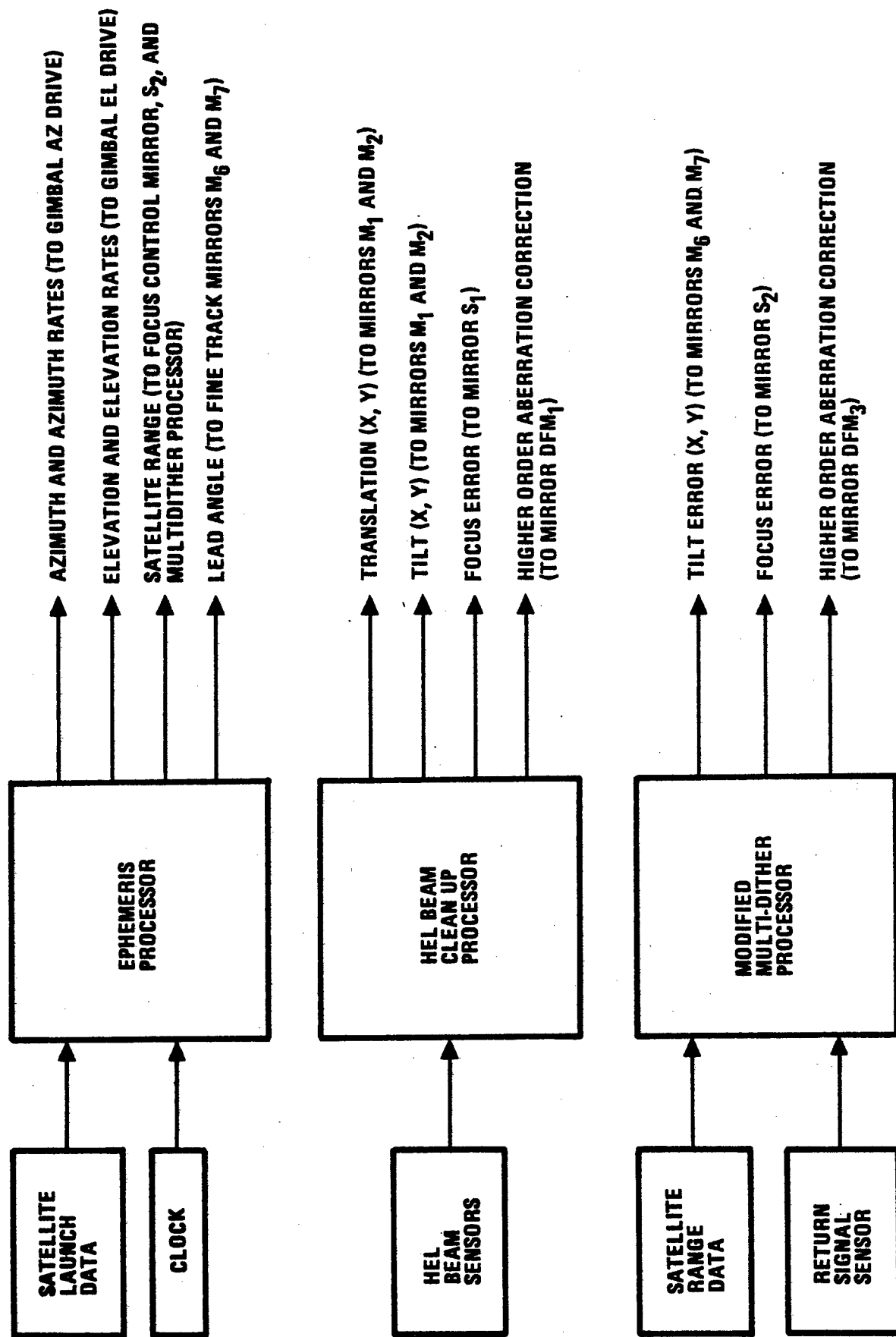


Figure VI-10. Multidither Concept Information Processors

priate mirrors. In Figure VI-11, we have shown the details of the multi-dither processor. Here, we are using a set of oscillators to produce dither signals at DFM_2 in a zonal fashion. We have selected this approach rather than modal dither, so that very narrow bandwidth mirror actuators could be used. However, in an effort to reduce the magnitude of the phase corrections necessary at DFM_3 , the correction signals out of the synchronous demodulator are used to calculate modal correction signals so that the tilt and focus errors can be compensated for separately. Because of the target distance, the optical transit time delay can result in significant errors in the correction signals that are introduced to the processor. Therefore, the target range data are used to calculate the proper compensation for each of the dither channels.

As might be expected, without the backscatter problem, this concept enjoys good signal to noise, even for the worst conditions. If, as has been stated, the acquisition process begins when the satellite is 60° from the zenith and the transmitted beam is spread to a diameter of about 50 meters in the target plane, the signal collected for a single channel can be written as

$$S_C = P_T \left(\frac{m}{N} \right) \left(\frac{d_{cr}^2 d_r}{50 R \lambda} \right)^2 \epsilon_a \epsilon_t \epsilon_r, \quad (3)$$

where P_T is the laser output power

m is the dither modulation index ($\sim .05$)

N is the number of dither channels (19)

d_{cr} is the diameter of the corner reflector (.1 m)

d_r is the dither receiver diameter (1 m)

R is the maximum target range (370 km)

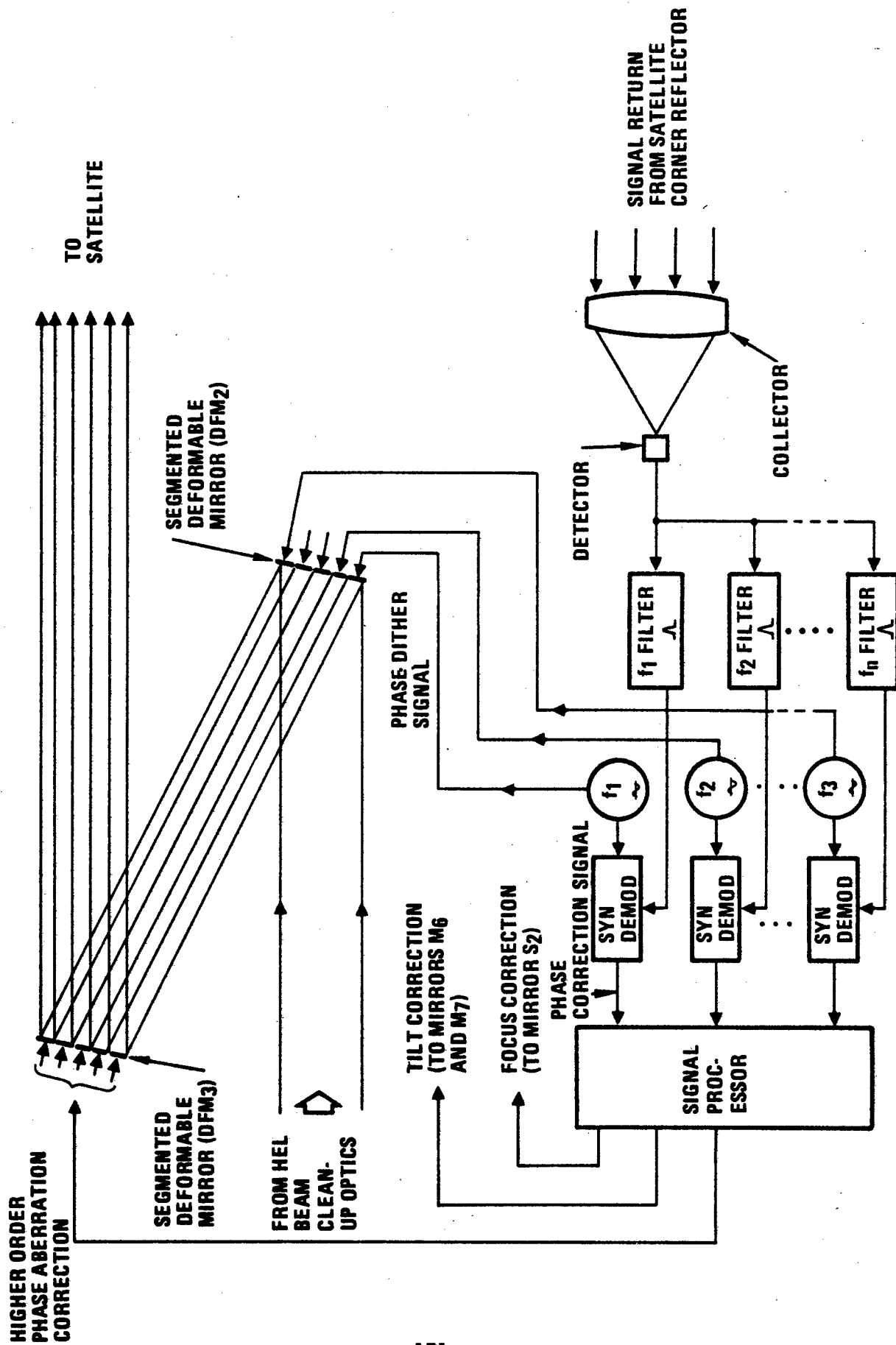


Figure VI-11. Multidither Adaption Processor

λ is the optical wavelength (1.06×10^{-5} m)

ϵ_a is the atmospheric transmission (worst condition $\sim .2$)

ϵ_t is transmitter optical circuitry efficiency ($> .7$)

ϵ_r is the receiver optical circuit efficiency ($> .9$)

Using these values the signal collected at target acquisition is

$$S_C(\text{ACQ}) = P_T 1.72 \times 10^{-13} \text{ watts.}$$

Since this is a direct detection process, the signal to noise can be written as

$$S/N = S_C D_\lambda^* / (A_d N \Delta f)^{1/2}, \quad (4)$$

where D_λ^* is the detector detectivity at λ ($2 \times 10^8 \text{ m sec}^{-1/2} \text{ watt}^{-1}$)

A_d is the detector area ($1 \times 10^{-7} \text{ m}^2$), and

Δf is the bandwidth of a single dither channel (100 Hz),

the acquisition signal to noise is

$$S/N(\text{ACQ}) \approx P_T 2.5 \times 10^{-3}.$$

For the lowest HEL power transmitted, 0.5 MW, the signal to noise is

$$S/N(\text{ACQ}) = 1.25 \times 10^3.$$

When the satellite has been acquired and tracking starts, the signal collected for a single dither channel can be expressed as

$$S_C = P_T \left(\frac{m}{N} \right) \left(\frac{d_{cr}}{\lambda R} \right)^4 \left(D_T d_r \right)^2 \epsilon_a^2 \epsilon_t \epsilon_r, \quad (5)$$

where D_T is the diameter of the transmitted beam (4.8 m). Under these

conditions, the signal to noise

$$S/N(\text{TRACK}) \approx 5.1 \times 10^6.$$

This concept, by using the outgoing wave adaption approach, provides a very straightforward system configuration. Since the transmitter and receiver optical circuits do not share a common aperture, the very severe backscatter problems are avoided and a simple direct detection receiver can be used with a rich signal to noise. With this concept, however, the tracking mount must handle a very large transmitter telescope at low-earth orbit tracking rates. Also, the processor is somewhat complex. There is an additional condition that must be considered when outgoing wave systems are used, and it has to do with the optical transit time. This condition can be stated as

$$\frac{.2 C}{R} > \Delta f \quad (6)$$

where C is the speed of light

R is the maximum satellite range, and

Δf is the adaption bandwidth requirement.

For the scenario investigated here, the adaption bandwidth requirement (atmospheric turbulence correction) was such that we can operate at the 370 km range, but this condition would soon limit the extension of the target range.

3. Multiaperture MOPA System

The multiaperture MOPA system conceptually is a substantial deviation from the first two concepts, although it uses several of the early features such as the acquisition techniques using ephemeris data. First, as the name implies, this concept uses a master oscillator power amplifier configuration.

Next, heterodyne detection is used for the phase measurements and, finally, to reduce somewhat the problem of a single large telescope, a multielement unit is used, but contained in the same tracking mount.

The multielement block diagram for a single channel is shown in Figure VI-12. For this concept, the output beam of the master oscillator is expanded so that it can be conveniently divided into six beams by an optical polygon. If we follow one of the beams, the next element is a grating beam sampler. At this point a portion of the beam is extracted for use as a local oscillator and is directed to a multi-detector wavefront analyzer. The output part of the beam reflected from the grating is then directed through two phase control operators, one for average phase and the other for phase structure control. In Figure VI-13, we show an optical schematic for this concept. Here, it can be seen that one phase control operator is a flat mirror, MM_1 that is moved back and forth for altering the average beam phase. The other is a deformable mirror, DFM_1 , for controlling the spatial structure of the beam phase. Both operators receive control signals from the wavefront analyzer and processor. From this point, the six beams are reassembled with another polygon and directed through the power amplifier. This reassembled beam is then directed up through the tracking mount, expanded to reduce the power density, and once again dissected into six beams and directed through six beam expansion telescopes. Before each of the beams is fed into the beam expanders, however, it is reflected from a mirror (see Figure VI-13) which has a small area of the surface that can be dithered in a conical angular scan. This is a technique developed at Rockwell called Subaperture Angle Dither, or SAND. Each of the outgoing beams is dithered at a different frequency and after the transmitted beam is reflected from the satellite corner reflector, the return dither signals are sensed by a receiver mounted

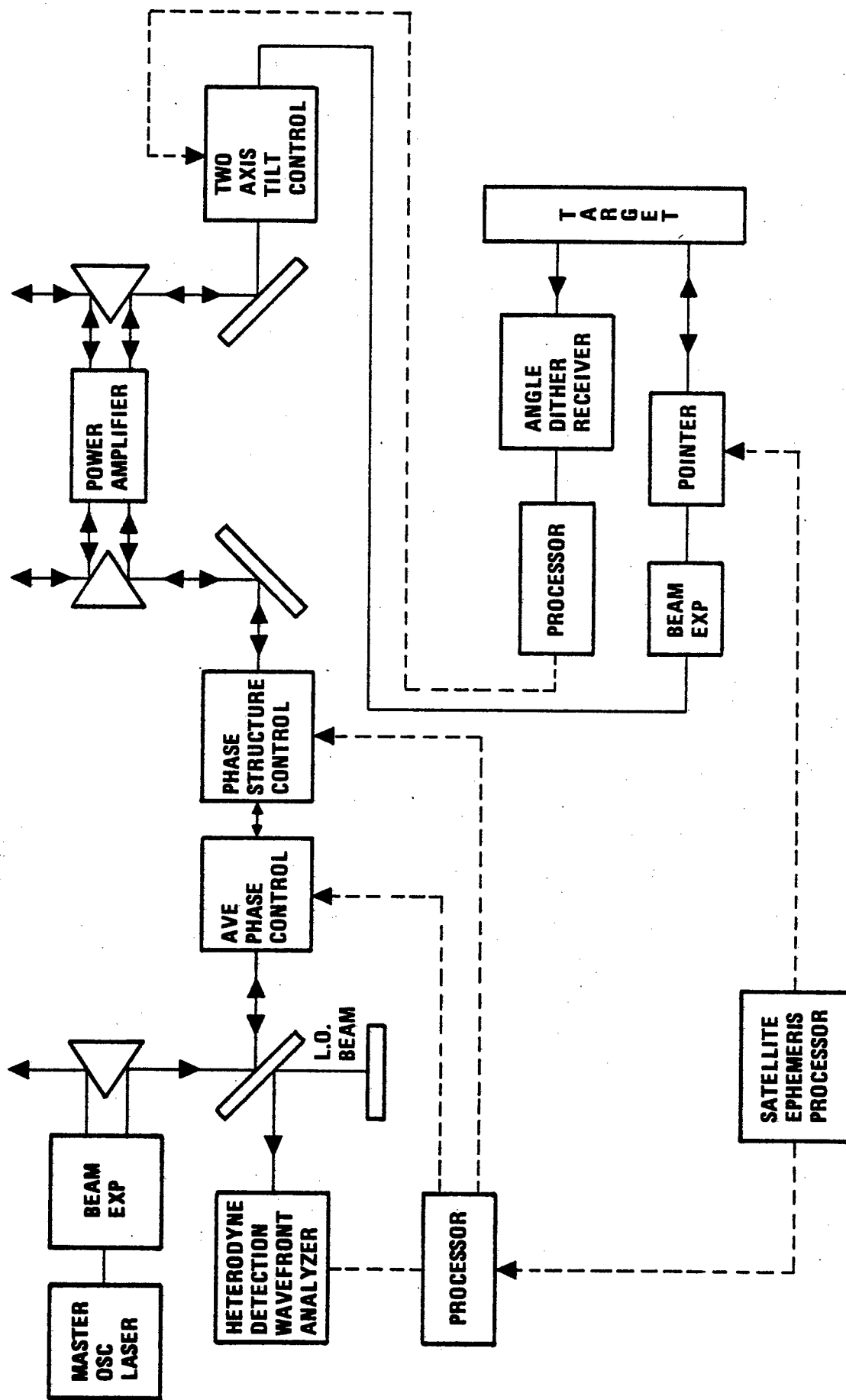


Figure VI-12. Multiaperture MOPA System Block Diagram

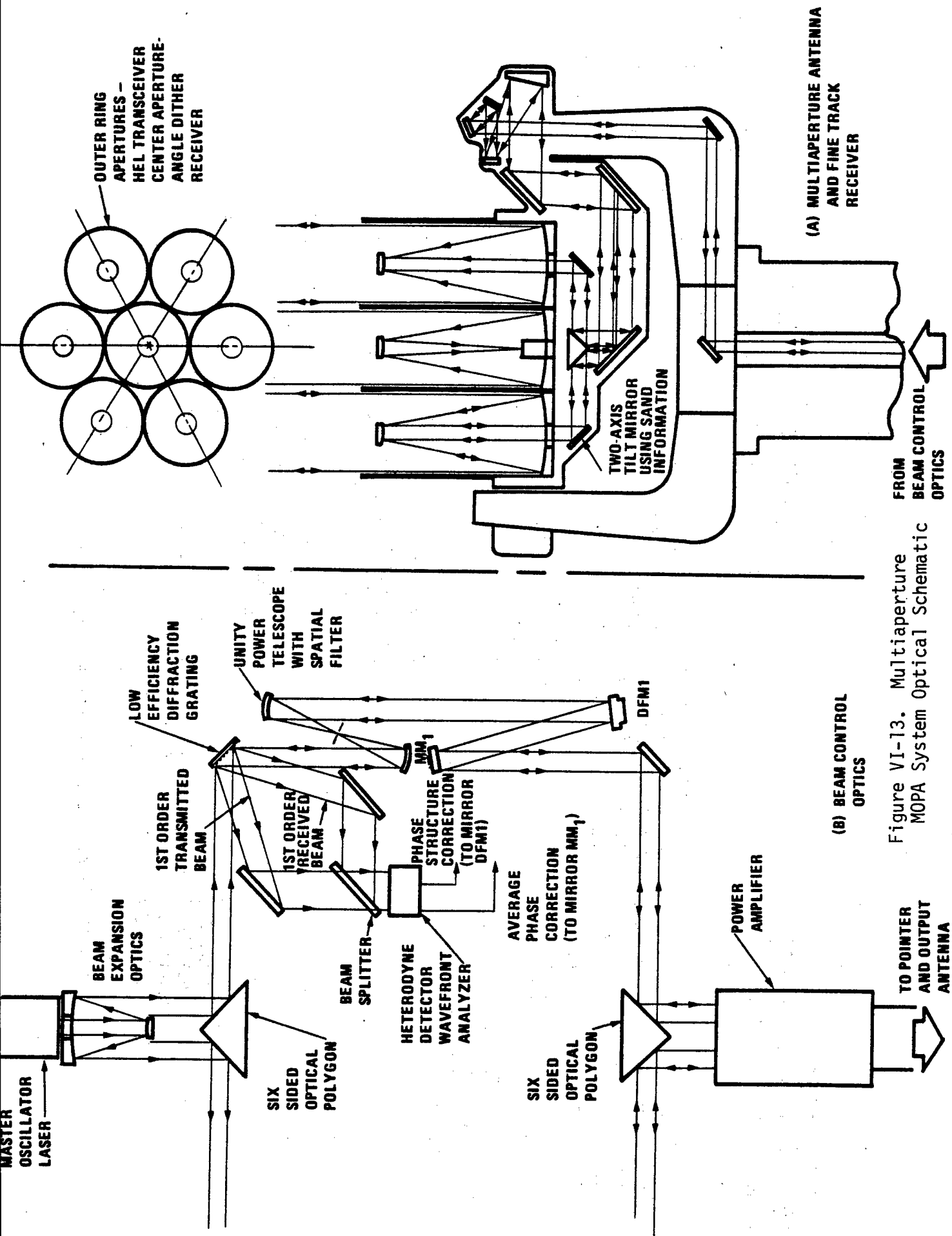


Figure VI-13. Multiaperture MOPA System Optical Schematic

in the center of the six transceiver telescopes. When the return dither signals have been processed, the tilt control signals are directed to the mirrors having the small dithered segments so that each of the six outgoing beams can be pointed at the satellite. The return signal which is collected by the six transceiver telescopes is directed back over the same path as the outgoing beam, until it arrives at the grating beam sampler. Here, a portion of the return is diffracted from the grating and directed into the wavefront analyzer where direct phase measurements are made using heterodyne detection. As was mentioned previously, these signals are processed into average phase corrections and phase structure corrections.

Because of the use of heterodyne detection, this concept must operate with large Doppler bandwidths. In Figure VI-14, we have plotted the expected Doppler frequency as a function of encounter time (0 seconds corresponds to -60° zenith, 80 seconds to $+60^\circ$ zenith) for an overflight directly overhead (offset = 0) and for an overflight offset of 185 km. These data indicate a bandwidth requirement of approximately 1.3 GHz. In an effort to reduce the wavefront analyzer processor bandwidth requirements, the satellite ephemeris processor predicts the expected Doppler frequency as a function of time and sends these data to adaptive filters in the return signal processor (see Figure VI-12).

For this concept, as with the previous ones, the system operates with a rich signal to noise, even for the worst conditions. During the acquisition phase when the beams are spread to a 50 meter diameter in the target plane, the signal to noise can be expressed as

$$S/N(ACQ) = \left\{ \frac{PA}{Nn} \left(\frac{(d_{cr})^2 D_T}{50 \lambda R} \right)^2 \frac{\eta \lambda \epsilon_a^2 \epsilon_t \epsilon_r}{h c \Delta f} \right\}^{1/2}, \quad (7)$$

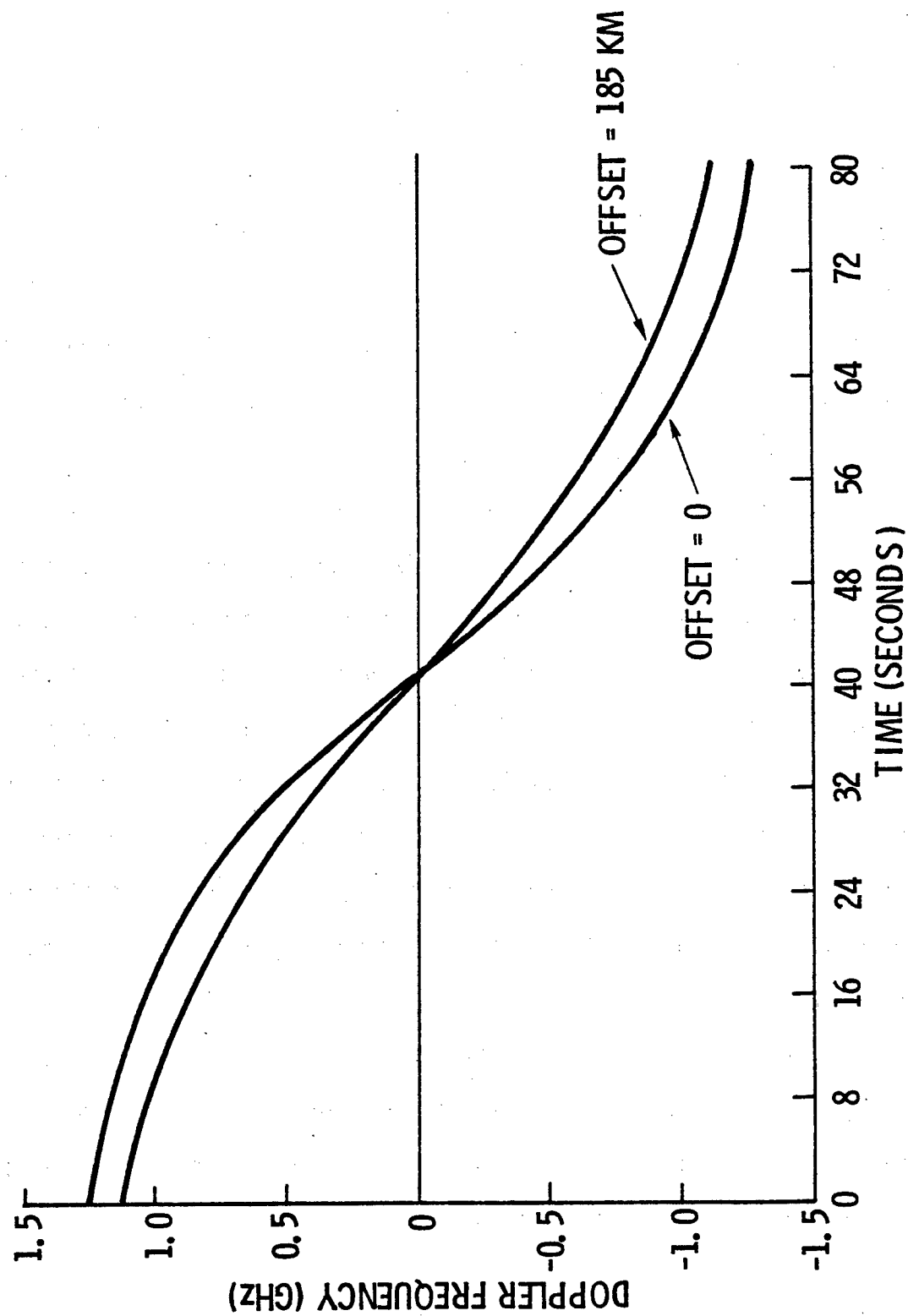


Figure VI-14. Expected MOPA System Doppler Frequency

where PA is the master oscillator power amplification product

N is the number of channels (6)

n is the number of sensors in the wavefront analyzer (19)

η is the quantum efficiency at a wavefront analyzer detector (.5)

h is Planck's constant

Δf is the signal bandwidth (1×10^6 Hz), and

D_T is the output transmitter diameter (1.67 m).

The other parameters have the same values as before, except for ϵ_r . Because of the low efficiency grating beam sampler $\epsilon_r \approx 7 \times 10^{-3}$. When these parameter values are used, the signal to noise for acquisition is

$$S/N(ACQ) \approx \sqrt{PA} \cdot .58, \quad (8)$$

or for PA = .5 MW

$$S/N(ACQ) \approx 4.1 \times 10^2.$$

For the target tracking conditions, the signal to noise is expressed as

$$S/N(TRACK) = \left\{ \frac{PA}{Nn} \left(\frac{D_T d_{cr}}{\lambda R} \right)^4 \frac{\eta \lambda \epsilon_a^2 \epsilon_t \epsilon_r}{h c \Delta f} \right\}^{1/2}, \quad (9)$$

or using the proper parameter values

$$S/N(TRACK) \approx \sqrt{PA} \cdot 12.3, \quad (10)$$

and for PA = 0.5 MW

$$S/N(TRACK) \approx 8.68 \times 10^3.$$

This concept offers a number of system advantages. First, all of the beam control optics, with the exception of the angle dither optics, is in the

low power section of the optical circuit. Next, by using the multiaperture output antenna, both the weight and moment of inertia that must be handled by the tracking mount can be reduced. Finally, the heterodyne detection makes possible direct phase measurements which in turn means the phase correction processor can be straightforward in design. On the negative side, this concept requires a relatively complex optical train and the antenna configuration, because of a non-transmitting unit in the center of the array, will aggravate the thermal blooming problem. In addition, the angle dither control system will suffer the same optical transit time delay problem as indicated for the multidither concept.

4. Multiple Source Phased Array

In this fourth concept we have made use of a technique perfected at Rockwell International; that of phase locking multiple independent laser oscillators to the same reference, so that a multichannel phased array could be configured without many of the problems inherent in the other concepts. By using this technique, it is possible to make each channel of the array independent from the others in a hardware sense. That is, each channel has a separate HEL source and tracking mount which helps increase system reliability and reduce cost. For this concept we have also changed the acquisition technique from that used in the other concepts. Here, an auxiliary laser is used to floodlight the target plane and thus provide signals for both the acquisition sequence and tracking.

A simplified block diagram for a single channel of this fourth concept is shown in Figure VI-15. From the HEL source, the beam is directed through a set of beam "clean-up" optics, very similar to that used in the multidither concept, and then to a Hartmann plate hole coupler where a portion of the beam

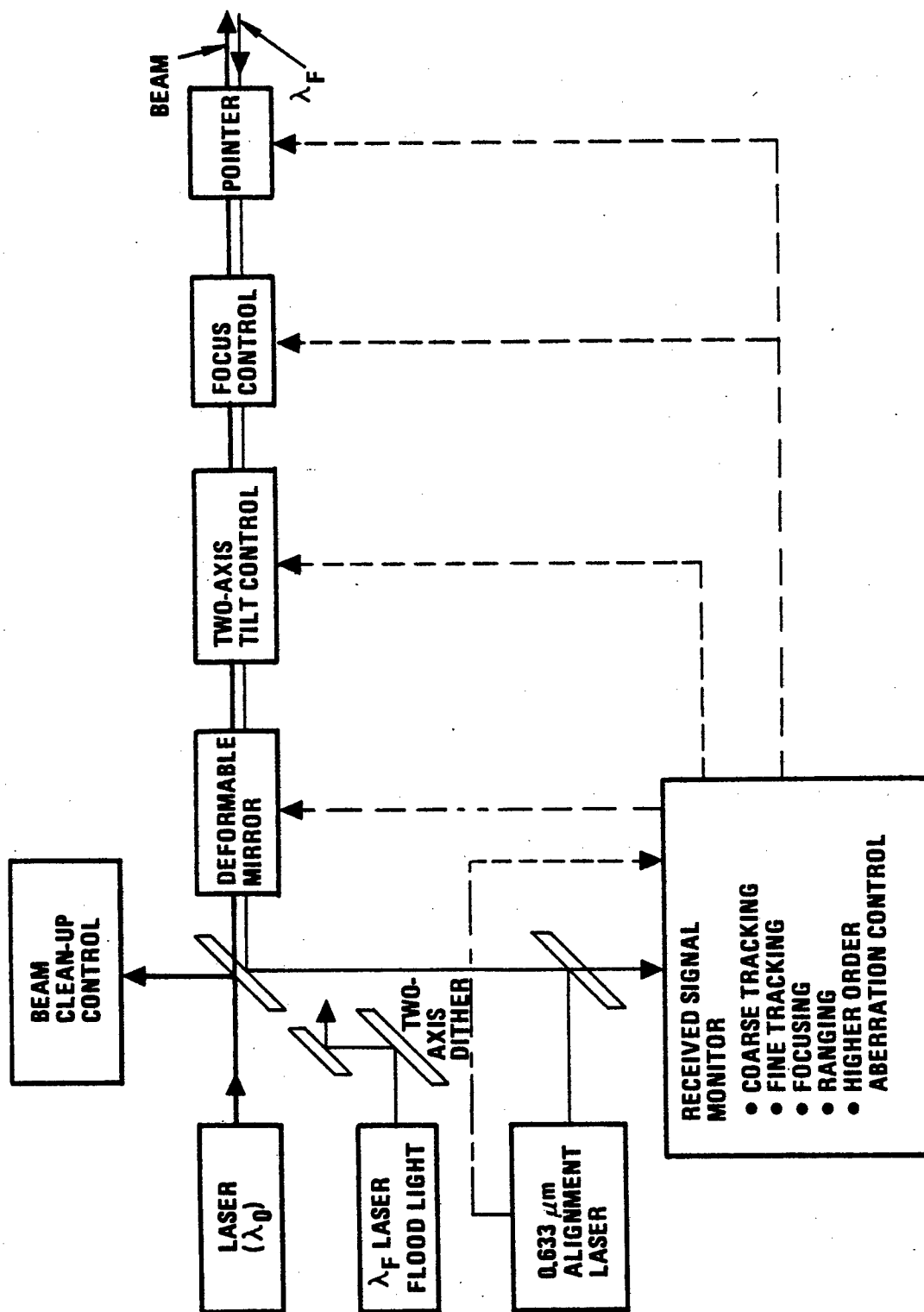


Figure VI-15. Multiple Source Phased Array Block Diagram

is extracted and sent to a wavefront analyzer, WFA (see Figure VI-16). The signals from the wavefront analyzer are then directed back to the proper control optics for tilt, focus, and higher order aberration correction, as was shown for the multidither concept (see Figure VI-10). This wavefront analyzer, as in the MOPA concept, uses heterodyne detection with the local oscillator provided by a separate stable laser source (not shown in the schematic). This local oscillator is common to each of the adaption channels and provides the reference to which each of the HEL sources is locked. From the Hartmann plate the reflected beam is directed through the beam control optics and finally out of the beam expansion telescope toward the target. The error signals for beam control are produced in two ways. The first method uses a relatively low-power auxiliary laser source with a wavelength slightly different from that of the HEL sources, so the problem with backscatter can be avoided. Here, we have selected 9.4 microns. For this source, a small transmitter aperture is used so the beam has a diameter of approximately 50 meters in the target plane and to point this auxiliary laser, or floodlight, a separate tracking mount is used. In addition, a small portion of this floodlight laser output is extracted by means of an acousto-optic Bragg cell and then further divided so equal amounts are sent to each of the λ_F wavefront analyzers (see Figure VI-16) for a local oscillator source. The floodlight signal reflected from the satellite corner reflector is collected by the HEL transmitter telescope and fed back through the optical circuit to the Hartmann plate hole coupler and λ_F wavefront analyzer. Here, signals for tilt, focus, and higher order aberration control are produced and directed to the appropriate beam control operators. The other method of beam control is concerned with the proper phasing of the HEL sources to compensate for atmospheric effects.

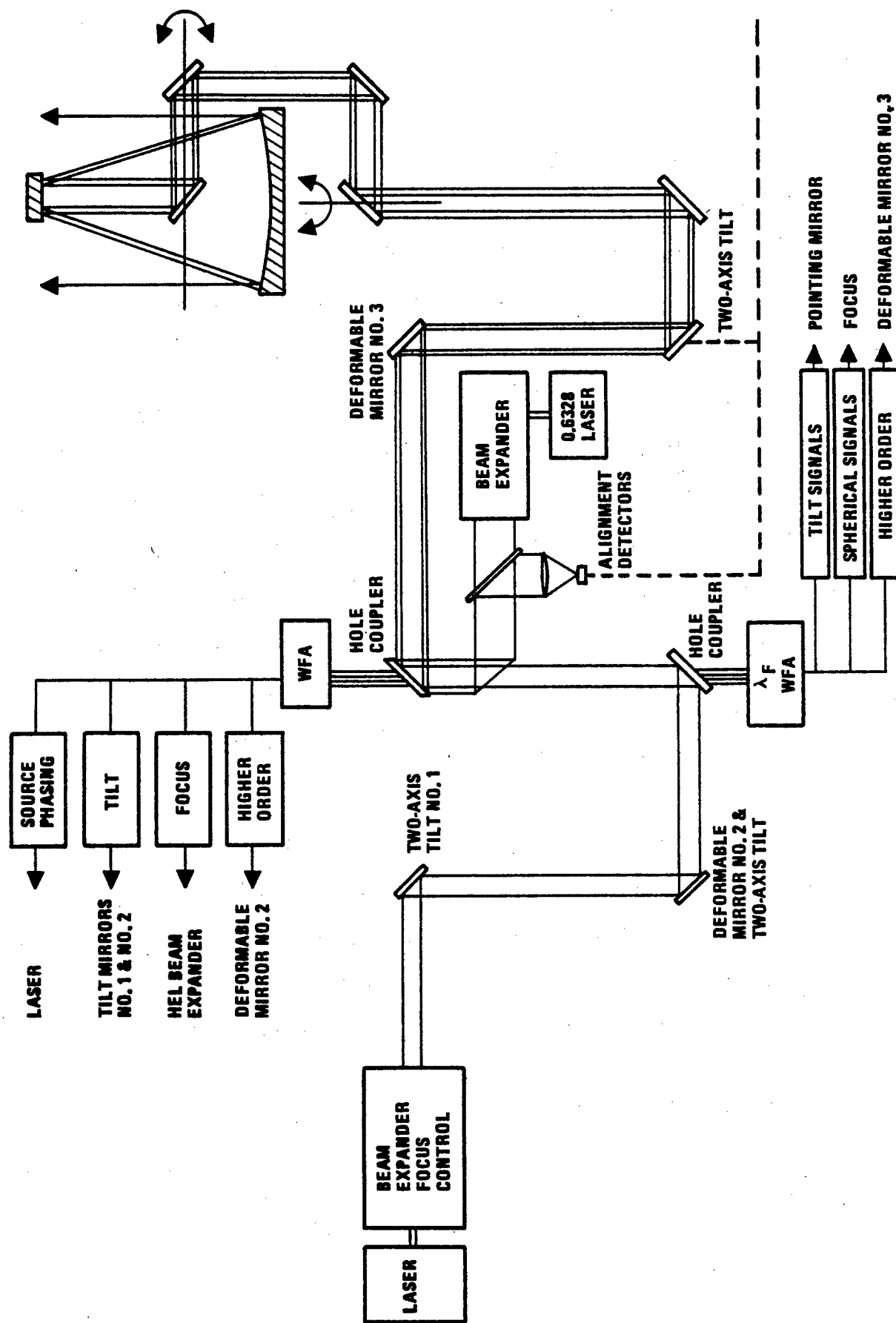


Figure VI-16. Multiple Source Phased Array Optical Schematic

For this control, a small phase dither with a characteristic frequency, such as used in the multidither concept, is introduced to each laser source, then a small receiver (0.3 m diameter) mounted on the floodlight laser tracking mount monitors the intensity fluctuations in the signal return produced by the phase dither. These signals are then processed similar to that shown in Figure VI-11 and the resulting phase correction signals are added to those measured in the beam "clean-up" processor (see Figure VI-16).

The analysis previously presented for the outgoing wave, or dither, system has shown that a superfluity of signal can be expected, even when the difference in apertures ($D_T = 1.67$ m, $d_r = 0.3$ m) is considered. Therefore, with this concept only the performance of the laser floodlight system is of concern. Here, heterodyne detection is used so the signal to noise, as measured at one of the detectors in the λ_F wavefront analyzer, can be expressed as

$$S/N = \left\{ P_t \left(\frac{d_{cr}}{\lambda R} \right)^4 \frac{(d_t D_T)^2 \eta \lambda \epsilon_a^2 \epsilon_t \epsilon_r \alpha}{h c \Delta f} \right\}^{1/2}, \quad (11)$$

where P_t is the power transmitted by the floodlight laser

d_t is beam diameter of the floodlight laser (0.07 m)

λ is the optical wavelength of the floodlight laser (9.4×10^{-6} m), and

α is the ratio of the sample hole area to the total beam area at the hole coupler for the λ_F wavefront analyzer.

For this concept we considered

$$\alpha = \left(\frac{2 \times 10^{-3}}{2 \times 10^{-1}} \right)^2 = 1 \times 10^{-4},$$

and assumed the other parameters to be the same as for concept three, except for ϵ_r , which was changed to $\epsilon_r = .7$. When these parameters are used to compute the signal to noise, we obtain

$$S/N \approx \sqrt{P_t} \cdot .75, \quad (12)$$

or for a modest laser power, $P_t = 100$ watts, we have

$$S/N \approx 7.5$$

which is adequate to begin the acquisition process.

The multiple source phased array concept, as was previously stated, uses a separate pointer/tracker for each of the adaptive channels. Because of thermal blooming effects, this operation could present a problem if the array of output beams is not kept tightly packed when the satellite is tracked from plus to minus 60° zenith angle. A method suggested for coping with this problem is shown in Figure VI-17. Here, we have shown a seven-element hexagonal array mounted on translation platforms where the center three elements move in only a single direction and the outer element pairs can move in two orthogonal directions. To visualize the type of motion required, let us consider a satellite flight directly overhead, or offset = 0. For this condition, the spacing between the center three elements (see Figure VI-17) would be increased by translating the end elements when the satellite is acquired at the 60° zenith angle. As the zenith angle decreases and then increases during the overflight, the end elements are translated so the spacing properly matches the zenith angle and the outer element pairs are translated in a likewise manner. With this approach, the spacing between beams can be kept small and near constant while tracking the satellite.

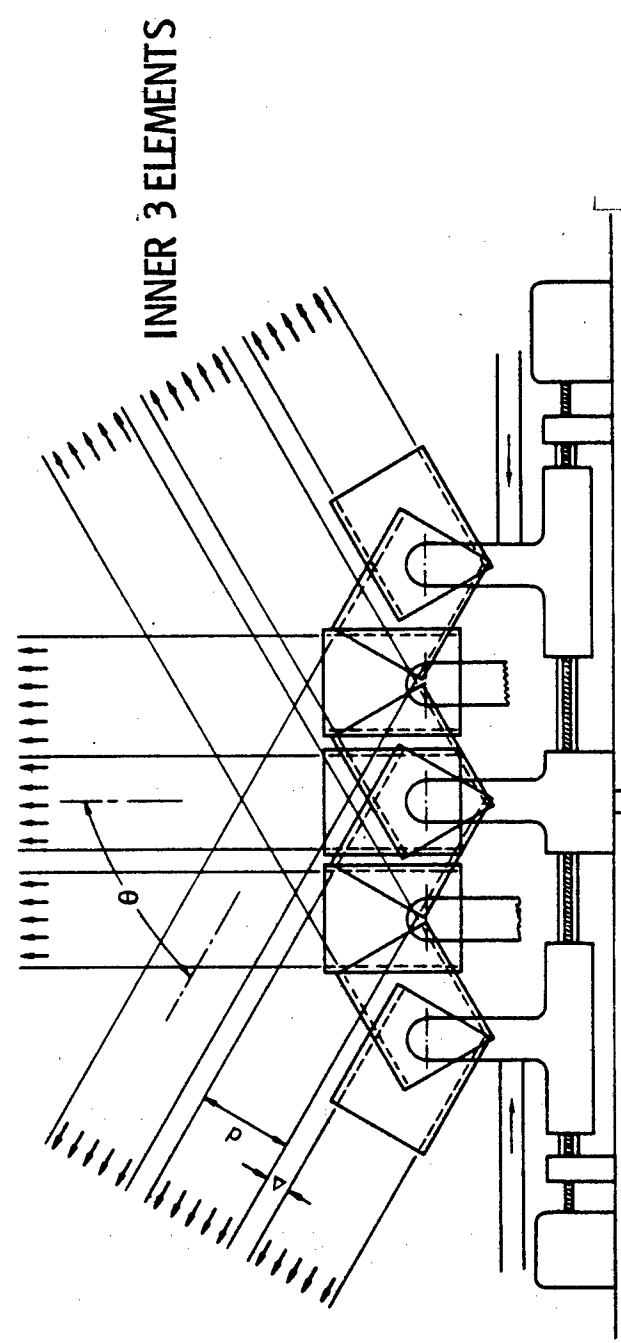
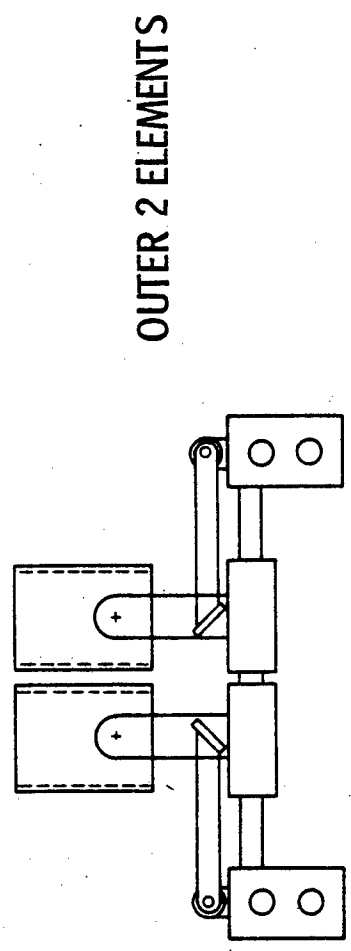
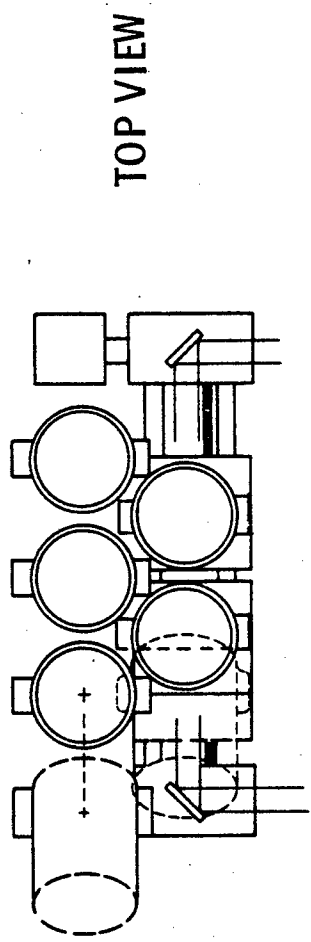


Figure VI-17. Pointing Mount Array Configuration

This system concept makes it possible to use a separate pointer/tracker for each of the adaptive channels and in terms of overall system reliability the improvement is obvious, but it appears that reduced costs are also possible. To illustrate this, a brief telephone survey was made to determine the approximate cost of large tracking antennas. The results of our survey are shown in Figure VI-18. For the very large aperture optical tracking antennas, we obtained from the California Institute of Technology an estimate of the replacement cost of the Palomar instrument (~ 5 m) and from the University of Arizona the estimated cost of the seven-element Multiple Mirror Telescope (MMT) that is being constructed there and also their estimate of the cost of a single element 150 inch system that would be the equivalent of the MMT. The Cloudcroft instrument has a 1.2 meter antenna size and was designed to track low-earth orbit satellites. Here, we obtained an estimate of its original cost and its replacement cost. The unit designated by LRTS is a laser radar which has an 0.3 meter antenna in a mount designed for tracking high acceleration missiles. When a best fit is constructed through the data obtained, we find that the cost can be reasonably approximated by the following expression,

$$\text{COST (\$M)} = 0.35 D_T + 0.45 D_T^2 + 0.2 D_T^3, \quad (13)$$

where D_T is the antenna diameter. If we use this approximation, it is possible to estimate the cost savings of a close packed hexagonal array antenna, such as suggested for this multiple source phased array concept. For such an array, the number of elemental apertures can be expressed as

$$N_e = 3Z(Z + 1) + 1, \quad (14)$$

where Z is the number of rings of apertures about a center aperture in the hexagonal array and in the same terms the elemental aperture diameter is given as

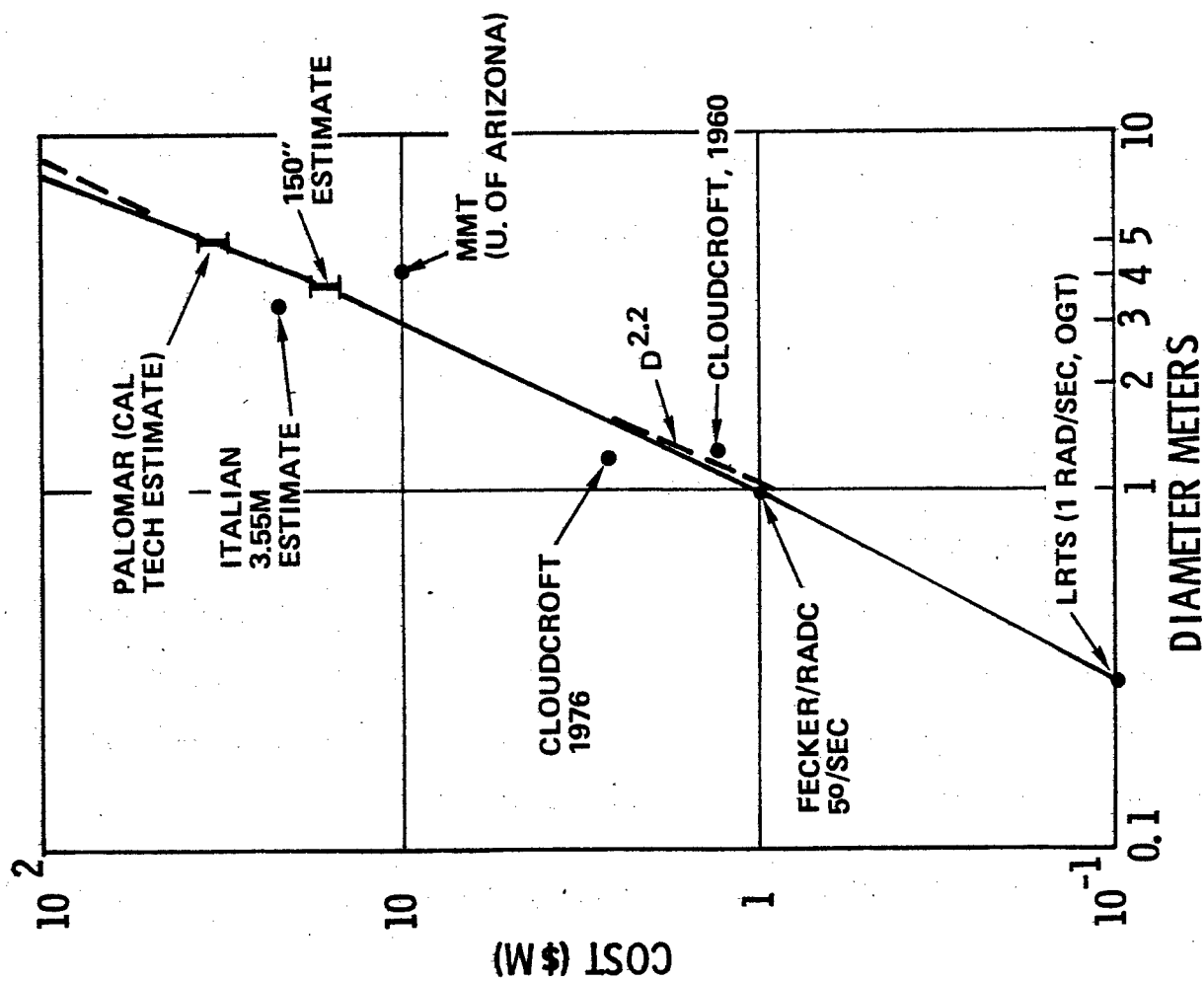


Figure VI-18. Pointing System Cost vs Diameter

$$D_e = D_T / (2Z + 1). \quad (15)$$

With these expressions, it is possible to establish a simple expression for the ratio of cost of an hexagonal close-packed configuration to that of a single aperture equivalent diameter. This ratio is expressed as

$$C_a/C_s = \frac{N_e (0.35 D_e + 0.45 D_e^2 + 0.2 D_e^3)}{0.35 D_T + 0.45 D_T^2 + 0.2 D_T^3}, \quad (16)$$

where C_a is the total cost of the multiple element antenna array and C_s is the cost of a single aperture antenna of equivalent diameter to the array. Figure VI-19 is a plot of this cost ratio versus the number of array rings for different values of D_T . For this fourth concept, if we use a seven-element (1 ring) close-packed array, then the cost would be only about 51% of that if a single element tracking antenna was used.

This fourth concept offers a number of outstanding advantages when compared to the evaluation parameters that were given for this program. First, since the concept makes use of independent laser oscillators, it is possible to achieve the maximum required power level (5 MW) using state-of-the-art lasers and thus save the cost of HEL development. The concept makes use of small pointing/tracking systems (~ 1.7 m) and yet achieves effective 5-meter performance, which also appears to provide a substantial cost savings. The system is redundant with each channel structured identically and therefore insensitive to failure of any major array element. Only the auxiliary laser assembly is common to all channels and this is such a minor part of the overall cost that redundancy can easily be considered. In addition, the auxiliary laser allows the adaption process to

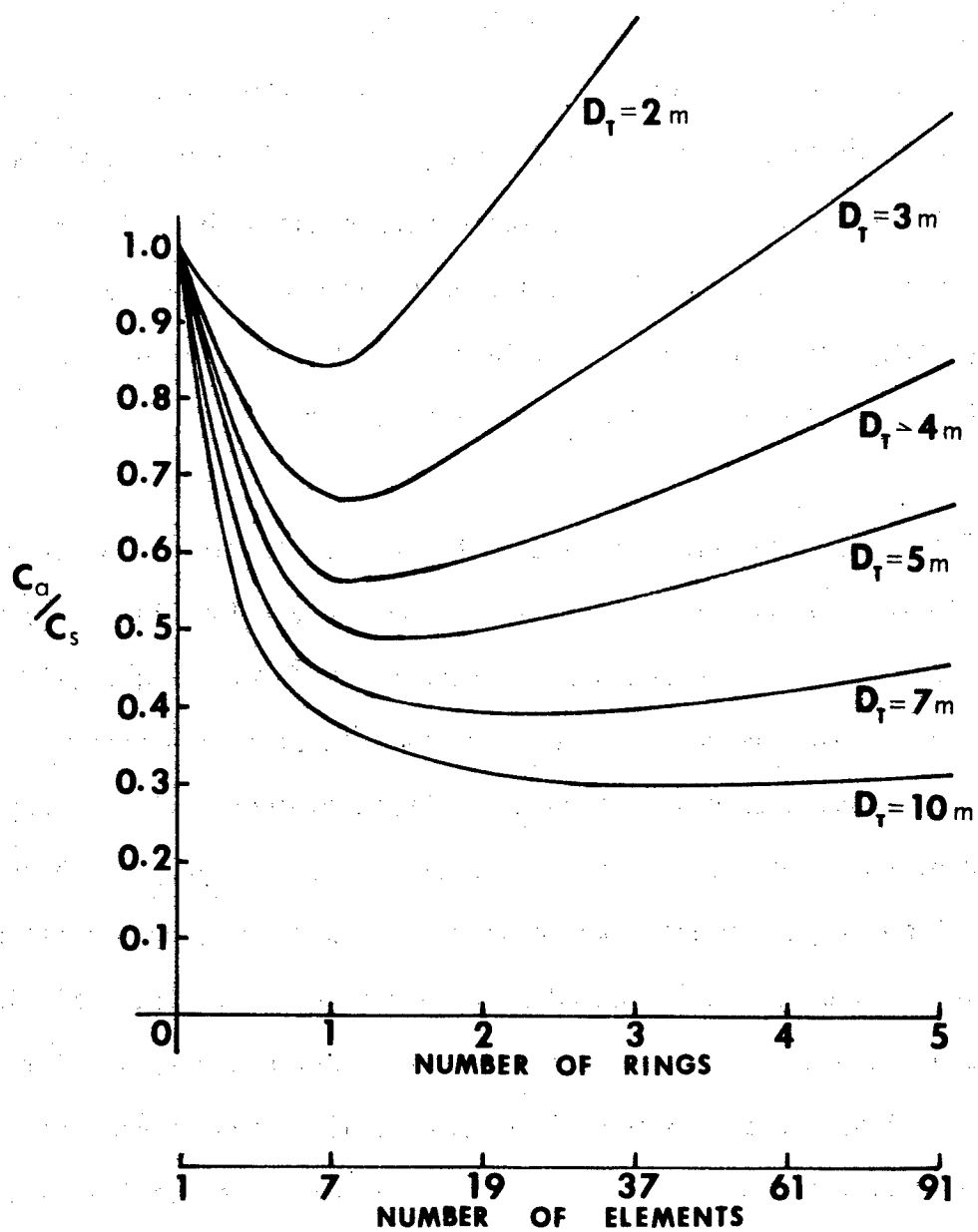


Figure VI-19. Cost Saving Factor for Hexagonal Close Packed Array

begin before the HEL sources are activated. The technique of phase locking multiple laser oscillators has been demonstrated with low power sources,¹ but not HEL devices characterized by unstable resonator configurations and herein lies the main disadvantage of the concept. In addition, because it uses the dither approach for target adaptive control signals, it is also susceptible to the optical transit time problems discussed for concept number two.

B. System Evaluations

The evaluations of the four system concepts, following the directives of this program, were based on (1) overall efficiency, (2) reliability, (3) size and weight, (4) technology advancement requirement, and (5) potential cost. Also following the program directives these conditions, where applicable, were applied to both sea level and mountain top operation (3.5 km above sea level). We have in each of the evaluations, except that of efficiency, produced an evaluation index by normalizing the results to unity. The final concept comparisons were then made by taking the product of these evaluation indexes for each concept and then ranking the concepts according to the values obtained.

1. System Efficiency

The performance efficiencies (ratio of power collected at the satellite to power transmitted) of the four concepts for 10.6 μm transmission are shown in Table VI-1. Here, we have tabulated separately the results for each source of power loss considering both sea level and mountain top operations. As

1. C. L. Hayes and L. M. Laughman, Appl. Opt. 16, 263 (1977).

Table VI-1
Transmission Efficiency of System Concepts

	SEA LEVEL				3.5 KM			
	I	II	III	IV	I	II	III	IV
ABSORPTION	0.18	0.18	0.18	0.18	0.45	0.45	0.45	0.45
DIFFRACTION	0.86	0.86	0.75	0.82	0.86	0.86	0.75	0.82
TURBULENCE	0.83	0.68	0.83	0.83	0.83	0.68	0.83	0.83
BLOOMING { 0.5 MW 1.0 MW 5.0 MW	0.926	0.926	0.797	0.996	0.93	0.93	0.8	1.0
	0.923	0.923	0.794	0.993	0.93	0.93	0.8	1.0
	0.443	0.443	0.381	0.476	0.837	0.837	0.72	0.9

	SEA LEVEL				3.5 KM			
0.5 MW	0.12	0.097	0.089	0.122	0.30	0.24	0.22	0.31
1.0 MW	0.015	0.097	0.089	0.121	0.30	0.24	0.22	0.31
5.0 MW	0.057	0.047	0.004	0.058	0.27	0.22	0.20	0.28

these results indicate, the transmitter parameters have been selected so that diffraction losses are small. Also, the atmospheric turbulence effects were weak enough at this wavelength that good compensation could be affected and the losses were not serious. The absorption losses and subsequent thermal blooming effects, however, are such that sea level operation cannot be a viable consideration, especially for the 5 MW transmission. When mountain top operation is used, and much of the water vapor absorption is avoided, the efficiency is much improved at the higher power levels, but it remains serious because more than two thirds of the transmitter power is lost. These data also indicate that the overall transmission efficiency is only weakly dependent on system configuration.

2. Reliability

We have made estimates of concept reliability, shown in Table VI-2, based on relative system complexity. Concept I is the most simple, configured with a stationary beam expander, direct detection, non-complex adaption algorithm and a very large, but straightforward tracking mount. For this system we assigned an index of 0.9. Concept II was only slightly more complex in configuration and operation than the first system, so it was assigned a near equivalent index of 0.85. The third concept was by far the most complex of the systems configured, so it was assigned the lowest index. Concept IV is, admittedly, a relatively complex system, but because it is configured such that any major component can fail in one of the adaptive channels and the system will continue to function, it was assigned the highest reliability index. The reliability estimates given are for 0.5 MW operation. To account for the possible problems associated with operating at higher power densities, we have assigned adjustment terms of 0.97 and 0.93 to correct the reliability

Table VI-2
Estimated Reliability of Conceptual Systems

CONCEPT I	0.90	SIMPLEST SYSTEM
CONCEPT II	0.85	MORE COMPLEX THAN I
CONCEPT III	0.70	BY FAR THE MOST COMPLEX AND SUSCEPTIBLE TO PROBLEMS
CONCEPT IV	0.95	REDUNDANT SYSTEM

FOR 1.0 MW MULTIPLY BY 0.97
FOR 5.0 MW MULTIPLY BY 0.93

indexes for operation at 1 and 5 MW, respectively. We have also assumed that the system reliability is independent of operating altitude, at least for the two locations considered.

3. Weight and Size

To obtain conceptual systems weight and size estimates, we assumed that the pointing system would dominate the overall system size and that the moving weight of the pointer/tracker was the more important design parameter. Therefore, simplified models for calculating the weight and size of beam expansion optics and tracking mounts were developed and used. The results obtained from the models are shown in Table VI-3. Here, we have listed the moving weight of the tracking mount and the dimensions of a dome needed to cover the pointing system assembly. The characteristic size dimension of each concept was then obtained using the average of the dome dimensions. In Table VI-3, we show Concept I, with the 7-meter mirrors in a coelostat tracking mount, has the greatest size and weight of the four concepts. Concept II, which uses a single aperture beam expander mounted in the tracking mount, is also characterized by large weight and size. When multielement transmitter antennas are used in the systems, as with Concepts III and IV, both the moving weight and size are reduced substantially. Of the two, however, Concept IV fairs better because it has both individual beam expanders and tracking mounts for each adaptive channel. To complete this evaluation, the reciprocal of the weight-characteristic length product was calculated as the quality factor of interest. These values were then normalized to provide the evaluation index.

4. Technology Advancement Requirement

The technology advancement requirements for the four concepts are tabulated in Table VI-4. From the technology requirements list of each

Table VI-3

Weight and Size Estimates for the Conceptual Systems

	CONCEPT				
	I	II	III	IV	
WEIGHT (kg)	382,000	215,000	28,000	17,000	(MOVING WEIGHT)
SIZE Height Diameter	29 30	20 25	14 15	6 18	(DOME SIZE)
L (m)	29.5	23	14.5	12	
$\frac{1}{WL}$	8.87×10^{-8}	2.02×10^{-7}	2.46×10^{-6}	4.9×10^{-6}	
$(1/WL) / (1/WL)_{MAX}$	0.02	0.04	0.5	1	INDEX

Table VI-4

Technology Advancement Requirements for the Four Concepts

INDEX

CONCEPT I	1
• Hartmann Sensor	
• Coelostat	
• High Level Quadrant Detectors	
• Segmented Adaptive Corrector (With Tilt)	
CONCEPT II	0.8
• AZ-El / Alt-El Mount	
• ALOT Dither Data Processing	
• Segmented Adaptive Piston Corrector	
CONCEPT III	0.4
• Power Amplifier	
• High Speed Heterodyne Detectors	
• Subaperture Mirror Development	
• Gimbal Development	
• Deformable Mirror	
• Low Level Wavefront Analyzer	
CONCEPT IV	0.6
• Traversal Assembly	
• High Power Phase Lock Techniques	
• Deformable Mirror	
• High Speed Heterodyne Detectors	

concept, we have estimated, based on present day technology, the degree of difficulty in making the required advancement. Most of the technology needs of Concepts I and II should not require too much advancement, consequently they have been assigned the higher indexes. Concept III, mainly because of the power amplifier, has been assigned the lowest index of the four concepts and Concept IV, because phase lock techniques have not been attempted on high power lasers, also received a low index.

5. Potential Costs

To evaluate the potential cost of the four systems, we singled out what were assumed to be the three most costly items in each system, laser, optics and pointer, and then made estimates of their cost for the three power levels of interest. Table VI-5 gives the results of these cost estimates. For the laser evaluation we used a cost of \$5/watt, except for the MOPA system (Concept III) where a value of \$7/watt was used. For the optics cost, the number of elements in each concept was counted and then an average cost of about 80K per element was assumed, except in Concept III where some of the elements were more complex. We also assumed that the cost of the optics, in the range of interest, was independent of the laser power. The pointer/tracker costs were estimated in terms of size and moving weight, and using the data shown in Figure VI-18 as a reference. The quality factor used in the evaluation was the reciprocal of the total cost and when these values are normalized, the clear winner for all power levels was Concept IV.

6. Overall System Evaluation

When the evaluations of the five considerations were completed, the indexes were tabulated and their products taken so that an overall evaluation of the concepts could be made for the three power levels of interest and for

Table VI-5

Estimated Cost (\$M) of Major System Components for Four Concepts

		LASER	OPTICS	POINTER	TOTAL	1/π	$(1/\pi)/(1/\pi)_m$
5 MW	I	25	1	45	71	0.014	0.58
	II	25	1.4	30	56.4	0.018	0.75
	III	35	5	20	60	0.017	0.708
	IV	25	1.1	15	41.1	0.024	1
1 MW	I	5	1	45	51	0.024	0.51
	II	5	1.4	30	36.4	0.027	0.574
	III	7	5	20	32	0.031	0.66
	IV	5	1.1	15	21.1	0.047	1
0.5 MW	I	2.5	1	45	48.5	0.21	0.40
	II	2.5	1.4	30	33.9	0.029	0.55
	III	3.5	5	20	28.5	0.035	0.66
	IV	2.5	1.1	15	18.6	0.053	1

sea level and mountain top operation. The result of this evaluation is given in Table VI-6 for mountain top operation and it shows that Concept IV ranks first. The evaluation was also performed for sea level operation (only the efficiency indexes change) with the same final results. Based on these evaluation results, Concept IV was selected for further detailed consideration.

Table VI-6

Overall Concept Evaluation for Mountain Top Operation (3.5 km)
Considering 0.5, 1.0, and 5.0 MW Operation

CONCEPT	I			II			III			IV		
EFFICIENCY	0.30	0.30	0.27	0.24	0.24	0.22	0.22	0.22	0.20	0.31	0.31	0.28
RELIABILITY	0.9	0.87	0.84	0.85	0.82	0.79	0.70	0.68	0.65	0.95	0.92	0.88
WEIGHT & SIZE	0.02			0.04			0.5			0.1		
TECHNOLOGY NEEDS	1			0.8			0.4			0.6		
POTENTIAL COST	0.4	0.51	0.58	0.55	0.57	0.75	0.66	0.66	0.71	1	1	1
Π	2.16 X 10^{-3}	2.66 X 10^{-3}	2.63 X 10^{-3}	3.59 X 10^{-3}	3.59 X 10^{-3}	4.17 X 10^{-3}	0.02	0.0197	0.0185	0.177	0.171	0.148

RANK

4

3

2

1

4

3

2

1

4

3

2

1

VII. DETAILED CONCEPTUAL DESIGN

In this chapter we shall relate the results of an investigation made to define with greater detail the Multiple-Source Phased Array (MSPA) concept. The results of the investigation will be related by first covering the overall system aspects and then system particulars, which include the multiple servo loops, intermediate optics considerations, tracking mount dynamics, and weight and size considerations.

Before we start these discussions, however, it should be mentioned that some changes have been made in the MSPA system as presented in the previous chapter. First, we have exchanged the multidither, or outgoing wave, target adaption concept for a return wave, or phase conjugation, approach. This change was made so that the optical transit time limitation of the outgoing wave concept could be avoided and the use of the adaption system could be extended to greater target ranges, when needed. As part of this change in adaption algorithms, the small diameter direct detection receiver was eliminated and heterodyne detection was used at the HEL wavelength. Next, because this concept uses multiple independent sources, we felt that the auxiliary floodlight laser concept could be replaced by using one of the HEL's as a source for target acquisition and improve the signal-to-noise ratio. Since the multidither photon bucket receiver had been eliminated, removing the floodlight laser requirement also resulted in eliminating the special tracking mount that was used to point these two operators at the target. We also decided to remove the lateral motion mechanization concept that had been proposed for the MSPA system, as a means of keeping the center-to-center spacing between the output antenna elements (beam expansion telescopes) constant and replace it with a concept that simply drives each

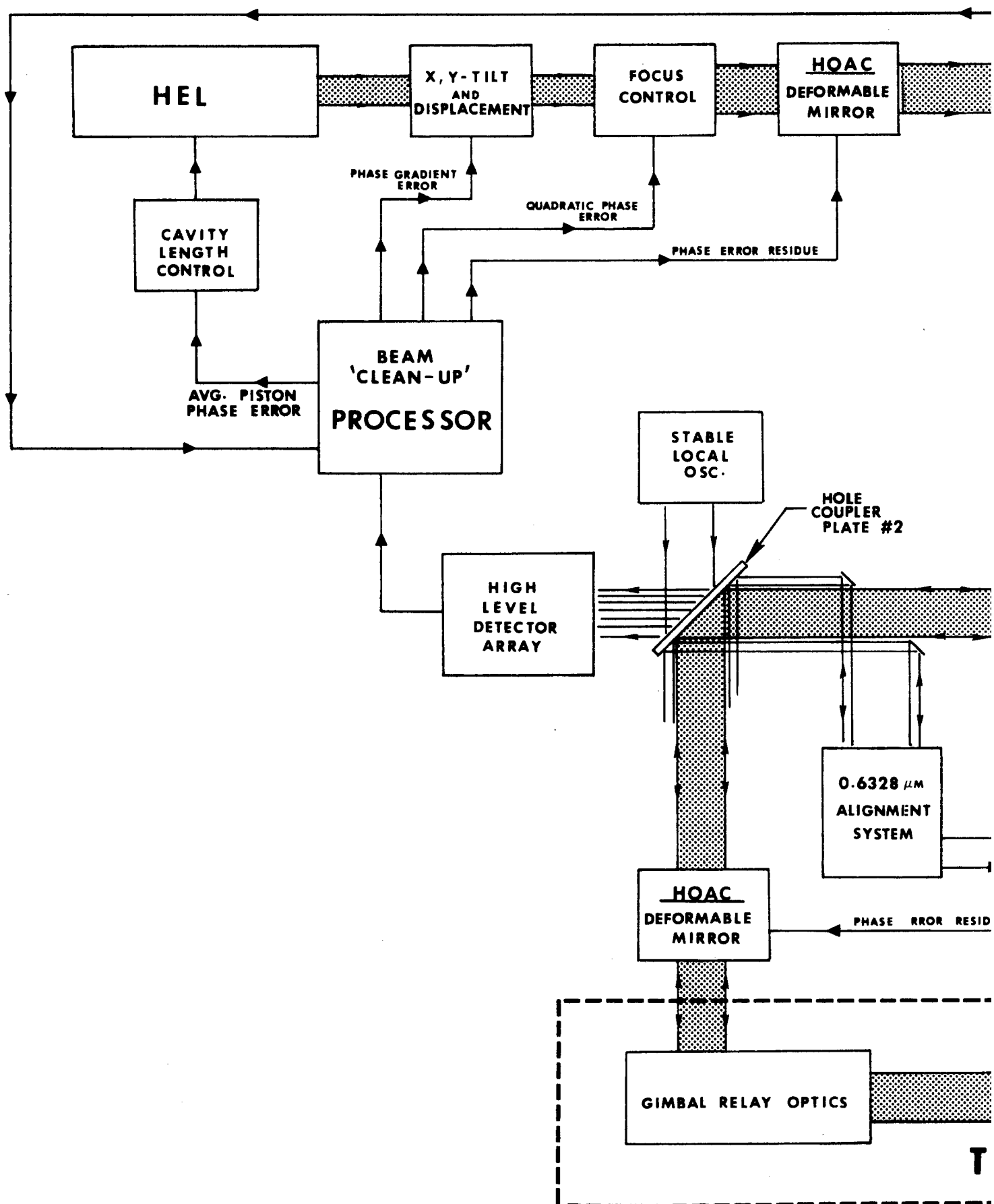
tracking mount up and down with a hydraulic piston. This change was made primarily because it simplified the intermediate optics circuit, but it also appears to be a more straightforward mechanical approach. Finally, because the atmospheric transmission at $10.6\text{ }\mu\text{m}$ was so dismal, we have elected to use an isotope source operating at $9.1\text{ }\mu\text{m}$. This change of direction was encouraged because (1) it was not an aberrance from the original directives of this program, since it does not make a significant change from the laser technology required for $10.6\text{ }\mu\text{m}$ operation, and (2) it improves the expected atmospheric transmission dramatically, especially for mountain top operation.

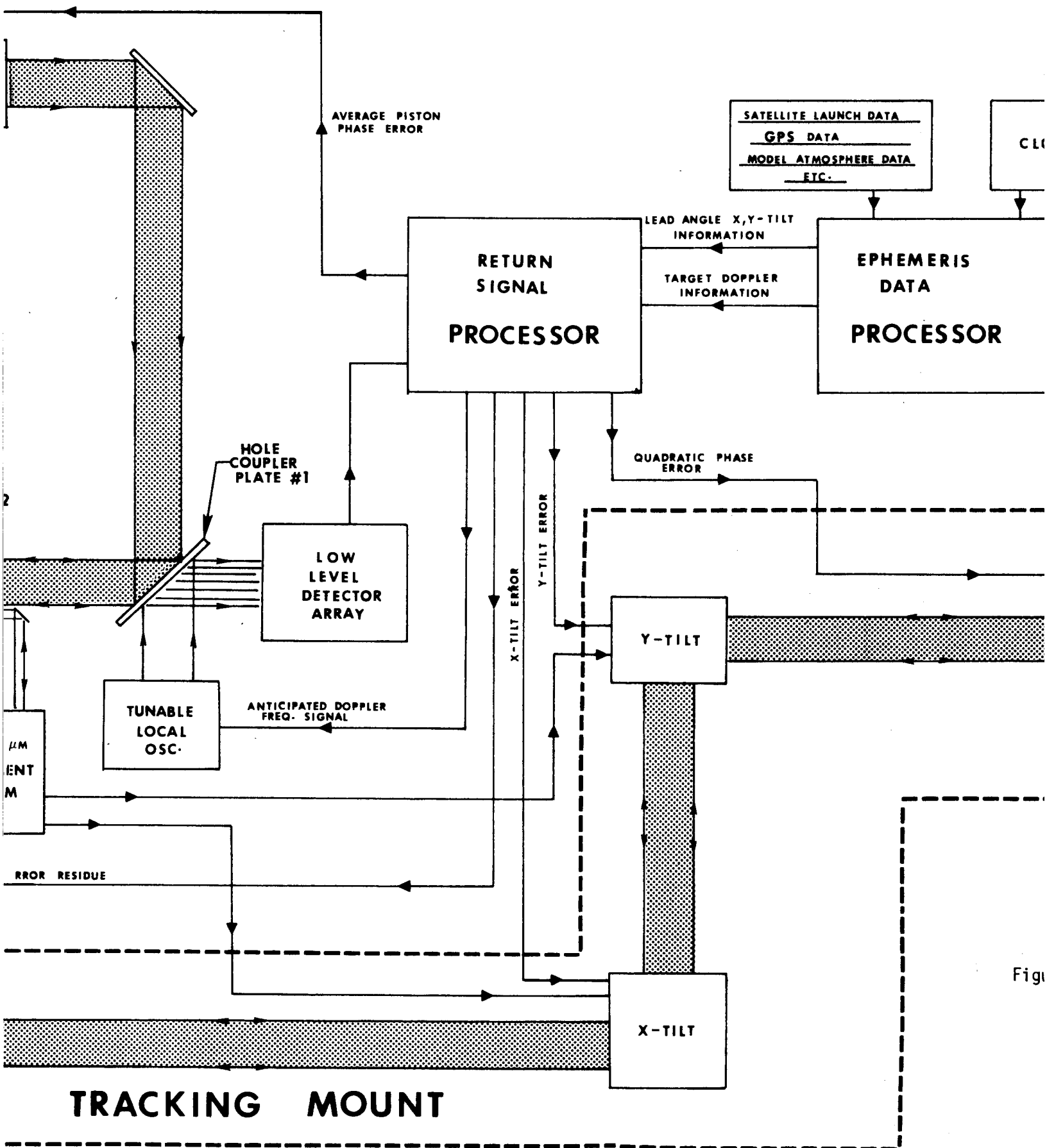
A. System Details

1. Overall Concept Description

In Figure VII-1, we present a detailed block diagram for a single channel of the MSPA system. We will describe this system and its operation by following the HEL beam shown in this figure through the circuit to the target and then its return back through the system to the signal detectors and processor. When this is completed, a brief description of the ephemeris data processor operation will be given. Then, to put all of these system operations in the proper time perspective, a chronology of events will be presented in the following subsection.

Starting at the HEL source, the beam is directed through a set of beam control optics, identical in configuration to those shown in Figure VI-8b (M1 to DFM₁), and then reflected from a hole coupler plate toward a second hole coupler plate. At this second plate, a small portion of the beam ($\sim 6 \times 10^{-4}$) is extracted from the outgoing beam by a set of regular spaced small holes ($\sim 1 \times 10^{-3}\text{m}$). The light transmitted through each hole





Fig

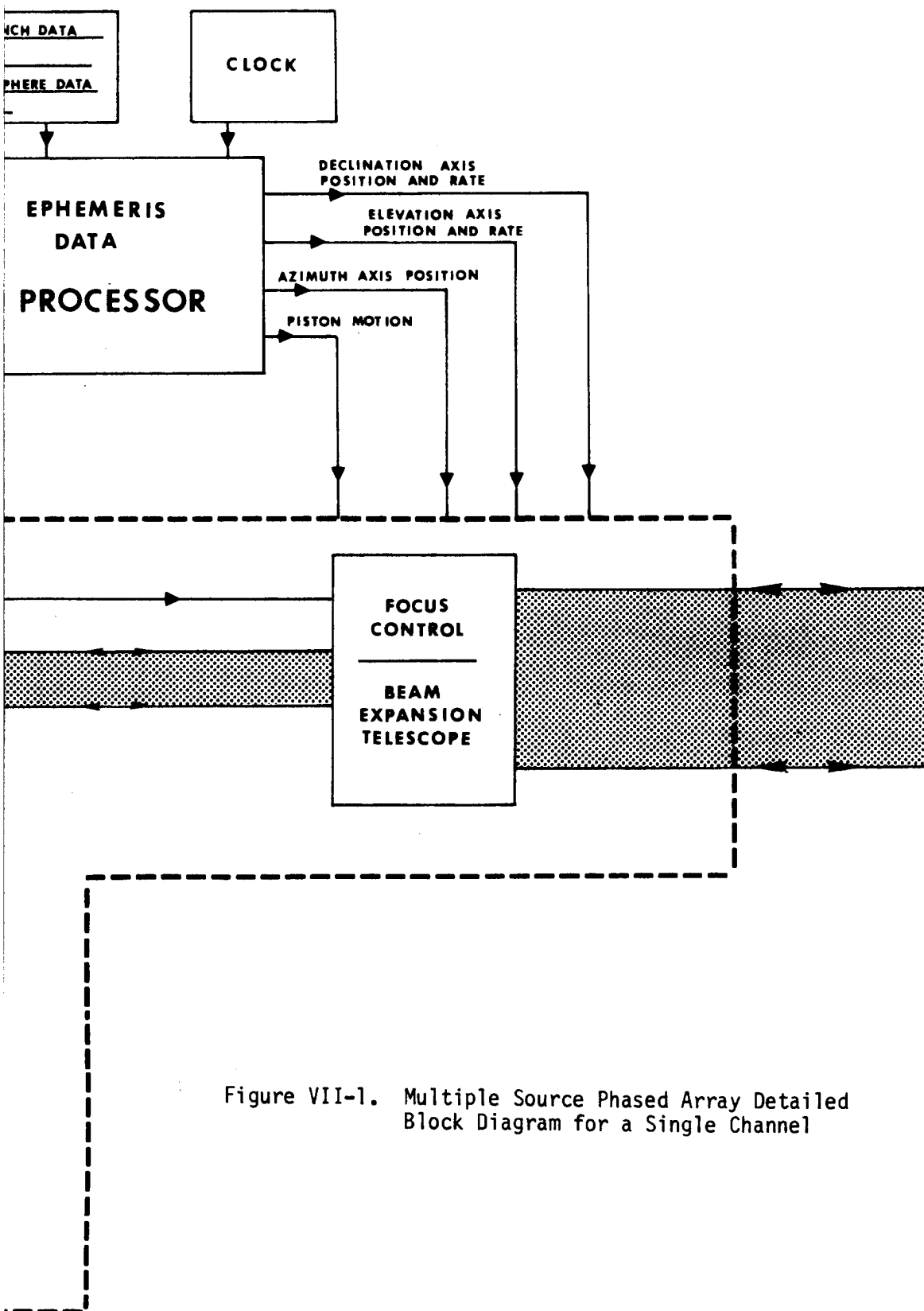


Figure VII-1. Multiple Source Phased Array Detailed Block Diagram for a Single Channel

is directed toward a single detector in the array. Also, as shown, the beam from a stable oscillator is reflected from the back of the hole coupler plate onto the detector array (37 detectors) to provide a local oscillator signal.

All of the operations shown in Figure VII-1 are for a single channel of the adaption array, but the high level local oscillator beam, as well as the one used for the low level detector array, provide common phase references for all channels. This is accomplished using an optical configuration, such as shown in Figure VII-2. Here, all of the hole coupler arrays are fabricated into a single liquid cooled mirror (reflective on both sides) and an off-axis cylindrical lens beam expansion telescope is used to produce a single local oscillator beam that is fed to all of the detector arrays.

The measured set of phase signals from the high level detector array are sent to the beam "clean-up" processor that, in turn, uses these data to calculate the correction signals that go to the beam control operators, as well as the HEL source to control its phase (because a common reference is used, all of the sources are made cophasal at the hole coupler plate). This processor computes the average phase from the signal set for the laser phase control and then with the average value extracted decomposes the phase signals into orthogonal modes (Zernike coefficients) made up of phase gradient and quadratic phase errors for tilt and focus correction, respectively. When these data are also extracted from the signal set, the remaining phase error residue is directed to a deformable mirror for Higher Order Aberration Control (HOAC).

The portion of the HEL beam reflected from the hole coupler plate #2 is reflected from a second deformable mirror and then directed through a set of gimbal relay optics. This set of optics is used to direct the HEL beam through the inner and outer gimbals of the tracking mount to the final beam

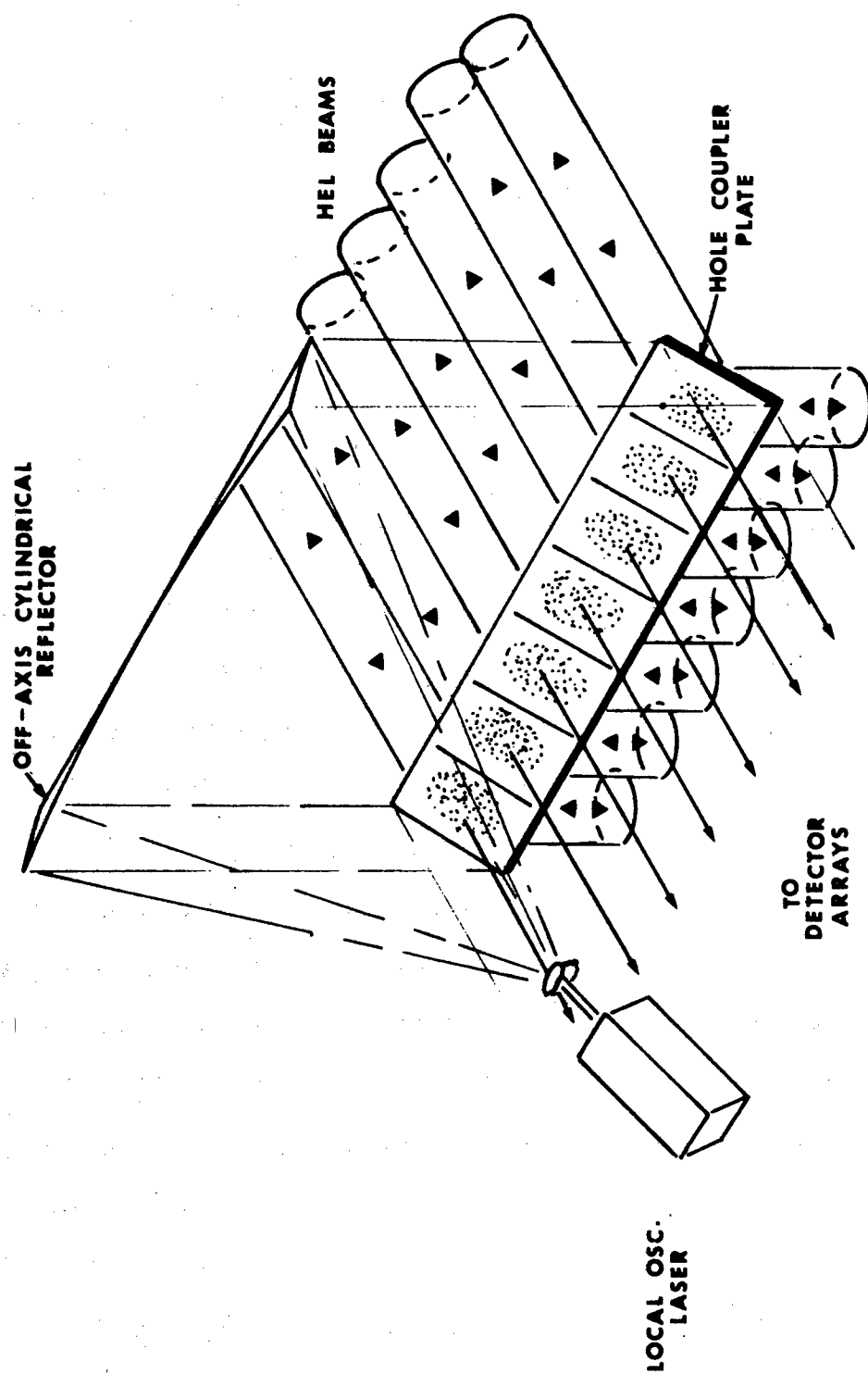


Figure VII-2. Optical Configuration for Providing a Common Local Oscillator to all Channels

expansion telescope (see Figure VII-3). Also shown in this figure are the locations of the X-tilt and Y-tilt mirrors shown in Figure VII-1. The last operator in the system is the beam expansion telescope. A drawing of a dimensional model of this operator developed for this investigation (discussed later in this chapter) is shown in Figure VII-4. The outgoing beam then propagates through the atmosphere to the satellite target where a 10 cm corner reflector returns some of the incident power back through the atmosphere and finally along the same optical circuit as the outgoing beam up to the hole coupler plate #1 (see Figure VII-1). Here, similar to the process used in the outgoing beam control, a portion of the return beam is extracted and sent to an array of low-level detectors. Again, the same local oscillator configuration, as shown in Figure VII-2, is used, except that for this case the local oscillator source is frequency tunable. This procedure is followed to reduce the bandwidth response of the detectors in the presence of large Doppler frequencies (see Figure VI-14) and also reduce the bandwidth requirements of the detection circuitry. The source considered for this local oscillator is a high-pressure capillary laser using a regenerative amplifier, so that we have both a broad frequency tuning range and a moderate output power (~ 10 watts at line center). The frequency of this device will be controlled in two ways. First, the ephemeris data processor will calculate anticipated Doppler frequency based on the satellite's line of sight velocity component and this will be used for control until a measurable return signal is obtained. At this time, the return signal processor will measure the beat frequency of the return signal and then produce a control signal to regulate the frequency of the local oscillator, so the beat is reduced to near zero.

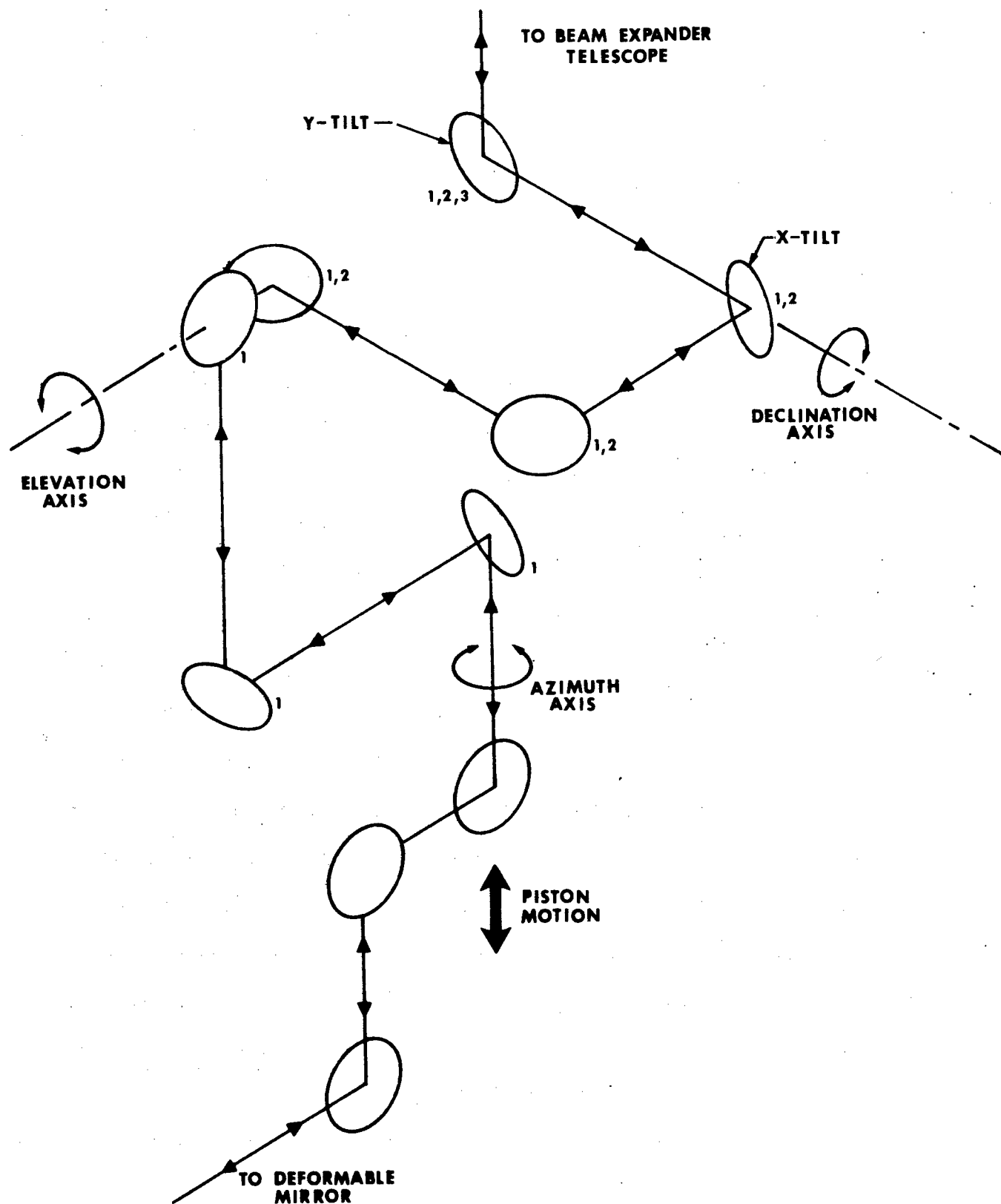


Figure VII-3. Gimbal Relay Optic Circuit. Mirrors Designated by 1 Move About the Azimuth Axis, 2 Indicates Motion About the Elevation Axis, and 3 Motion About the Declination Axis.

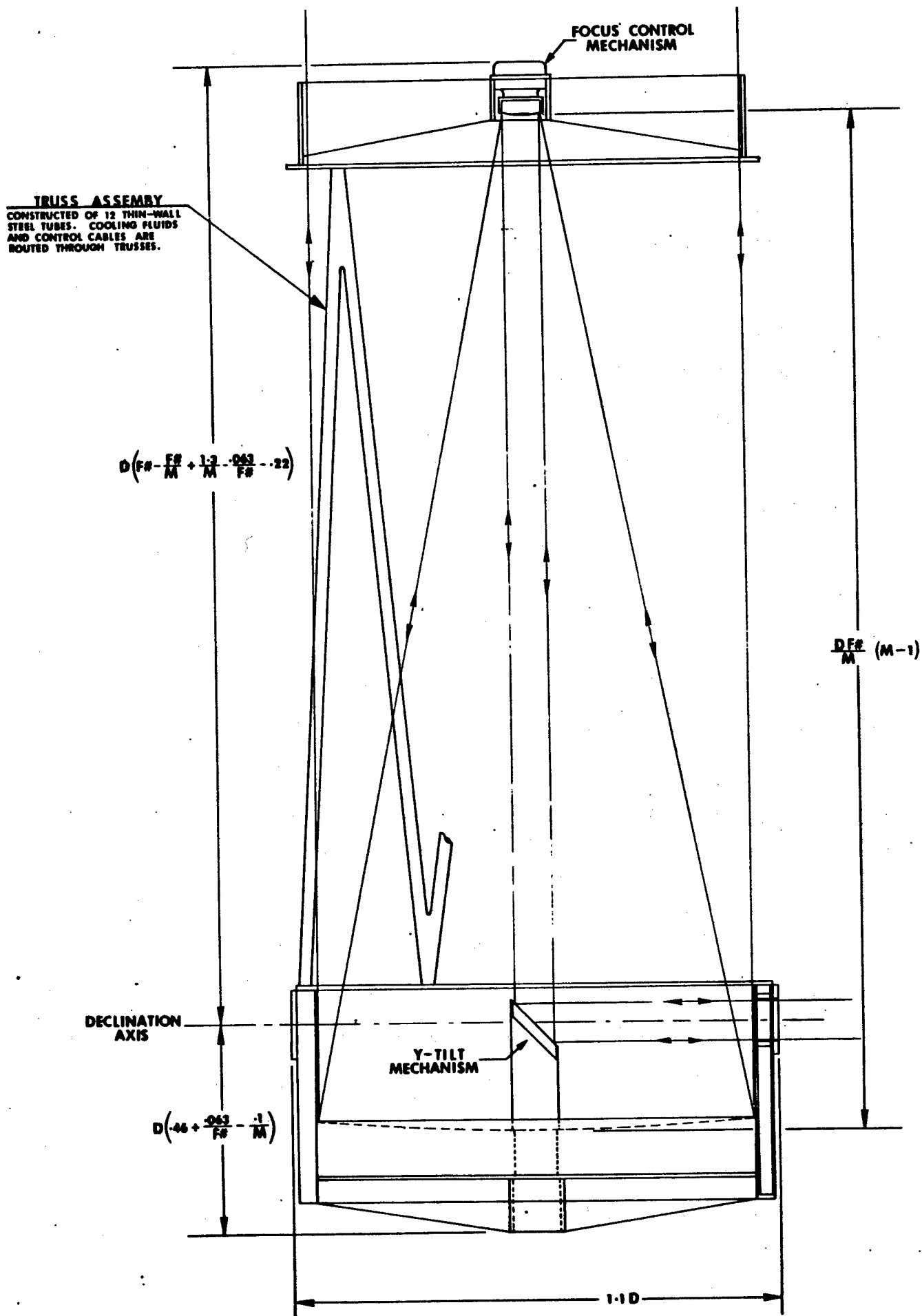


Figure VII-4. Beam Expansion Telescope Model

The return signal processor operational character is the same as that for the beam "clean-up" processor. That is, the beam control signals are determined by a similar process. The average piston phase error is transmitted to the "clean-up" processor where it is added to the average phase error produced there and in this way the proper output phase distribution (conjugate of that received) is produced at the array output. The phase gradient signals go to the X and Y tilt mirrors and the focus error is controlled with the beam expansion telescope. The remaining phase error residue is corrected by the deformable mirror that is just before the gimbal relay optics in the system optical circuit (see Figure VII-1). The return signal processor differs mainly from the beam "clean-up" processor in that it interacts with the ephemeris data processor (EDP). We have mentioned the target Doppler information, but the signal processor also gets lead angle information in the form of X and Y tilt information. Here, the EDP computes the lead angle (ratio of satellite velocity normal component to speed of light) and converts it into delta changes in the declination axis position (X-tilt) and elevation axis position (Y-tilt). The return signal processor uses these data to put in the correct X and Y tilt bias angles.

In Figure VII-1, we show that the EDP is supplied with several forms of basic data. The first is normal satellite launch parameters and orbital data obtained from standard techniques of microwave radar and passive optical tracking. This form of information can, under the better conditions, provide rms positional data of about 100 meters and the velocity to about 1 m/s. The second source of data comes from using the navstar global positioning system, or GPS. This system consists of 24 satellites at an orbital altitude of 2×10^4 km and in three different orbital planes. When fully operational in

1984, the system will allow our satellite target with relatively simple equipment on board to measure its position to an accuracy of 9 meters in the horizontal and 10 meters in the vertical about 90% of the time. These data can then be transmitted to the ground and fed directly into the EDP, so that it can compute pointing angles and rates for the tracking mount. Since all EDP computations must be made as a function of time, an accurate clock is provided for a time reference. In addition to pointing angles and rates, the EDP uses satellite position data to compute the piston motion for moving the tracking mounts up and down in an effort to keep the center-to-center spacing of the antenna elements constant for different pointing angles.

2. System Operation Chronology

In Figure VII-5 we show the details of a MSPA operation chronology. It starts with the actuation of the automatic optical alignment system. This is the 0.6328 μm alignment system shown in Figure VII-1, and is coupled into the system's optical circuit by means of an annular mirror and is reflected from the outer edge of system components, as shown in Figure VI-16. The beam continues through the optical circuit until it reaches the beam expansion telescope primary where it is reflected back on itself and returns along the same path until it reaches the alignment receiver located at the transmitter. This is basically an automatic autocollimator system and directs control signals to the X and Y tilt mirrors to compensate for alignment errors. If the measured alignment errors are outside the range of correction, a warning is given and then the error must be reduced manually until the system reaches its auto-control region. Next, all of the data processors are actuated and brief checkout algorithms are operated to assure correct performance. During the same time period, both local oscillator sources are turned on and each of the detectors in the two arrays is checked for response.

AUTOMATIC OPTICAL
ALIGNMENT SYSTEM
ACTUATED

(IF ANY ELEMENT IS
OUTSIDE RANGE OF
SMALL CORRECTIONS,
WARNING IS GIVEN)



ALL DATA PROCESSORS AND
BEAM CONTROL OPERATORS
ARE ACTUATED WITH BRIEF
AUTO CHECKOUT AND INITIAL
CONDITIONS SET (SYSTEM
CLOCK, ALL COMPUTATIONAL
AND CONTROL CONSTANTS)

STABLE OSCILLATORS
ACTUATED AND DETECTOR
ARRAYS CHECKED



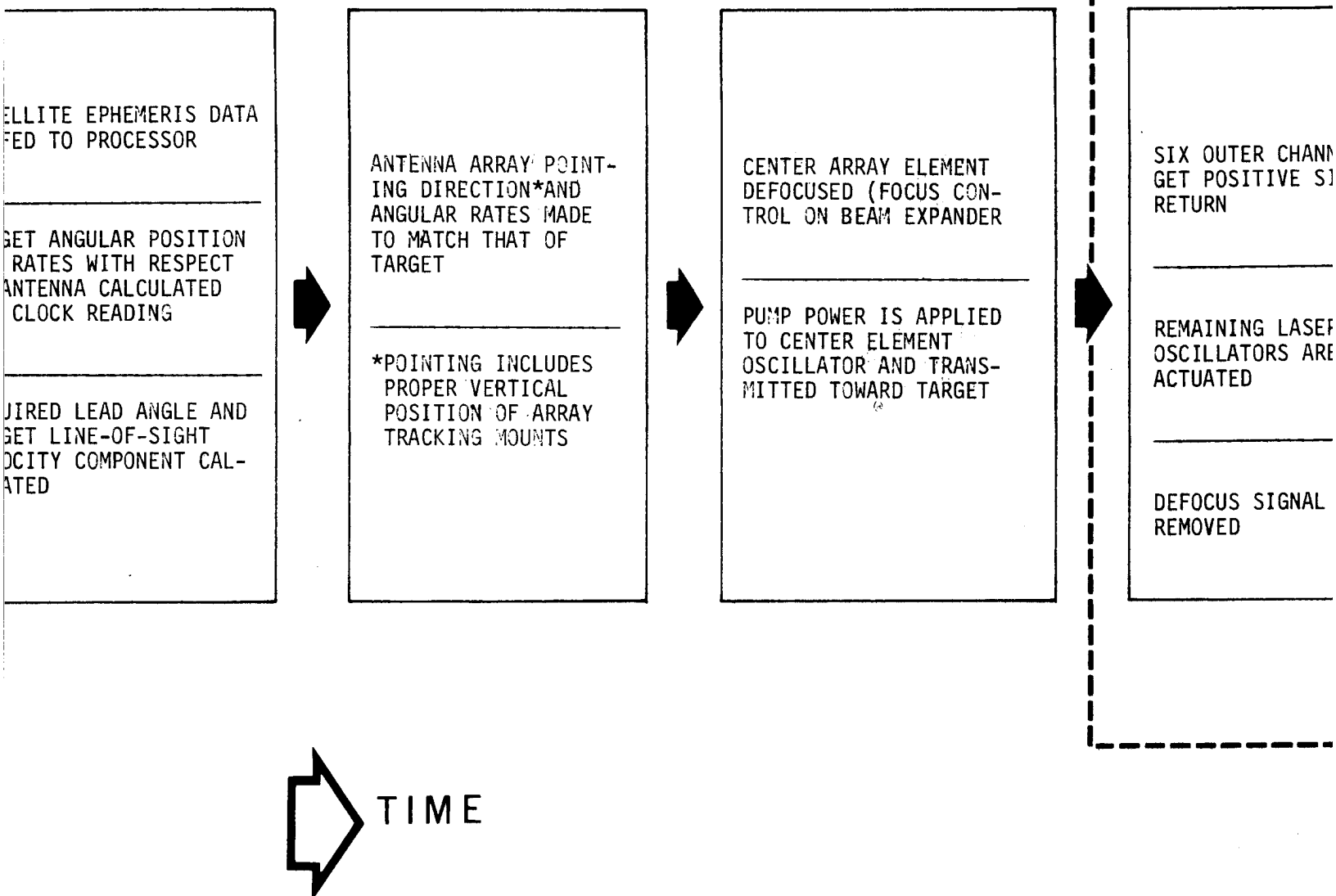
LASER SYSTEMS
CLOSED CYCLE
GAS FLOW IS
ACTUATED AND
FLOW CONDITIONS
STABILIZED



SATELLITE EPHEMERIS
IS FED TO PROCESSOR

TARGET ANGULAR
AND RATES WITH
TO ANTENNA CALCULATED
FOR CLOCK READING

REQUIRED LEAD AND
TARGET LINE-OF-SIGHT
VELOCITY COMPONENTS
CALCULATED



Figure

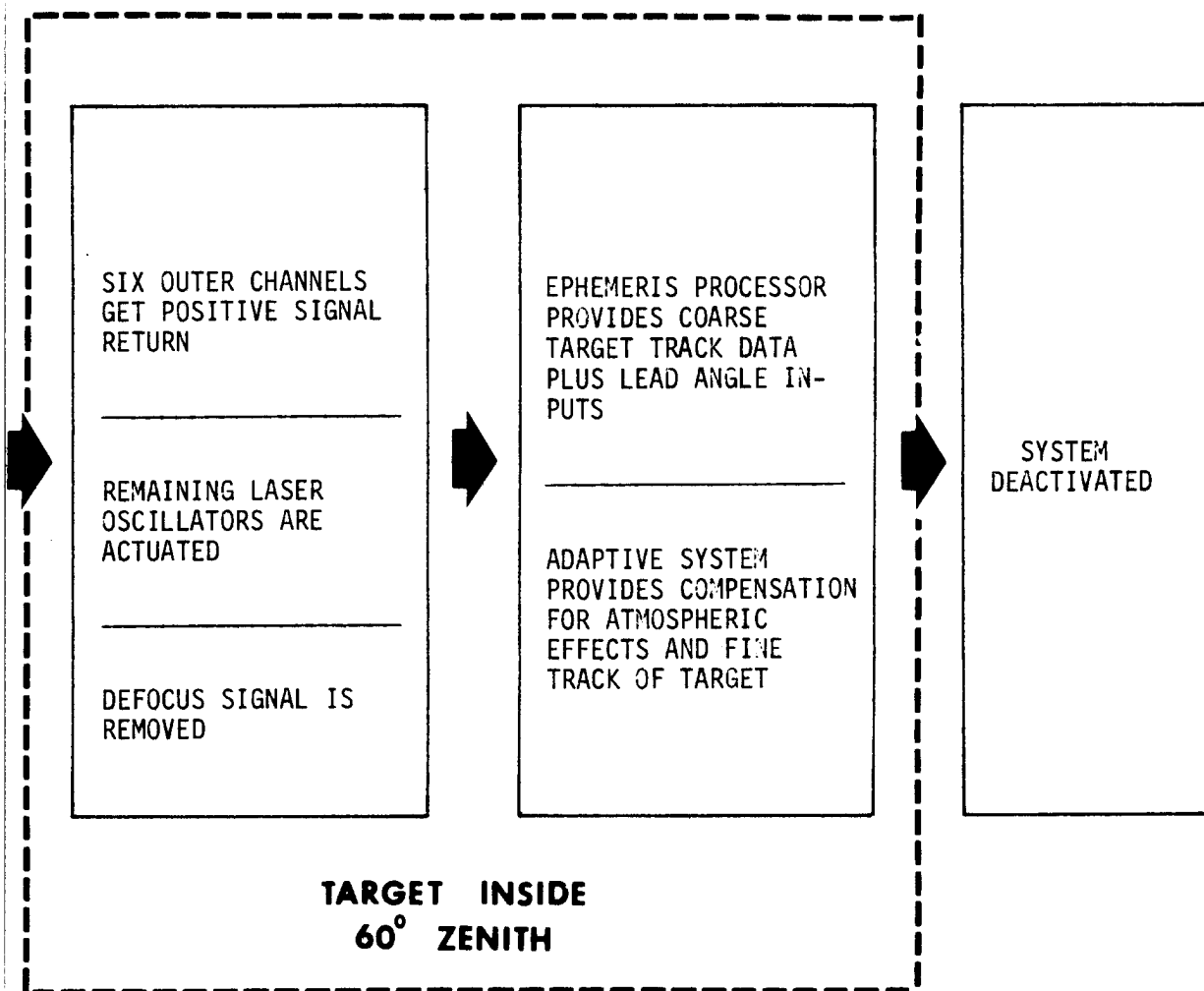


Figure VII-5. Multiple Source Phased Array Operation Chronology

Sometime before the satellite target crosses the horizon, the laser systems closed cycle (because of the cost of isotope lasants, closed cycle operation is required) gas flow pumps are actuated and the flow conditions stabilized. With this step under way, the satellite orbital data are fed into the EDP and the pointing angle and rates computations, as a function of time, are started. The lead angle x and y tilt components and Doppler frequency predictions are also started in this time frame. When the target is at about the 80° zenith position, the pointing and rate data are delivered to the tracking mounts, so that it can be brought up to speed without undue torque requirements. In this process, each mount is rotated in azimuth until the declination axis is set parallel to the predicted satellite ground track and then motion of the other two gimbals is started. Next in time, a focus control signal is sent to the center array element beam expansion telescope, so that it is slightly defocused, the pump power is applied to the center element oscillator, and its output transmitted to the target. When all of the low level detector arrays get a positive signal return from the target corner reflector the remaining six laser oscillators are actuated, the defocus signal is removed from the center element and the adaption process is started. For the remaining time period (~ 80 sec.) of the encounter, the EDP provides the coarse target track data and the adaptive system compensates for the atmospheric turbulence and thermal blooming effects and provides the fine track data. At the end of the encounter, the system is deactivated.

3. System Performance

As mentioned at the start of this chapter, we changed from the flood-light concept to the present one to improve the signal-to-noise conditions for target acquisition and this is indeed the case. Since heterodyne detection is used, we can express the signal to noise as measured at one of the detectors in the low level array as

$$S/N = \left\{ \frac{P_T}{k^2} \left(\frac{d_{cr} D_T}{\lambda R} \right)^4 \frac{\eta \lambda \epsilon_a^2 \epsilon_t \epsilon_r \alpha}{h c \Delta f} \right\}^{1/2} \quad (1)$$

where P_T is the power transmitted by a single oscillator (7.5×10^5 watts)

d_{cr} is the diameter of the corner reflector (.1 m)

D_T is the diameter of the output from the beam expansion telescope (1.37 m)

λ is the optical wavelength (9.1×10^{-6} m)

R is the maximum target range (370 km)

η is the detector quantum efficiency (0.5)

a is the atmospheric transmission (0.85)

r is the corner reflector reflectivity (0.8)

t is the system optical efficiency (0.5)

h is Planck's constant (6.626×10^{-34} J.S)

c is the speed of light (3×10^8 m/s)

Δf is the signal bandwidth (1×10^6 Hz)

α is the ratio of the sample hole area to the total beam area at the hole coupler #1.

For this system,

$$\alpha = \left(\frac{1 \times 10^{-3}}{2 \times 10^{-1}} \right)^2 \quad (2)$$

the parameter k in this expression is defined as

$$k = \frac{D_T^\theta}{\lambda}, \quad (3)$$

where θ is the output beam spread in radians. To produce a 100 m beam diameter in the target plane, $k \approx 40$. Using the parameter values listed, the expected signal to noise for acquisition is

$$S/N = 461,$$

which is more than adequate for positive acquisition.

B. Servo Systems

The system described is composed of three servo systems which all function in the same basic way; only the control variables are different. In one case, the control signals are modified by ephemeral data for tracking purposes, but the same techniques are applicable in implementing each control function. Perhaps the most important servo subsystem "locks" the lasers in frequency and phase to produce a coherent beam. Since the principles of operation which characterize this servo are the same for the beam clean-up and tracking subsystems, a general (simplified) approach to defining the filtering required is presented.

1. Laser Phase Lock Systems

Following standard techniques, the fundamental control loop is illustrated in Figure VII-6. The control elements are an optical phase detector, filter, and laser functioning as a voltage controlled oscillator. As in all servo loops, the controlling variable is an error voltage. In this particular case, the phase difference between optical frequencies (10^{13} Hz) generates the necessary driving function. The filter, $F(s)$, conditions this signal to suppress noise and set the dynamic response of the system. Ultimately, phase control of carriers having a cycle time of 10^{-13} to 10^{-14} seconds is to be established. The characteristics of the processing filter are the key to successful operation, along with performance parameters of the laser source.

To evaluate the requirements placed on $F(s)$, consider the following system equations written in LaPlace notation. From Figure VII-6,

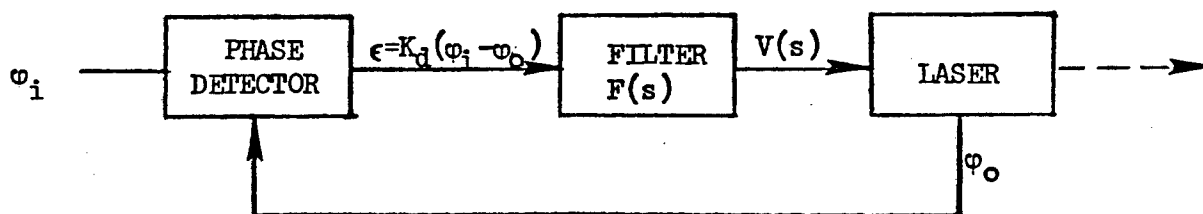


Figure VII-6. Basic Control Loop

$$\epsilon(s) = K_d [\varphi_i(s) - \varphi_o(s)] \quad (4)$$

$$V(s) = \epsilon(s) F(s) \quad (5)$$

$$\varphi_o(s) = \frac{K_L V(s)}{s}, \quad (6)$$

where K_d is the phase detector gain constant and K_L is the laser voltage/frequency conversion constant. Combining these equations

$$\epsilon(s) = \frac{s}{s + K_d K_L F(s)} \varphi_i(s). \quad (7)$$

Since the objective of the servo is to reduce the error $\epsilon \rightarrow 0$, the form of $F(s)$ can be specified for various types of input disturbances. To determine $F(s)$, recall the final value theorem

$$\epsilon(t) = \lim_{t \rightarrow \infty} \epsilon(t) = \lim_{s \rightarrow 0} [s \epsilon(s)]. \quad (8)$$

Since we require $\epsilon(t) = 0$ as $t \rightarrow \infty$,

$$\lim_{s \rightarrow 0} \left[\frac{s^2}{s + K_d K_L F(s)} \varphi_i(s) \right] = 0 \quad (9)$$

Consider a step change in the input phase signal $\phi_i(s) = \frac{\phi_1}{s}$. Then

$$\lim_{s \rightarrow 0} \left[\frac{s \phi_1}{s + K_d K_L F(s)} \right] = 0, \quad (10)$$

which yields $F(s) = C$, a constant gain factor. If the input is a ramp change in phase, $\phi_i(t) = \omega_0 t$, where ω_0 is the frequency difference between the input and the feedback from the laser, $\phi_i(s) = \frac{\omega_0}{s^2}$ and

$$\lim_{s \rightarrow 0} \left[\frac{\omega_0}{s + K_d K_L F(s)} \right] = 0. \quad (11)$$

To satisfy this condition $F(s) = \frac{C}{s}$, i.e., the filter must integrate the error signal.

If the input signal is a changing frequency $\phi_i(t) = \omega_1 t^2$, where ω_1 is the magnitude of the rate of change in rad/sec^2 ,

$$\lim_{s \rightarrow 0} \left[\frac{\omega_1}{s (s + K_d K_L F(s))} \right] = 0 \quad (12)$$

requires the form $F(s) = \frac{C(s)}{s^2}$. With this background, we are in a position to specify the character required of $F(s)$ for the laser phase-lock technique. Table VII-1 summarizes the results.

Table VII-1

Filter Type

Input	Type 0	Type 1	Type 2
$\phi(t)$	Zero Error	Zero Error	Zero Error
$\dot{\phi}(t) = \omega$	Constant Error	Zero Error	Zero Error
$\ddot{\phi}(t) = \omega$	Increasing Error	Constant Error	[Zero Error]

The type of filter refers to the number of poles at the origin. Thus, dependent upon the character of the reference and the laser which functions as the VCO, the requirement for the servo amplifier can be completely determined.

Typically, all laser sources display some degree of frequency instability. Thus, the minimum type of filter to be used is the Type 2 (see Table VII-1). Of course, the constraints of physical realizability must also be satisfied which leads to a second order function.

When combined within a loop with the variable oscillator, the filter function must also compensate those errors introduced by finite response times of available components. Ultimately, the overall system functional response—lock-on time, capture range, tracking range, are set by component limitations and available gain. However, experiments have shown the utility of this approach and have demonstrated the ability to match frequency and phase of an optical carrier to such a precision that independent lasers function as one laser.

To this point, laser operation can be described as rather routine. That is, phase-lock operation is achieved by basic servo principles, albeit, the carrier is 10^{13} Hz. The ability to control the relative phases among lasers has been limited to coincident (in-phase) operation. By modifying the control loop of Figure VII-6, total phase control among lasers is possible (Figure VII-7).

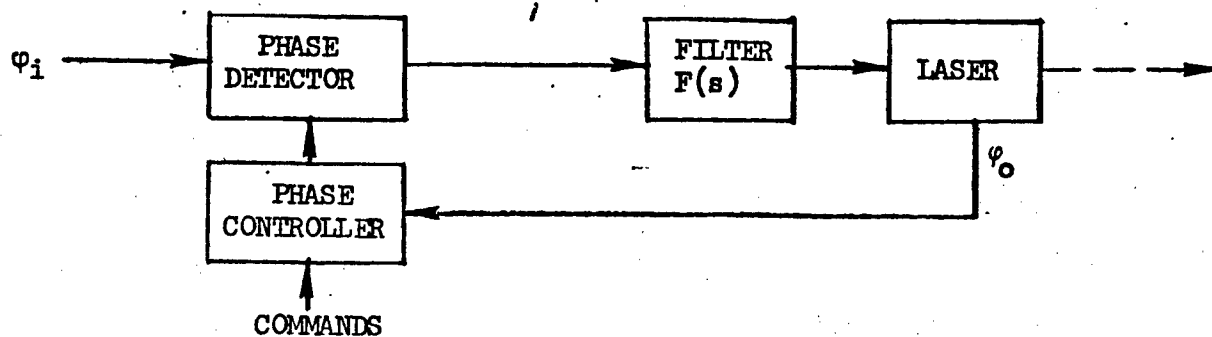


Figure VII-7. Modified Control Loop

In this configuration, the phase variable is programmable. Any functional phase distribution can be synthesized and maintained. For this system, compensation signals from the target adaption loop (return signal processor) directed to the command input modifies the frequency control loop to provide the necessary shift in phase to obtain coherent operation among the lasers referenced to the outgoing wave.

2. Target Adaption Loop and Beam "Clean-Up" Subsystems

The previous discussion described the processing required to achieve overall frequency (phase) control of the total array. Independent of this function is the requirement for spatially modifying the wavefront from each laser to achieve diffraction limited performance. Thus, two subsystems are necessary for each channel of the array; one to correct aberrations of the wavefront emitted from the sources and one to compensate for aberrations introduced by the atmosphere or elements in the transmitting path. Since the only difference between these two subsystems is the signal level which must be processed -- high for the "clean-up" loop and low for the target adaption loop -- operation of both can be described in the following discussion.

Figure VII-8 illustrates the basic elements of the servo system. The combination of the spatial beam sampler, spatial array of detectors, and the processor comprises the wavefront analyzer. Of interest is the control algorithm associated with a single channel as shown which consists of the HEL, x and y tilt mirrors, a focus control, a deformable mirror, and the wavefront analyzer optically coupled to a stable local oscillator.

The stable oscillator provides a reference phase, ϕ_0 , which is mixed with the laser signal, ϕ , which may be aberrated. Let x_i and y_j represent an aperture point in the laser beam being sampled by the i,j th detector. The detector output produces the signal, $\Delta\phi$,

$$\Delta\phi(x_i, y_j) = \Delta\phi_{ij} = \phi(x_i, y_j) - \phi_0. \quad (13)$$

The objective of the control system is to drive the quantity S to some value which would assure diffraction-limited performance:

where

$$S = \sum_i \sum_j (\Delta\phi_{ij})^2 < (2\pi/20)^2 N, \quad (14)$$

and N is the number of detectors.

To accomplish this objective and to make full use of the lower order (tilt and focus) controls, the signals $\Delta\phi_{ij}$ are decomposed into a Zernike orthonormal expansion,

$$\Delta\phi_{ij} = \sum_k a_k Z_k(x_i, y_j), \quad (15)$$

where the functions $Z_k(x,y)$ are the normalized Zernike polynomials. The aperture coordinates x_i and y_j are assumed to be normalized to a unit semi-diameter aperture. Thus, the mean square wavefront error turns out to be the sum of the a_k^2 coefficients over k . Furthermore, the coefficients a_k are proportional to the particular control signals we are seeking.

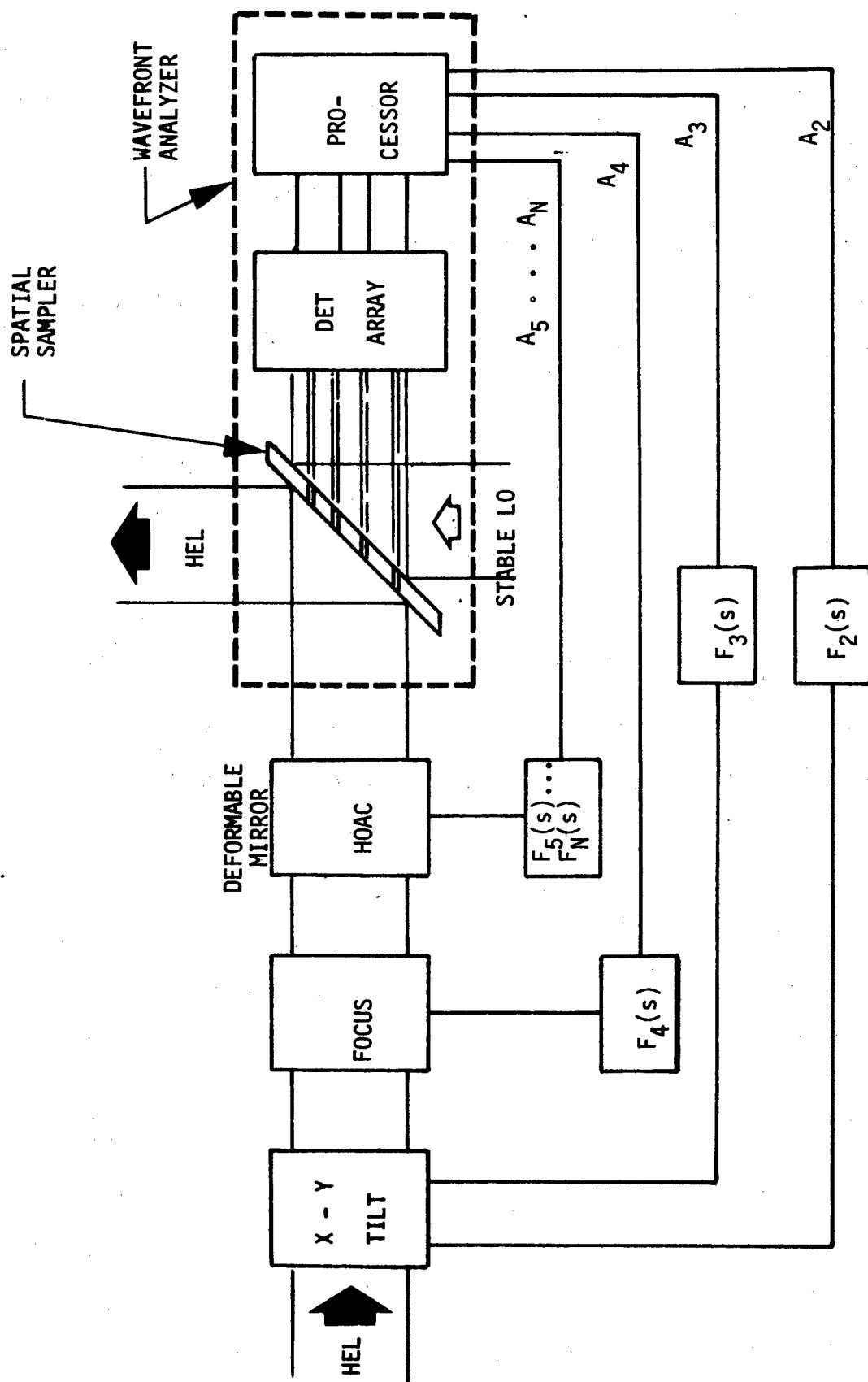


Figure VII-8. Beam Clean-up Control Loop (Target Adaption Control Loop)

The first few terms of the expansion in Eq. (15) are

$$\Delta\phi_{ij} = \frac{1}{N} [a_1 + 2a_2x_i + 2a_3y_j + \sqrt{3} a_4(2x_i^2 + 2y_j^2 - 1) + R(x_i, y_j)] \quad (16)$$

The function $R(x, y)$ represents the higher order aberrations. It is defined as the residual after the four other terms have been subtracted. This residual function R determines the control signals for the deformable mirror actuators. The quantity a_4 is the focus control signal, a_3 and a_2 are Y and X tilt signals, and a_1 is the piston phase error.

The purpose of the processor is to determine these coefficients a_j . Due to the orthogonality of the Zernike functions, all of these coefficients may be evaluated as simple weighted sums of $\Delta\phi_{ij}$.

$$a_k = \sum_{ij} Z_k(x_i, y_j) \Delta\phi_{ij} \quad (17)$$

Thus, the piston phase error is just the mean of $\Delta\phi_{ij}$. The x and y tilts are means of the measurements $\Delta\phi_{ij}$ weighted by x_i and y_j , the detector positions.

A particular advantage of this heterodyne detection system over Shearing interferometer or Hartmann sensors (direct detection) is immediately obvious. The phase errors are determined directly. That is, they are not deduced from aperture phase difference measurements. Furthermore, the implementation of the weighted signal summations is straightforward.

The cross coupling between correction loops is essentially eliminated by using the orthogonal decomposition. This means that for a given detection-correction period, the order of applying the adaptive tilt and focus adjustments makes no difference on the stability of the control loops. This same statement will also apply to the deformable mirror if its control modes can

also be chosen to be orthogonal over the aperture. Further analysis of this point with regard to the deformable mirror, however, must await more detailed definition of the deformable mirror.

The target adaption loop operation is basically the same algorithm as the beam "clean-up" system with the filter functions, $F_x(s)$, determined to drive the error signals (a_x) to zero. Typically, a type 1 system is all that will be required. Only a slight change in implementation is required to accommodate the ephemeral data for keeping energy on the target.

3. Ephemeral Processor and Distribution

Interaction of the system with the target introduces two additional processing inputs; Doppler frequency offset due to the moving target and a lead angle requirement due to the finite velocity of light.

The Doppler offset will vary with the encounter geometry from 0 Hz to 1.3 GHz and would require broadband processing if not compensated. Since the orbiting parameters are known to good precision (see previous discussion), the amount of frequency shift is well known. Tracking loops based upon electronic or tunable laser oscillators are available to reduce the effective bandwidth and keep the processing signal within a specified frequency range. As shown in Figure VII-6, the optical technique reduces the bandwidth requirements of the optical phase detectors and was chosen on that basis.

The lead ahead angle can also be computed very precisely, since the cross velocity of the satellite is also known very accurately. Thus, the amount of bias angle which must be introduced between the receiver and transmitter in the x-y tilt servo of target adaption loop is well defined. Thus, operating under closed loop control, the lead ahead command is continuously updated and used to direct energy to the intercept point on a real time basis.

C. Intermediate Optics Considerations

1. Irradiance Mapping Thermal Distortion

A high power laser beam incident on a water cooled reflecting element within the optical train heats the surface, causing it to distort. The surface distortion can be calculated on the assumption that it is a mapping of the incident intensity profile. Under steady state conditions, the surface deformation is given by

$$\Delta l(x,y) = a \epsilon_1 I(x,y) \cos \theta_i, \quad (18)$$

where a is the absorption coefficient, $I(x,y)$ is the intensity of the incident beam, θ_i is the incident angle, and ϵ_1 is an irradiance mapping thermal distortion parameter. From a simple mirror model previously developed,¹ the theoretical value of ϵ_1 is

$$\epsilon_1 = \alpha l^2 / 2K, \quad (19)$$

where α is the thermal expansion coefficient, l is the faceplate thickness, and K is the thermal conductivity. Recent experimental and calculated data indicate that ϵ_1 is a function of mirror diameter d , as well as incident angle θ_i . An approximate empirical value for ϵ_1 is

$$\epsilon_1 = \epsilon_1 (7/20) 10^{-8} d / \cos \theta_i (\text{cm}^3/\text{watt}), \quad (20)$$

where d is measured in cm and ϵ_1 is a constant whose value is expected to depend upon the state of cooled mirror technology. The phase error associated with the deformation $\Delta l(x,y)$ is given by

$$\Phi_M(x,y) = \frac{4\pi}{\lambda} a \epsilon_1 I(x,y) \cos^2 \theta_i, \quad (21)$$

and the rms phase error for a train of m mirrors is

$$\phi_M = \frac{4\pi}{\lambda} I_{\text{rms}} \sum_{i=1}^m a_i \xi_1(d_i, \cos \theta_i) \cos^2 \theta_i, \quad (22)$$

where the assumption has been made that all mirrors in the optical train are in the near field of the laser beam, so that phase errors due to the mirror distortions add coherently. It is convenient to relate the rms laser intensity to the average laser intensity through the relation

$$I_{\text{rms}} = \epsilon_0 I_{\text{ave}}, \quad (23)$$

where ϵ_0 ($0 \leq \epsilon_0 \leq 1$) is a measure of the amount of intensity variation across the beam.

The irradiance mapping thermal distortion phase error for the optical circuit of Figure VII-1 is calculated using the following parameter values:

$$\theta_i = 45^\circ \quad (i = 1 \text{ to } 18)$$

$$\theta_i = 0^\circ \quad (i = 19)$$

$$\epsilon_0 = 0.5$$

$$\epsilon_1 = 1.5$$

$$a_i = 2 \times 10^{-3} \quad (i = 1, 18)$$

$$A_i = 10^{-2} \quad (i = 19)$$

$$\xi_1(d_i, \cos \theta_i) = 7.4 \times 10^{-8} \text{ cm}^3/\text{W} \quad (i = 1 \text{ to } 3)$$

$$\xi_1(d_i, \cos \theta_i) = 14.8 \times 10^{-8} \text{ cm}^3/\text{W} \quad (i = 4 \text{ to } 18)$$

$$\xi_1(d_i, \cos \theta_i) = 9 \times 10^{-7} \text{ cm}^3/\text{W} \quad (i = 19)$$

$$d_i = 10 \text{ cm} \quad (i = 1 \text{ to } 3)$$

$$d_i = 20 \text{ cm} \quad (i = 4 \text{ to } 18)$$

$$d_i = 1.67 \text{ m} \quad (i = 19)$$

Substituting these parameter values into Eq. (22) yields a total rms phase error

$$\phi_M = 4.5 \times 10^{-2}$$

for a laser power of 5/7 MW. For a seven element array of total power 5 MW, if the phase errors in each channel are uncorrelated, then the total phase variance is

$$\phi_T^2 = 7\phi_M^2 = .014$$

and the loss of peak far field intensity is estimated from the Strehl ratio

$$I/I_0 = e^{-\phi_T^2} \quad (24)$$

to be only 1.4%. Since the 2 m diameter receiver of the satellite is equal to $5(\lambda R/D)$ at the 185 km range, if $D = 4.8$ m, the loss of power collected in the 2 m diameter bucket will be even less than 1.4%. Therefore, irradiance mapping thermal distortion is not a significant error source for the 5 MW optical system.

2. Thermal Bowing

A second distortion mode of a high power mirror is a bowing of the mirror surface due to axial temperature gradients, which is modeled as spherical aberration. The amount of mirror sag, δ , is written as

$$\delta = \xi_2 a I_{ave}, \quad (25)$$

where ξ_2 is a "bowing" constant, which is modeled by the equation

$$\xi_2 = \epsilon_2 \left(\frac{d}{\cos \theta_i} - 10 \right) 10^{-8} \text{ (cm}^3/\text{watt)}, \quad (26)$$

where d is in cm and ϵ_2 is a constant whose value reflects the state of cooled mirror technology. The phase error variance due to faceplate sag is given by

$$\phi_B = (r/\sqrt{45})(2\pi/\lambda) \epsilon_0 I_{ave} \sum_{i=1}^m \xi_2 \tan \theta_i \sin \theta_i. \quad (27)$$

The estimated value of ϕ_B is even smaller than the irradiance mapping phase error ϕ_M , and can be ignored.

D. Tracking Mount

The tracking mount originally suggested for the MSPA system was a straightforward single-gimbal azimuth-elevation (Az-El) configuration, as shown in Figure VI-16. For tracking a low earth orbit satellite, however, the required azimuth axis angular accelerations, and consequently the drive torque, is excessive. This can clearly be demonstrated if we use a "flat earth" approximation, the Az-El configuration schematic shown in Figure VII-9 and the angle designations given in Figure II-1. For the azimuth axis, if we let

$$K = \frac{OD}{(-OD \tan \phi_0 + Vt)} \quad (28)$$

where

$$\phi_0 = \cos^{-1} \left(\frac{OD}{R \tan \theta_0} \right) \quad (29)$$

OD is the offset distance of the satellite ground

track from the transceiver

θ_0 is the initial elevation angle

R is the satellite orbit altitude

t is time, and

v is the satellite linear velocity

where

$$v = \left(\frac{G m_e}{r_e + R} \right)^{1/2} \quad (30)$$

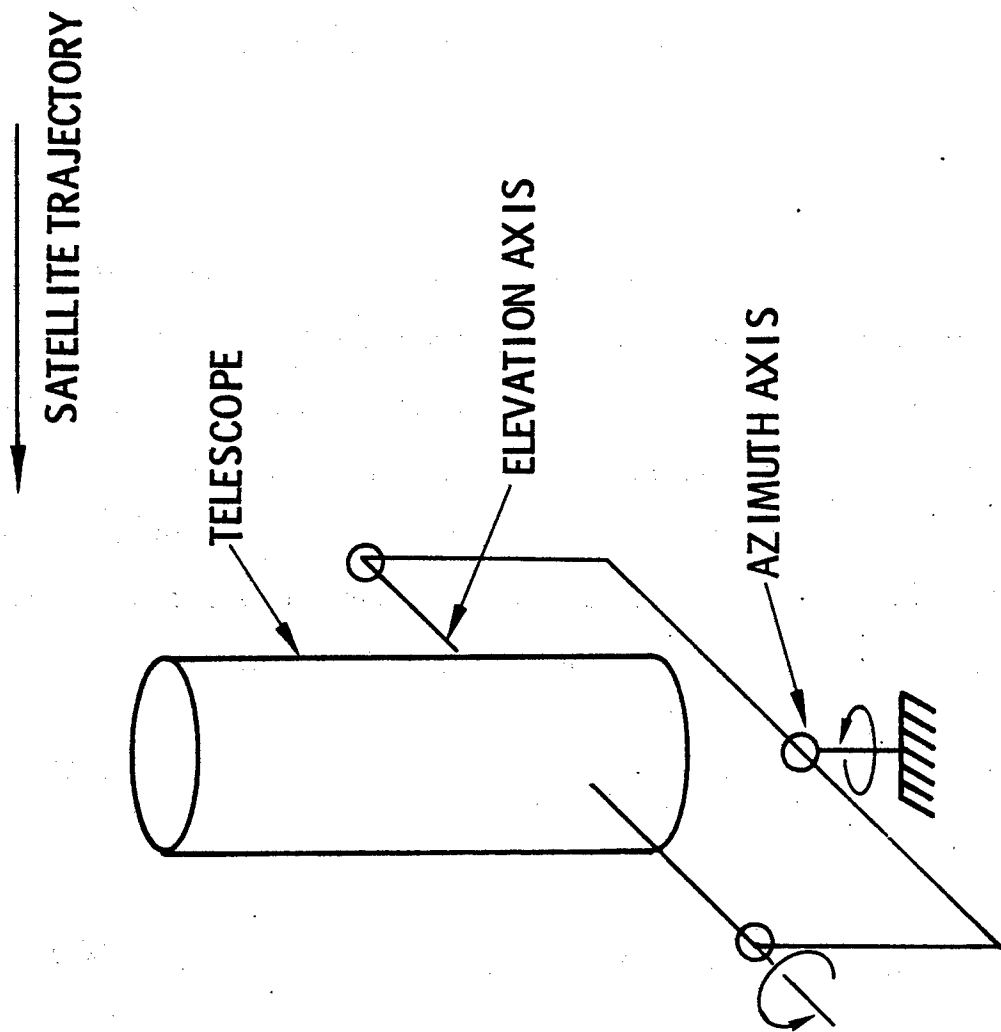


Figure VII-9. Azimuth-Elevation Tracking Mount Configuration

G is the gravitational constant

m_e is the earth's mass, and

r_e is the radius of the earth,

then the azimuth angle as a function of time can be written as

$$\phi(t) = \sin^{-1} \left(\frac{1}{1 + K^2} \right)^{1/2}. \quad (31)$$

These data are plotted in Figure VII-10. From Eq. (31) we can determine the angular velocity, which is

$$\dot{\phi}(t) = \frac{V}{OD} \frac{K^2}{1 + K^2} \quad (32)$$

and the angular acceleration

$$\ddot{\phi}(t) = 2 \left(\frac{V}{OD} \right)^2 \frac{K^3}{(1 + K^2)^2}. \quad (33)$$

These data are presented in Figures VII-11 and VII-12, respectively. The angular acceleration data indicate that if the offset distance was always large, the drive torque (plus gimbal and telescope stiffness) could be kept to reasonable values. However, it is clear from these data that designing a mount to perform for offset distances of less than 50 km, as well, would be costly. Therefore, this configuration was dropped from consideration.

A tracking mount configuration which solves the problem of large angular accelerations is shown schematically in Figure VII-13. This arrangement adds the complication of an additional gimbal, which, in turn, requires three additional mirrors in the gimbal relay optics, but it reduces the angular acceleration requirements to values that are readily controlled without

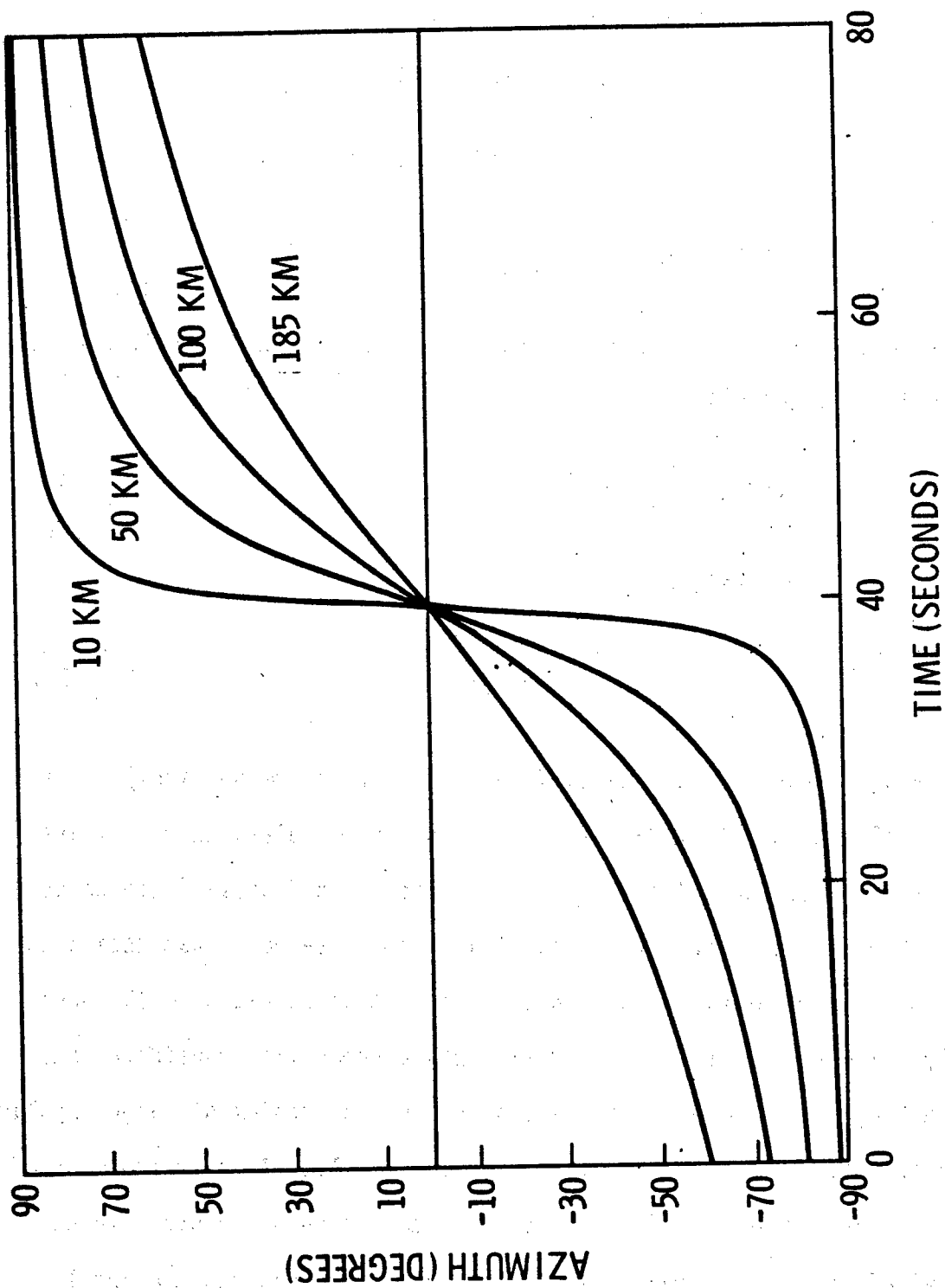


Figure VII-10. Azimuth Angle Versus Time for Various Track Offsets

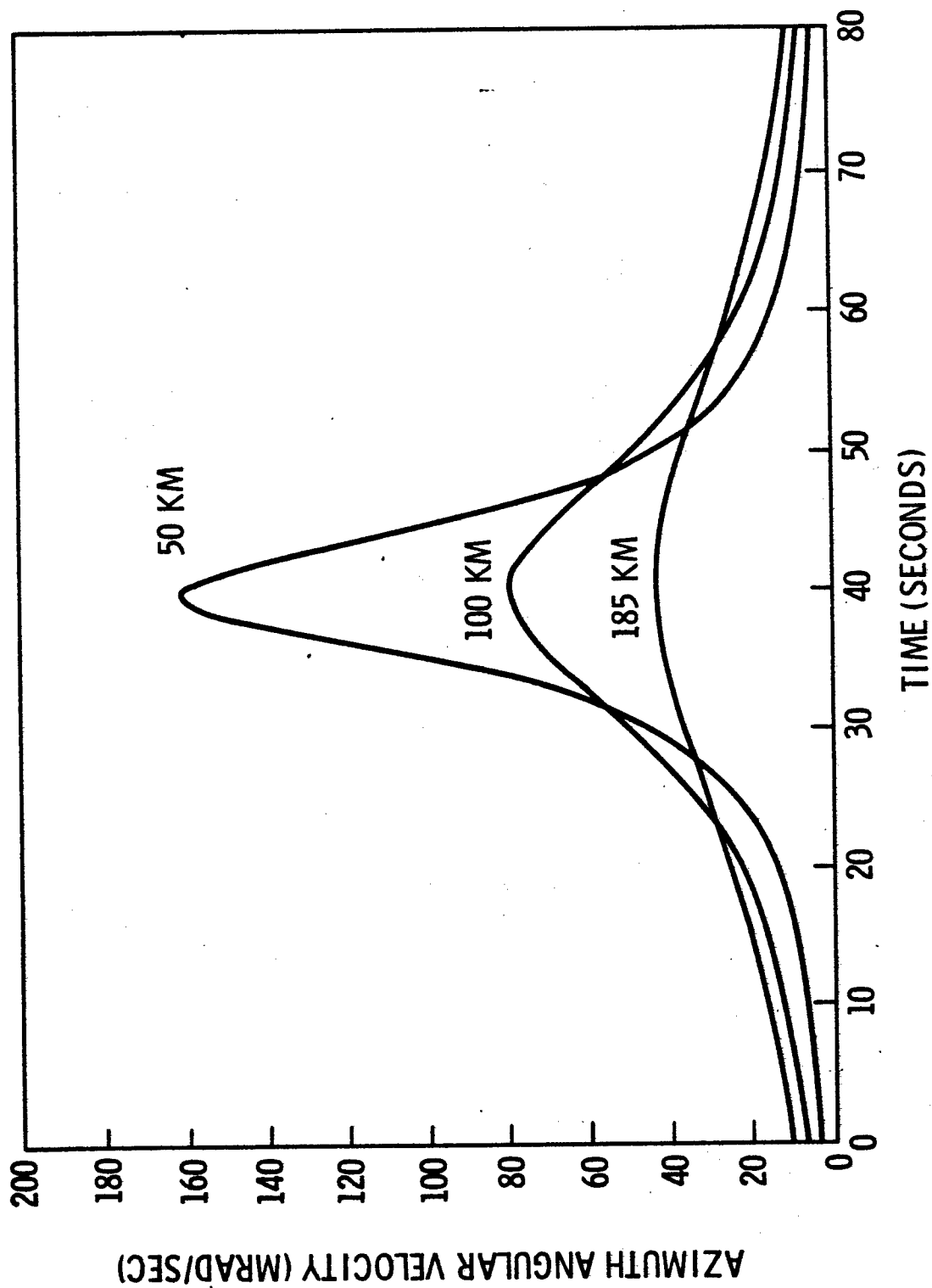


Figure VII-11. Azimuth Angular Velocity Versus Time for Various Track Offsets

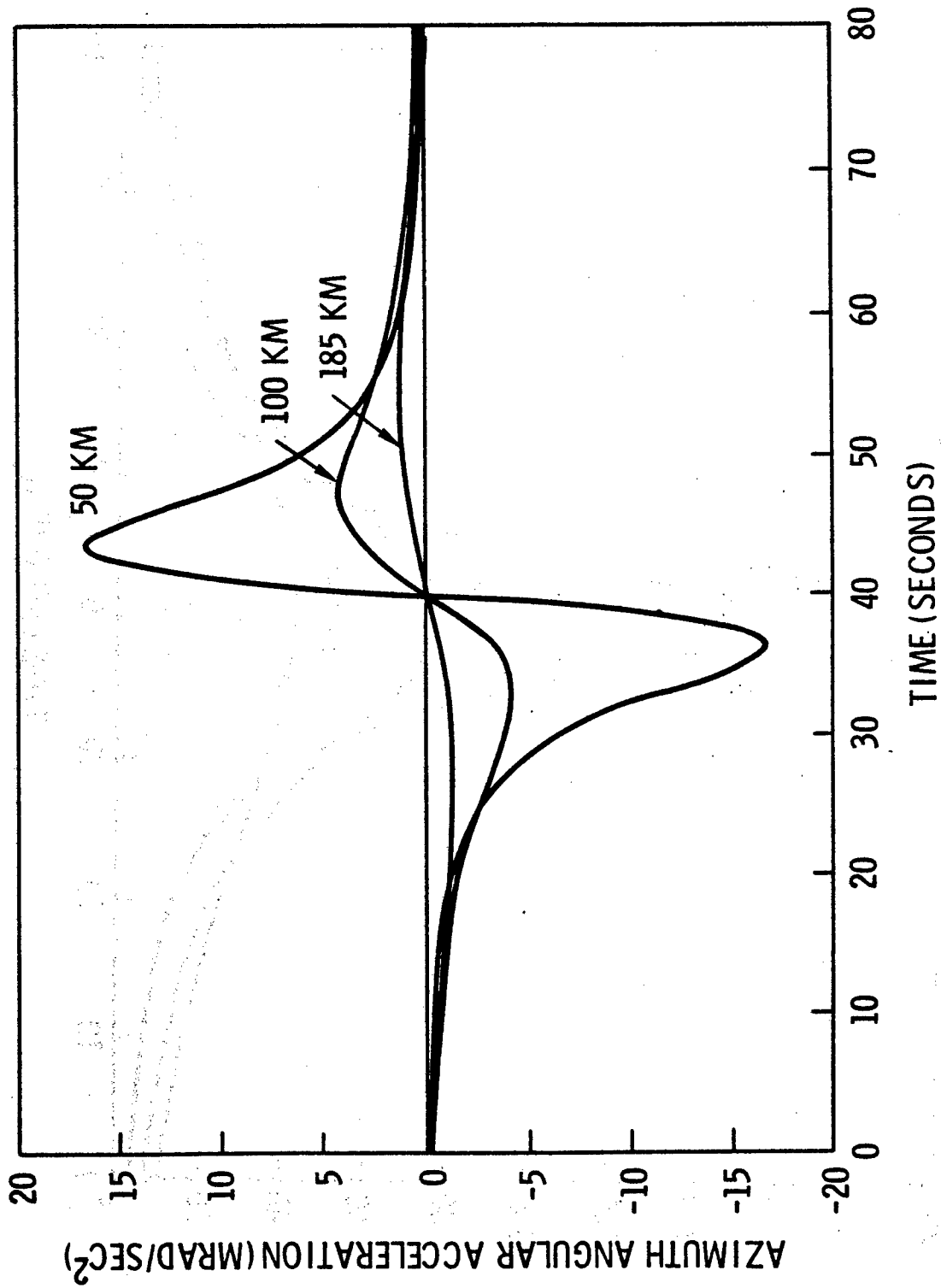


Figure VII-12. Azimuth Angular Acceleration Versus Time for Various Track Offsets

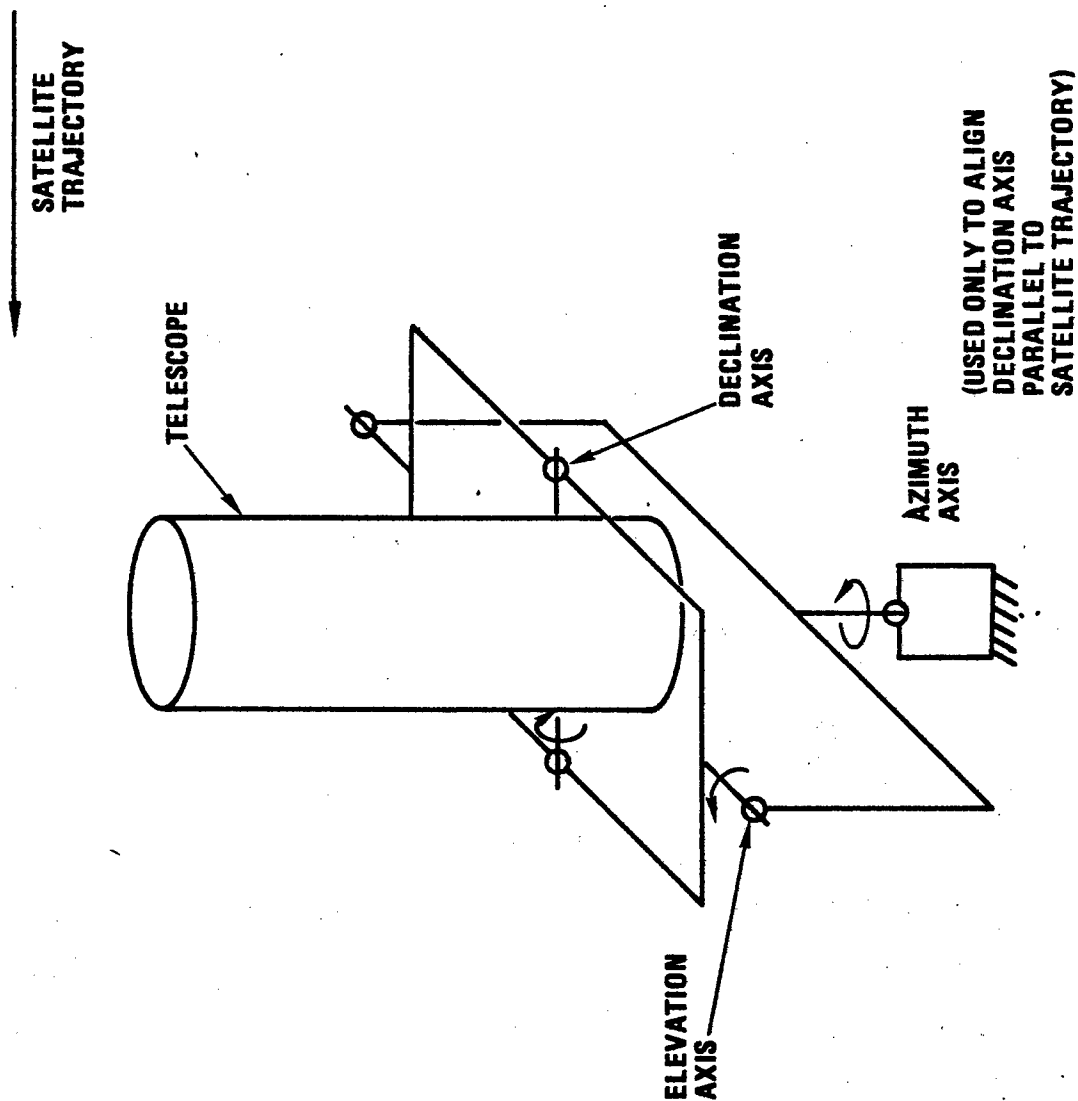


Figure VII-13. Elevation-Declination Tracking Mount Configuration

extraordinary design considerations. With this configuration, if we consider that prior to the satellite fly-by, the azimuth axis is rotated to a position so that the declination axis is parallel to the ground track, then the equations of angular motion can be written in the following manner. For the elevation axis, if we assume

$$J = \frac{R}{(-R \tan \theta_0 + Vt)} , \quad (34)$$

then the angular position with time is

$$\theta(t) = \sin^{-1} \left(\frac{1}{1 + J^2} \right)^{1/2} \quad (35)$$

and is plotted in Figure VII-14, the angular velocity is

$$\dot{\theta}(t) = \frac{V}{R} \frac{J^2}{1 + J^2} \quad (36)$$

plotted in Figure VII-15, and the angular acceleration is

$$\ddot{\theta}(t) = -2 \left(\frac{V}{R} \right)^2 \frac{J^3}{(1 + J^2)^2} \quad (37)$$

plotted in Figure VII-16. As the equations show, the angular motion of this axis is independent of the offset distance and the angular acceleration requirements are quite mild; less than 1.5 mrad/sec². For the declination axis, if we use Eq. (34), the angular position as a function of time can be written as

$$\psi(t) = \tan^{-1} \left[\frac{OD}{R} \left(\frac{J^2}{J^2 + 1} \right)^{1/2} \right], \quad (38)$$

with the values plotted in Figure VII-17. If we let

$$\frac{OD}{R} = \gamma ,$$

then the angular velocity for this axis can be expressed as

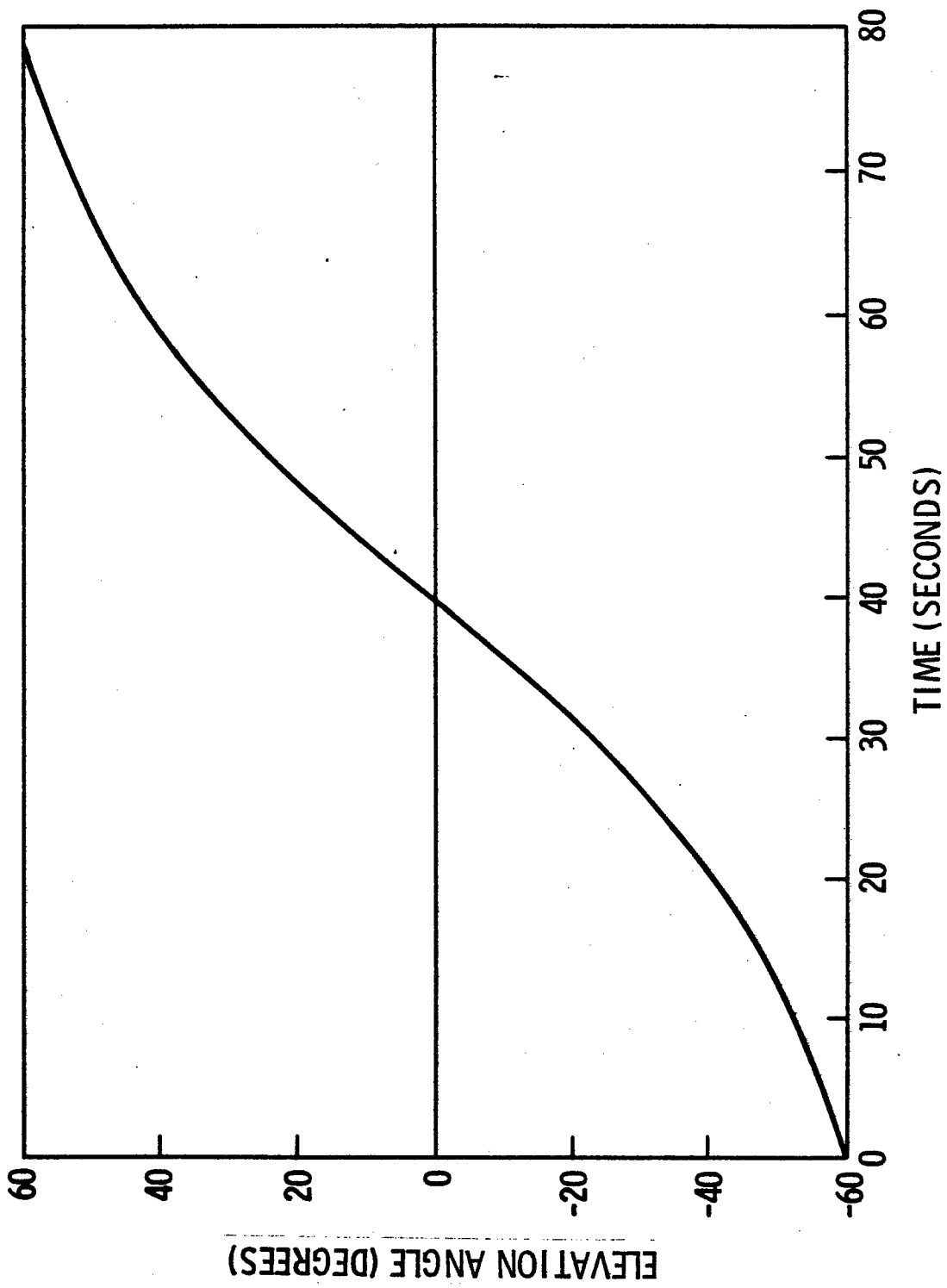


Figure VII-14. Elevation Angle Versus Time

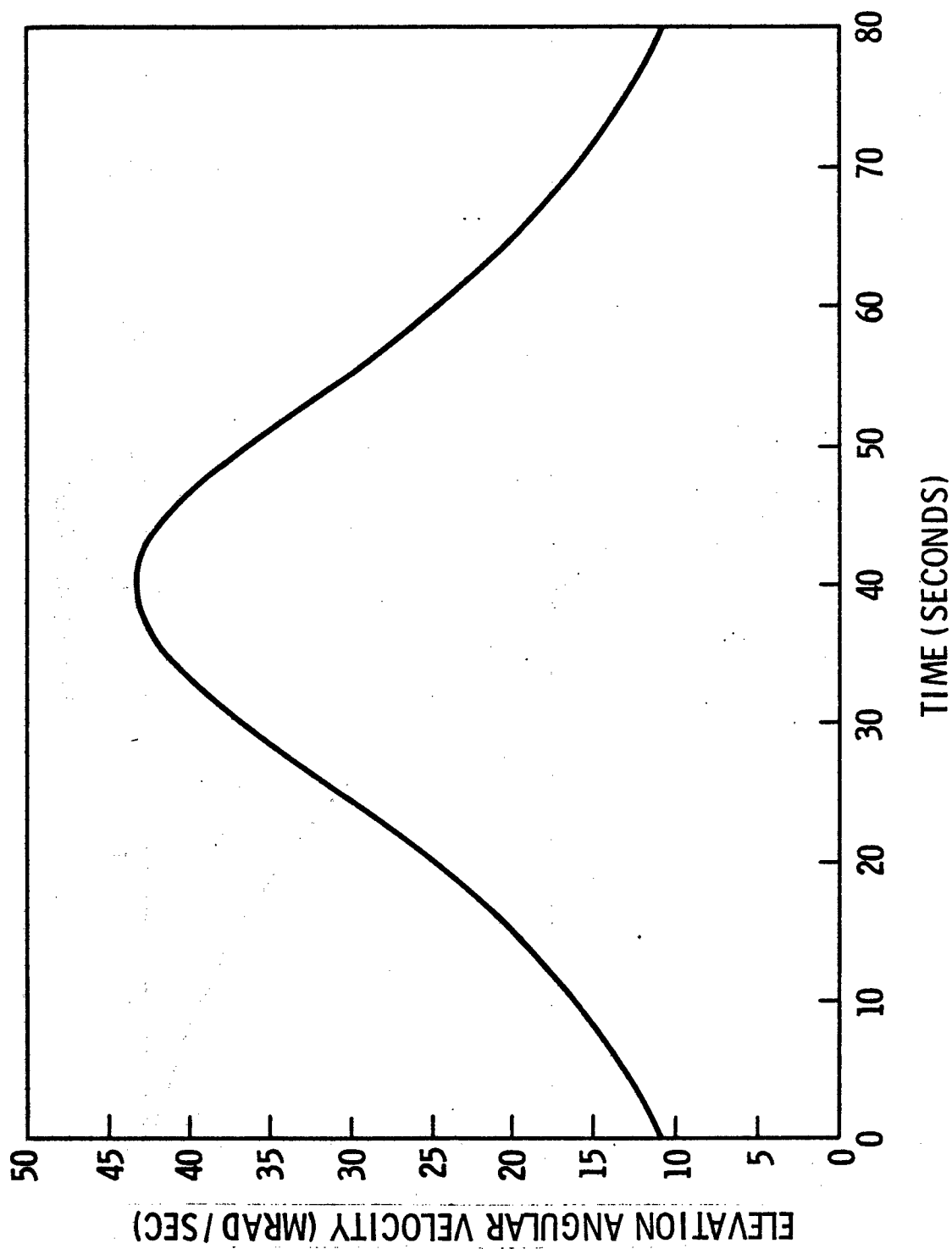


Figure VII-15. Elevation Angular Velocity Versus Time

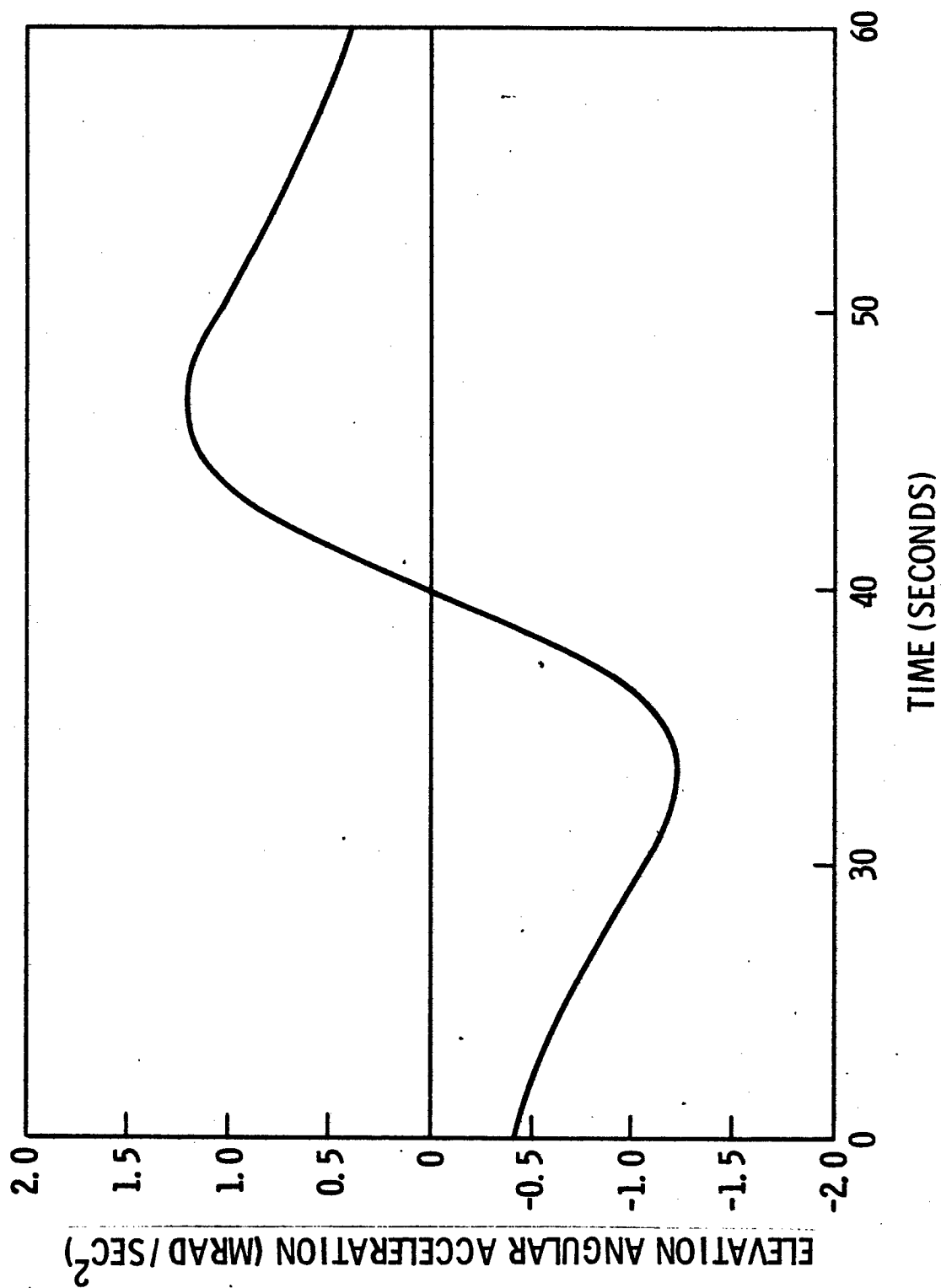


Figure VII-16. Elevation Angular Acceleration Versus Time

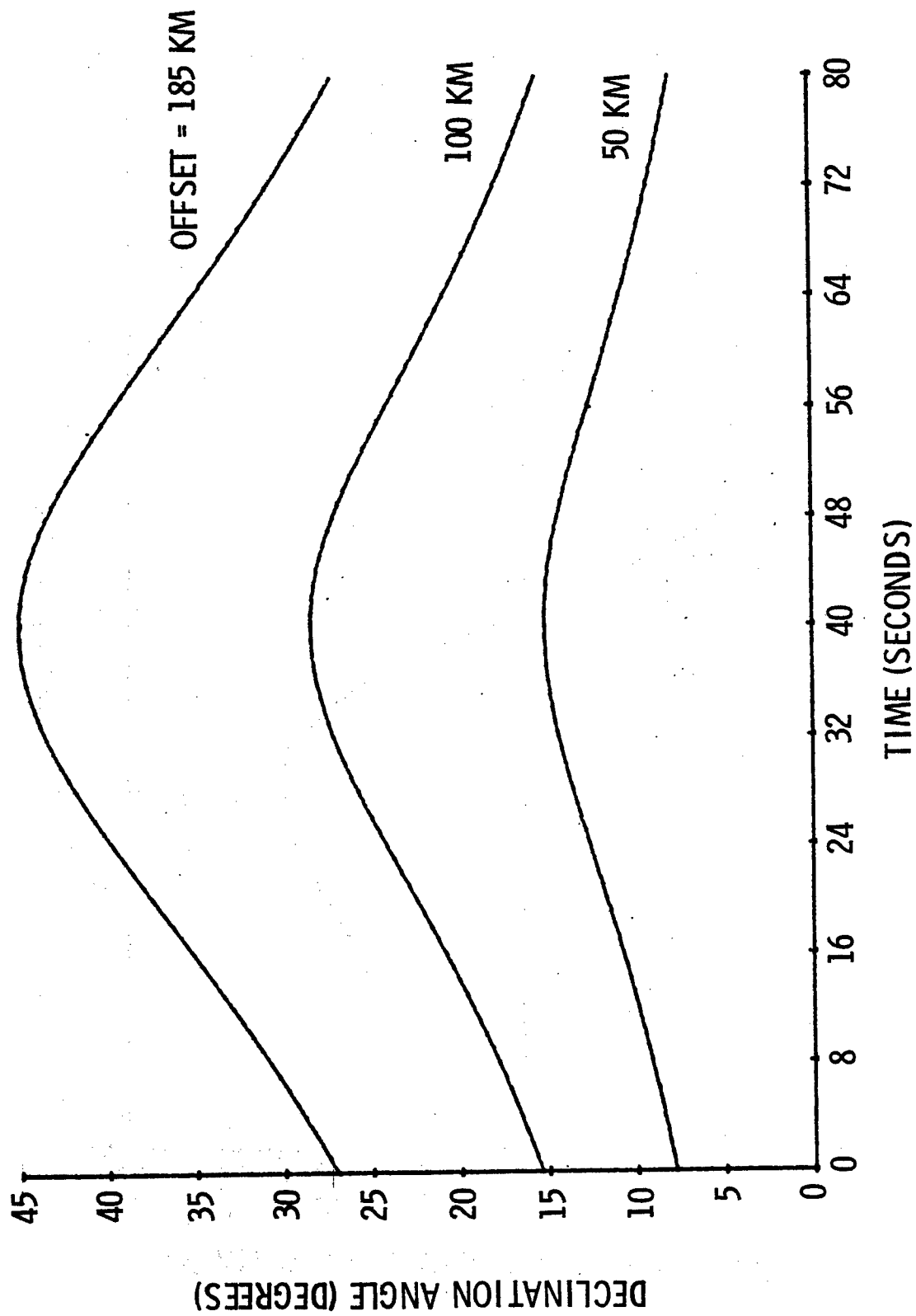


Figure VII-17. Declination Angle Versus Time for Various Track Offsets

$$\dot{\psi}(t) = \frac{\gamma V}{R} \frac{J^2}{(1 + J^2)^{1/2}(1 + J^2(1 + \gamma^2))} , \quad (39)$$

where $\dot{\psi}(t)$ is positive for negative values of J and negative for positive values, and the angular acceleration as a function of time is

$$\ddot{\psi}(t) = \gamma \left(\frac{V}{R} \right)^2 \left\{ \frac{(2 + J^2 - J^4(1 + \gamma^2)) J^2}{\{(1 + J^2)^{1/2}(1 + J^2(1 + \gamma^2))\}^2} \right\} . \quad (40)$$

The angular velocity and acceleration as a function of time is shown in Figures VII-18 and VII-19. These results indicate that the maximum angular accelerations on this axis are even less than that required for the elevation axis. In our opinion, the mild angular acceleration requirements of this tracking mount configuration would, in practice, more than offset the cost of an additional gimbal and the extra gimbal mirrors. Therefore, we selected it for use in the MSPA system.

For the output antenna of the MSPA system, the tracking mounts with beam expansion telescopes are assembled in a close-packed hexagonal arrangement, as shown in Figure VII-20. With the units in such a configuration as the satellite target is tracked during the encounter period, the center-to-center spacing between the units will change. In an effort to keep this spacing small, we have mounted each of the tracking mounts on a hydraulic piston, as shown in Figure VII-21, so that the units of the array can be raised and lowered, keeping the intersection point of the elevation and declination axes of each mount in a plane orthogonal to the satellite line of sight. To evaluate this piston motion, let us imagine the target lies in the direction of the arrow shown in Figure VII-20. Now, if we construct a normal to that line through the center element, those units above the line (top of page) must be raised and those units below the line lowered by an amount proportional

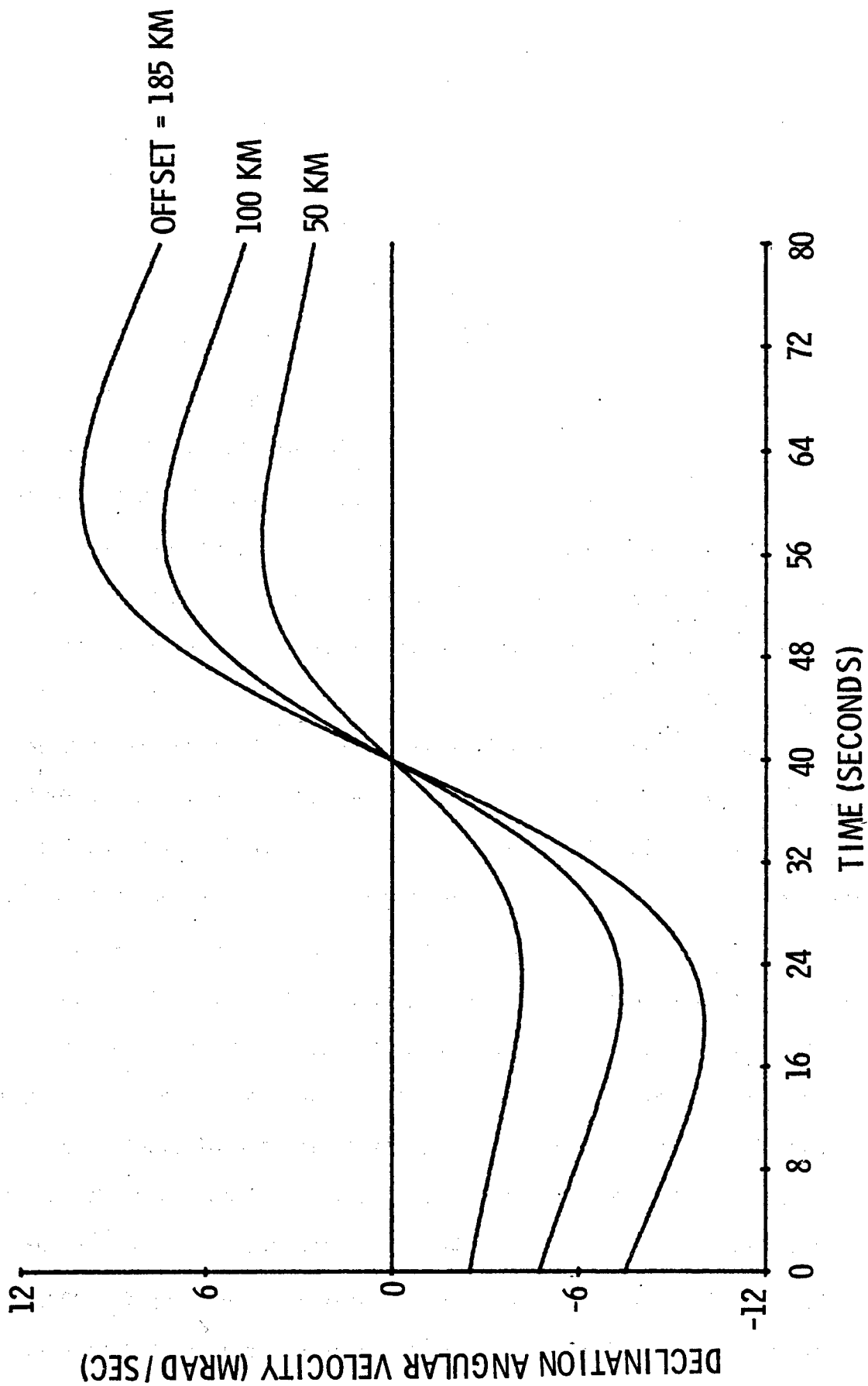


Figure VII-18. Declination Angular Velocity Versus Time for Various Track Offsets

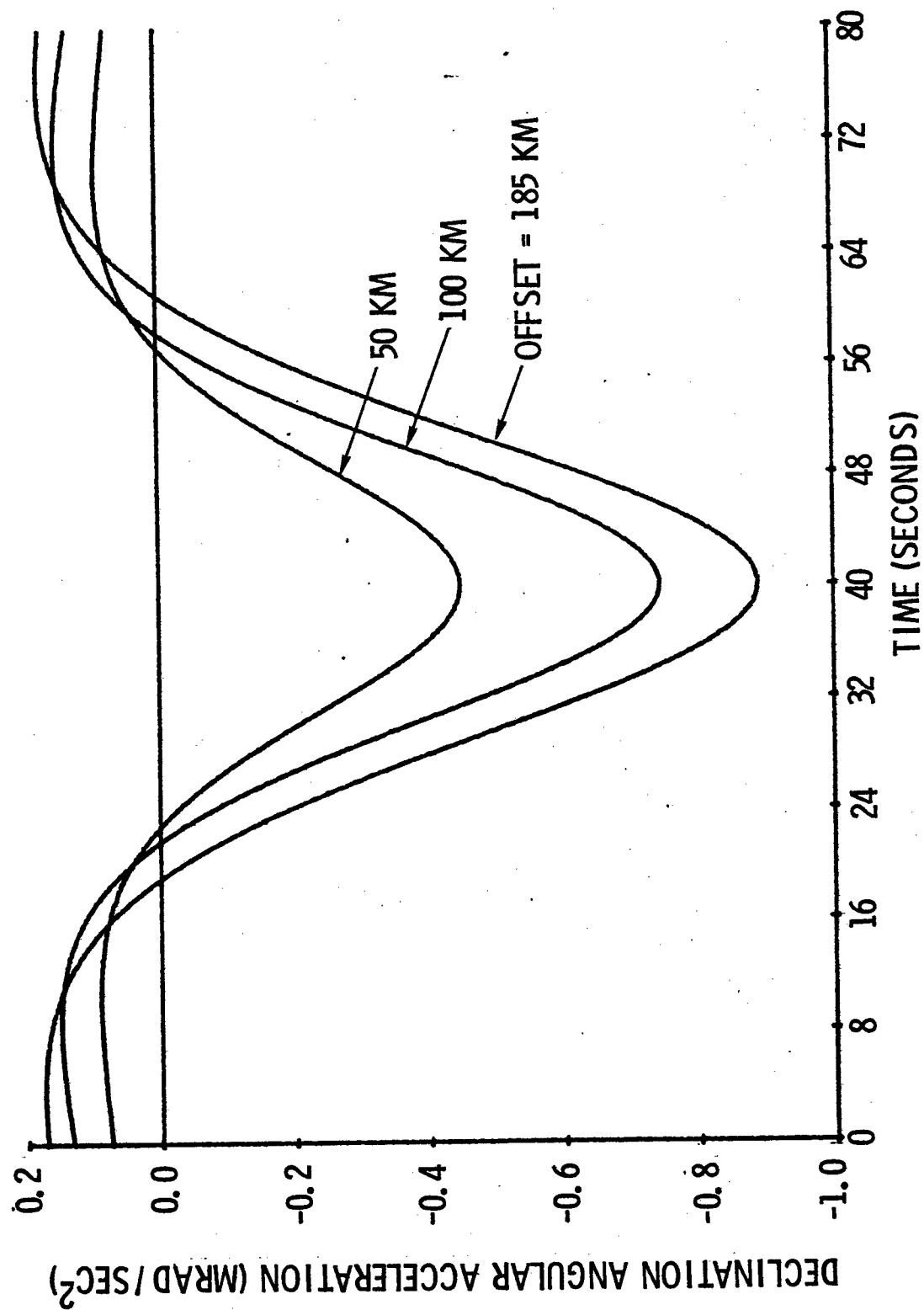


Figure VII-19. Declination Angular Acceleration vs Time for Various Track Offsets

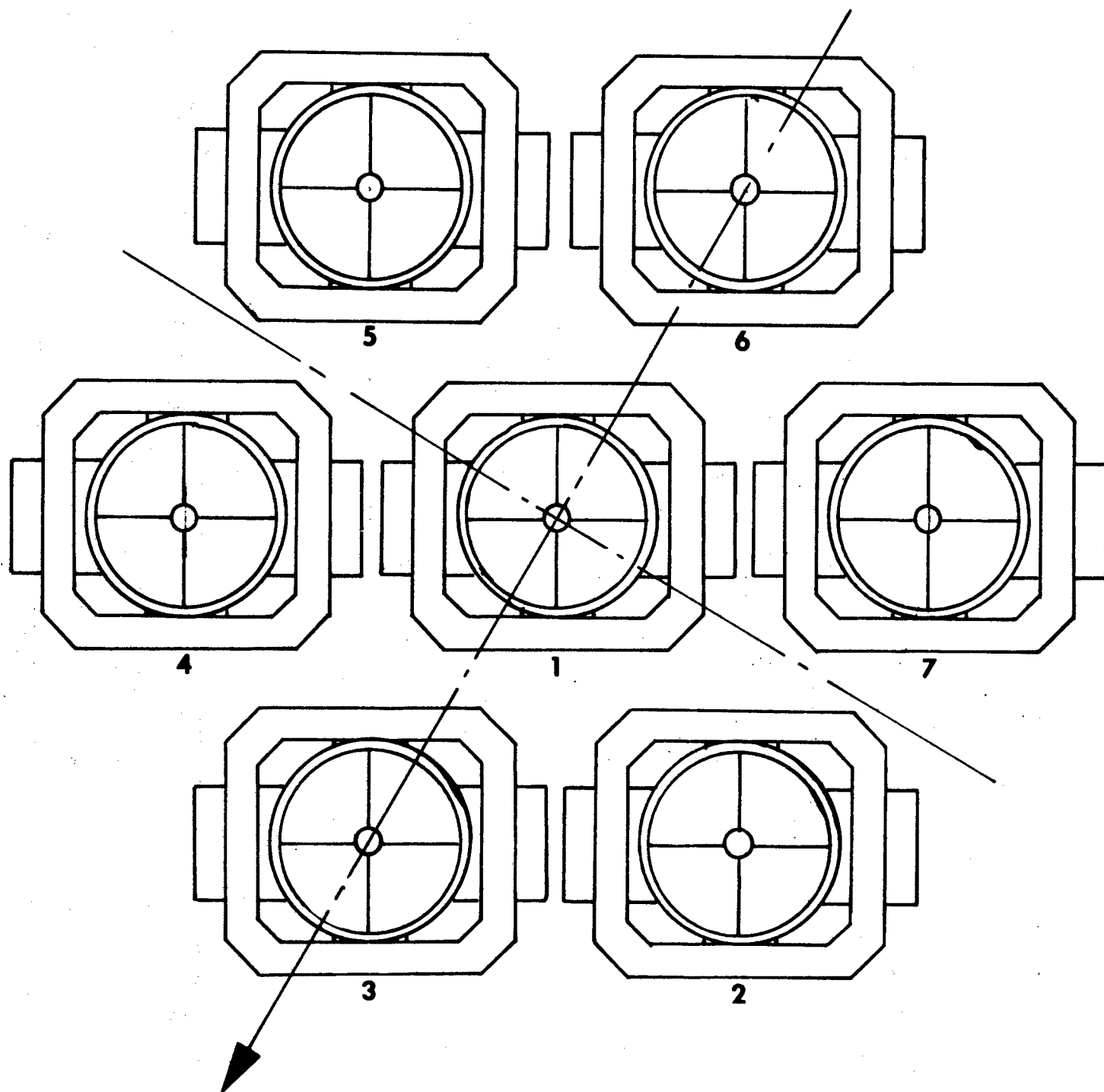


Figure VII-20. Seven-Element Output Antenna Array of Multiple Source Phased Array System Using Elevation-Declination Configured Tracking Mounts

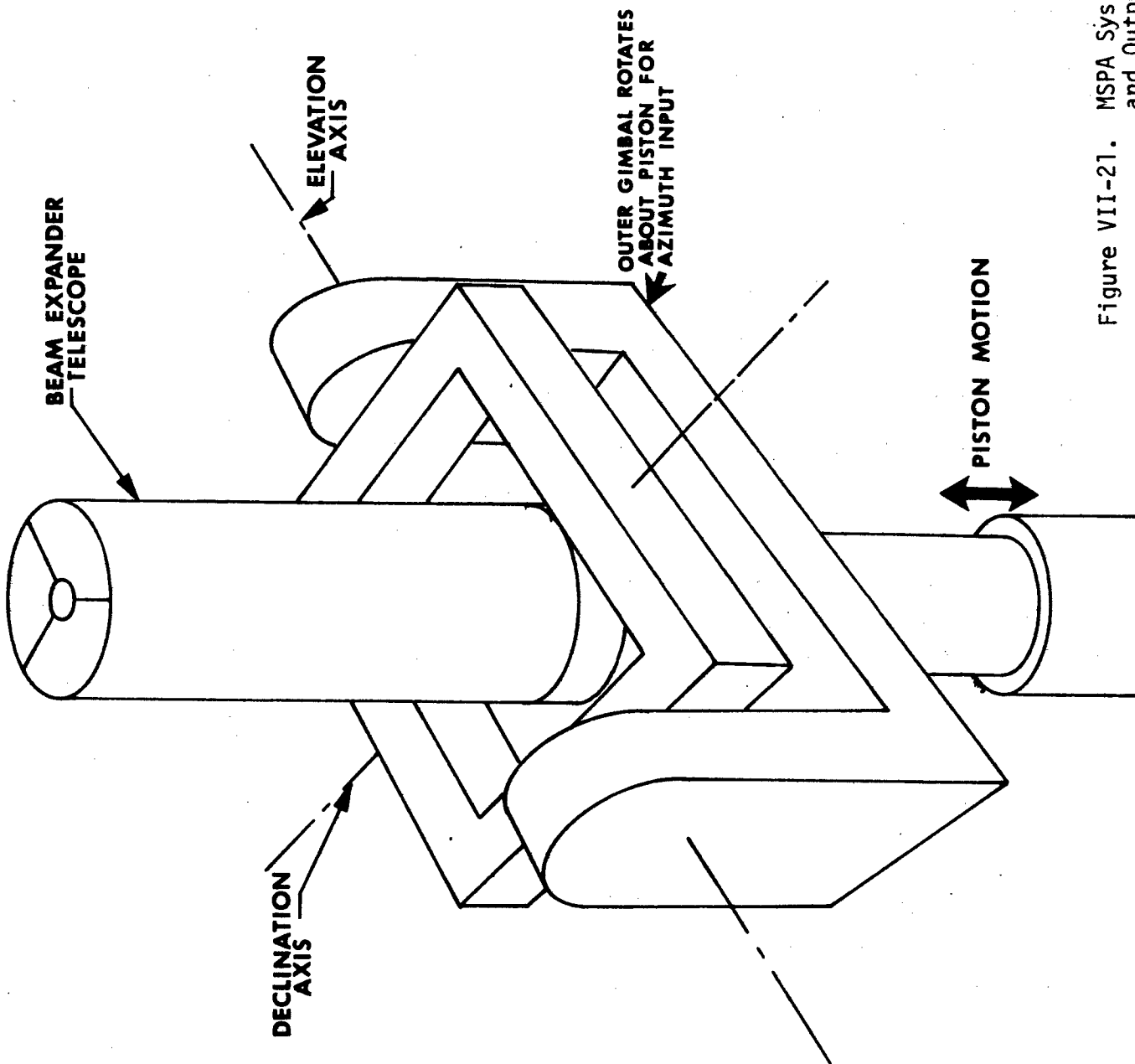


Figure VII-21. MSPA System Tracking Mount and Output Telescope -- One Element of Antenna Array

to the distance of the unit's center from the line. Therefore, the maximum piston displacement of the unit is

$$P_d(\max) = \frac{S(1 - \cos \theta)}{\sin \theta} \quad (41)$$

where S is the center-to-center spacing between units and θ is the zenith angle. Since this system must operate for zenith angles of $\pm 60^\circ$, the total piston excursion must be

$$P_e = 1.15 S.$$

This magnitude of travel, however, is more than what is absolutely required. As the telescopes are changed from a 0° zenith angle, their center-to-center spacing decreases, which serves to improve system operation. What must be avoided, however, is two adjacent telescopes making contact. Therefore, to prevent contact, the following condition must be satisfied

$$S \cos \theta - D_s \geq 0, \quad (42)$$

where D_s is the outer diameter of the telescope assembly. If we assume that S is some portion of D_s , such that

$$S = k D_s, \quad (43)$$

then

$$D_s(k \cos \theta - 1) \geq 0. \quad (44)$$

Thus, we have a critical zenith angle,

$$\theta_c = \cos^{-1}(1/k), \quad (45)$$

where, after this angle is exceeded, a piston displacement such that

$$D_s(k \cos \theta - 1) + P_d \sin \theta \geq 0 \quad (46)$$

is required. This can be restated as:

for $\theta > \theta_c$

$$P_d(\max) \geq -D_s(k \cot \theta - \csc \theta) . \quad (47)$$

Now, if we assume $k = 1.5$, then $\theta_c \sim 48^\circ$ and the maximum piston displacement for 60° (assuming $D_s = 1.5$ meters) is

$$P_d(\max) \geq .433 \text{ meters}$$

and

$$P_e = 0.866 \text{ meters.}$$

Therefore, if we set a requirement of one meter piston travel, this should be adequate for the MSPA system.

Another advantage of the piston displacement technique is that for a required displacement of one unit, there is an equal and opposite displacement required of the unit directly across from the center element. Thus, units 2-5, 3-6, and 4-7 (see Figure VII-20) could each share a common hydraulic pump so that, say, as the fluid was removed from 2 it would be added to unit 5 and vice-versa.

E. Weight and Size Considerations

As part of this investigation of design details for the MSPA system, a set of dimensional models covering the beam expansion telescope and tracking mount gimbals were generated so that good estimates of size and moving weight for the overall output antenna could be made. These models were dimensioned in terms of the primary mirror diameter of an individual antenna element, the focal length, or f-number, of the primary, and the size of the input beam, or magnification of the telescope. In Table VII-2, we provide a list of formulae for the volume of different components and subassemblies that were determined from the dimensional models. Then, in Table VII-2, we have tabulated the computed weight of each item and the total of seven units for the array. Of interest is that this detailed model produced almost identical results to that of the simple model used in the concept generation (see Table VI-3).

In terms of size, if we consider, as in the concept generation, a dome of such size that it could cover the same volume as the full array uses during a target encounter, then we obtain dimensions slightly different than those given in Table VI-3. Using the model of the beam expansion telescope (see Figure VII-4) and the parameters given in Table VII-3, we find that the overall telescope length is 3.5 meters and then from the model of the gimbals an additional 1.25 meters must be added to this for a total dome height of 4.75 meters. When a seven element array is configured (see Figure VII-20), the dome diameter needed to enclose the array and let the telescopes tilt 60° from the zenith is 12.4 meters. These dimensions are about 25% less than those given in Table VI-3.

Table VII-2

Volume Formulae for MSPA System Major Moving Parts

COMPONENT OR SUBASSEMBLY	VOLUME FORMULA
PRIMARY MIRROR	$D^3 \left(7.85 \times 10^{-2} + \frac{2.45 \times 10^{-2}}{F\#} - \frac{5.89 \times 10^{-2}}{F\# M^2} - \frac{9.42 \times 10^{-2}}{M^2} \right)$
PRIMARY MIRROR CELL PLUS Y-TILT MIRROR ASSEMBLY	$D^3 \left(1.37 \times 10^{-2} + \frac{1.77 \times 10^{-2}}{M} + \frac{1.64 \times 10^{-1}}{M^2} + \frac{5.84 \times 10^{-1}}{M^3} \right. \\ \left. + \frac{1.2 \times 10^{-3}}{F\#} + \frac{2.3 \times 10^{-2}}{F\# M^2} \right) + D^2 \left(\frac{2.27 \times 10^{-1}}{M^2} \right)$
SECONDARY MIRROR CELL PLUS MIRROR AND FOCUS CONTROL ASSEMBLY	$D^3 \left(7.4 \times 10^{-3} - \frac{9.9 \times 10^{-4}}{M} + \frac{3.4 \times 10^{-3}}{M^2} + \frac{1.24}{M^3} + \frac{2.45 \times 10^{-2}}{F\# M^2} \right) \\ + D^2 \left(1.3 \times 10^{-3} + \frac{3.9 \times 10^{-3}}{M} + \frac{3.65 \times 10^{-2}}{M^2} \right)$
TRUSS ASSEMBLY	$D^3 \left(2.45 \times 10^{-3} + 2.1 \times 10^{-3} F\# - \frac{2.1 \times 10^{-3} F\#}{M} \right. \\ \left. - \frac{4.2 \times 10^{-5}}{M} - \frac{1.3 \times 10^{-4}}{F\#} \right)$
INNER GIMBAL	$D^3 \left(\frac{.717}{M^2} + \frac{.737}{M^3} \right)$
OUTER GIMBAL	$D^3 \left(\frac{7.1 \times 10^{-2}}{M} + \frac{3.54 \times 10^{-1}}{M^2} + \frac{4.17 \times 10^{-1}}{M^3} + \frac{3.97 \times 10^{-3}}{F\# M} + \frac{7.56 \times 10^{-3}}{F\# M^2} \right)$
COOLED ELLIPTICAL MIRRORS IN GIMBAL	$D^3 \left(\frac{.444}{M^3} + \frac{.155}{M^2} \right)$

D is diameter of beam expansion telescope primary mirror.

F# is the f-number of the primary mirror.

M is the magnification of the beam expansion telescope.

M = D/d, where d is the diameter of the input beam to the beam expansion telescope.

Table VII-3

Moving Weight for MSPA System

D = 1.37 m, F# = 2.5, M = 6.85, d = 0.2 m

COMPONENT OR SUBASSEMBLY	WEIGHT* (KG)
PRIMARY MIRROR	882.4
PRIMARY MIRROR CELL PLUS Y-TILT MIRROR AND ASSEMBLY	265.4
SECONDARY MIRROR CELL PLUS MIRROR AND FOCUS CONTROL ASSEMBLY	135.2
TRUSS ASSEMBLY	141.4
	1424.4
INNER GIMBAL	180.8
OUTER GIMBAL	200.4
SIX COOLED ELLIPTICAL MIRRORS IN GIMBALS	(87.8 ea) 526.6
	907.8
TOTAL	2332.2

FOR A SEVEN ELEMENT ARRAY THE
TOTAL WEIGHT WOULD BE 16,325.4 KG

*An average density of 4000 kg/m³ has been assumed for all items except the truss assembly and the cooled mirrors. For the truss assembly, we considered the material to be steel and assumed a density of 8000 kg/m³ and for the mirrors the material was mostly molybdenum and the assumed average density was 9000 kg/m³.

F. Technology Development Requirements

Although the Multiple Source Phased Array system has been designed conceptually to make maximum use of existing technology, there are some areas of advanced technology required. In the paragraphs to follow, we have listed these areas with some brief comments.

1. Laser - Each channel of this system uses a high energy (~ 750 kw) closed-cycle electrical discharge laser (EDL) with a $^{12}\text{C}^{18}\text{O}_2$ isotope lasant that is capable of continuous output for a time period of about 100 seconds. The EDL was selected because of its advanced technology as compared to the closed cycle gas dynamic laser and because, for mountain top operation, the logistics of supplying input power are easier. The problem lies in that present closed-cycle EDL laser technology is in the 100 kw ballpark. This must be extended to the higher levels and for isotope operation.

2. Laser Phase Control System - The many advantages of the MSPA system are achieved because the principle of phase-locking independent laser oscillators allows almost completely separate adaption channels. This phase locking concept has been demonstrated at low power levels, but must be extended to higher power levels. Here, the problem is not simply greater power, but the non-uniform gain media and unstable oscillator configurations that characterize HEL's and which tend to increase the performance demands of the phase locking concept.

3. Moderate Power Tunable Laser Oscillator - The signal return from the satellite will be Doppler shifted in frequency by as much as 1.3 GHz. We must either provide detectors (low-level detector array) and associated electronics with this bandwidth capability or attempt to track the Doppler

with a tunable oscillator. It is unlikely that a local oscillator source can be tuned over the full range (gain-bandwidth product limits), but it can be tuned over a range of, say, 800 MHz, which would mean that detector circuits would operate over a reasonable bandwidth of 500 MHz. The problem with the local oscillator concept used is that we need both a broadband tuning range and, because of the many detectors (seven detector arrays), a moderate output power of about 10 watts. To achieve this condition will most likely require a waveguide laser and amplifier with a gain of 10. The technology to accomplish this, to the best of our knowledge, does not exist. Presently, however, Rockwell is working with a regenerative feedback amplifier concept that shows promise of meeting these conditions, so it was suggested for use in the MSPA system.

4. Hartmann Plate Beam Sampler - Present liquid cooled optics technology would probably permit the successful fabrication of a small hole coupler beam sampler with one side reflective. The MSPA system concept, however, requires multiple hole sampler arrays (7) fabricated into a single liquid cooled mirror with the approximate dimensions of 30 x 150 cm. Both sides of the beam sampler plate must be reflective and each side must exhibit diffraction limited performance.

5. Detector Arrays - If the tunable laser source is completely successful, the detectors and associated electronics of the low-level detector array must be responsive over a bandwidth of 500 MHz. Single detectors with this performance are possible, but reliable arrays (19 or 37 detectors) will require some development.

6. Data Processor - Both the beam "clean-up" processor and the return signal processor perform similarly in that the set of phase measurements are

decomposed into an orthogonal set of phase aberrations which are then sent to the appropriate beam control operators. The beam "clean-up" processor will more than likely require a wide bandwidth response for at least the average phase error loop which controls the source phase. The return signal processor has additional complications because of its interaction with the ephemeris data processor and the additional loop to control the tunable local oscillator. These processors, at least, will require system design development.

7. Deformable Mirror - Each adaptive channel of the MSPA system uses two deformable mirrors for a system total of 14. Deformable mirrors with the power handling ability and the probable spatial frequency requirements have been either constructed with some experimental verification or have been subjected to sufficient development to demonstrate that the technology exists to fabricate the device. The temporal frequency requirements may be another matter, but in any case, the technology is in its infancy and the costs associated with these units is extremely high. The development of a fabrication technique that would serve to drive down unit cost would be appropriate.

G. MSPA System Details

In Table VII-4 we have presented a brief summation of the major details of the MSPA system. As part of this presentation, we also give a tabulation of the predicted efficiencies which result in an overall efficiency of 53%. Of the items on the list, diffraction efficiency is the worst problem which suggests possible consideration of a shorter wavelength source. As has been mentioned in Chapters III and V, however, the CO and DF sources would have less atmospheric transmission and the results in Chapter III also show slightly less turbulence adaption efficiency. In addition, these sources have not had the benefit of the extensive technology development as has been enjoyed by the longer wavelength source. Consequently, it may prove beneficial to consider enlarging the satellite collector.

Table VII-4

MSPA SYSTEM DETAILS

LASER	CLOSED-CYCLE ELECTRICAL DISCHARGE USING $^{12}\text{C}^{18}\text{O}_2$ ISOTOPE FOR LASANT -- OUTPUT POWER ~ 750 KW, WAVELENGTH $9.1 \mu\text{m}$.
OPERATING LOCATION	MOUNTAIN TOP OPERATION -- APPROXIMATELY 3.5 KM ABOVE SEA LEVEL.
ELEMENTAL ANTENNA SIZE	1.37 METERS
NUMBER OF ADAPTIVE CHANNELS	7
ADAPTIVE ALGORITHM	RETURN WAVE, OR PHASE CONJUGATION, APPROACH. MEASURED PHASE ABERRATIONS ARE DECOMPOSED INTO ORTHOGONAL MODES AND CORRECTED WITH APPROPRIATE BEAM CONTROL OPERATOR. UNIQUE PHASE LOCKING TECHNIQUE IS USED FOR BASIC PISTON PHASE ERROR CONTROL.
TRACKING MOUNT CONFIGURATION	ELEVATION-DECLINATION -- MAXIMUM ANGULAR ACCELERATIONS ARE ABOUT 1.5 MR/SEC^2 FOR ELEVATION AXIS.
TOTAL MOVING WEIGHT	16,325.4 KG
OVERALL TRANSMITTER ARRAY DIMENSIONS	4.75 M HIGH 12.4 M DIAMETER
PREDICTED EFFICIENCY	
A. OPTICAL TRAIN EFFICIENCY	20 MIRRORS AT 0.99 PER SURFACE (0.82)
B. DIFFRACTION EFFICIENCY	SEGMENTED ARRAY PRODUCES MORE DIFFRACTION LOSS THAN CONTIGUOUS ANTENNA (0.72)
C. ATMOSPHERIC TRANSMISSION EFFICIENCY	AVERAGED OVER TOTAL PERIOD OF ENCOUNTER (0.95)
D. TURBULENCE ADAPTION EFFICIENCY	WITH ADAPTION BANDWIDTH OF $> 80 \text{ HZ}$ (0.95)
E. THERMAL BLOOMING ADAPTION EFFICIENCY	WHEN HOAC IS PERFORMED IN EACH CHANNEL ON RETURN BEAM (~ 1.0)
OVERALL	0.53

References

1. R. A. Brandewie et al, Long Range Optical Systems Study, Final Report, Contract F29601-75-C-0047, AFWL-TR-75-291, May 1976.

VIII. CONCLUSIONS

This program has been devoted to evaluation of techniques for transmitting substantial (up to 5 MW) quantities of power to satellites in low (185 km) circular orbit. Powers of this level could be used to supply the energy for orbital maneuvers, and would result in significant cost savings when compared with transporting fuel for these maneuvers into orbit by means of conventional vehicles. In order to evaluate the feasibility of this proposal, we have examined the transmission limitations resulting from diffraction effects, atmospheric turbulence, and thermal blooming, and the improvements in transmission that result from the use of adaptive optics. Four candidate systems were developed and evaluated, and one, a multielement array of phase locked laser oscillators, was selected for detailed analysis and design. A principle overall conclusion of the study is that a system for transmitting up to 5 MW of power to satellites in orbit can be developed to operate with reasonable efficiency using, for the most part, components and devices which are reasonable extensions of the current state-of-the-art. In the following paragraphs, the principle results and conclusions of the study are summarized.

Diffraction effects at the transmitting aperture provide a limitation on system efficiency that decreases with increasing aperture size. However, the size of the tracking mount cannot be increased arbitrarily because of size, weight, cost, and technology limitations. Our calculations of the diffraction limited transmission efficiency, at $10.6\text{ }\mu\text{m}$, show that an aperture size greater than about 3.5 meters is needed to keep the mission integrated diffraction efficiency above about 85%. A somewhat larger beam diameter of 4.8 meters was selected and used for most of the calculations.

Atmospheric transmission calculations were performed for natural and isotopic CO_2 , DF, and CO laser lines for transmitter elevations of 10 m and 3.5 km above sea level, and for various atmospheric conditions. For the sea level site, we found the transmission to be rather low for all lasers, except DF. Therefore, we conclude that for the CO_2 laser, which is the principal laser of interest in this study, that the 3.5 km site is far superior. If a sea level site is preferred for some other reason, then the DF laser provides superior transmission ($\approx 75\%$, average). However, the conclusions change dramatically when laser wavelengths are compared at the high altitude 3.5 km site. For this case, we consider the $^{12}\text{C}^{18}\text{O}_2$ ($\lambda = 9.1 \mu\text{m}$) isotope of CO_2 to minimize absorption due to atmospheric CO_2 . Since most of the continuum absorption due to water vapor is below 3.5 km, this $9.1 \mu\text{m}$ CO_2 line gives excellent transmission ($> 90\%$). From the high altitude site we conclude that isotopic CO_2 is best, followed very closely by CO. Both of these are better choices than DF, and all are substantially better than natural CO_2 . The conclusion with respect to atmospheric transmission is therefore clear. The sight should be chosen at 3.5 km in any event. The laser should use either isotopic CO_2 or CO, with $^{12}\text{C}^{18}\text{O}_2$ slightly preferred. It is doubly important to minimize absorption in this way, since absorption represents not only an energy loss, but contributes to thermal blooming as well.

Turbulence in the atmosphere spreads the transmitted beam and therefore limits energy delivery to the satellite collector. This loss can be serious if not compensated by a suitable adaptive system with adequate bandwidth. Calculations of adaption for turbulence were performed using a wave optics FFT approach for five different classes or types of adaptive compensation for zenith angles of 0° and 60° . For the 0° case at 10.6 or $9.1 \mu\text{m}$, an unadapted

uniform aperture distribution delivered about 40% of the transmitted power into the two meter collector. The best adaptive system studied using phase and tilt adaption with a seven-element hexagonal close packed array increased this value to 87%. For these parameters, a perfect diffraction limited lens in vacuum will deliver 92%, so adaptive compensation for turbulence is quite acceptable. Very similar results were obtained at 3.8 and 5.0 μm , where the aperture is scaled in proportion to the wavelength. The loss due to isoplanatism was time averaged over the total encounter and found to be negligible for 9.1 and 10.6 μm operation. For the 3.8 and 5.0 μm wavelengths, however, the loss due to isoplanatism increases significantly for offset distances greater than 100 km. The required control bandwidth was also evaluated. For the 10.6 μm wavelength systems, a 60 Hz bandwidth is adequate to provide 90% correction. For 9.1 μm , this requirement increases to 80 Hz. At 5.0 μm , 305 Hz is required, and at 3.8 μm , 440 Hz is needed. The implication of these results is that state-of-the-art deformable mirror surfaces needed to achieve 90% correction at 5.0 or 3.8 μm . These results also have implications in the selection of adaptive algorithms. Outgoing wave dither systems become bandwidth limited by transit time at long ranges. For 10.6 and 9.1 μm systems with a satellite orbital altitude of 185 km, this is not a limitation at any zenith angle under consideration because of the low bandwidth requirements. However, a 3.8 μm outgoing wave dither system would be bandwidth limited at a zenith angle of 40° and a 5.0 μm system would be limited at 50°. In any case, the adaption bandwidth requirements would eventually limit the propagation range of an outgoing wave system. Therefore, a return wave adaption technique has been used with the system concept selected. Summarizing the turbulence results, we obtain essentially complete correction at the longer wavelengths at quite reasonable bandwidths. For the shorter wavelengths,

noticable but not terribly serious losses occur, because of isoplanatism, and the bandwidth requirements increase considerably. This bandwidth increase limits the usefulness of outgoing wave multidither systems, particularly for the shorter wavelengths.

Our analysis of thermal blooming produced some unexpected results. Whereas previous calculations of blooming for near horizontal propagation have produced a classical "half-moon" irradiance distribution (distortion, astigmatism, and comma), our results showed beam broadening predominately in one direction (distortion and astigmatism). More important, previous results where the focal plane is in a "thick" atmosphere the required correction antenna size gets to be much greater than the actual antenna size and consequently the adaptive ability suffers and only partial compensation of thermal blooming can be accomplished. However, our results show very substantial correction capability. The reason for both of these results is that the blooming phase error source is near to the aperture for our case, and the results are both quantitatively different and almost fully correctable, when compared with previous calculations for horizontal propagation. The calculations done with a three-dimensional full wave optics FFT propagation code, coupled with an accurate model of thermal blooming and kinetic cooling, for each of the wavelengths of interest. For all calculations, aperture diameter was scaled with wavelength. We found that blooming increases with laser power, zenith angle, and, of course, atmospheric absorption coefficient. It decreases with aperture diameter and elevation of the transmitter site. For some cases, the losses are very serious, particularly for high absorption wavelengths at the low altitude site. For example, at $5.0 \mu\text{m}$, the relative power in the 2 m diameter bucket is decreased by a factor of ≈ 6 at $P = 5 \text{ MW}$ at zenith, and then by another

factor of ≈ 2 at 60° zenith angle. These results illustrate again the extreme undesirability of the low altitude transmitter site. However, detailed computations at $10.6 \mu\text{m}$ and $9.1 \mu\text{m}$ showed that the blooming effect could be essentially completely compensated and near diffraction limited performance obtained, even from the low level site, if a deformable mirror is used in each channel of the seven-element array. At the 3.5 km altitude site, blooming effects are significantly reduced, and are well corrected by adaptive optics. For example, for 5.0 MW transmitted at $10.6 \mu\text{m}$ and 60° zenith angle, the power delivered is 1.7 MW, compared to a diffraction limit of 3.0 MW. Use of piston and tilt adaption increases this value to 2.3 MW, a significant improvement. Incorporating deformable mirrors in each channel makes the compensation essentially perfect. Summarizing our results on blooming, we find that this energy loss source is serious, but essentially completely correctable with adaptive optics. A high level site is again strongly preferred, to minimize blooming effects. From the high level site $9.1 \mu\text{m}$ is the preferred wavelength, followed by 5.0, 3.8 and $10.6 \mu\text{m}$. From the low level site, the wavelength preference order changes, and we would recommend 3.8, 5.0, 9.1, or $10.6 \mu\text{m}$, in that order.

Four different optical system concepts were analyzed. These systems were:

1. Coelostat Hartmann Tracker
2. Modified Multidither Receiver
3. Multiaperture MOPA system
4. Multiple Source Phased Array

Each of these systems were found to meet the performance requirements. They were evaluated with respect to the following criteria:

1. Overall efficiency
2. Reliability
3. Size and weight
4. Technology advancement requirement
5. Potential cost

Quantitative evaluation standards were developed with respect to these criteria. The results, using a product of terms evaluation procedure, in which larger numbers indicate the more desirable system, were:

Concept 1 - 0.003

Concept 2 - 0.004

Concept 3 - 0.019

Concept 4 - 0.148

Based on these results, Concept 4, the multiple source phased array, was selected for more detailed preliminary design and analysis. This concept showed advantages with respect to each of the evaluation criteria; however, the really critical benefits of this concept follow from its modular approach that allows parallel arraying of components within specified technological limits. For example, at 10.6 μm , the multiple source phased array is the only concept investigated with the potential for eliminating the requirement for developing a "Mt. Polomar" class tracking mount, with all of the attendant cost, size, weight, and technology requirements.

The multiple source phased array was developed further in our detailed conceptual design task. The system was defined in sufficient detail to predict with reasonable accuracy the energy transmission efficiency which can be attained, and to establish those components or subassemblies of the system for which research or technological development work would be required.

For the 9.1 μm system, operating at 3.5 km above sea level on overall (laser to 2 m collector) efficiency of 53% is predicted. This efficiency is the product of the following terms:

Optical train efficiency	- 82%
Diffraction efficiency	- 72%
Atmospheric Transmission	- 95%
Turbulence adaption efficiency	- 95%
Thermal blooming adaption efficiency	- 100%

Thus, the system conceptual design has been carried to a level where diffraction is the most serious contributor to overall system efficiency.

Seven specific areas of technological development were isolated. They are summarized as follows:

1. Closed cycle $^{12}\text{C}^{18}\text{O}_2$ laser
2. Laser phase control technology
3. Moderate power tunable laser oscillator
4. Hartmann plate beam sampler
5. Detector arrays
6. Data processor
7. Deformable mirror.

In addition, we conclude that the multiple source phase array system shows considerable promise. We believe that a low or moderate power system feasibility test would be of benefit and merit. Such a test could be carried out using the NASA pilot laser facility and we recommend that planning for such a test program be initiated.

APPENDIX A

THERMAL BLOOMING DISTORTION PARAMETER AS A FUNCTION OF ALTITUDE

Distortion Parameter

The refractive index change due to heating of the atmosphere by a high power laser beam is given in Eq. (V-1) as

$$\Delta n(x,y,z) = \frac{-\alpha (\partial n_o / \partial T)}{n_o \rho c_p V(1 + \omega z/V)} \int_{-\infty}^x I(x',y,z) dx', \quad (1)$$

where all of the symbols are previously defined. The dependence of refractive index change on atmospheric parameters is contained in a distortion parameter defined here as

$$M_D = \frac{\alpha}{\rho c_p n_o} \left(\frac{\partial n_o}{\partial T} \right). \quad (2)$$

Variation of M_D

The parameters constituting M_D are examined individually here. The total variation of M_D will be displayed in the conclusion.

Specific heat -- The densities of the two major constituents of the atmosphere, O_2 and N_2 , show an exponential decrease with altitude. The individual scale heights are slightly different, giving rise to a slightly varying relative composition of the atmosphere.² However, since the specific heats of the two gasses are identical to within 1%, the total variation of the specific heat will be only a tiny fraction of a percent, and C_p will be taken to be a constant.

Index of Refraction -- The index of refraction of air varies between $n_o = 1 + 2.9 \times 10^{-4}$ at sea level to $n_o = 1$ at the highest altitudes. Therefore, we will take n_o to be identically equal to 1.

Index of Refraction Temperature Gradient -- First, a simple form for the functional dependence of n_o on T will be suggested. Then, a rigorous theory will be presented to support the simple model. The theoretically derived values will be shown to correspond to one another and values in the literature.

$$\text{Let } n_o \equiv 1 + n_1 \quad n_1 \equiv \beta N_o, \quad (3)$$

where β = proportionality constant at STP, and

N_o = gas density at STP.

$$\text{For an ideal gas, } P = NkT. \quad (4)$$

So, for a constant pressure

$$0 = \frac{\partial N}{\partial T} T + N$$

and

$$\frac{\partial N}{\partial T} = - N_o/T \text{ at STP.} \quad (5)$$

We have from Eq. (3) that $\frac{\partial n_o}{\partial T} = \frac{\partial n_1}{\partial T} = \beta \frac{\partial N}{\partial T}$.

Thus, giving the result that

$$\boxed{\frac{\partial n_o}{\partial T} = - \frac{n_1}{T} \left(\frac{N}{N_o} \right)} \quad (6)$$

The variation of number density and temperature will be discussed later, and integrated into the final result. Attention is now turned toward a rigorous approach to the variation of n_o with T .

Our starting point will be with the Clausius-Mossotti equation, which is derived from fundamental principles. It is valid for gasses and liquids, and is well verified experimentally.³ The explicit form is

$$\frac{K - 1}{K + 2} = \frac{N\alpha}{3\epsilon_o} \quad (7)$$

where K = relative dielectric constant

N = number density

ϵ_o = dielectric constant of free space, and

α = molecular polarizability (not to be confused with the absorption coefficient)

We define

$$K \equiv 1 + K_1,$$

where for air $K_1 \ll 1$. So, the Clausius-Mossotti equation gives

$$\boxed{K_1 = \frac{N\alpha}{\epsilon_o}} \quad (8)$$

To relate this to the index of refraction, we note that $n_o^2 = K$. Now, define $n_o \equiv 1 + n_1$, and note that $n_1 \ll 1$. For these conditions of relative smallness,

$$2n_1 \approx K_1, \quad (9)$$

giving as a final result

$$\boxed{n_1 = \frac{N\alpha/2}{\epsilon_o}} \quad (10)$$

This gives our linear dependence of n_1 on N !

Before these results are compared to published values, we make an additional theoretical comparison. In Ref. 4, an equation relating n_0 and T is given, taken from a NBS report. Their equation gives K_1 as a function of (p, T) for a restricted T range (about $T = 293^\circ$). This equation is

$$\frac{K_1'(p, T)}{K_1(\text{STP})} = \frac{p}{760 [1 + \zeta \Delta T]} \quad (11)$$

where $\zeta = 3.411 \times 10^{-3}$ and $\Delta T = (T - 293^\circ)$. We note that this value of ζ equals $1/T$ for $T = 293^\circ$. For $p = 760$, and inserting $\zeta = 1/T$, we have

$$\frac{K_1'}{K_1} = \frac{1}{1 + \Delta T/T} \approx 1 - \Delta T/T. \quad (12)$$

From Eq. (12), and using $2n_1 \cong K_1$, we have

$$\boxed{\frac{\Delta n_1}{\Delta T} = -K_1/2T} \quad (13)$$

for constant p . This establishes the inverse T dependence, leaving us to postulate the N dependence of K_1 .

For comparison with experiment, the values of $T = 293$, $n_1 = 2.9 \times 10^{-4}$, and $K_1 = 5.4 \times 10^{-4}$ are inserted into Eqs. (6) and (13) to give

$$\frac{\partial n_1}{\partial T} = -\frac{n_1}{T} = \frac{-2.9 \times 10^{-4}}{2.9 \times 10^2} = -10^{-6} \quad (14)$$

$$\frac{\Delta n_1}{\Delta T} = -\frac{K_1}{2T} = \frac{-5.4 \times 10^{-4}}{5.8 \times 10^2} = 0.93 \times 10^{-6}$$

The result used in Ref. 1 is 10^{-6} , giving a very favorable comparison.

Density -- The mass density is the sum of the products of the number densities and molecular weights of each species. As previously stated, the relative composition of the atmosphere's major components vary little with altitude to 80 km. This statement is further verified in Ref. 2. With this in mind, we will write the mass density in the form

$$\rho = MN \quad (15)$$

where M = mean molecular weight ($= 29.0$)

N = mass number density.

Temperature -- Since the index of refraction derivative depends on temperature, the values of temperature versus altitude are listed in Table 1. As can be seen, between 0 to 80 km, the changes are small.

Absorption Coefficient -- This coefficient has several determining factors, and is a non-analytical function of altitude, and is discussed at length in another technical memo. The absorption coefficient for 3.83 and 10.6 μ is tabulated in Table 1, along with $\alpha' = \alpha/T$. Additionally, α' is plotted in Figures 1 and 2. Note carefully that the vertical scale for the 3.83 μ plot is 10^{-2} that of the 10.6 μ plot.

Total Variation of M_D

From Eq. (2) we have

$$M_D = \frac{\alpha}{\rho C_p n_o} \left(\frac{\partial n_o}{\partial T} \right). \quad (16)$$

We insert the results of our parameter analysis to obtain

$$M_D = \frac{\alpha}{MN C_p n_o} \left(- \frac{n_1}{T} \frac{N}{N_o} \right) \quad (17)$$

$$= - \frac{n_1}{M N_o C_p n_o} \left(\frac{\alpha}{T} \right).$$

Since $n_o = 1$,

$$M_D = - \frac{n_1}{\rho_o C_p} \left(\frac{\alpha}{T} \right) \quad (18)$$

This is our final result. We now define $\alpha/T \equiv \alpha'$, and give this number as a function of altitude in Table 1 and Figures 1 and 2. Suggested values for the constants are:

$$n_1 = 2.9 \times 10^{-4}$$

$$C_p = 0.242 \text{ cal/gm } (15^\circ \text{C})$$

$$\rho_o = 1.225 \frac{\text{kg}}{\text{m}^3}$$

Table I
10.6 μ Atmosphere II

Z (km)	T ($^{\circ}$ K)	α (1/km)	α' (1/km $^{\circ}$ K)
0	288	3.85 E-1	1.34 E-3
0-1	286	2.98 E-1	1.04 E-3
1-2	278.5	1.89 E-1	6.61 E-4
2-3	272	1.22 E-1	4.49 E-4
3-4	265.5	8.90 E-2	3.35 E-4
4-5	259	6.85 E-2	2.64 E-4
5-6	252.5	5.75 E-2	2.28 E-4
6-7	246	4.88 E-2	1.98 E-4
7-8	239.5	3.95 E-2	1.65 E-4
8-9	233	3.12 E-2	1.34 E-4
9-10	226.5	2.57 E-2	1.13 E-4
10-11	220	2.07 E-2	9.41 E-5
11-12	217	1.64 E-2	7.56 E-5
12-13	217	1.26 E-2	5.81 E-5
13-14	217	1.10 E-2	5.07 E-5
14-15	217	1.15 E-2	5.30 E-5
15-16	217	1.12 E-2	5.16 E-5
16-17	217	1.10 E-2	5.07 E-5
17-18	217	1.12 E-2	5.16 E-5
18-19	217	1.13 E-2	5.21 E-5
19-20	217	1.18 E-2	5.44 E-5
20-21	217	1.21 E-2	5.58 E-5
21-22	217	1.28 E-2	5.90 E-5
22-23	217	1.33 E-2	6.13 E-5
23-24	217	1.47 E-2	6.77 E-5
24-25	217	1.47 E-2	6.77 E-5
25-30	224	1.75 E-2	7.81 E-5
30-35	233.5	1.52 E-2	6.51 E-5
35-40	253.5	1.38 E-2	5.44 E-5
40-45	269	1.11 E-2	4.13 E-5
45-50	280	7.71 E-3	2.75 E-5
50-70	246.5	1.19 E-3	4.83 E-6
70-100	204.5	1.74 E-3	8.51 E-8

Units of α are (1/km)

Table I-A
 $\lambda = 3.83 \mu$ Model II

Z	T(°K)	Without Aerosol Absorption			With Aerosol Absorption		
		α	α'	α (Clear)	α (hazy)	α' (Clear)	α' (hazy)
0	288	8.7 E-3	3.02 E-5	1.40 E-2	6.83 E-2	7.88 E-5	2.67 E-4
0-1	286	7.02 E-3	2.45 E-5	9.56 E-3	4.30 E-2	5.79 E-5	1.75 E-4
1-2	278.5	4.49 E-3	1.61 E-5	4.17 E-3	1.38 E-2	3.1 E-5	6.57 E-5
2-3	272	2.80 E-3	1.03 E-5	1.78 E-3	4.81 E-3	1.69 E-5	2.80 E-5
3-4	265.5	1.73 E-3	6.53 E-6	8.27 E-4	2.10 E-3	9.63 E-6	1.44 E-5
4-5	259	1.12 E-3	4.32 E-6	5.15 E-4	7.67 E-4	6.31 E-6	7.29 E-6
5-6	252.5	7.63 E-4	3.02 E-6	3.76 E-4	3.75 E-4	4.45 E-6	
6-7	246	5.49 E-4	2.23 E-6	3.03 E-4	3.03 E-4	3.46 E-6	
7-8	239.5	3.90 E-4	1.63 E-6	2.96 E-4	2.96 E-4	2.86 E-6	
8-9	233	2.82 E-4	1.21 E-6	2.95 E-4	2.95 E-4	2.48 E-6	(Same as Clear)
9-10	226.5	2.07 E-4	9.14 E-7	2.85 E-4	(Same as Clear)	2.17 E-6	
10-11	220	1.50 E-4	6.82 E-7	2.72 E-4		1.92 E-6	
11-12	217	1.11 E-4	5.12 E-7	2.70 E-4		1.76 E-6	
12-13	217	8.00 E-5	3.69 E-7	2.66 E-4		1.59 E-6	
13-14	217	5.97 E-5	2.75 E-7	2.53 E-4		1.44 E-6	
14-15	217	4.44 E-5	2.05 E-7	2.43 E-4		1.32 E-6	
15-16	217	3.13 E-5	1.44 E-7	2.29 E-4		1.20 E-6	
16-17	217	2.25 E-5	1.04 E-7	2.22 E-4		1.13 E-6	
17-18	217	1.66 E-5	7.65 E-8	2.17 E-4		1.08 E-6	
18-19	217	1.21 E-5	5.58 E-8	1.97 E-4		9.64 E-7	
19-20	217	8.87 E-6	4.09 E-8	1.55 E-4		7.55 E-7	
20-21	217	6.49 E-6	2.91 E-8	1.13 E-4		5.50 E-7	
21-22	217	4.80 E-6	2.21 E-8	8.34 E-5		4.06 E-7	
22-23	217	3.47 E-6	1.60 E-8	6.33 E-5		3.08 E-7	
23-24	217	2.66 E-6	1.23 E-8	4.92 E-5		2.39 E-7	
24-25	217	1.91 E-6	8.80 E-9	4.02 E-5		1.94 E-7	
25-30	222			2.15 E-5		9.68 E-8	
30-35	240			6.27 E-6		2.61 E-8	
35-40	252			1.65 E-6		6.55 E-9	

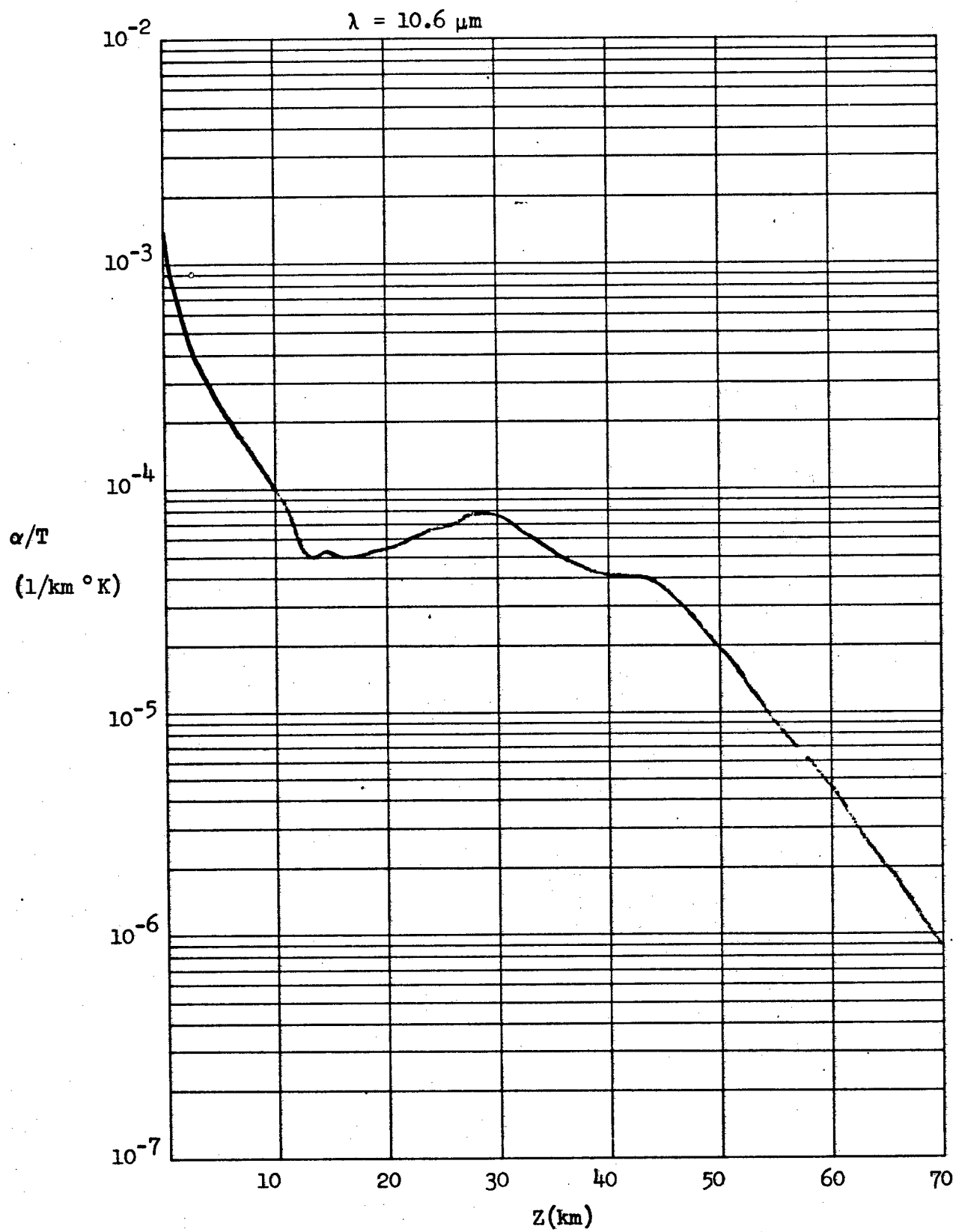


Figure 1

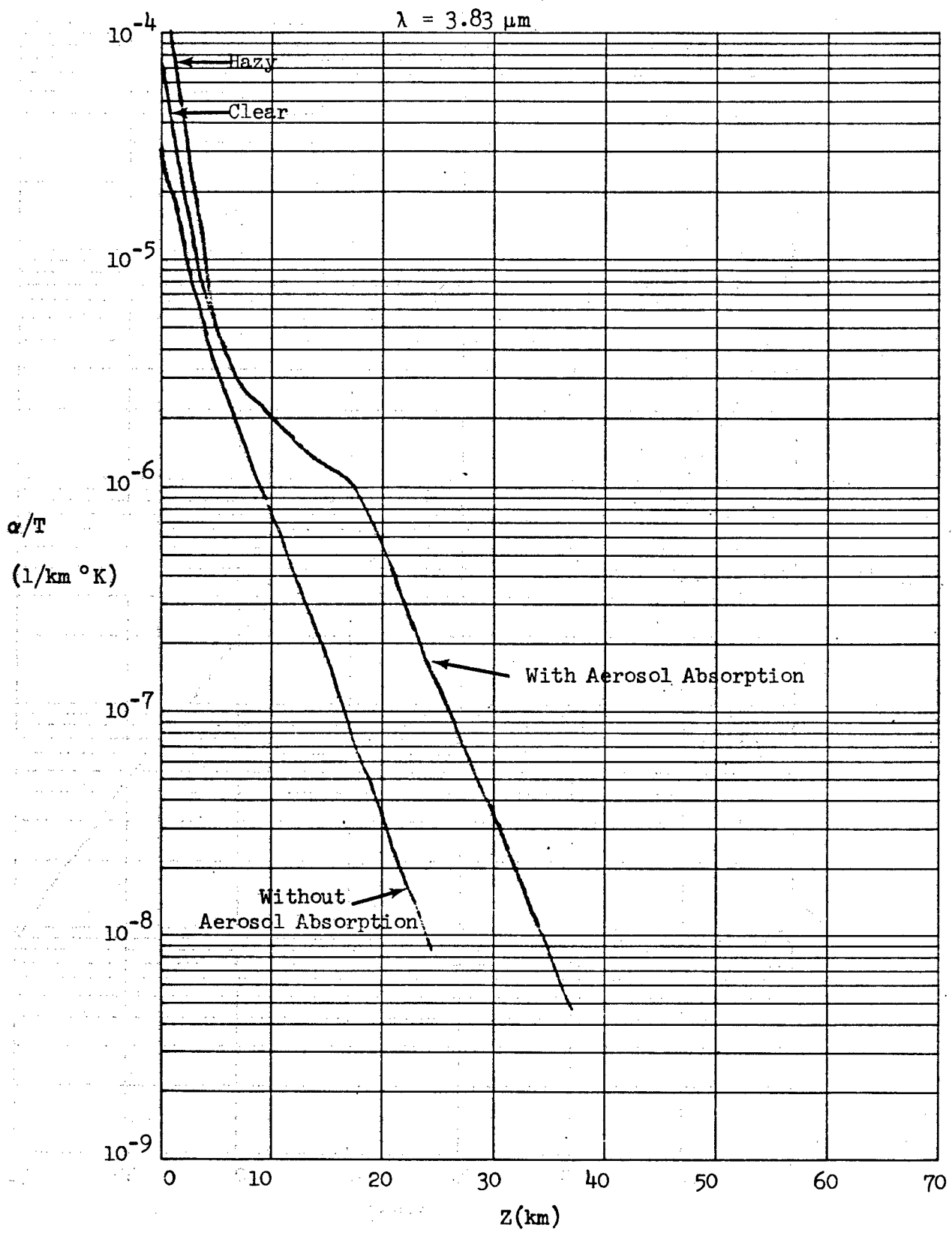


Figure 2

References

1. J. Winocur, "Adaptive Optics Technology Study," Final Report, C74-261/501, Rockwell International, December 1974, NSWC Contract N60921-74-C-0221.

See Also

- F. G. Gebhardt and D. C. Smith, IEEE Journal of Quantum Electronics, QE-7, pp. 63-73, 1971.
- L. C. Bradley and J. Herrmann, Applied Optics, 13, No. 2, pp. 331-334, 1974.
2. Handbook of Geophysics, Revised Edition, USAF Air Research Development Command, the MacMillan Co., New York, 1960.
 3. "Introduction to Electromagnetic Waves and Fields," D. Carson and P. Lorrain, Freeman and Co., San Francisco, 1962.
 4. CRC Handbook of Chemistry and Physics, 53rd Edition, CRC Press, Cleveland, Ohio.